



**Concordia**  
UNIVERSITY

**TN-EMC-99-01**

March 31, 1999

Final Report

**NEAR FIELD COMPUTATIONS WITH MODEL HEADS  
AND FAR FIELD COMPUTATIONS FOR THE MODEL  
CELLULAR RADIO**

Dr. C.W. Trueman

Dr. S.J. Kubina

**FACULTY OF  
ENGINEERING  
AND COMPUTER  
SCIENCE**

TK  
6553  
T787  
1999  
#01

**IC**

**EMC LABORATORY**

DEPARTMENT OF ELECTRICAL AND COMPUTER ENGINEERING

7141 Sherbrooke St. West, L-AD-532

Montreal, Quebec, Canada H4B 1R6

Tk  
6553  
T787  
1999  
#1  
c-a  
S-Gen

**TN-EMC-99-01**

March 31, 1999

Final Report

**NEAR FIELD COMPUTATIONS WITH MODEL HEADS  
AND FAR FIELD COMPUTATIONS FOR THE MODEL  
CELLULAR RADIO**

Dr. C.W. Trueman

Dr. S.J. Kubina



---

Dr. S.J. Kubina, Eng.



---

Dr. C.W. Trueman, Eng.

Industry Canada  
Library - Queen

AOUT 20 2012  
AUG

Industrie Canada  
Bibliothèque - Queen

Prepared For:

Communications Research Centre  
CRC Contract No. U6800-9-0390

## Table of Contents

### Near Field Computations with Model Heads and Far Field Computations for the Model Cellular Radio

	Page
<b>Table of Contents .....</b>	<b>i</b>
 <b>1. Introduction .....</b>	 <b>1</b>
1.1 Project Objectives .....	1
1.2 The Portable Radio.....	1
1.3 Method of Analysis .....	2
1.4 Review of Previous Work .....	2
1.4.1 Near Fields .....	2
1.4.2 Measurement of the Far Fields.....	3
1.4.3 Creation of a Cell Model of an Anatomical Head.....	3
1.4.4 Creation of a Cell Model of the Phantom Head .....	4
1.5 Conference Papers Published in this Contract Period.....	4
1.5.1 ANTEM Conference .....	4
1.5.2 APS Wireless Conference .....	5
1.5.3 ACES Conference .....	5
1.6 Far Field Paper Prepared for Submission.....	5
1.7 Overview of the Present Report .....	6
 <b>2. Near Fields of the Handset Alone.....</b>	 <b>11</b>
2.1 FDTD Model of the Handset.....	11
2.2 Computation of the Handset Near Fields .....	11
2.3 Preparing Contour Maps of the Field Strength .....	12
2.4 Near Field Maps At the Antenna.....	13
2.5 Field At the Surface of the Case.....	14
2.6 Computed Fields at the Measurement Planes .....	15
2.7 Measurement of the Handset Near Fields .....	17
2.8 Scaling the Measured Data.....	17
2.9 Superimposing Contour Maps.....	18
2.10 Comparison of the Measured and Computed Contour Maps.....	19
2.10.1 At About 20 mm From the Antenna.....	19
2.10.2 At About 40 mm From the Antenna.....	20
2.11 About Contour Maps.....	22
2.12 Conclusion.....	23

<b>3.</b>	<b>Near Fields of the Handset and Box Head .....</b>	<b>48</b>
3.1	FDTD Model of the Handset and Box Head.....	48
3.2	The Computed Fields .....	49
3.2.1	Fields at 20 mm.....	49
3.2.2	Fields at 40 mm.....	50
3.3	Comparison with the Measured Fields.....	50
3.3.1	At 20 mm.....	50
3.3.2	At 40 mm.....	52
3.4	Conclusion.....	53
<b>4.</b>	<b>Near Fields of the Handset and Sphere Head.....</b>	<b>69</b>
4.1	The FDTD Model of the Handset and Sphere Head.....	69
4.2	Computed Near Fields of the Handset and Sphere .....	70
4.2.1	Computed Fields at 20 mm Distance .....	70
4.2.2	Computed Fields at 40 mm Distance .....	71
4.3	Comparison with the Measured Near Fields.....	71
4.3.1	Comparison at 20 mm Separation .....	72
4.3.2	Comparison at 40 mm Separation .....	73
4.4	Conclusion.....	74
<b>5.</b>	<b>Far Fields of the Handset Alone .....</b>	<b>90</b>
5.1	Cell Model of the Handset .....	90
5.2	Wire-Grid Model vs. FDTD Cell Model.....	91
5.3	Scaling the Measured Patterns .....	91
5.4	Comparison of the Measured and Computed Patterns .....	92
5.5	Conclusion.....	93
<b>6.</b>	<b>Far Fields of the Tilted Handset .....</b>	<b>98</b>
6.1	Tilting the FDTD Model of the Handset.....	99
6.2	Far Field Coordinate Transformation For Use With FDTD .....	99
6.3	Software for Coordinate Transformations.....	101
6.4	Verification of the Angle Transform Software .....	102
6.5	Tilted Handset Solved with FDTD.....	102
6.6	Tilted Handset Patterns Compared with Vertical Handset Patterns.....	103
6.7	Tilted Handset: Computed vs. Measured Radiation Patterns.....	104
6.8	Conclusion.....	105



<b>7.</b>	<b>The Head Phantom.....</b>	<b>117</b>
7.1	CT Scans .....	117
7.2	Identifying Tissue Types .....	118
7.3	Creating an FDTD Cell Model from the CT Scan Data Set.....	120
7.4	Cell Model of the Handset and Head in the Measurement Jig.....	121
7.5	The FDTD Model of the Phantom Head Oriented Vertically.....	121
7.6	Conclusion.....	122
<b>8.</b>	<b>Far Fields of the Handset and Phantom Head .....</b>	<b>129</b>
8.1	FDTD Model of the Tilted Head.....	129
8.2	Handset and Head Model Without the Bolts.....	129
8.3	Material Properties of the Phantom Cell Model.....	130
8.4	Bandwidth of the Cell Model .....	131
8.5	Handset Alone Patterns Compared to Handset and Head Patterns .....	131
8.6	Measured Patterns Compared with the FDTD Computation .....	133
8.7	Conclusion.....	134
<b>9.</b>	<b>Conclusions and Recommendations .....</b>	<b>145</b>
9.1	Conclusions and Comparisons with Previous Results .....	145
9.1.1	Near Field Measurements and Computations .....	145
9.1.1.1	The Measurement System.....	145
9.1.1.2	The FDTD Computation.....	145
9.1.1.3	The Scaling Method.....	146
9.1.1.4	Format For Computing the Measurements and the Computations .....	146
9.1.1.5	Improvement in the Agreement .....	147
9.1.2	Far Field Measurements and Computations.....	148
9.1.2.1	Vertical Handset .....	148
9.1.2.2	Handset at a Realistic Angle.....	149
9.2	Recommendations for Further Work.....	149
9.2.1	Near Fields .....	149
9.2.1.1	Contour Maps in Front Of and on the Far Side of the Head.....	149
9.2.1.2	Near Fields with the Phantom Head .....	150
9.2.1.3	Scaling the Computed Near Field.....	150
9.2.2	Far Fields.....	151
9.2.2.1	Error Bounds on the Measurements.....	151
9.2.2.2	Differences Between Measurements and Computations .....	151
9.2.2.3	Computed Patterns at Finite Range .....	152
9.2.2.4	Measurement of the Volumetric Radiation Patterns.....	152
9.2.2.5	Material Parameters of the Phantom Head .....	153
9.2.2.6	Explorations of the Radiation Patterns of the Handset Near the Phantom.....	153

9.2.2.7	Effect of the Hand.....	153
9.2.2.8	Realism of the Phantom Head .....	154
9.3	New Directions.....	154
9.3.1	PCS Frequencies .....	154
9.3.2	Real Cellular Telephone Handsets .....	155
9.3.3	Other Applications .....	156
9.4	Conclusion.....	156

<b>References .....</b>	<b>158</b>
-------------------------	------------

<b>Appendix 1 – Reference [13], “Portable Radio Handset Patterns in the Presence of a Model of the Head,” Trueman, Kubina, Roy, Lauber.....</b>	<b>160</b>
---	------------

<b>Appendix 2 – Reference [15], “Validation of FDTD Handset and Head Patterns by Measurement,” Trueman, Kubina, Roy, Lauber.....</b>	<b>169</b>
--	------------

<b>Appendix 3 – Reference [16], “Validation of the FDTD Near Fields of a Portable Radio Handset and a Simple Head,” Trueman, Kubina, Cule, Lauber.....</b>	<b>174</b>
--	------------

<b>Appendix 4 – “Radiation Patterns of a Portable Radio Handset and Simple Head Models,” Trueman, Kubina, Lauber, Roy .....</b>	<b>183</b>
---	------------

## Chapter 1

### Introduction

This is the Final Report in Contract Number U6800-9-0390. It reports work completed in the period April 1, 1998 to March 31, 1999. The current project carries on the work of previous projects[1,2,3,4,5], and prepares for the next phase of the project.

#### 1.1 Project Objectives

The major objective of the work is the investigation of the near field and far field of a portable radio such as a cellular telephone handset. The fields are of interest both for the handset operating in isolation, and near models of the human head. The Final Report prepared in March, 1998[1] opens with a detailed description of the projective objectives and this need not be repeated here. The specific objective of the present report is the comparison of computations of the field using the finite-difference time-domain(FDTD) method[6,7] against measured near and far fields. Specifically, the measured near fields of the handset alone, the handset and box head, and the handset and sphere head for all three components of the field will be compared with computations. The measured far fields of the vertical handset, the handset held at a realistic angle and the handset held near the phantom head will be compared with the computed far fields in this report.

#### 1.2 The Portable Radio

Fig. 1.1 shows the portable radio handset used in this study[8]. It has the approximate dimensions of cellular telephone handsets that were common in 1994 and is quite large compared to newer handsets. It represents a handset operating in the "analog" frequency band centered at 850 MHz. The handset has an internal, battery-operated oscillator at 850 MHz, as shown in Fig. 1.2. Hence the handset does not have an external feed cable used in previous measurements of the near field[3]. The batteries can operate the oscillator for about 1 hour. The oscillator delivers about 100 mW at 850 MHz. Fig. 1.3 shows the dimensions of the handset[9]. The model handset comprises an aluminum box measuring 5.35 by 1.74 by 16.77 cm, with a quarter-wave monopole on the top, near one corner.

In the "global" coordinate system, the head is oriented with its vertical axis parallel to the z axis. The operator of the portable radio faces in the +x direction. The operator holds the radio handset set in the right hand, with the antenna towards the rear of the handset. With the handset held vertically, Fig. 1.4 shows the orientation of the handset in the global coordinate system. The antenna is positioned along the z-axis or "vertical" axis, with the base of the antenna at the origin, and the antenna on the -x side of the handset case. When the handset is operated near a model of the head, it is held in the operator's right hand and so the head must be positioned in the +y half space in the

global coordinate system. Most of the work in this report maintains the handset vertical with the antenna on the  $z$  axis. Handsets are typically held tilted at about 65 degrees to the vertical, and results will be presented in Chapters 6 and 8 using this more realistic orientation.

### 1.3 Method of Analysis

This report will use the finite difference time domain(FDTD) method to determine the near fields and far fields of the handset[6,7]. The FDTD method has been reviewed for the purposes of this project in previous reports[1,2,3,4,5] and the review need not be repeated here. The specific FDTD code used was developed by C.W. Trueman from the Penn State FDTD-C code[10] and is called "FDTD PML". The Penn State code has been substantially changed and revised. It was a "scattering" code aimed at radar cross-section analysis. The ability to model a radiating antenna was added. The ability to model a sinusoidal generator was added. The feature of computing and reporting the steady state amplitude and phase of the near field was added to the code. The perfectly-matched layer absorbing boundary was added[11,12]. An efficient near-to-far zone transformation in the frequency domain was added, as a post-processing program called FARZONE.

In conjunction with FDTD PML, a program called EDITCEL was created for building and modifying cell models conveniently. Ref. [1] described the input file for EDITCEL, called a "make" file, that permits the input geometry to be described in global coordinates rather than FDTD cells. EDITCEL converts the input geometry to an approximately equivalent cell model for analysis by FDTD PML. EDITCEL allows the model to be examined and modified in  $xy$ ,  $xz$ , or  $yz$  cross-sections. In the present work, the feature of specifying planes of near field data has been added to the "make" file for processing by EDITCEL, and a post-processing program called NRFIELD has been developed to conveniently extract planes of near field data in the sinusoidal steady state.

### 1.4 Review of Previous Work

This section summarizes work previously reported that is relevant to the present report.

#### 1.4.1 Near Fields

In Ref. [3], extensive comparisons of computed and measured near fields were reported. The vertical component of the near field was measured for the handset alone, the handset and box head, and the handset and sphere head. The measurement was done in  $xz$  planes adjacent to the handset, in  $yz$  planes in front of the head, and in  $xz$  planes on the other side of the head from the handset. Each configuration was solved with the FDTD method and the computed vertical component of the field was compared with the measured field.

In this set of measurements, the handset's monopole antenna was fed with a cable from an external oscillator. The cable entered the handset at the bottom corner, opposite the location of the antenna. The vertical component of the near field was measured with a

probe intended for wideband EMC measurements. This probe tended to average the fields over a significant volume of space. The comparisons of the computations with the measurements showed quite a good correlation, but also showed some important differences. In particular, the  $E_z$  component has very high local values near the tip of the antenna, the top of the handset case, and the base of the case. The averaging effect of the measurement probe tended to round these maxima, leading to poor agreement between the measured and computed fields. Also, the feed cable tended to distort the field contours in the region of space near the cable.

The present work overcomes these difficulties. The handset is powered by an internal, battery-operated oscillatory, thus eliminating the feed cable. The probe used for the present set of measurements is designed for measuring the near field and averages the field over a much smaller region of space than that previously used. Also, in the present work, all three spatial components of the field were measured and will be reported and compared with the computation.

#### 1.4.2 Measurement of the Far Fields

Ref. [1] reported measured patterns done at CRC for the principal plane patterns of the handset alone, the handset and box head, and the handset and sphere head. Very good agreement was achieved between the measurements and the computed far fields. The handset was oriented vertically for this set of measurements. The present report repeats the measurement and computation for the handset alone to try to improve on last year's measurement and as a confidence check in the measurement system. This serves as a verification of the computation as well. Then measurements were done for the handset held in a realistic position, both without and with the phantom head. This report compares these measurements with computations.

#### 1.4.3 Creation of a Cell Model of an Anatomical Head

In Ref. [4] the process of developing an anatomically-based cell model of the head was begun by digitizing published sections of the head of a cadaver. In Ref. [1], a software program called "MKHEAD" or MaKe HEAD" was developed to assemble a cell model of the head from this "data base" of anatomical sections. The software setup permits the user to specify the cell size and the rotation angle of the handset to the vertical in the  $xz$  plane. The software is made complex by the fact that the head sections are not in parallel planes[1]. The resulting cell model of the head is somewhat cruder than we would like because the sections of the head are spaced as much as 1 cm apart, too far for an accurate cell model with 2.2 mm cells. The head was used for initial explorations of the patterns of the handset in Refs. [1] and [13].

In 1997 the development of a better anatomically-based head was undertaken based on the data of the "visible man" web site[14]. Every second cross-section was digitized, to provide a data base of sections spaced 2 mm apart. The MKHEAD program was adapted to the new data base, and permits the creation of cell models that are credible with 2.2 mm cells. The handset can be rotated in the  $xz$  plane relative to the head. This new anatomically-based cell model has not been used as yet except for initial exploratory calculations. It will not be described further in the present work.

To use this head model for future work, it would be necessary to adapt the MKHEAD software to permit a second rotation of the handset, about the global  $z$  axis, so that the handset could be positioned realistically relative to the head model. This is described in Chapter 7 for the phantom head, and similar geometric transformations could be used for the anatomical head.

#### **1.4.4 Creation of a Cell Model of the Phantom Head**

The phantom head was described in Ref. [1] and will be discussed in Chapter 7. To create a cell model of the phantom, detailed cross-sectional information was obtained by having the phantom CT-scanned. Ref. [1] describes a program called EDITMAP that was developed to identify the regions of skin, muscle, bone and brain tissue in each CT scan cross-section of the head. The present work improves the EDITMAP software considerably and then uses it to process all 117 CT scan sections to develop a data base of geometric information on the phantom head. A program called "MKPHANT" or MaKe PHANTom head was written by adapting the MKHEAD program mentioned above. The MKPHANT program initially permitted the rotation of the handset in the  $xz$  plane only. When our sponsors at CRC let us know that a second rotation about the  $z$  axis was to be used to position the handset realistically relative to the phantom head, the MKPHANT program was adapted to include that rotation as well. Chapter 7 describes the creation of a cell model of the phantom head using the EDITMAP and the MKPHANT programs.

### **1.5 Conference Papers Published in this Contract Period**

During this contract period, three conference papers were published and are included as Appendices 1,2 and 3 of this report. Their contents are briefly summarized in the following.

#### **1.5.1 ANTEM Conference**

A paper entitled "Portable Radio Handset Patterns in the Presence of a Model of the Head" was prepared by C.W. Trueman and presented at the Symposium on Antenna Technology and Applied Electromagnetics, Ottawa, August 9-12, 1998. The paper is included in this report as Appendix 1. This paper examines the principal plane radiation patterns of a portable radio handset at 850 MHz operating near models of the human head: the box, the sphere and an anatomical head. To validate the computed patterns, they are compared with measured radiation patterns from Ref. [1]. The paper demonstrates the excellent agreement for the handset alone and very good agreement for the handset and the box model of the head, and the handset and the sphere head model that was presented in Ref. [1].

The paper in Appendix 1 uses the anatomical model of the head that was discussed in Ref. [1] to have a preliminary look at the radiation patterns of the handset near a realistic head model. The anatomical head[1] uses 12 different tissue types: bone,

nerve, white matter, grey matter, average brain, skin, cartilage, gland, blood, muscle, eye and cerebral spinal fluid. The "anatomical" head is 60 cells or 13.23 cm across the ears, much smaller than the 20.68 cm sphere used in the measurements. The principal plane patterns of the handset and anatomical head are shown to be very similar to those of the handset near a sphere of size comparable to the head. The oral presentation compared the radiation patterns for the vertical handset and the anatomical head with the radiation patterns of the handset near the FDTD model of the phantom head. The two cases have surprisingly similar patterns, even though the two head models are quite different both in size and in detailed structure.

The present report does not present the computations done with the handset and the anatomical head model, other than in Appendix 1.

### **1.5.2 APS Wireless Conference**

A paper entitled "Validation of FDTD Handset and Head Patterns by Measurement" was prepared by C.W. Trueman and presented at the APS Wireless Conference in November, 1998[15]. The paper is reproduced in Appendix 2. This paper compares the principal plane radiation patterns of the portable radio handset at 850 MHz computed with the finite difference time domain method with the measured radiation patterns reported in Ref. [1]. The comparison was done for the handset alone, the handset and box head, and the handset and sphere head. The comparisons demonstrate the effect of simple head models on the radiation patterns of a vertical handset, and provide a validation of the FDTD computations. The oral presentation included some preliminary results of computations with the handset and both the anatomical head model, and the phantom head model.

### **1.5.3 ACES Conference**

A paper entitled "Validation of the FDTD Near Fields of a Portable Radio Handset and a Simple Head" was prepared by C.W. Trueman and presented at the Applied Computational Electromagnetics Society conference in March, 1999[16]. The paper is reproduced in Appendix 3. This paper contains some of the comparisons of the near fields between computations and measurements that are presented in this report. The vertical component of the field is compared between measurements and computations for the handset alone, the handset and box head, and the handset and sphere head. The good agreement that is shown in this report was demonstrated in the conference paper.

### **1.6 Far Field Paper Prepared for Submission**

The final report prepared for the 1997-98 year of this project[1] contained a substantial comparison of the measured principal plane patterns with FDTD computed patterns for the handset alone, the handset and box head and the handset and sphere head. The comparisons between the measured and the computed principal plane patterns was extended and quantified in a paper prepared by C.W. Trueman entitled "Radiation Patterns of a Portable Radio Handset and Simple Head Models", which was intended for

submission to a refereed journal. The contribution of J. Roy and W. Lauber in the form of the measured principal plane data was acknowledged by including them as co-authors. This paper is included as Appendix 4 in this report. Comments from co-authors required close scrutiny and review and have delayed the submission of this paper until the completion of this report. The Journal of the Canadian Society for Electrical and Computer Engineering will be asked to consider the paper for publication.

The paper in Appendix 4 examines and compares the far fields of the handset alone, the handset and the box model of the head, and the handset and the sphere model of the head. The thrust of the paper is to compare the errors seen between the measured and computed far fields for the three cases. The handset alone can be very precisely modeled with FDTD, hence the error between the measurement and the computation might be expected to be the least for this case. The box head shape can be modeled well with FDTD, but the spacing between the box head and the handset has to be approximated with an integer number of cells. Hence the agreement between the measurement and the computation might be expected to be poorer, because we are introducing a systematic error into the computational model. Further, for the sphere head, the curved surface of the sphere must be approximated with a staircase of cells. Hence the FDTD results from the sphere introduce further systematic error, and this might be expected to be seen in the comparison of the measured and computed far fields.

Tables 1, 2 and 3 in Appendix 4 compare the difference between the measured and the computed field strength in the maxima and in the minima of the principal plane patterns in the three cases. However, because of the relatively short distance between the handset and the measurement horns in the anechoic chamber, the measured minima in the patterns have poor accuracy and are not useful for evaluating the FDTD results. The measured maxima are expected to be reliable. The tables show that the agreement between the computation and the measurement is slightly better for the handset alone than the handset and either the box head or the sphere head. But the agreement is about the same between the computation and the measurement for the handset and the box head, and for the handset and the sphere head. We do not see a larger error due to staircasing the surface of the sphere. Evidently, a staircased model of the sphere's curved surface permits the prediction of the field strengths to an accuracy comparable to that of our measurements.

### 1.7 Overview of the Present Report

The present report has two major parts. Chapters 2, 3 and 4 are concerned with near fields, and Chapters 5, 6, 7, and 8 deal with far fields.

Over the summer of 1998, a new set of measurements of the near fields of the handset alone, the handset and box head, and the handset and sphere head, were carried out at CRC[17]. The field was measured in two  $xz$  planes, at 20 mm and 40 mm distance from the antenna to the tip of the probe. The near field section of this report compares this measured near field data with FDTD computed data, for all three field components:  $E_x$ ,  $E_y$ , and  $E_z$ . Chapter 2 presents the FDTD model of the handset using 2.205 mm cells, and then uses FDTD to compute the near fields in a plane through the antenna, and an  $xz$  plane through the surface of the handset case. Examining the field in these two planes lends insight into the fields of the handset that were measured. The near field of



the handset over planes at the distances used in the measurement is then presented, but over somewhat larger regions than are included in the measurement. Then the method used to scale the measured data to a level comparable to the computations is discussed. The chapter finishes with comparisons of the measured and computed  $E_x$ ,  $E_y$ , and  $E_z$  field components at 20 mm and at 40 mm from the probe tip to the antenna.

Chapter 3 presents the FDTD model of the handset and the box head, and then presents contour maps of the computed field of the handset at the 20 mm and 40 mm distances. These are compared with the handset-alone fields. Chapter 4 gives the cell model of the handset and the sphere head, and then compares the handset plus sphere near fields with those of the handset and box head, and of the handset alone. Then the measured  $E_x$ ,  $E_y$ , and  $E_z$  field components at 20 mm and 40 mm distance are compared with the computed fields.

The second part of this report is concerned with the far fields of the handset. In the summer and fall of 1998 a new set of far field measurements were done at CRC[18]. The measurement of the field of the handset alone held vertically that was reported in Ref. [1] was repeated to re-establish the measurement system and to try to clear up small problems with asymmetry in the measured field that were noted in Ref. [1]. The far fields of the handset in the mounting jig to be used with the phantom head were then measured, but without the head present. The jig holds the handset at a realistic angle to the head, tilted about 65 degrees from the vertical. Thus the principal plane patterns were measured for the handset alone, held at an angle that is representative of actual use. Finally, the phantom head was mounted in the jig and the principal plane patterns of the handset held at a realistic angle to the head were measured.

Chapter 5 presents a comparison of the computed far fields of the vertical handset with the measured far fields. In the computation the radiated power of the handset is found by calculating the far field over the whole surface of the radiation sphere, and then integrating the power flow density to find the radiated power. Radiation patterns are then presented in dB using the "isotropic level" field strength[1] as the 0 dB reference level. The measured principal plane patterns must be scaled to a level comparable with the computed data. Chapter 5 reviews the method presented in Ref. [1] for scaling the measured data to approximately the same radiated power as the computed data, based on the principal plane patterns alone. The chapter then compares the measured and computed patterns for the handset alone, held vertically.

Chapter 6 presents the geometry involved in using FDTD with the handset oriented vertically in the FDTD coordinate system to compute the radiation patterns of the handset as if it were held at our "realistic" angle. The coordinate transformations involved are somewhat complex and the measurement of the handset in the phantom jig, but with no phantom head, provides a convenient reference point for validating the coordinate transformation computation. This lends considerable confidence to this part of the computation process in dealing with the fields of the handset and the phantom head.

Chapter 7 discusses the process of deriving a cell model of the phantom head. In Ref. [1], it was reported that the phantom head was CT-scanned to obtain a set of 117 cross-sections to reveal the internal structure. Ref. [1] reported a computed program that was in the course of development to aid in the identification of the skin, muscle, bone, brain, and wood regions of material in each CT scan cross-section. In Chapter 7 it is

reported that this program was improved and modified, and then used to identify material types in each of the 117 CT scan cross-sections. This included comparing each cross-section to those just below and just above, to ensure reasonable continuity of the material regions from one layer to the next.

Chapter 7 then discusses the development of a cell model of a specified cell size, suitable for analysis by FDTD, from the material cross-sections. This is complicated by the fact that a new cell model is required for each angle of the handset to the head. Thus one cell model is used for the vertical handset, and a different cell model for the handset held at our realistic angle of approximately 65 degrees.

A cell model of the handset and head is then developed for the handset held at precisely the angles used in the CRC measurement, and in precisely the correct position relative to the head. The wood base of the phantom head, and the column supporting the base of the neck, and the wooden post supporting the chin were included in the model. Also, the fiberglass bolts, plexiglas washers and fiberglass nuts used to assemble the measurement jig were included in the model.

Chapter 8 presents a comparison of the computed handset and phantom head principal plane patterns with the measured patterns. The cell model including the four bolts proved far too large to analyze on the available computers and the bolts had to be removed from the model. It was possible to analyze the handset, head and full wood base supporting the head. The computation is regarded as preliminary because time did not permit the detailed verification of the model that is needed to ensure that it is the best possible representation.

The final chapter summarizes the results. The near field results are briefly compared to those obtained in previous work and report in Ref. [3]. The far field results are briefly contrasted to that reported in Ref. [1]. Some recommendations are made for further work.



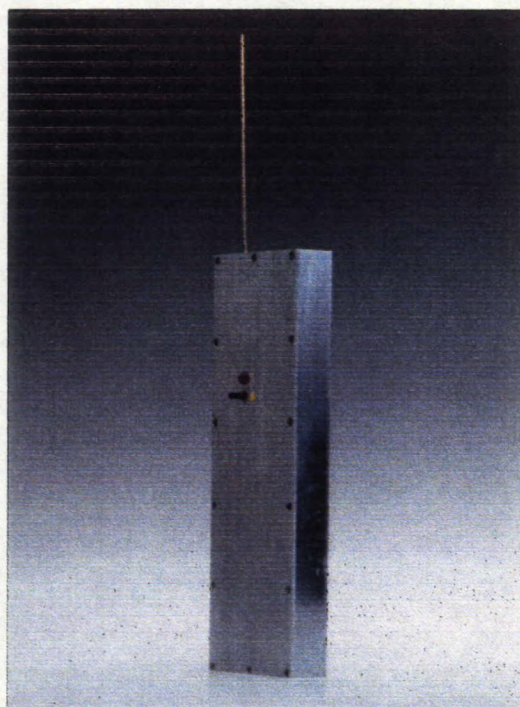


Fig. 1.1 The portable radio handset used in this study[8,9].

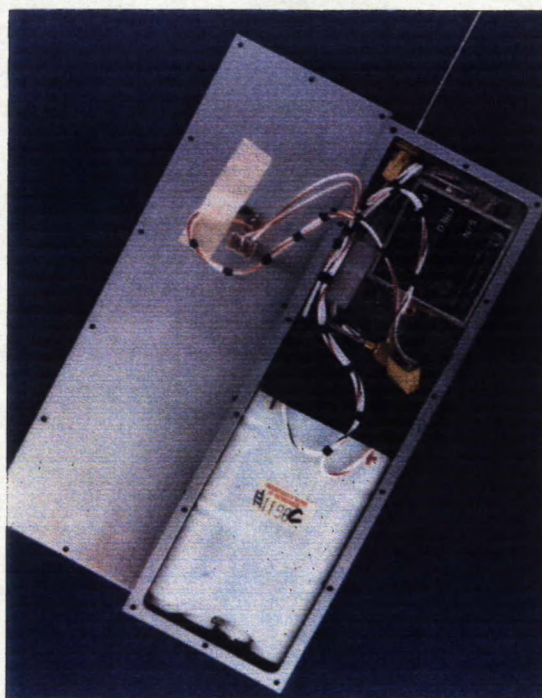


Fig. 1.2 The handset case houses the RF oscillator and a rechargeable battery pack[8].



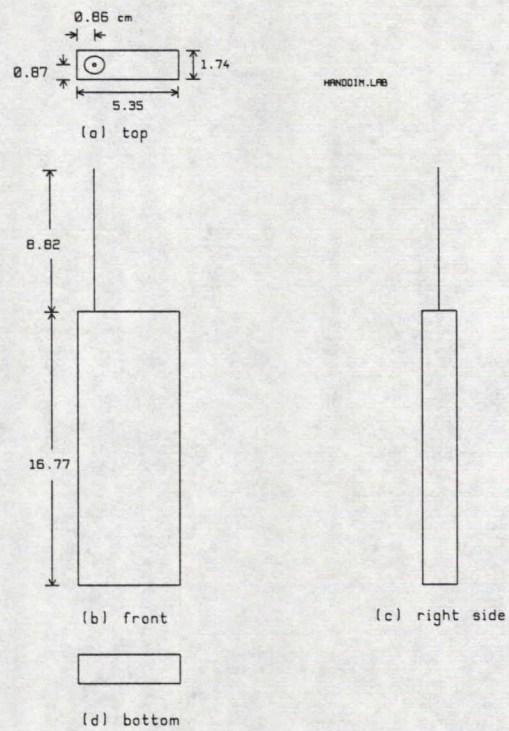


Fig. 1.3 The dimensions of the portable radio handset[9].

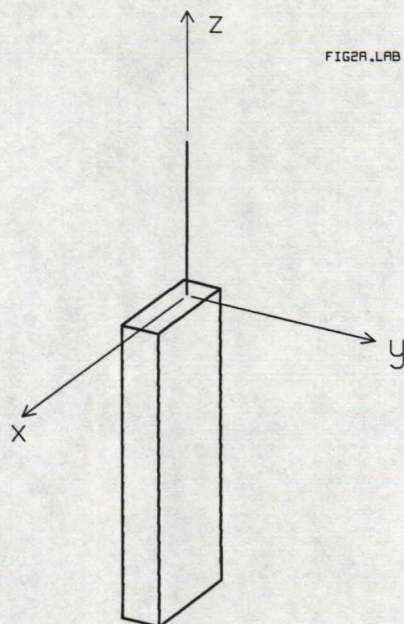


Fig. 1.4 The portable radio handset in the standard orientation in the coordinate system.



## Chapter 2

### Near Fields of the Handset Alone

This chapter presents a comparison of the measured and computed near fields of the handset in isolation. The handset is oriented vertically, as in Fig. 1.3. The details of the cell model of the handset are discussed. FDTD is used to solve the handset and contour maps of the computed near field of the handset are given for the three field components,  $E_x$ ,  $E_y$ , and  $E_z$ , in  $xz$  planes at various distances from the antenna. The location of the near field planes is shown in Fig. 2.1 for the 21.8 mm distance from the antenna. The method used to scale the measured near field data is presented. Finally, maps of the three components of the near field of the handset are compared with the CRC measured near fields[17].

The next two chapters will examine the near field of the handset near the box head and near the sphere head

#### 2.1 FDTD Model of the Handset

The handset used in this study was shown in Fig. 1.1 and 1.2. Its dimensions are 5.35 by 1.74 by 16.77 cm, with a monopole antenna of length 8.82 cm. The handset is modeled in this report with 2.205 mm cells, and so is 24 by 8 by 76 cells, with an antenna made up of 40 cell edges. Fig. 2.3 shows the cell model of the handset, with the cells drawn individually to give a sense of the fineness of the representation of the geometry. The handset was embedded in an FDTD cell space having 36 cells of free space separating the handset surfaces from the PML layers, to accommodate the region over which the near field is wanted. The overall cell space size is 96 by 80 by 188 cells, for a total of 1,443,840 cells. The layer of 6 cells on the outer surfaces of the cell space is used to implement the perfectly-match layer absorbing boundary. The FDTD PML code was run for 4096 time steps to reach sinusoidal steady state, although for the handset alone problem only 2048 steps would have been sufficient.

#### 2.2 Computation of the Handset Near Fields

The software system used in the computation of near fields described in Ref. [2] was extensively revised, and the new set of processing steps is shown in Fig. 2.2. The new setup is less cumbersome and less prone to human error in the preparation of input data files for the FDTD code. The complication in computing near fields arises because FDTD computes the near field at the cell faces, in  $xz$  planes that are integer numbers of cells from the base of the antenna. But the desired locations for the near field planes lie between FDTD cell faces. Hence interpolation is needed between two planes of FDTD data to find the near field at the desired location. The older software setup required the

user to calculate, manually, which FDTD cell planes were on either side of the desired location. Counting FDTD cell face locations is confusing. Since the count must be made from the base of the antenna, the locations in absolute numbers of cells changes if the whitespace layer thickness is changed. The user included "NEMAP" commands in the FDTD PML input file to ask for near fields at the required cell faces planes. After running FDTD, individual processing steps were used to interpolate between the FDTD cell face planes and remove the PML cells from the boundary of the near field data.

The revised software setup permits the user to specify the needed location for near field planes in global coordinates in centimeters. The software does the counting of FDTD cell planes, accounting for the whitespace thickness. Fig. 2.3 illustrates the steps used to produce a near field map in the revised setup. A file editor is used to construct a "mak" file such as "phone.mak", which specifies the geometry of the cell phone and head model, and where the near field maps are to be computed, all in global coordinates. A new command was created, MAKENE, that can be included in the "mak" file to request the computation of the near field at a plane specified relative to the location of the antenna on the handset. The EDITCEL program interprets the "mak" file and creates the FDTD cell model in a "bld" file for input to FDTD PML. The MAKENE command in the "mak" file causes "NE" commands to be included in the "bld" file requesting that FDTD PML compute the near field at planes of cell faces on either side of the location of the desired near field plane. Then FDTD PML is run to generate these planes of near field data as "tbl" files such as EZXZ0024.TBL and EZXZ0025.TBL in Fig. 2.3. A new program called NRFIELD was written to interpret the "mak" file to find the desired location of the near field map, then look for planes of field values computed by FDTD PML at appropriate locations on either side. NRFIELD then uses interpolation to obtain the near field values at the precise location requested by the user. Also, NRFIELD trims the PML layers from the near field data.

### 2.3 Preparing Contour Maps of the Field Strength

The next step in preparing a contour map of the computed field is that of normalization to the desired radiated power level. FDTD is used to compute the "conical cut" set of radiation patterns[1], which permits the power flow density to be computed over the radiation sphere. In turn, the power flow is integrated over the sphere to find the radiated power. The field strengths in the FDTD near field data are then scaled to a radiated power of 600 mW by running a program called "RENORM". This program multiplies all the data in a "tbl" file by a desired scale factor.

The contour mapping program called "CPLOT" is then used to prepare a contour map from the "tbl" file of field strength data. The map is written as a "lab" file, in which the map is described line-by-line for manipulation by other programs. To add the outline of the handset to the "lab" file, program "MKMAP" is run. This program determines the size of the field map from the "tbl" file, and positions the handset outline correctly within the "lab" file description of the contour map. The program called "LABLING" is used to draw the map with the handset on the computer screen, and then an "extended meta file" or "emf" file is created, containing the drawing, in a format suitable for import into the Microsoft WORD word-processing program. The "emf" file will print on any printer at

the highest resolution the printer has to offer, and is vastly superior to a bit map. It is also more convenient than a "postscript" file because the drawing can be seen within WORD, and can be printed on any printer, not just postscript-compatible printers.

## 2.4 Near Field Maps At the Antenna

This section examines the near field in an  $xz$  plane through the antenna. Fig. 2.4(a) graphs the  $E_x$  or horizontal component of the electric field. We will present contour maps of the electric field strength in decibels, with a reference level of 1 volt/meter field strength. The plane of the paper is the  $xz$  plane, hence the  $x$  direction is horizontal, across the page. Along the antenna,  $E_x$  is the radial component of the field. Hence  $E_x$  is proportional to the charge density on the antenna. As we approach the surface of the antenna,  $E_x$  gets larger and larger, and the contours are very closely spaced. The largest values of  $E_x$  are found near the tip of the antenna, where we have a 75 dB contour. It is interesting to note that there is a minimum or trough in  $E_x$  that starts at the top of the case and runs diagonally to the upper right edge of the contour map. The smallest contour found in this trough is 3 dB. Along the top and bottom edge of the handset case,  $E_x$  is tangent to the metal surface, and indeed it can be verified in the data underlying Fig. 2.4 that  $E_x$  falls to zero at these locations. It is interesting to note that  $E_x$  can be substantially larger than zero a very small distance from the case surface, but equal to zero at the case surface. The contours of constant  $E_x$  that are graphed in Fig. 2.4(a) ultimately become tangent to the surface as we approach the top surface or the bottom surface of the case. The top or bottom surface itself is a contour of zero field strength. Because the contour plotter cannot evaluate "zero field" in decibels; the user must specify the minimum dB value for which a contour is to be drawn.

Along the vertical edges of the case, field component  $E_x$  is normal to the surface, hence proportional to the surface charge density on the case. The surface charge density tends to be large where the surface current is changing rapidly with distance. We see large  $E_x$  values at the top and bottom corners of the handset case, with much smaller values towards the center of the case. At the top right corner, the largest contour is 57 dB. At the bottom right, there is a 54 dB contour. The smallest contour found near the surface is 39 dB on the right edge and 36 dB at the left.

The field strength has a minimum in the bottom center of the graph. This minimum extends vertically upward to meet the case at the bottom center of the case.

Our contour map includes a section through the center of the handset case. In the FDTD model the case is a solid metallic object. The field strength inside the case is equal to zero for all three field components everywhere inside.

Fig. 2.4(b) shows the  $y$  component of the electric field, which is perpendicular to the plane of the paper. The  $E_y$  field component tends to have many more contours than  $E_x$  or  $E_z$ . It becomes impossible to label the contours around the antenna in a meaningful way. The  $E_y$  field rises to a maximum value as we approach the antenna. There are many closely spaced contours; the largest contour found along the antenna is 78

dB, right at the tip of the antenna. The field falls rapidly in strength as we move away from the antenna, giving rise to the closely spaced contours seen in Fig. 2.4(b). Over all four surfaces of the case,  $E_y$  is tangent to the metallic surface and hence falls to zero at the surface.

We note that  $E_y$  has a deep minimum in the upper right corner of the contour plot. The smallest contour in the minimum is  $-45$  dB.

Fig. 2.4(c) shows the vertical component of the electric field,  $E_z$ . This component is strongest in value at the tip of the antenna, at the top of the case and at the base of the case. We are enforcing  $E_z=0$  along the wire antenna, hence the contours become closely spaced near the wire surface as the field rapidly drops in value to zero field strength. Fig. 2.5 enlarges this region of the contour plot for visibility. We find a 75 dB contour at the tip of the antenna. Near the tip the contours are very closely spaced as the field rapidly drops in value. The tip of the antenna carries a charge that behaves like a point charge. Hence near the tip there is a strong radially directed electric field. This is seen in the contour maps of  $E_x$  and  $E_z$  quite plainly. In Fig. 2.5,  $E_z$  has a 30 dB contour close to the antenna near the center of the antenna. At the base of the antenna,  $E_z$  has 66 dB contours. We are applying the voltage generator at this location, and these field contours represent the applied field that excites the antenna.

Returning to Fig. 2.4(c), along the top surface and the bottom surface of the handset case,  $E_z$  is normal to the surface and thus proportional to the charge density. At the top of the case there is a 51 dB field contour. At the bottom corners of the case there are two small 54 dB contours. Along the vertical sides of the case,  $E_z$  is tangent to the metallic surface and is expected to be equal to zero at the surface. There is a 15 dB contour close to the case surface, and then a group of very closely spaced contours very near the surface, in which the field falls to small values.

The general behavior of the three field components in the plane of the antenna in Fig. 2.4 carries over into planes adjacent to the handset case. In the next section we will examine the field in the plane of the broad face of the handset case.

## 2.5 Field At the Surface of the Case

Fig. 2.6 presents contour maps of the three field components at the surface of the case. The surface is located at  $y=-0.87$  cm in Fig. 1.3. Part (a) shows the  $x$  component of the field, which lies in the plane of the paper oriented horizontally. The general configuration of the field at the surface of the case is quite similar to that at the plane of the antenna. Adjacent to the body of the antenna, the field reaches a maximum of 51 dB, less strong than in Fig. 2.4, the plane through the antenna. There is a trough in the field starting at the top right of the handset case and running diagonally to the upper right. The field falls to about  $-1$  dB in the trough. Along the sides of the case,  $E_x$  is normal to the surface and has maxima near the corners of the case. The field is 60 dB near the upper right corner, and 57 dB at the lower right corner. It is 57 dB at the upper left, and 54 dB at the lower left. The field is much less towards the center of the sides of the case, falling to 42 dB a third of the distance from the bottom to the top of the case. There is a



trough in the  $E_x$  component at the bottom center of the case, where the field falls to 3 dB. Over the main body of the handset case,  $E_x$  is zero because this field component is tangent to the metallic surface.

Fig. 2.6(b) shows the  $E_y$  component of the field. This component is perpendicular to the plane of the paper. Near the antenna,  $E_y$  shows a maximum contour of 57 dB, though the field strength rises to almost 60 dB. There is a minimum in the region of the antenna feed, where the field strength falls to 39 dB. The field has local maxima near the top corners of the case. At the left corner there is a 51 dB contour; and near the right, a 45 dB contour. The  $E_y$  component is normal to the surface of the case and so is non-zero over the whole surface. It falls to a minimum contour of 30 dB about a third of the distance up from the bottom to the top of the case. The field has local maxima at the bottom corners of the case, of 51 dB at left and the same at the right corner.

Fig. 2.6(c) shows the  $E_z$  or vertical component of the field at the surface of the case. This field component is tangent to the metallic surface, so is zero over the whole surface of the case. The vertical field has a maximum at the tip of the antenna, of 51 dB, associated with the point charge at the antenna's tip.  $E_z$  has a maximum contour of 57 dB near the feed point of the antenna. The field rises to a contour of 60 dB at the upper right hand corner of the handset case. Along the vertical sides of the handset case,  $E_z$  falls to zero because it is tangent to the metallic surface and must be zero at the surface. Along the bottom of the case, the field has maxima near the corners of the case, of 57 dB at left and the same at the right hand corner.

The fields of the handset through the plane of the antenna in Fig. 2.4 and through the handset surface in Fig. 2.6 are useful for understanding the contour maps of the field at the distances from the handset surface that were used in the measurement.

## 2.6 Computed Fields at the Measurement Planes

In the following sections, measured data for the near fields of the handset will be compared with the FDTD computation in  $xz$  planes at 20 mm and 40 mm from the base of the antenna to the tip of the probe. Because of the configuration of measurement dipoles within the probe, the probe measures  $E_x$  and  $E_z$  at 1.8 mm from the tip, and  $E_y$  at 2.9 mm from the tip[17]. This section presents computed contour maps of the three field components at the same distances from the antenna as used in the measurement. The computed data is presented over a rather wider area than was measured.

Fig. 2.7(a) shows the computed  $E_x$  field at  $y=-21.8$  mm from the base of the antenna. The field bears a strong resemblance to the same component at the surface of the handset, in Fig. 2.6(a). We see strong fields along the antenna, and a trough in the field extending from the upper right of the handset case, diagonally out of the picture. The field strength has a 39 dB contour to the left of the antenna, and a 42 dB contour to the antenna's right. The field strength in the trough falls to about 1 dB. This field component is strong near the four corners of the case, with a maximum contour of 42 dB near the upper left corner, 45 dB near the upper right corner, and 39 dB near the bottom

corners of the case. The field has a trough at the bottom center of the case that extends vertically upward over the surface of the case and then runs diagonally out of the graph at the upper right.

Fig. 2.7(b) shows the  $E_y$  component of the field at  $y=-22.9$  mm from the base of the antenna, corresponding to the distance of the center  $y$  directed dipole antenna in the measurement probe to the base of the antenna. This field component is normal to the plane of the paper. The field has a maximum of 48 dB along the antenna. There is a maximum contour of 48 dB at the upper right corner of the handset case, and a maximum contour of 45 dB over the bottom of the case. The field falls to 36 dB over the lower center part of the handset case. We note there is a trough in the field in the upper right corner of the graph, where the field strength falls to -27 dB.

Fig. 2.7(c) shows the vertical component of the field at  $y=-21.8$  mm from the base of the antenna. The vertical component of the field has a 42 dB contour near the tip of the antenna, a 45 dB contour near the top of the case, and a 42 dB contour at the base of the case. Over the surface of the case the field has a 24 dB contour.

Fig. 2.8 shows the fields at "40 mm" from the antenna. Part (a) shows the  $E_x$  component at  $y=-41.8$  mm from the antenna. The field is similar but simpler than that in Figs. 2.6(a) or 2.7(a). There is a trough running from the bottom center of the contour map, vertically upward through the center of the case, and then diagonally from the upper right of the case. The field in the trough falls to about 12 dB near the bottom of the case, and is about 21 dB near the top of the case. The field has a deep minimum where it falls to about 3 dB, just above the right hand corner of the case.

The  $E_x$  component has a maximum of about 30 dB to the left of the antenna and about 33 dB to the right of the antenna. There is a minimum in the field above and to the left of the tip of the antenna, where the field falls to about 15 dB. The field has maximum contours of 36 dB to the left and to the right of the top of the handset case. There is a maximum contour of 30 dB to the left of the bottom of the case, and 33 dB to the right of the case bottom.

Fig. 2.8(b) shows the  $E_y$  component at  $y=-42.9$  mm from the base of the antenna. This component has a maximum of 39 dB near the top of the antenna, of 42 dB over the top of the handset surface, and 39 dB over the bottom of the handset surface. There is a minimum in the field of about -21 dB at the upper right of the graph, and of 3 dB at the upper left along the edge of the graph.

Part (c) shows the vertical component,  $E_z$ , at  $y=-41.8$  mm from the antenna. There is a maximum contour of 33 dB near the antenna tip, of 39 dB over the top of the case, and of 36 dB over the case bottom. The field strength over the center of the case has a 30 dB contour.

The following sections briefly describe the measurement of the near field of the handset, and then present a comparison of the measured near fields with the computations in Figs. 2.7 and 2.8.

## 2.7 Measurement of the Handset Near Fields

The handset near fields were measured using a "DASY-2" three-axis probe[19]. Fig. 2.9 shows the probe and the handset, held at its base in a styrofoam block. The probe is a plexiglas wand which has three small, orthogonal dipoles in the tip. The dipoles measure the magnitude of each of the three components of the near field. The dipoles are terminated with Schottky diodes, which are connected with high-resistance lines to a battery-operated data acquisition unit at the base of the probe. The signals are then sent via a fiber-optic cable to a computer plug-in card. We note that the probe does not measure  $E_x$ ,  $E_y$ , and  $E_z$  at exactly the same point. Components  $E_x$  and  $E_z$  are measured at slightly offset points in the same  $xz$  plane, a distance of 1.8 mm from the tip of the probe. Field component  $E_y$  is measured in an  $xz$  plane 1.1 millimeters further back, at a distance of 2.9 mm from the tip of the probe.

The probe was moved over the measurement plane using an Orbit Advanced Technologies planar scanner. The scanner was covered with 12 inch absorber as much as possible. Fig. 2.10 shows the planar scanner, and the probe mount assembly, which contains the data acquisition unit. The positioning mechanism was covered with three-inch absorber, not shown in Fig. 2.10. The measurement was carried out[17] in an anechoic chamber 2.5 m in height and 3.74 m in width and depth. The ceiling and walls were lined with 12 inch thick absorber.

The 850 MHz oscillator in the handset is powered by a rechargeable battery, with a life of about 2 hours, sufficient to measure a plane of the size roughly 15 cm in width by 30 cm in height. The oscillator output declines over the course of a measurement. The change in field strength over time was monitored and recorded, and the measured data presented in this paper has been compensated to account for declining battery power[17].

## 2.8 Scaling the Measured Data

The measured fields must be scaled to correspond in level to the computation. This is illustrated in Fig. 2.11. At the upper left we have a computed contour map of  $E_z$  as a function of  $x$  and  $z$ . At the upper right we have the corresponding measured contour map, unscaled. The area of the measured map is smaller than that of the computed map. To scale the measured data to a level corresponding the computed data, a procedure called "tie line normalization" was used. A "tie line" is defined, which is common to both the measured and computed data. This works best if the tie line is as far from the handset as possible; a line up the left side of the contour map works well. The field strength as a function of distance along the tie line is extracted from both the measured and the computed contour map, as shown at the bottom of the figure. We see that for this data set, the field strength in the unscaled measured data are far larger than in the computed data. Fig. 2.12 illustrates the idea that by multiplying the measured data by various factors, we can move the measured curve down on the graph until it coincides with the computed curve. A scale factor of about 0.10 works well. The RMS field strength along the tie line can be used to choose the scale factor systematically. The RMS field strength is defined as

$$E_{RMS} = \sqrt{\frac{1}{L} \int E^2 dz}$$

where  $L$  is the length of the tie line and the integration is along the tie line. The tie line was chosen as the left-hand edge of the computed contour map in Fig. 2.11, at  $x=-7.277$  cm, from  $z=-18.01$  cm to  $z=11.95$  cm. If  $E_c$  is the RMS field along the tie line in the computation, and  $E_m$  the RMS field in the measurement, then the measured data is scaled by  $E_c/E_m$ . Tie-line normalization aligns the measured and computed contours to approximately the same level at the left edge of the contour map. If the maps are in reasonable agreement, the remaining contours will then align well.

An alternate procedure was used in Ref. [3]. The process computes the RMS field strength over the entire contour map, which we can call "area normalization". This tends to weight the fields in the region of the feed point of the antenna heavily. If the contour maps are very similar, area normalization works as well as tie line normalization. But if the maps agree poorly, then area normalization can be quite misleading when the cause of the misalignment is sought. It was found that tie line normalization is a much better diagnostic tool when contour maps disagree.

Tie line normalization has been used throughout this report to scale measured contour maps to the same level as computed maps. In the following section and the following chapters, measured and computed maps of all three field components are compared. In general the scale factor for the measurement has been found from the contour map of the vertical component,  $E_z$ , and then the same scale factor used for the  $E_x$  and  $E_y$  components. Also, when maps are drawn at distances of 20 and 40 mm, the scale factor has been found from the vertical component at 20 mm, and the same scale used for the maps at 40 mm as well.

## 2.9 Superimposing Contour Maps

In Ref. [3], measured and computed contour maps were compared by drawing the measured map at the top of the page, and the computed map at the bottom, nearly the same size. In this format it is difficult to see whether the two contour maps correspond precisely, or if the contours are shifted a little or a lot from one map to the other. For the present report contour maps will be superimposed, one on the other, for a direct comparison, as in Fig. 2.13. The contour plotter CPLOT permits contour maps to be written as a graphical image file called a "lab" file. Thus a "lab" file is created for the computed contour map, and for the measured contour map. A program called "TWOMAPS" was created which reads each of these graphical image files, and does the necessary distance scaling and shifting to superimpose the two maps, one on the other. The computed map is drawn in light green; and the measured in black. These colors print quite well on a monochrome printer, showing the measured data boldly, with the computed data "in the background" but still quite visible for comparison.

It was found that a considerable effort was required to hand-edit the superimposed contour maps to make the comparison effective. Because the computed maps cover a much larger area than the measured maps, the computed data beyond the edges of the measured map had to be trimmed manually. Also it was found that the contour labels

often coincided in position between the computed and measured map, and so contour labels had to be laboriously moved, one by one, to separate them. The result is a quite effective comparison of the measured and computed contours.

## 2.10 Comparison of the Measured and Computed Contour Maps

Figs. 2.13 and 2.14 compare the measured and computed fields at 20 and 40 mm from the antenna, respectively. As before, we will present contours of the electric field strength in decibels with a reference level of 1 volt/meter.

### 2.10.1 At About 20 mm From the Antenna

In Fig. 2.13(a), the measured and computed  $E_x$  are compared at  $y=-21.8$  mm from the antenna. This is the horizontal component of the field, in the plane of the page. To the left of the antenna, both the measured and computed data have 39 dB contours; however the measured (black) contour is rather smaller in enclosed area than the computed (gray) contour. The 36, 33, 30 and 27 dB contours align well in this region. To the right of the antenna, the measured 42 dB contour is of about the same area as the computed contour, but the measured contour is rather closer to the antenna. The 39, 36 and 33 dB contours are also closer to the antenna in the measurement than in the computation. To the left of the top of the handset case, the measured data has a small 42 dB contour, whereas the computed data has a much larger 42 dB contour. Thus the computed field rises to somewhat higher values in this region than does the measured. The 39, 36 and 33 dB contours are closer to the handset in the measurement than in the computation, reflecting somewhat larger field strengths in the computation than in the measurement in this region. To the left of the bottom of the handset case, the computed data has a 39 dB contour but the measured data never gets as large as 39 dB. The 36, 33 and 30 dB contours are closer to the handset in the measurement, indicating that the computed data is larger in value over this region.

To the right of the top of the handset case, both the measurement and the computation have 45 dB contours. The 42, 39 and 36 dB contours align well. At the bottom right of the handset case, both the computed and measured data have a 39 dB contour, and the two data sets align well. The 36 dB contours also align well.

A striking feature of the computed data is the trough in the field which starts at the bottom center of the contour map, runs vertically upward over the center of the handset, and then exits diagonally at the upper right of the contour map. This feature is seen clearly in both the measured and the computed data. Because the closely-spaced contours make it difficult to superimpose meaningful labels on the contours, a quantitative comparison is difficult based on Fig 2.13(a). Where the trough exits the contour map at the upper right, the measured field falls to 15 dB. The computed field falls to 12 dB. Over the center of the handset case, the measured field falls to 6 dB; and the computed field also falls to 6 dB. However the location of the region of minimum field is much nearer the left edge of the case in the measurement than in the computation. These field strengths were read from the contour map by carefully counting the contours.

Fig. 2.13(b) compares the measured and computed  $E_y$  component at  $y=-22.9$  mm, the location of the  $y$  directed dipole in the measurement probe. This field component is

perpendicular to the plane of the page. Over the antenna, the computed data has a 48 dB contour. The measured data, however, is never as strong as 48 dB. The measured and computed 45 dB contours align towards the lower part of the antenna, but disagree near the top of the antenna. The measured and computed 42, 39, 36 and 33 dB contours are roughly in alignment as we move towards the left of the antenna, but comparing the 30 and 27 dB contours shows that the computed contours are clearly closer to the antenna than are the measured contours. To the right of the antenna, the measured contours are closer to the antenna than are the computed contours. Near the upper right in the map the measured contours are falling about half way between the computed ones.

Over the upper right corner of the handset case, both the measurement and the computation show 48 dB contours, with the computed contour larger than the measured, suggesting that the computed field rises to a higher peak than does the measured field. The 45 and 42 dB contours align well over the handset case, but poorly near the top right corner of the handset. To the left of the top of the case, the computed contours tend to be closer to the case than the measured contours, although the general shape of the contours is quite similar. To the right of the top of the handset case the contours align quite well.

Over the center of the case, there is reasonable alignment of the 45, 42, 39 and 36 dB contours. The 36 dB contour even shows the same general shape near the center of the case in both the computation and the measurement. At the bottom of the case both the computation and the measurement have a 45 dB contour with the computed contour rather larger in enclosed area. To the left of the bottom of the case the computed contours are rather closer to the case than are the measured contours. To the right of the bottom of the case the contours align quite well.

Fig. 2.13(c) compares the measured and computed vertical component of the field at 21.9 mm from the antenna. Near the tip of the antenna, both the measured and computed fields have a 42 dB contour that aligns very well. The 39 and 36 dB contours also align quite well, except over the antenna where the measured contours are closer to the tip. To the left of the antenna, the 36, 33 and 30 dB contours align well. To the right of the antenna, computed contours are closer to the antenna than the measured contours. Near the top of the case, both the measurement and the computation have 45 dB contours that superimpose quite well. The 42, 39 and 36 dB contours also superimpose very well. Over the body of the handset, the measured data has a large 27 dB contour but the field never falls as low as 24 dB. The computed data has a large 24 dB contour. The fields over the handset case are about 3 dB lower in the computation than in the measurement. This may be at the noise level for the probe system. At the bottom of the handset case, the measured field has a 42 dB contour, and the computed data a rather larger 42 dB contour, indicating a stronger maximum field in the computation than in the measurement. The 39 dB contour also encloses a larger area in the computation, and the 36 and 33 dB contours enclose a slightly larger area.

### 2.10.2 At About 40 mm From the Antenna

Fig. 2.14 shows the fields with the probe tip at 40 mm from the base of the antenna. Part (a) shows the  $E_x$  component at  $y=-41.8$  mm. The trough running from the bottom center upward over the handset case, and out of the picture at the upper right is still prominently seen. The measured field in the trough at the upper right is 15 dB. The

computed field has many closely spaced contours in the trough, and falls to 3 dB. The field in the trough near the bottom center of the case has a very small 12 dB contour in the measurement, and falls to 12 dB in the computation as well. However the location of these minima is somewhat different. The measured data has a point with zero dB value near the bottom of the case, much smaller than in the computed data. This point may be in error.

The field to the left of the antenna has a 30 dB contour in the computation, but the largest contour in the measurement is 27 dB. The 24, 27, and 30 dB contours correspond approximately in position. To the right of the antenna, the measurement and the computation both have 33 dB contours of about the same size. However, the measured contour is closer to the antenna. The 30 dB contour corresponds reasonably between the measurement and the computation.

To the left of the top of the case, the computed field has a large 36 dB contour, and the measured field a much smaller 36 dB contour, suggesting that the computed field has a larger maximum value. The 33 and 30 dB contours are also larger in the computation than in the measurement. To the right of the case, the measured 36 dB contour is about the same size as the computed contour, but the measured contour is closer to the center of the handset.

At the bottom left of the handset case, the measured field has a 30 dB contour which is much smaller than the computed 30 dB contour. At the lower right of the case the 33 dB contours correspond quite well.

Fig. 2.14(b) compares the measured and computed  $E_y$  components. Over the antenna, both the measurement and the computation have a 39 dB contour. The computed contour is larger in area. As we move away from the antenna to the left, the 36, 33, 30, and 27 dB contours remain quite well aligned. To the right, however, the contours tend to fall out of alignment. Thus the measured contours to the right of the antenna are closer to the antenna than are the computed contours.

Over the top of the case, both the measured and the computed field have a 42 dB contour. The computed contour is bigger in area. As we move to the left away from the top part of the handset, the 39, 36, 33 and 30 dB contours stay quite well aligned. To the right of the top of the handset, the contours tend to fall out of alignment, with the measured contours closer to the handset.

At the bottom of the case, both the measurement and the computation have a 39 dB contour, with the computed contour somewhat larger in enclosed area. To the left of the handset case, the computed 33, 30, 27 and 24 dB contours are closer to the case. To the right of the bottom of the handset, the 36 and 33 dB measured contours are closer to the case.

Fig. 2.14(c) shows the vertical component of the field at 41.8 mm from the base of the antenna. At the tip of the antenna, the measurement and the computation have 33 dB contours, with the measured contour rather larger in area and in fact joining to the 33 dB contour further down the antenna. The 30 dB contour to the left of the antenna aligns reasonably well. To the right of the antenna, the computed 30 and 27 dB contours are closer to the antenna. At the top of the handset case, both the measurement and the computation have a 39 dB contour, which are roughly the same size. The 36 and 33 dB contours align reasonably well, too. Over the body of the handset the computed field falls

below 30 dB, whereas the measured field has no 30 dB contour over the handset case. At the bottom of the handset case the measurement and the computation have 36 dB contours, with the computed contour larger in area. The nearby 33 dB contour is also somewhat larger in area in the computation than in the measurement.

## 2.11 About Contour Maps

Concerning contour mapping, the data in this and subsequent chapters has been presented as black contour lines on a white background. This is much less satisfactory than color contour mapping, in which the field strength is represented with a false color scale. The line drawing format was chosen as a trade-off between the cost reproduction of the report and the need to include a great many contour maps. A color map has much more impact in depicting the structure of the field than does a contour map. The color maps can include labeled contour lines to make the information more quantitative. However, the cost of color reproduction is still too high to include many color pages in a report.

Further limitations of contour mapping concern the need to provide many contours coupled with the difficulty of labeling closely spaced contours, and the depiction of the maximum and the minimum field. We have chosen to include contours separated by 3 dB in the maps, although this makes some maps rather crowded. Where contours are too closely spaced to permit meaningful labeling, the reader can often count up or down in 3 dB steps from a labeled contour. In the minima or maxima, where contours are too closely spaced to count, the value of the maximum or minimum contour has often been given in the text. Contour maps are poor at depicting the maximum field. Where a region is enclosed by, say, a 33 dB contour, and there are no contours inside, there is no way to know how strong the field gets within that region. As long as the field does not reach 36 dB there will be no contour inside.

In examining field strength data "live" on the computer, the contour map is not a static object as it is on a printed page. The contour mapping program CPLOT encourages the user to interact with the contour map. Thus a region of the map where the contours are very closely spaced can be "zoomed" or expanded to fill the screen and the detailed structure of the field can be studied. The user can click the mouse anywhere on the contour map to "read back" both the position coordinates and the field strength at that position. This allows the field strength within a region to be explored interactively. And of course, on the computer screen color maps can be used at no additional cost, except in taking longer to draw.

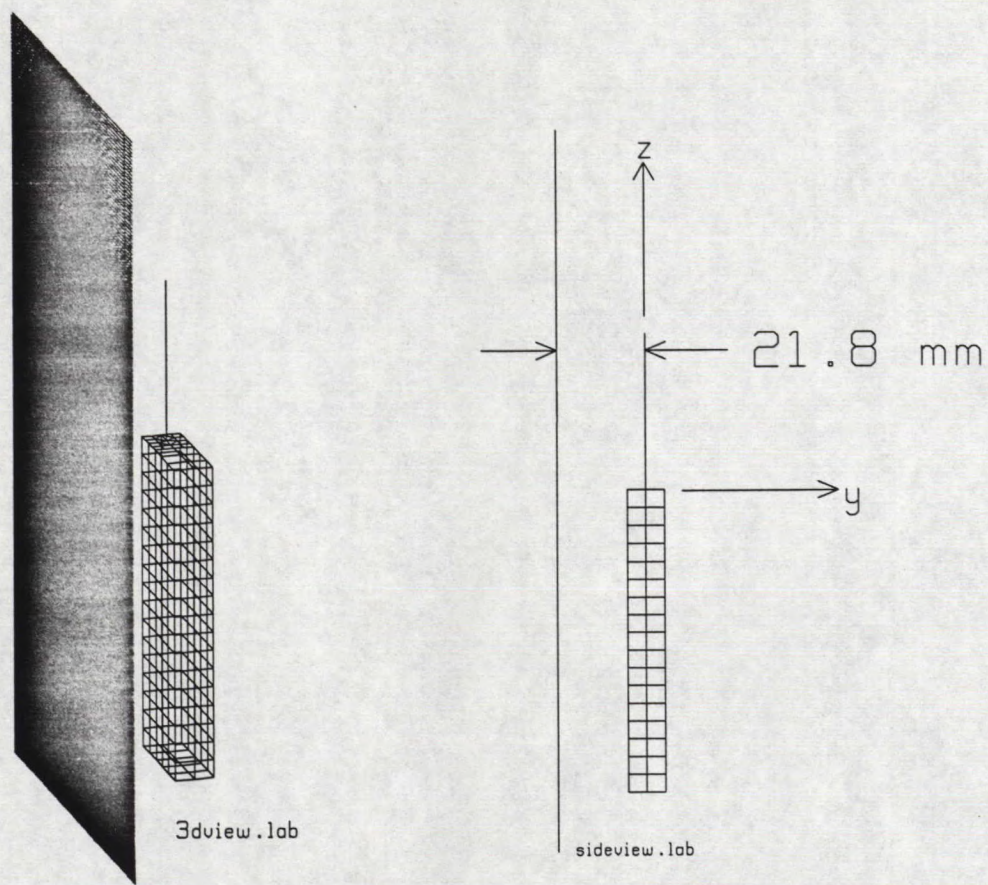
Color maps are *not* effective for comparing computed and measured data. This is because the comparison is best done by plotting the computed and measured data on the same axes. By superimposing two contour maps a direct comparison can be made, as in Figs. 2.13 and 2.14. This format will be used to compare computed and measured data in the following chapters.



## 2.12 Conclusion

This chapter has examined the near field of the handset at about 20 and 40 mm from the base of the antenna. The degree of agreement achieved in Figs. 2.13 and 2.14 is the best that has been obtained in this project. In all cases, the overall nature of the field corresponds very well between the measurement and the computation. In many cases the details of the contours are very close between the measurement and the computation.

The following chapters extend the comparison to the handset and simple head representations.



(a) 3d view.

(b) front view

Fig. 2.1 The planes in which we will graph the near field are  $xz$  planes parallel to the broad face of the handset case.

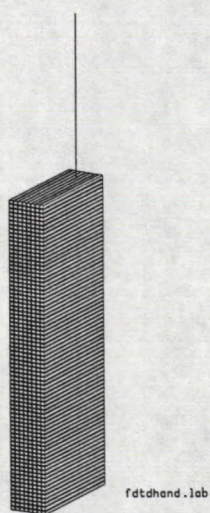


Fig. 2.2 The FDTD model of the handset.

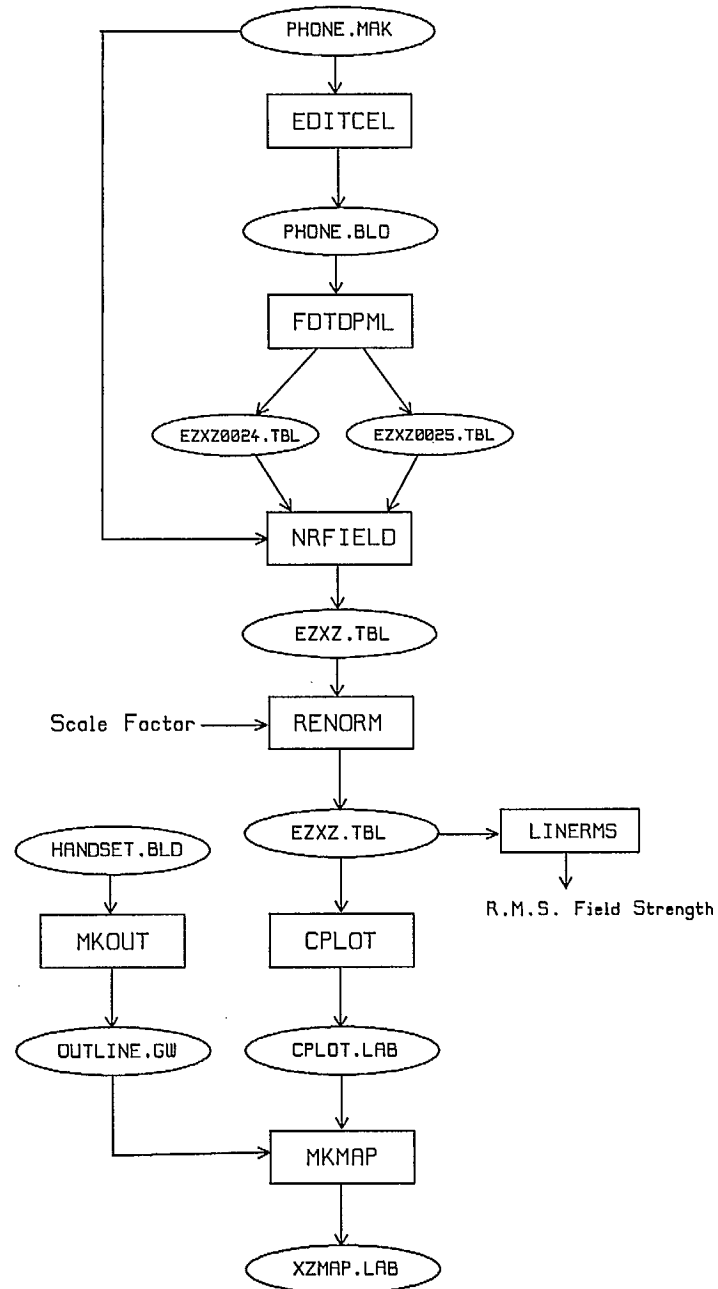


Fig. 2.3 The processing steps used to compute a map of near field data.



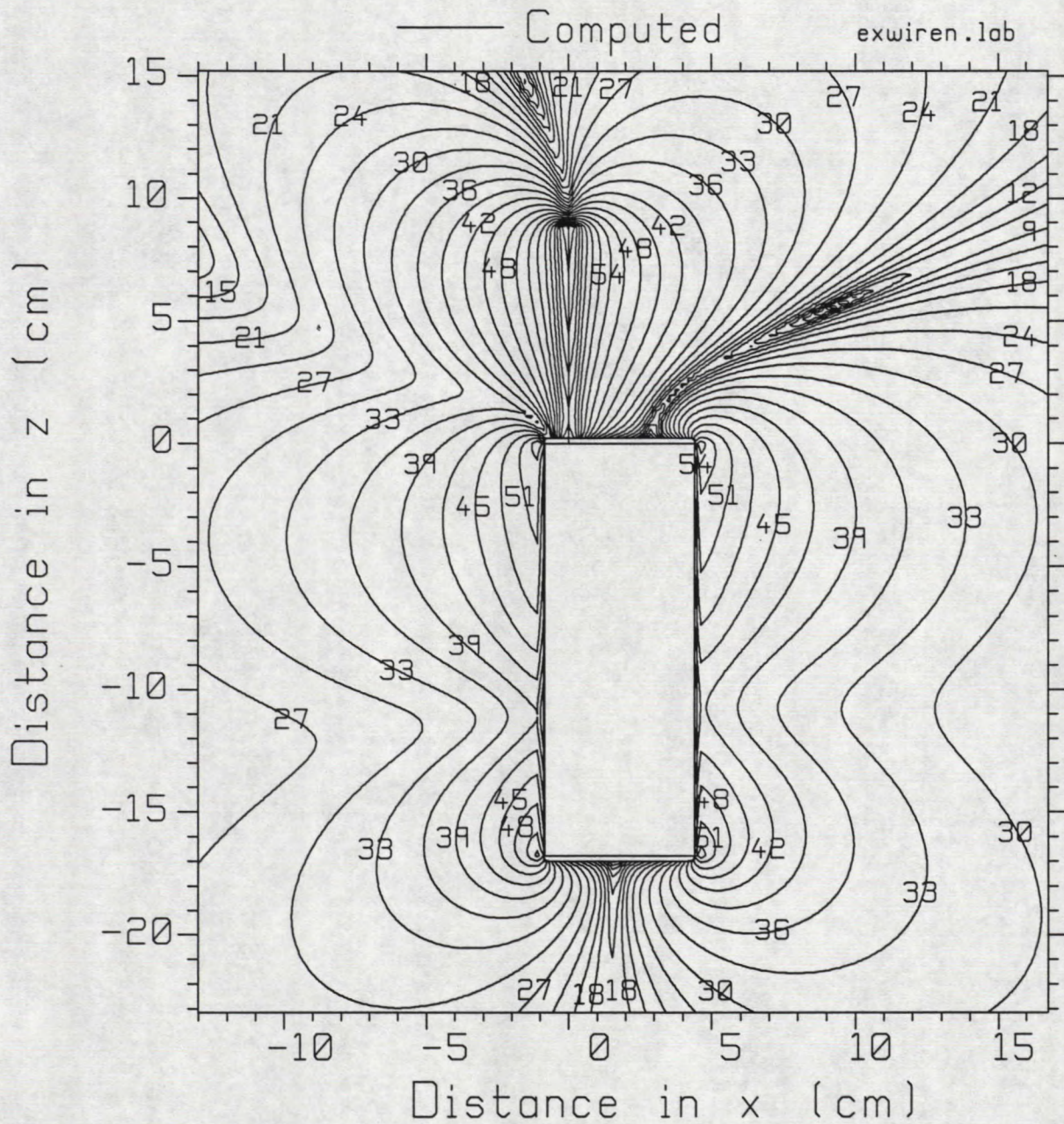


Fig. 2.4(a) The  $E_x$  component of the field in an  $xz$  plane through the antenna.



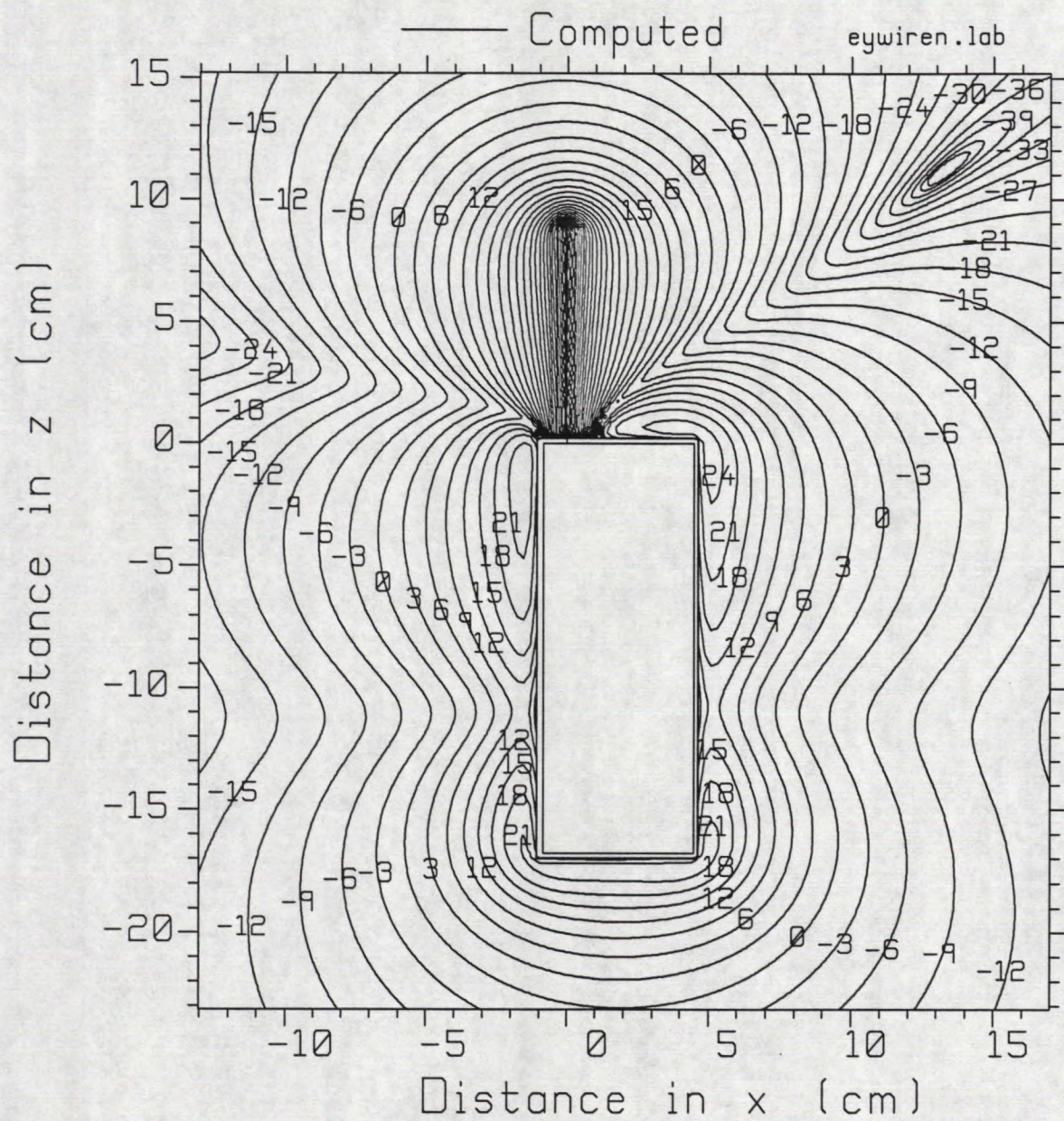


Fig. 2.4(b) The  $E_y$  component of the field in an  $xz$  plane through the antenna.



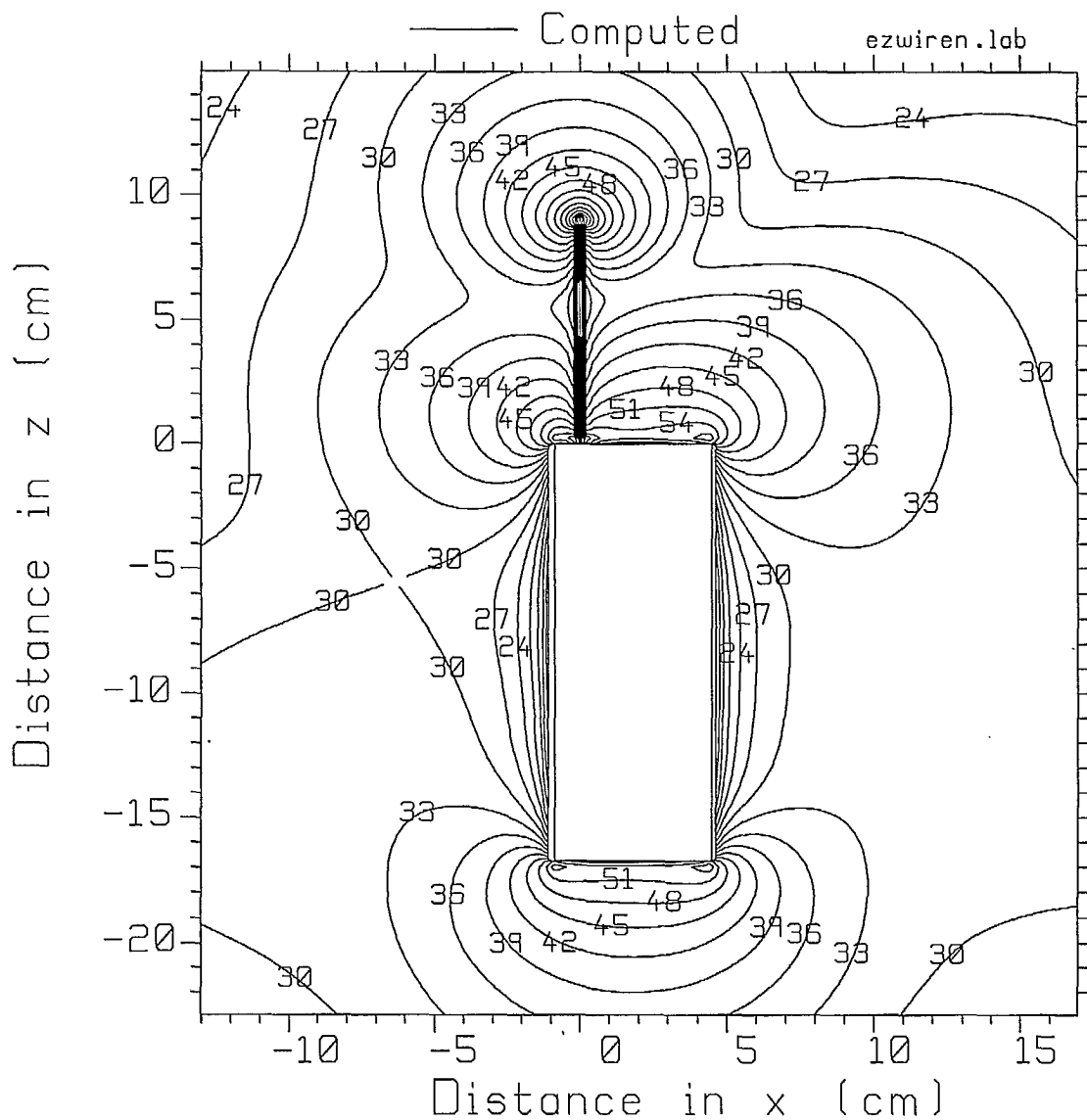


Fig. 2.4(c) The  $E_z$  component of the field in an  $xz$  plane through the antenna.

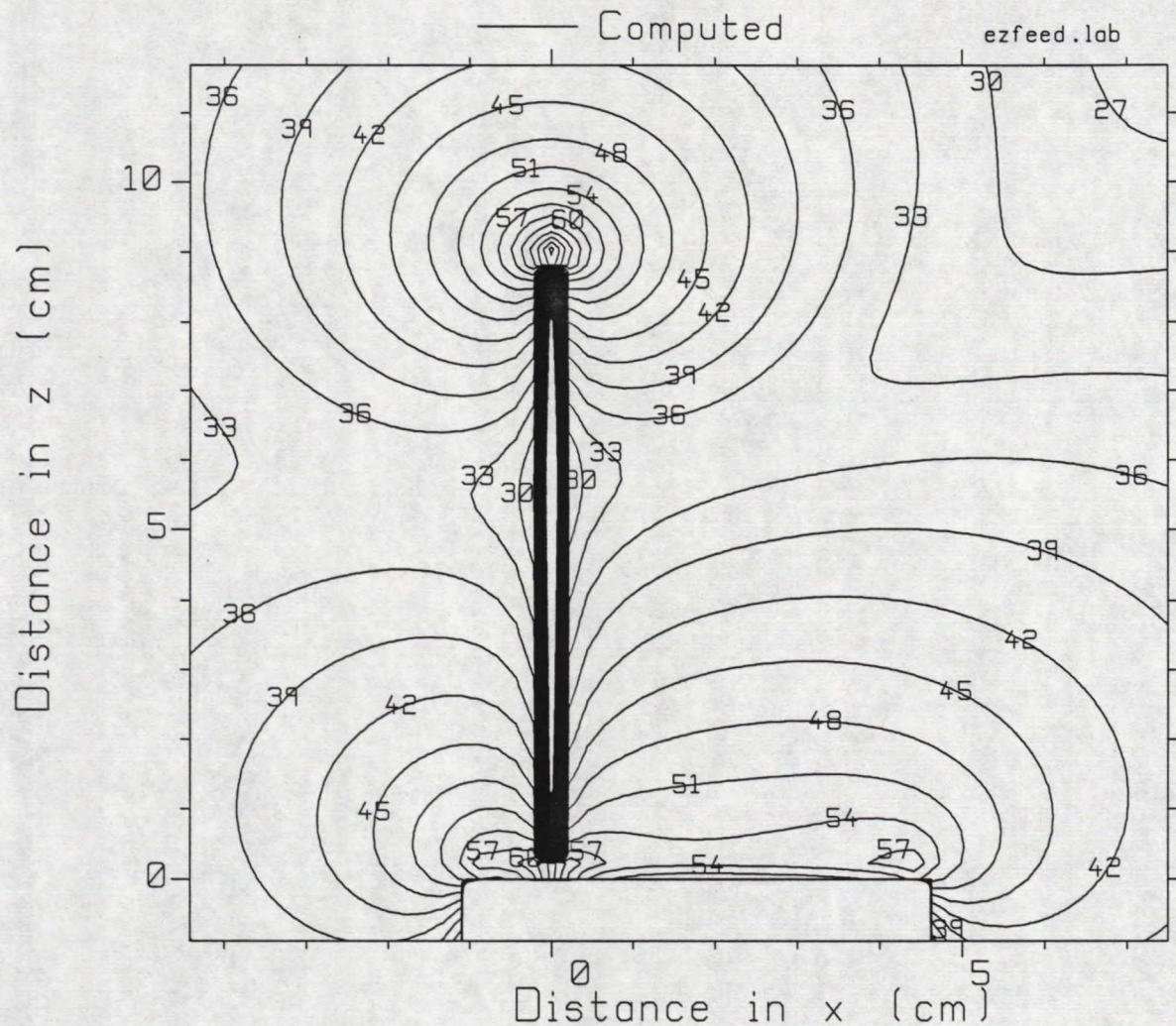


Fig. 2.5 The  $E_z$  component in the region of the tip of the antenna.



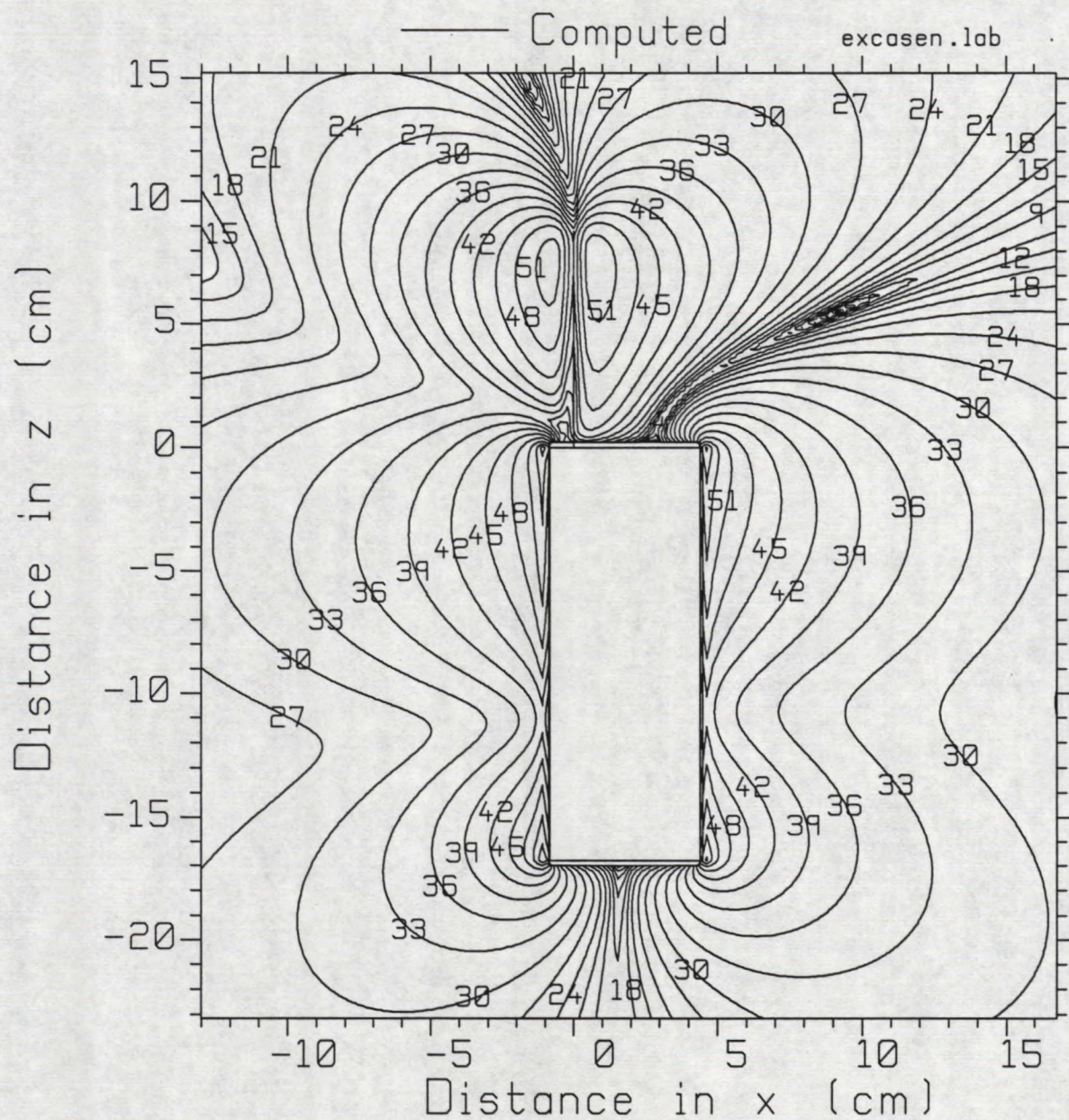


Fig. 2.6(a) The  $E_x$  component of the field in an  $xz$  plane through the surface of the case, at  $y = -8.7$  mm.



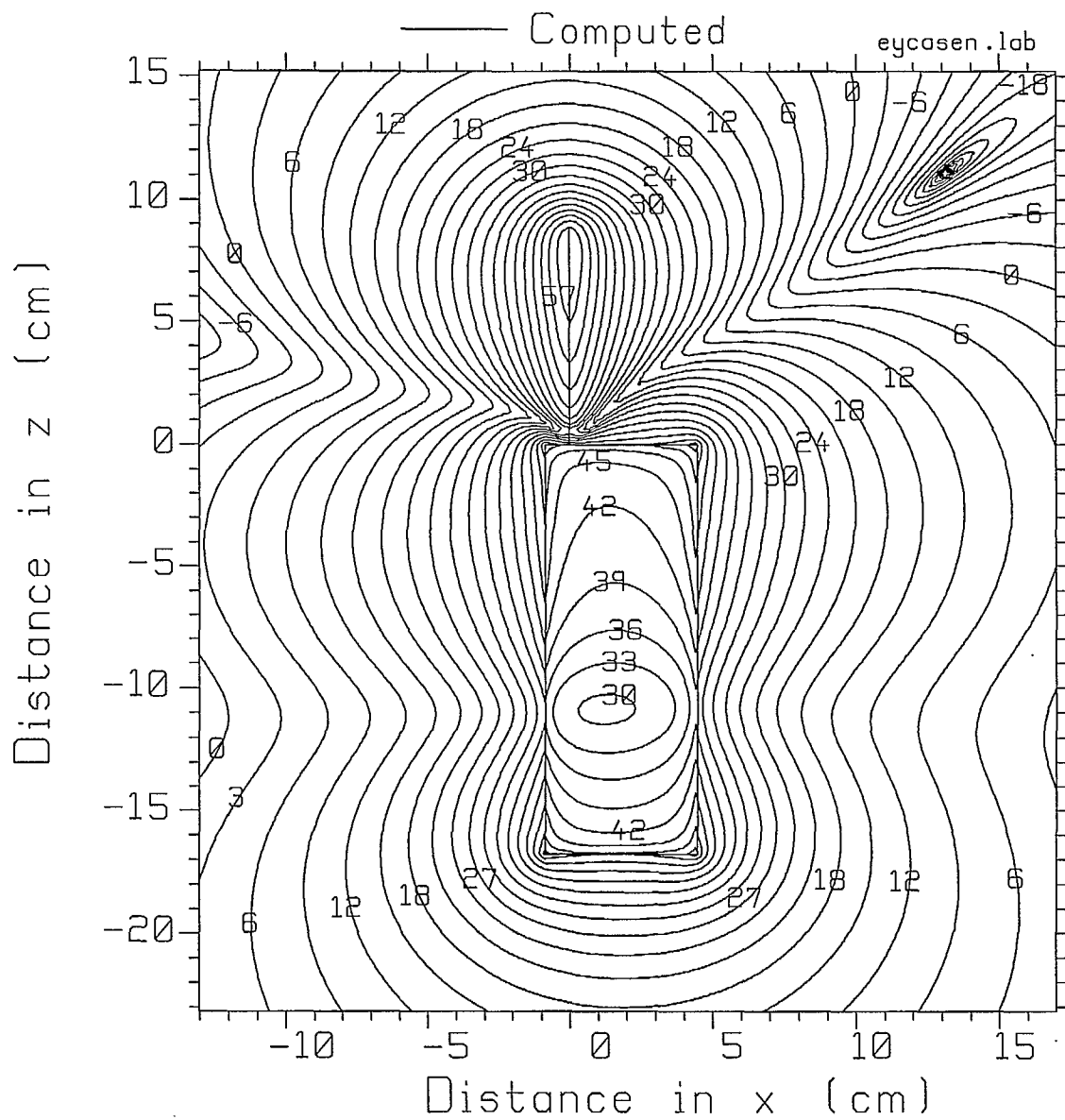


Fig. 2.6(b) The  $E_y$  component of the field in an  $xz$  plane through the surface of the case.

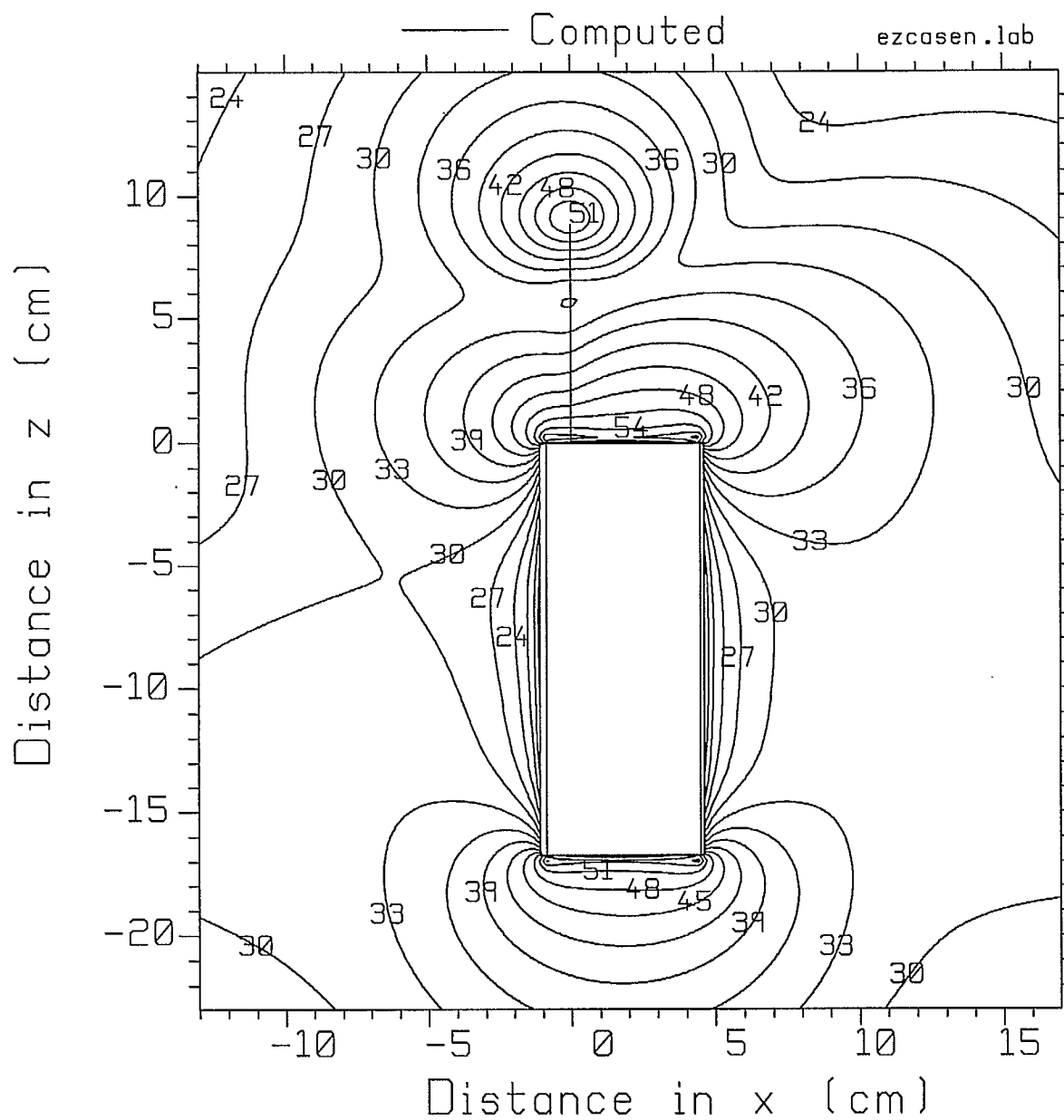


Fig. 2.6(c) The  $E_x$  component of the field in an  $xz$  plane through the surface of the case.



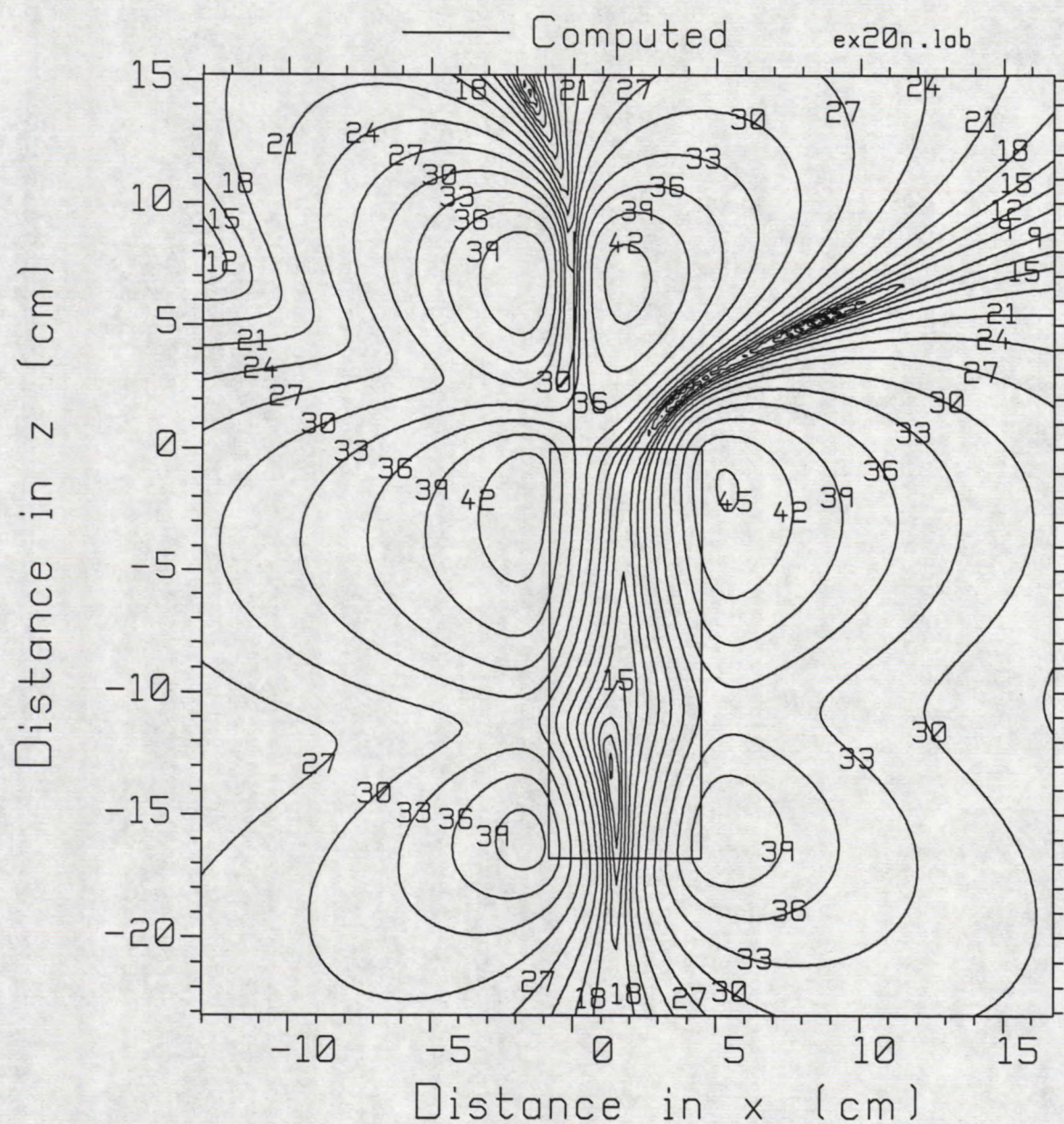


Fig. 2.7(a) The  $E_x$  component of the field in an  $xz$  plane at  $y = -21.8$  mm.



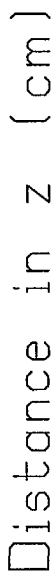


Fig. 2.7(b) The  $E_y$  component of the field in an  $xz$  plane at  $y=-22.9$  mm.

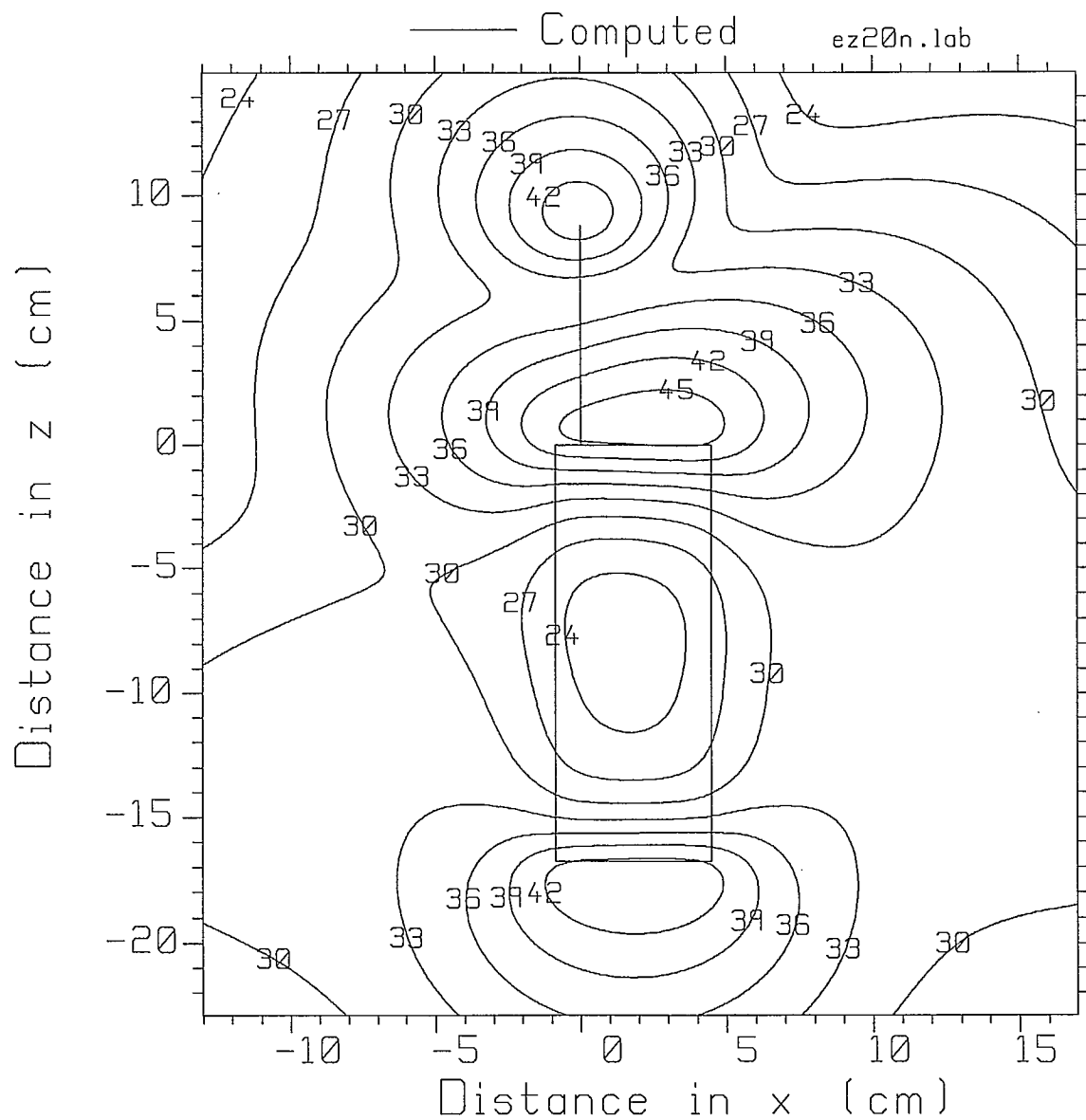


Fig. 2.7 (c) The  $E_z$  component of the field in an  $xz$  plane at  $y=-21.8$  mm.

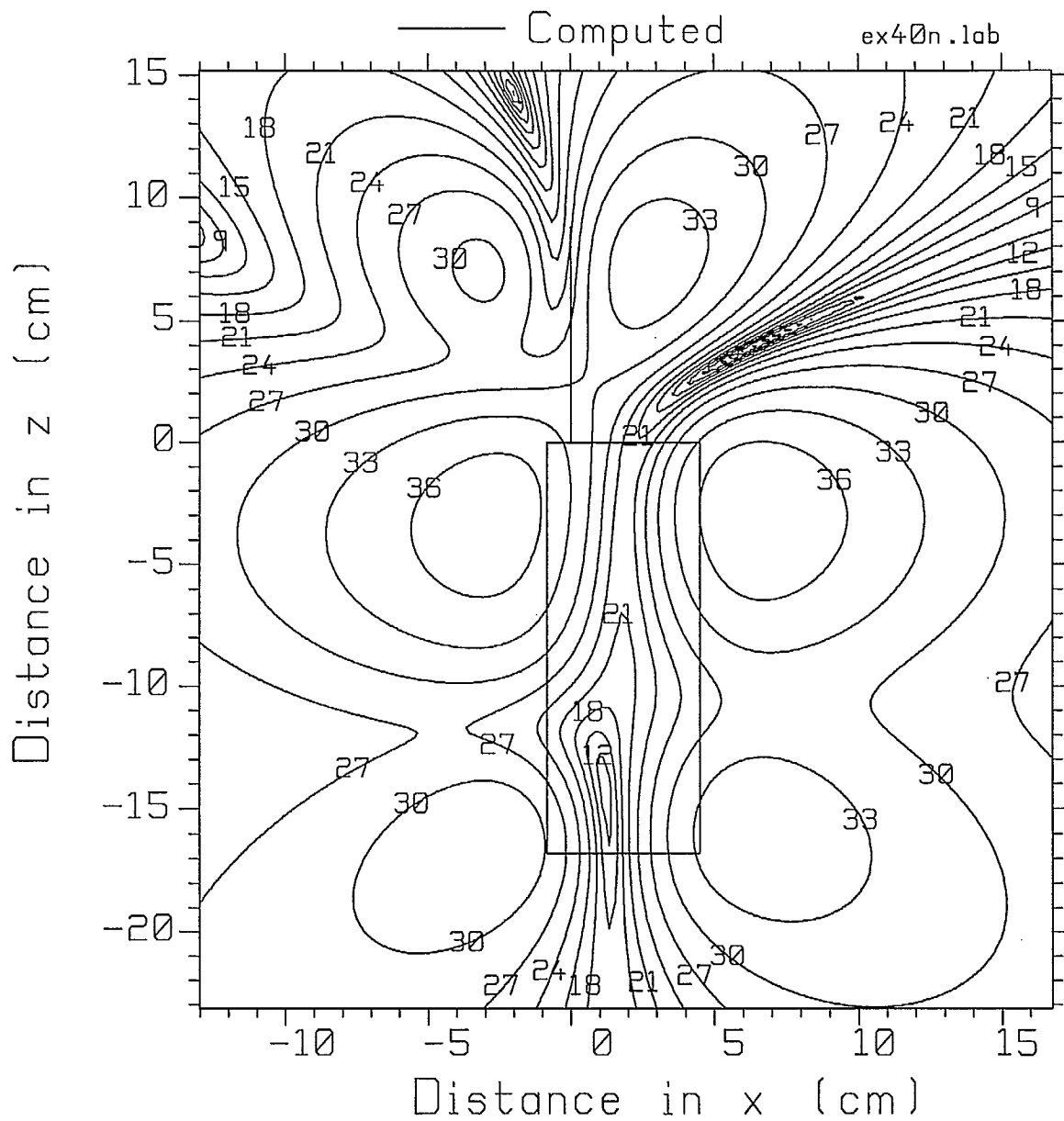


Fig. 2.8(a) The  $E_x$  component of the field in an  $xz$  plane at  $y=-41.8$  mm.

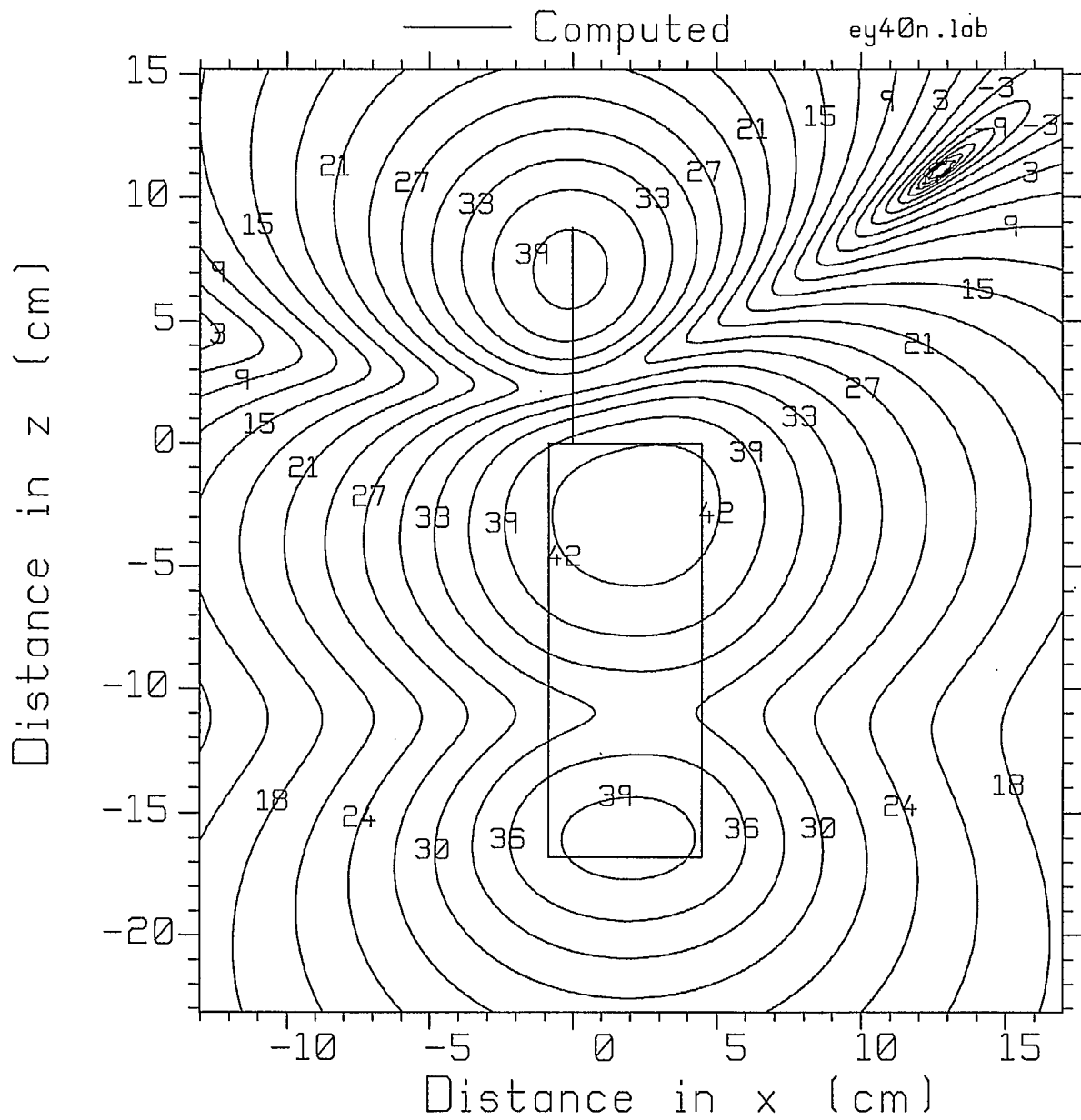


Fig. 2.8(b) The  $E_y$  component of the field in an  $xz$  plane at  $y=-41.8$  mm.

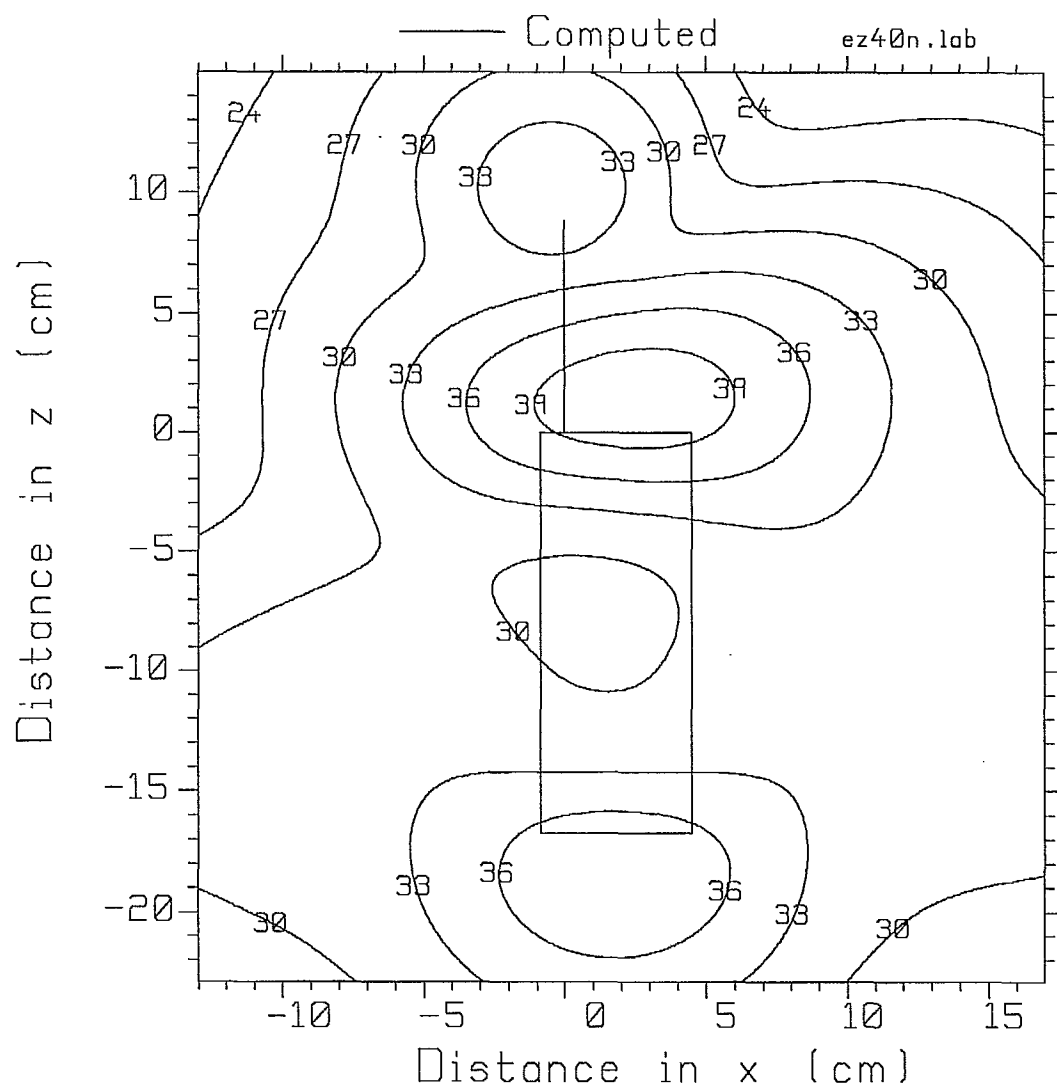


Fig. 2.8(c) The  $E_z$  component of the field in an  $xz$  plane at  $y = -41.8$  mm.



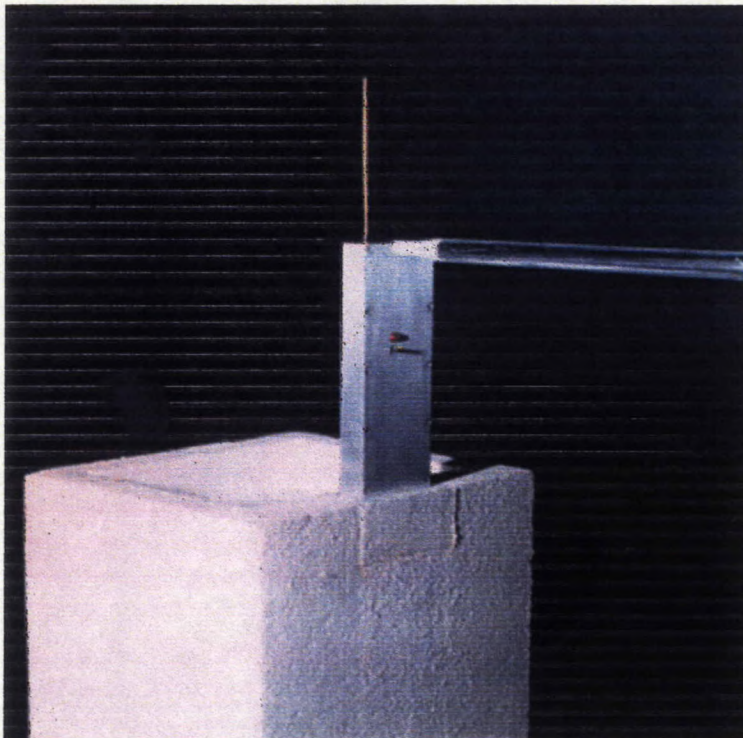


Fig. 2.9 The probe is a thin plexiglas wand with three perpendicular dipoles in the tip[17,19].

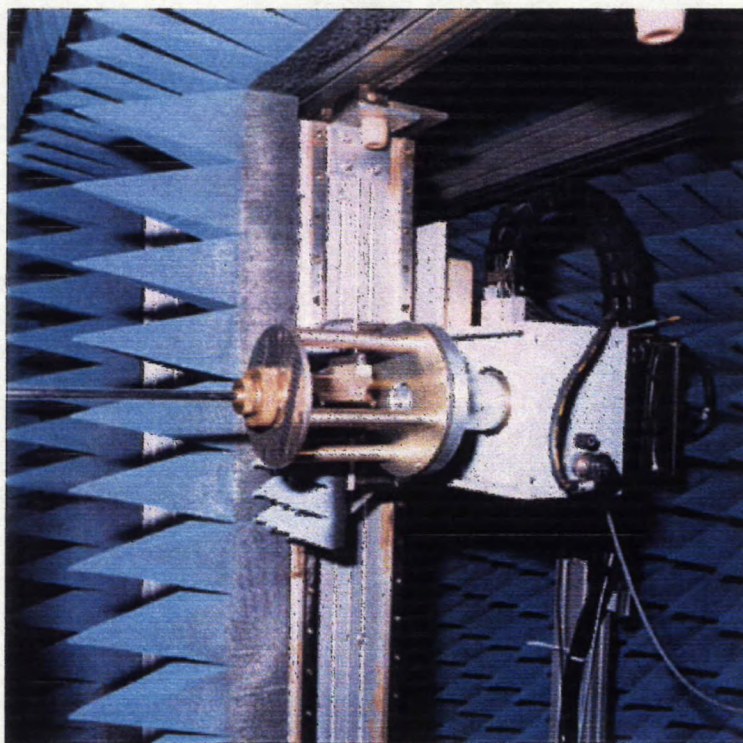


Fig. 2.10 The probe mount holds the base of the probe such that the probe can be rotated about its axis, and the distance from the handset can be adjusted precisely[17].

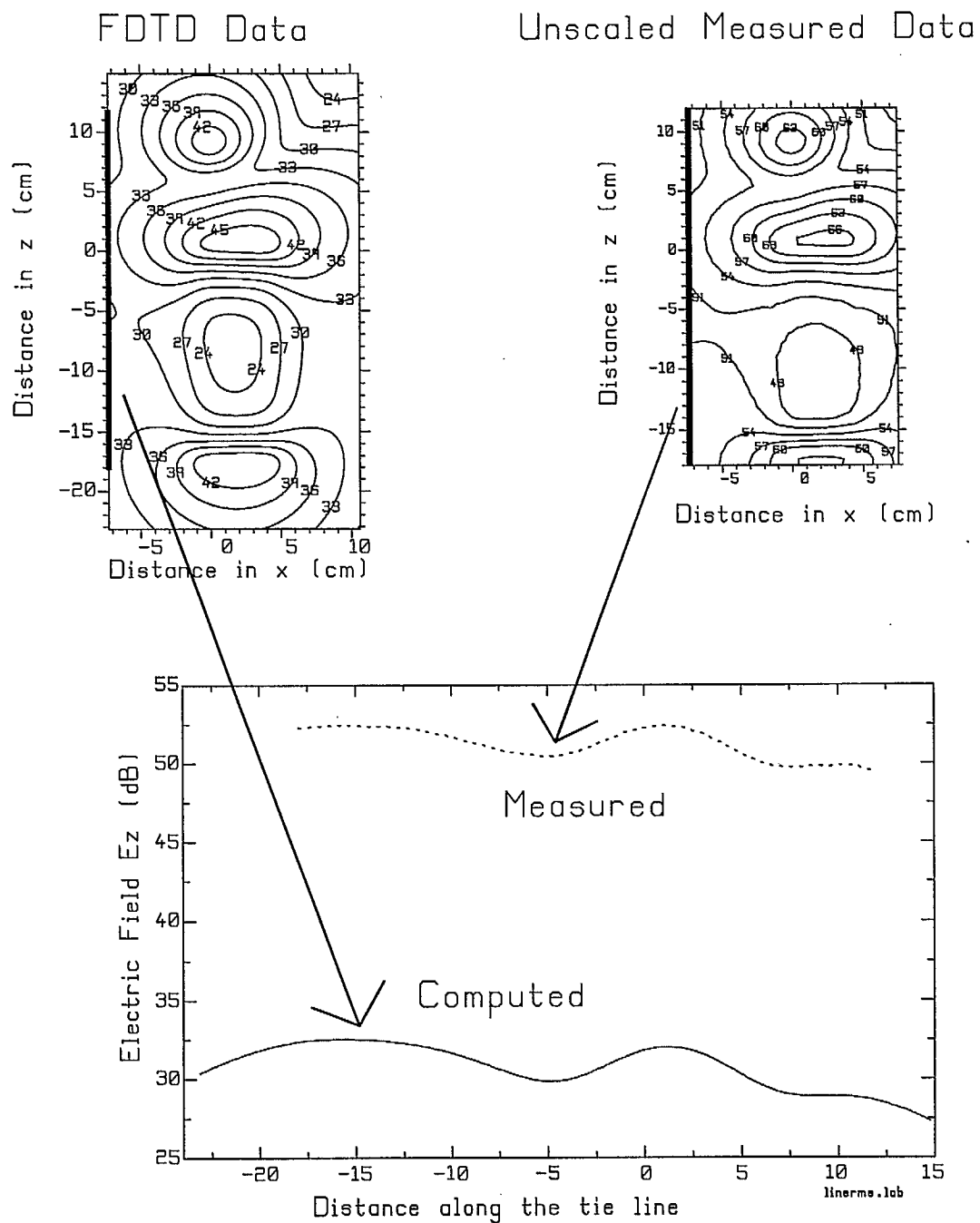


Fig. 2.11 The "tie line normalization process."



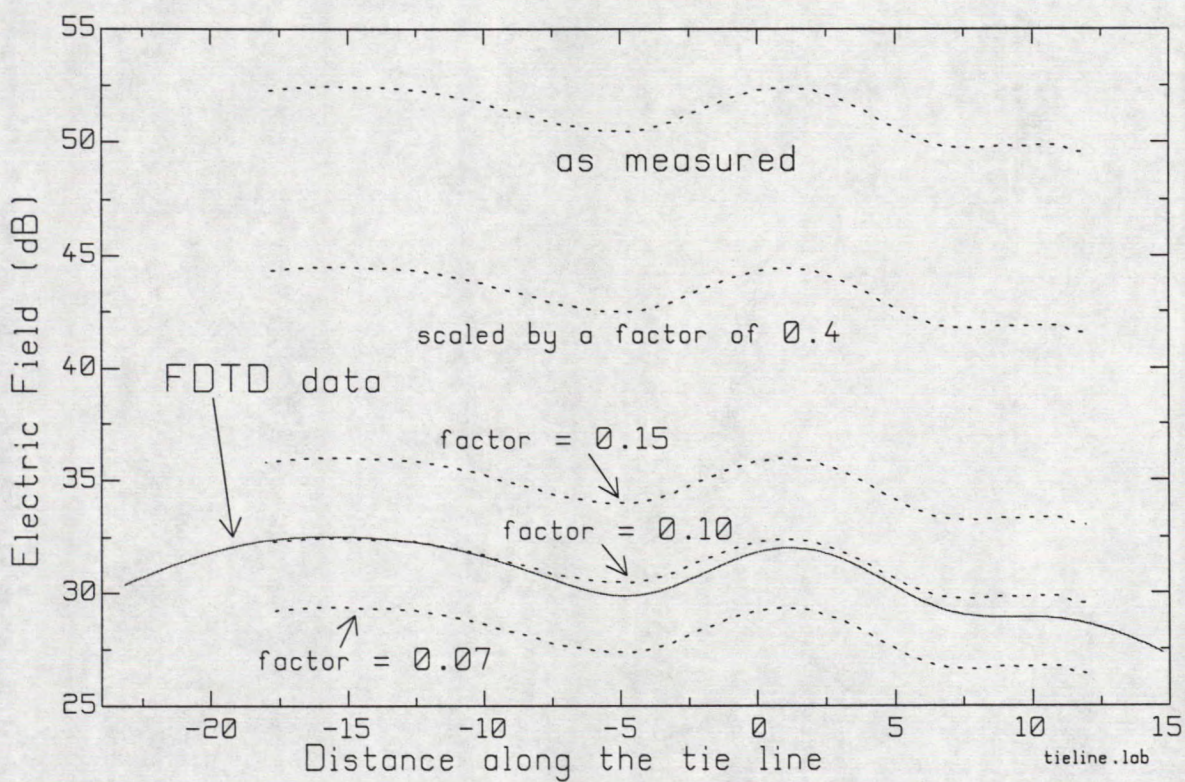


Fig. 2.12 Scaling the measured field to match the computed field along the tie line.



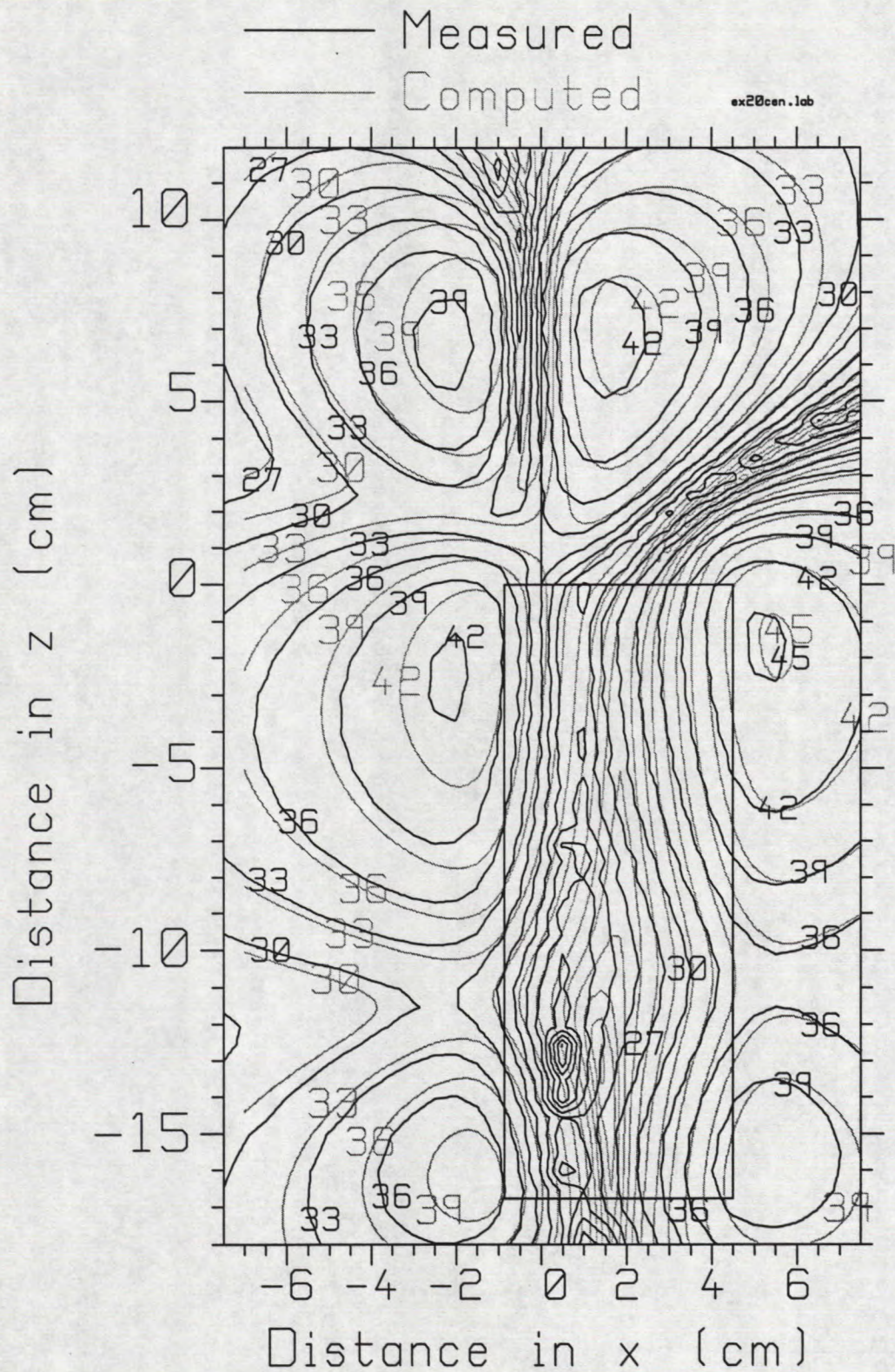


Fig. 2.13(a) Comparison of the measured and computed  $x$  component at  $y = -21.8$  mm.



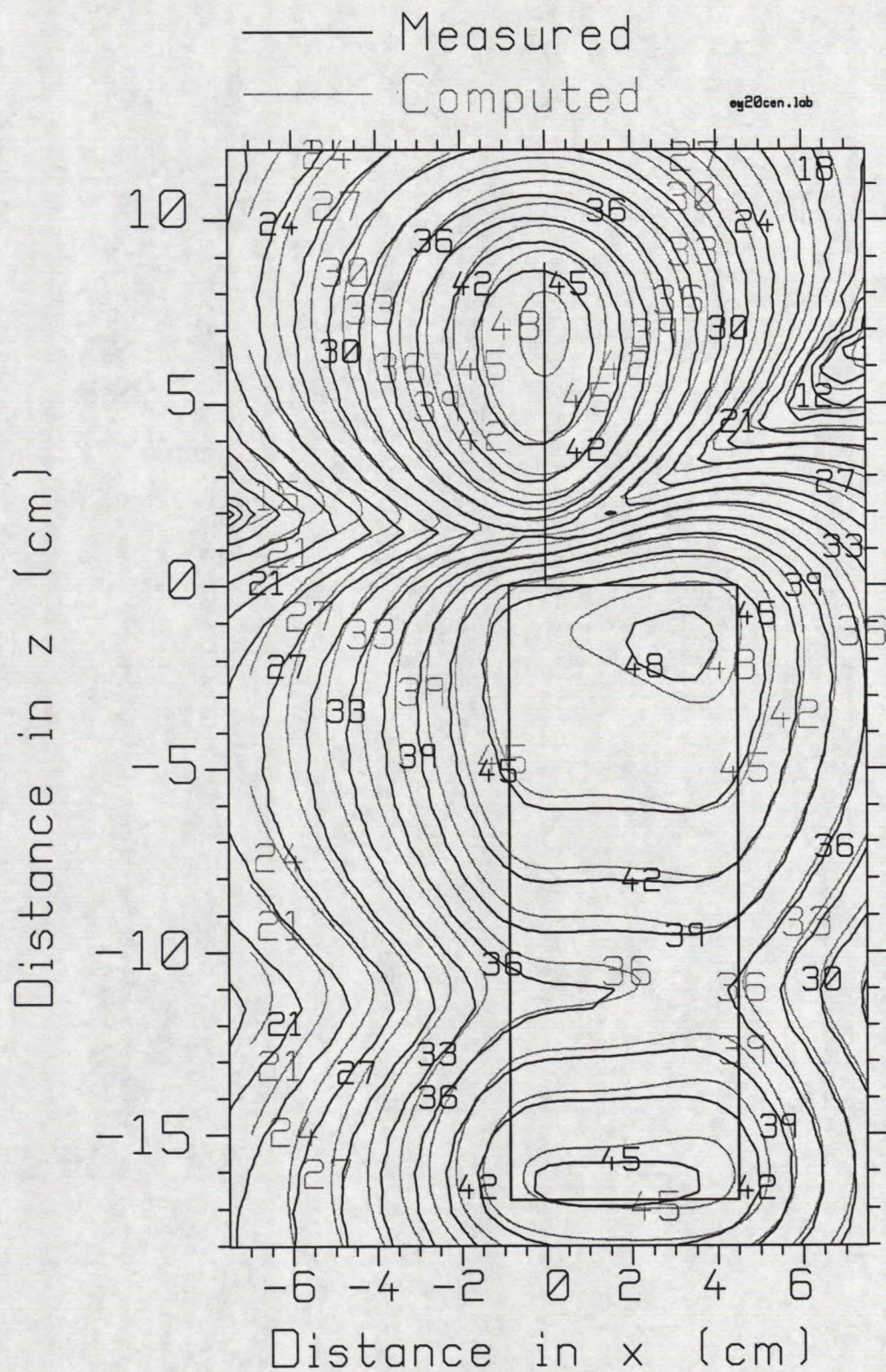


Fig. 2.13(b) Comparison of the measured and computed y component at  $y = -22.9$  mm.



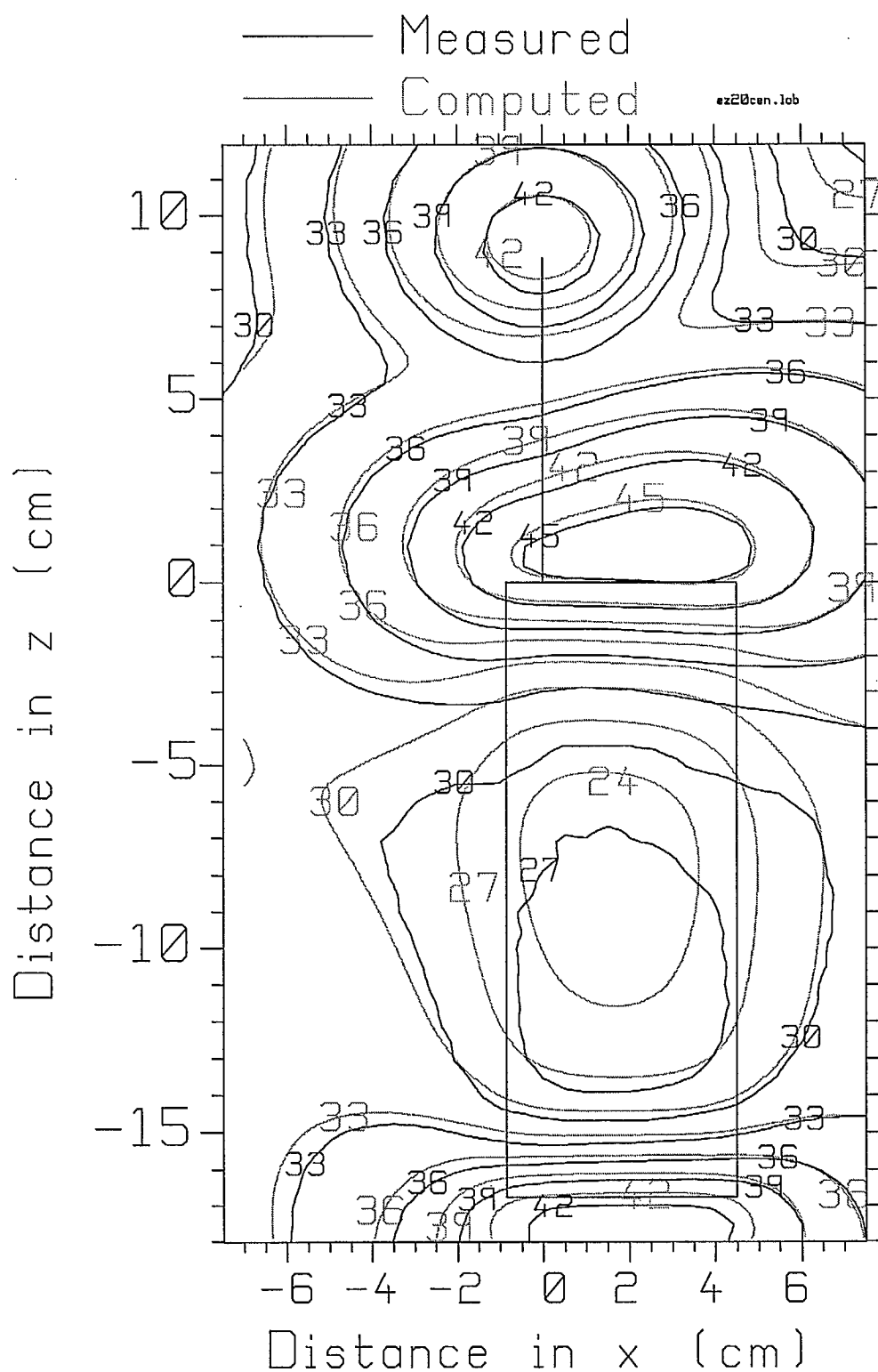


Fig. 2.13(c) Comparison of the measured and computed  $z$  component at  $y = -21.8$  mm.



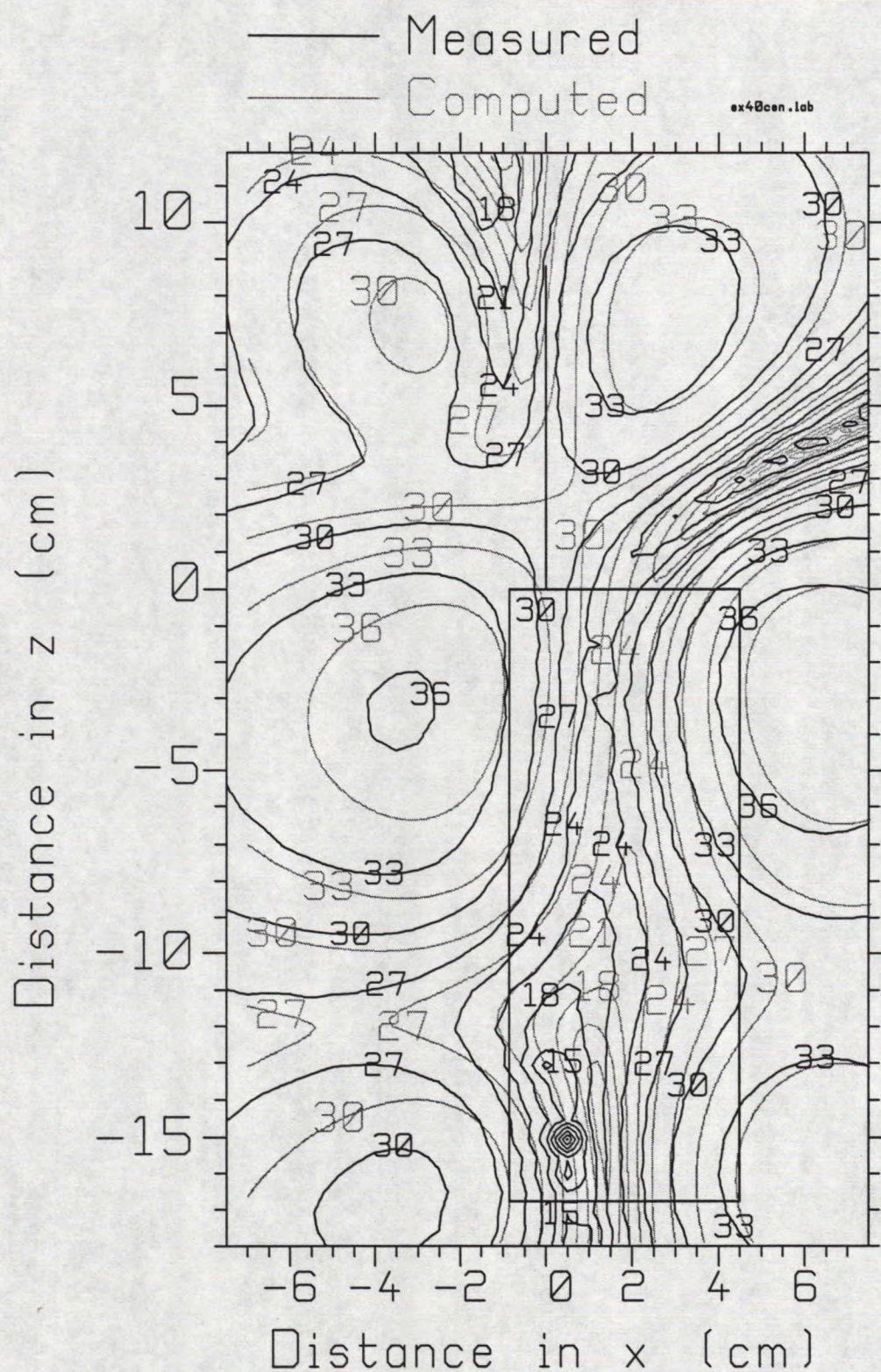


Fig. 2.14(a) Comparison of the measured and computed  $x$  component at  $y=-41.8$  mm.



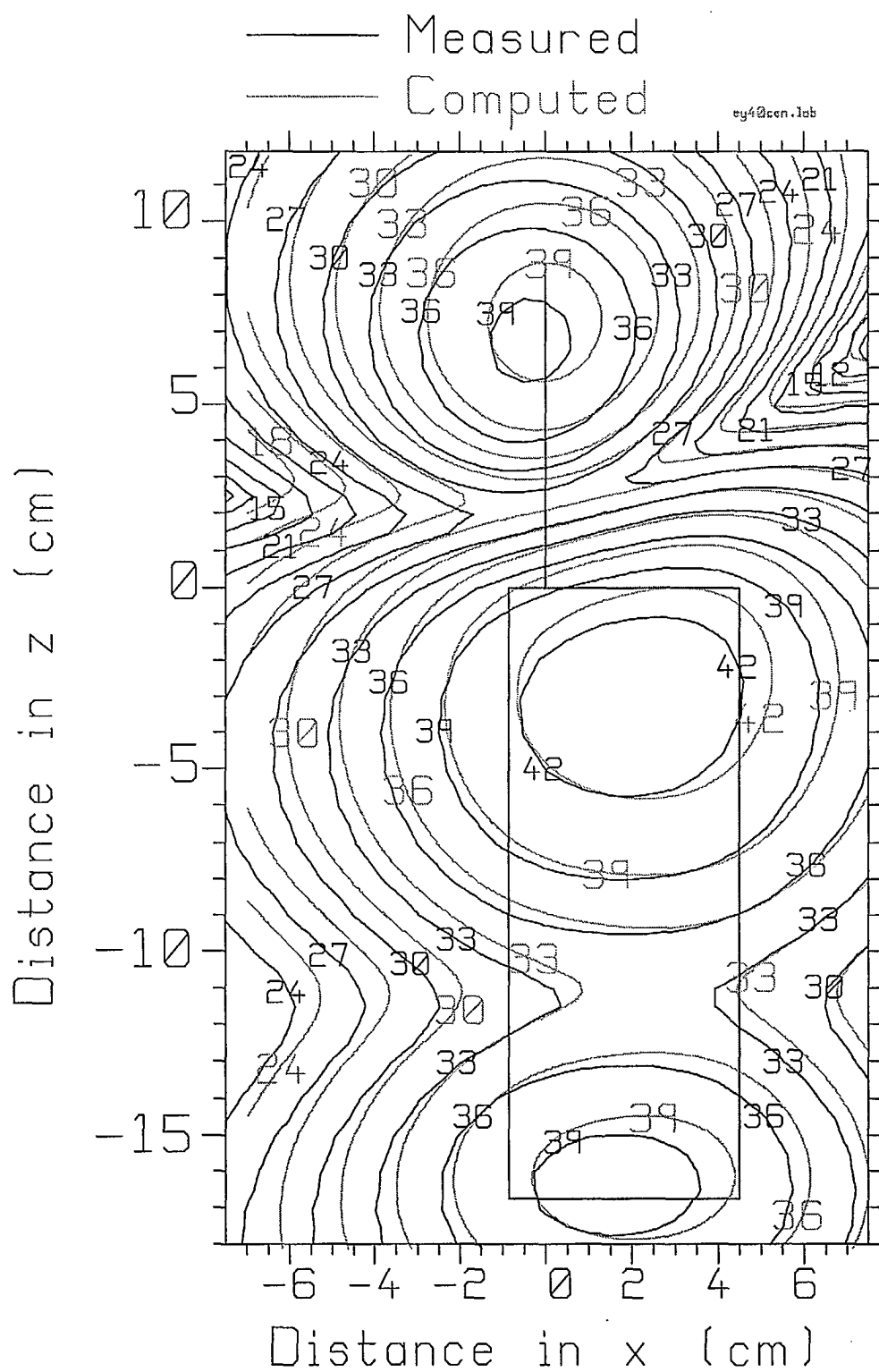


Fig. 2.14(b) Comparison of the measured and computed y component at  $y = -42.9$  mm.



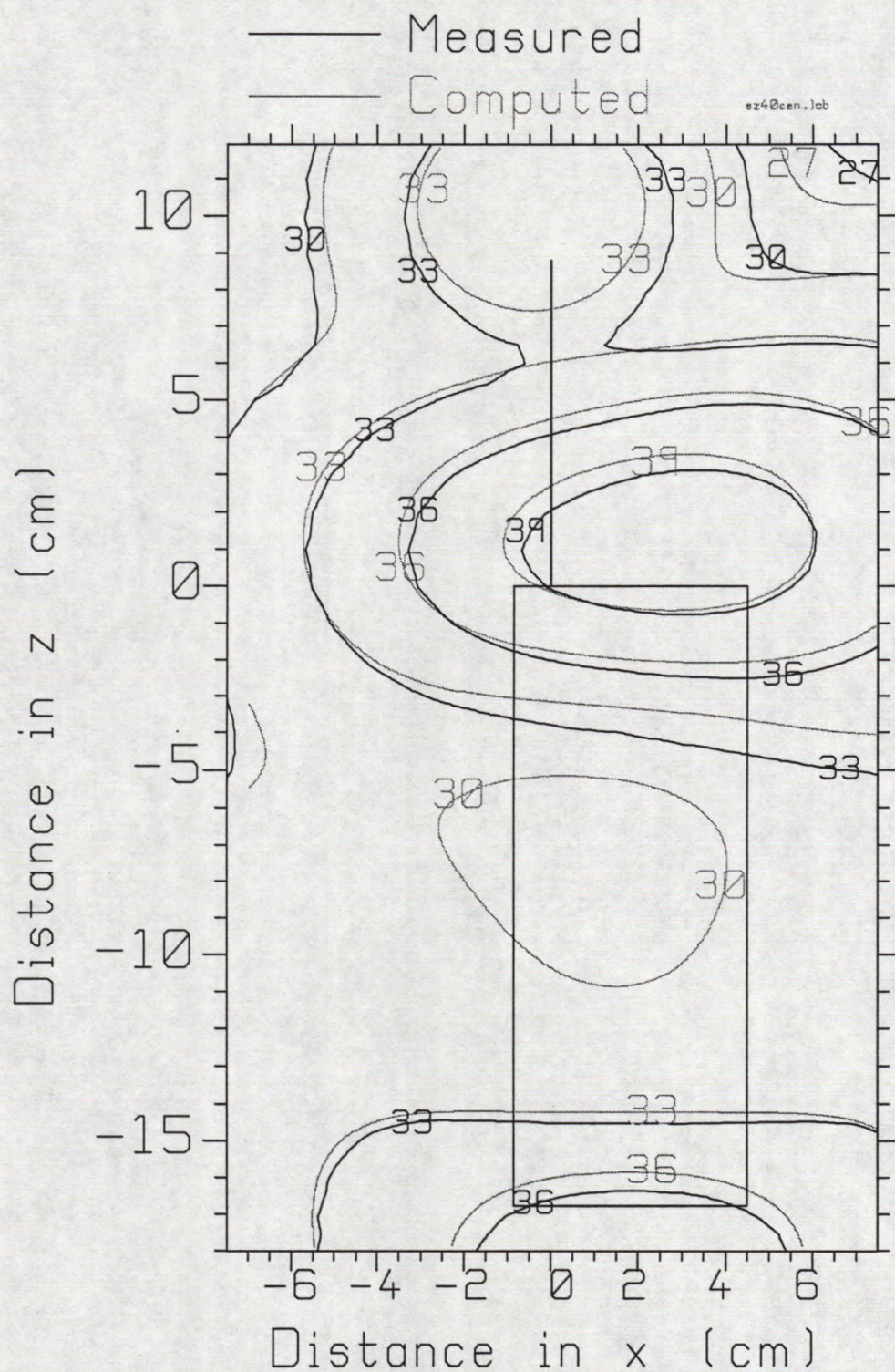


Fig. 2.14(c) Comparison of the measured and computed z component at  $y = -41.8$  mm.



## Chapter 3

### Near Fields of the Handset and Box Head

In use, a portable radio handset is held near the head. This chapter models the head as a box, with the handset close by, oriented vertically, as shown in Fig. 3.1. The "box head" was described in [1,2]. It is a thin-walled plexiglas box measuring 17.07 by 13.89 by 21.06 cm, with wall thickness 0.55 cm. The handset is spaced 0.94 cm from the box. The box is filled with a liquid mixed from deionized water, sugar and salt[20] having the electrical properties of brain material. The "brain liquid" was measured[21] to have a conductivity of  $\sigma = 1.064$  and a relative permittivity of  $\epsilon_r = 40.42$ . The plexiglas will be modelled with values taken from a standard textbook[22] of  $\sigma = 0.0049$  and  $\epsilon_r = 3.45$ . This chapter discusses the FDTD model of the handset and the box head. Then the computed near fields of the handset and box head are presented and discussed. Finally the measured near fields of the handset and box head are compared with the computations.

#### 3.1 FDTD Model of the Handset and Box Head

Fig. 3.2 shows the FDTD model of the handset and the box head. The cell size is 2.205 mm. The handset was modeled with 24 by 8 by 76 cells, with a 40 cell antenna, as before. The box is modeled with 77 by 63 by 96 cells, making its dimensions in the FDTD model 16.9785 by 13.8915 by 21.1680 cm, compared to the true size of 17.07 by 13.89 by 21.06 cm. The error is about 0.9 mm in  $x$ , 0.2 mm in  $y$ , and 1.1 mm in  $z$ , so the box size is close to the true size. The wall thickness is modeled with 3 FDTD cells, so is 0.6615 cm compared to the true thickness of 0.55 cm. The wall is thus about 1 mm too thick. The spacing from the handset to the box is modeled with 4 cells, so is 0.882 cm compared to the true spacing of 0.94 cm. This is an error of about 0.6 mm.

In order to obtain the near field over a reasonably larger region of the  $xz$  plane, the space size was chosen to be 150 by 148 by 189 cells, for a total of 4,195,800 cells. This is much larger than the handset-alone model of Chapter 2. The 6 cells at the outer face of the cell space are used to implement the perfectly-matched layer absorbing boundary. The FDTD code was run for 4096 time steps to allow the 850 MHz signal to reach steady state.

The near field data presented below is scaled to 600 mW of radiated power. This is done by using the FDTD program to compute the far fields over the radiation sphere and then integrating the power flow density to find the radiated power. Since the box head absorbs energy, the input power to the antenna is larger for the handset and box head case than for the handset alone, to achieve the same radiated power.

### 3.2 The Computed Fields

Fig. 3.3 presents the near fields of the handset and box head at “20 mm” from the antenna, and Fig. 3.4 at “40 mm” from the antenna. The distances are those from the base of the antenna to the tip of the probe in the measurements presented later in the chapter. The field strength is graphed in decibels above 1 volt per meter.

#### 3.2.1 Fields at 20 mm

Fig. 3.3(a) is a contour map of the computed  $E_x$  component at 21.8 mm from the base of the antenna. This field component is the horizontal component in the plane of the paper. The trough in the field that was noted for the handset alone is clearly seen for the handset and box head. The trough starts at the bottom center of the contour map, runs vertically up the center of the handset case, and then exits diagonally at the top right of the figure. The minimum field in the trough at the top right is 6 dB. At the bottom center of the handset there is a minimum in the field of 0 dB.

The field has contours of field strength 45 dB on either side of the antenna. At the top left of the case there is a 42 dB contour, and a 39 dB contour at the bottom left. The field on the right side of the case in the figure is stronger, with a 45 dB contour at the top right side of the case, and a 42 dB contour at the bottom right.

Comparing with Fig. 2.7(a), we see that the fields near the antenna are about 3 dB larger for the handset and box head than for the handset alone. The fields near the corners of the handset are also larger for the handset and box head, because the field contours in Fig. 3.3(a) are larger in area than in Fig. 2.7(a). These larger fields reflect the fact that the antenna must supply more power to radiate 600 mW in the presence of the box head.

Fig. 3.3(b) shows the  $E_y$  component at 22.9 mm from the antenna. This field component is normal to the page. The field over the antenna has a 51 dB contour, larger than in Fig. 2.7(b) where the largest contour is 48 dB. The field over the top of the handset has a large-area 48 dB contour for the handset and box head. For the handset alone, the 48 dB contour is much smaller. The field at the bottom of the case has a 45 dB contour for the handset and box head. For the handset alone, the 45 dB contour at the bottom of the case is about the same size.

The  $E_y$  component of the field has a feature not seen for the handset alone. There are two minima in the field, to the left and to the right of the tip of the antenna. At left the field drops to 9 dB, and at the right to -3 dB. These minima are introduced by the box head.

Fig. 3.3(c) shows the  $E_z$  or vertical field component at 21.8 mm from the base of the antenna. The field strength at the tip of the antenna is 48 dB, whereas in Fig. 2.7(c) for the handset alone, the field at the tip of the antenna is 42 dB. The field at the top of the case for the handset and box head has a small 48 dB contour. For the handset alone, the field has a larger 45 dB contour and does not get as strong as 48 dB. The field at the bottom of the case for the handset and box head has a small 45 dB contour. For the handset alone the field does not get as large as 45 dB.

### 3.2.2 Fields at 40 mm

Fig. 3.4(a) shows the  $E_x$  component at 41.8 mm from the base of the antenna. The field on either side of the antenna has 36 dB contours. The field at the top left of the case also shows a large 36 dB contour, and there is a small 33 dB contour at the bottom left of the case. To the top right of the case, there is a small 39 dB contour, and at the bottom right, a large 33 dB contour. The trough running up the center of the figure has two deep minima. Towards the bottom center of the case, the field falls to 0 dB. Just above the top right corner of the case the field falls to 12 dB.

Fig. 3.4(b) shows the  $E_y$  component at 42.9 mm from the base of the antenna. Over the antenna we see a 42 dB contour. Over the top of the case there is a 45 dB contour. At the bottom of the case we see a 39 dB contour. The minima in the field to the left and right of the antenna are also seen at this distance. To the left of the antenna the field drops to -9 dB, and to the right also to -9 dB.

Fig. 3.4(c) shows the vertical component of the field at 41.8 mm from the antenna. Near the tip of the antenna there is a 39 dB contour. Over the top of the case the field shows a 42 dB contour. Over the center of the case the field drops below 30 dB. At the bottom of the case there is a 39 dB contour.

In the following, these computed fields are compared with the measured data.

## 3.3 Comparison with the Measured Fields

Fig. 3.1 shows the box head and the handset adjacent to it, with the three-axis probe measuring the field near the handset. Fig. 3.5 shows the handset and box head atop the styrofoam support column, with the probe held in the probe mount on the three-axis scanner. The front face of the probe mount is "hidden" behind a layer of absorber. This section compares the fields reported in Ref. [17] with the computed field discussed above. The field strength is drawn as contours in decibels with a reference field strength of 1 volt per meter.

### 3.3.1 At 20 mm

Fig. 3.6 compares the measured and computed fields when the tip of the probe is 20 mm from the base of the antenna. Part (a) compares the  $E_x$  component, which is the horizontal component in the plane of the page. On either side of the antenna the field has a 45 dB contour, which is present in both the measurement and the computation. To the left of the antenna, this contour is rather smaller in the measurement than in the computation. To the left, the 42, 39, 36 and 33 dB contours align well between the measurement and the computation. To the right of the antenna, the 45 dB contours are about the same size but the measured contour is closer to the antenna than is the computed contour. The 42, 39, and 36 dB contours are somewhat closer to the antenna in the measurement than in the computation, as well.

To the left of the top of the handset case, the 42, 39 and 36 dB contours agree very well between the measurement and the computation. To the right of the top of the case, The measurement has a small 48 dB contour, not seen in the computation. The computed 45 dB contour is smaller than the measured 45 dB contour.

To the left of the bottom of the handset case, the measured and computed data have 39, 36, 33 and 30 dB contours that align very well. To the right of the bottom of the case, the 42, 39 and 36 dB contours also align very well.

A trough in the field strength runs up the center of the handset case. At the upper right where the trough exits the contour map, the measured field strength has a 24 dB contour. The computed field strength falls to 24 dB, though the precise location of the 24 dB contour is a bit different between the measurement and the computation. Along the top of the case, the measured field strength in the trough falls to 24 dB, whereas the computed field has a 21 dB contour. At about a third of the way up from the bottom of the handset case the measured field has a minimum of 6 dB. The computed data has a minimum at almost the same location, of 0 dB field strength.

Fig. 3.6(b) compares the  $E_y$  component of the field. The field over the antenna has a 51 dB contour in the measurement and a larger area 51 dB contour in the computation. To the left of the antenna, the contours tend to fall out of detailed alignment. There is a minimum in the field strength in the measurement of 9 dB at the upper left edge of the contour map. The location of the minimum in the computed field is somewhat different but close by, and the field falls to 0 dB. To the right of the antenna the measured and computed contours fall out of synchronization, with the 42 dB computed contour falling on the 39 dB measured contour, for example. There is a minimum in the field strength at the upper right of the contour map, where the field falls to 12 dB in the measurement, and to -3 dB in the computation. The location of the minimum field is almost the same in the computation and in the measurement.

At the top right corner of the handset case, there is a measured contour of field strength 51 dB; whereas the largest contour in the computation is 48 dB. The contours to the right of the top of the handset case align reasonably well. To the left of the top of the handset case the 48, 45, 42 39 and 36 dB contours reasonably coincide as well.

At the bottom of the handset case both the measurement and the computation have a 45 dB contour, which corresponds very well. The 42, 39 and 36 dB contours align well, too. To the left of the case the measured and computed contours tend to fall out of alignment with the computed contours closer to the bottom of the case than the measured contours. To the right of the bottom of the case, the same is seen in the contour map.

Fig. 3.6(c) compares the measured and computed vertical component of the field at 21.8 mm from the base of the antenna. Both the measured and computed field have a 48 dB contour at the tip of the antenna, of about the same size. The 45, 42, and 39 dB contours correspond quite well, as well. Near the top of the case the measured field has a larger 48 dB contour, and the computed field has a smaller 48 dB contour. The 45 and 42 dB contours are somewhat larger in the measurement than in the computation. Over the center of the case the measured field has a 27 dB contour, whereas the computed field has a 24 dB contour. At the bottom of the case, the computed field has a 45 dB contour, which is larger than is seen in the measured field. The 42, 39, 36 and 33 dB contours correspond quite well between the measurement and the computation.

### 3.3.2 At 40 mm

Fig. 3.7 compares the measured and computed fields when the probe tip is 40 mm from the base of the antenna. Part (a) compares the  $E_x$  component at 41.8 mm from the handset antenna to the measurement dipole in the probe tip. To the left of the antenna, there is a 36 dB contour in the measurement that is quite small compared to the area of the 36 dB contour in the computation. To the right of the antenna the 36 dB contours are much more nearly the same size.

To the left of the handset case, the measured field has a 36 dB contour that is a bit smaller in area than the computed 36 dB contour. The 33 dB contour is also smaller. To the right of the handset case, the measured 39 dB contour is much larger in enclosed area than the computed 39 dB contour, indicating that the measured field rises to higher values here than does the computed field.

To the left of the bottom of the handset case, the measured field has a contour of field strength 30 dB that coincides quite well with the computed 30 dB contour, except very close to the handset case. The computed field rises to have a 33 dB contour but the measured field is never this large. To the right of the bottom of the handset case, the measured and computed 33 dB contours are similar, with the measured contour somewhat larger in enclosed area.

The trough in the field has measured contours of 21 dB at the upper right edge of the contour map. The computed field is 21 dB at this location as well. There is a minimum in the field above the right corner of the handset case, where the measured field falls to 18 dB. The minimum in the computed field is shifted to the right and the minimum contour is 9 dB, so the minimum is sharper in the computed data. There is a minimum in the field about a third of the distance from the bottom to the top of the handset case. In the measured data the minimum field strength is 6 dB. The location of the computed minimum field is close by the measured minimum. The computed field falls to 0 dB, making this minimum deeper in the computation than in the measurement.

Fig. 3.7(b) compares the measured and computed  $E_y$  field component at 42.9 mm from the antenna. Both the measured and the computed field have a 42 dB contour over the antenna, with the measured contour smaller in enclosed area than the computed contour. As we move to the left of the antenna, the measured and computed contours fall out of alignment, with the computed contours somewhat closer to the antenna. To the right of the antenna the measured contours tend to be closer to the antenna than the computed contours.

There is a minimum in the field near the upper right corner of the contour map. The measured field falls to 6 dB. The computed field has its minimum contour at almost the same location, and the minimum contour is 3 dB.

Over the top of the handset case both the measured and the computed data have 45 dB contours, with the measured contour enclosing more area than the computed contour. The 42 and 39 dB contours coincide quite well.

At the bottom of the handset case, both the measured and the computed data have a 39 dB contour, with the measured contour somewhat bigger. The measured 36 and 33 dB contours are also somewhat larger in the measured data than in the computed data.



Fig. 3.7(c) shows the vertical component of the field at 41.8 mm from the antenna. At the tip of the antenna both the measured and the computed data have a 39 dB contour, and the two data sets agree quite well. The 36 dB contours are similar with the measured contour closer to the antenna than the computed contour at left, and the measured contour farther from the antenna at right. At the top of the handset case, the measured and the computed fields have 42 and 39 dB contours that coincide quite well. The 42 dB contour is smaller in enclosed area in the computed data. Over the center of the case the computed data has a 30 dB contour, but the measured field never falls as low as 30 dB. At the bottom of the case the measured and computed contours for 39, 36 and 33 dB coincide very well.

### 3.4 Conclusion

This chapter has presented the near fields of the handset and box head. The near fields in Fig. 3.3 were compared with the near fields of the handset alone and found to be similar. The principal difference is that the antenna must supply more power when the box head is present, in order that the radiated power be 600 mW. This leads to larger fields near the antenna when the box head is present.

Figs. 3.6 and 3.7 compare the measured near fields of the handset with those computed with the FDTD cell model. All three components of the field are compared at distances of 20 mm and 40 mm from the probe tip to the base of the antenna. In general good agreement has been shown. The overall configuration of the field in the measurement and in the computation is the same in every case. We have to look for differences in detail when we compare the measured and computed fields. Thus in some cases a measured maximum is greater than a computed maximum field. This manifests itself, for example, in Fig. 3.6(c) in a 48 dB contour that encloses more area near the top of the handset in the measured  $E_z$  than in the computed field. Or, for the  $E_y$  component in Fig. 3.6(b), the computed field along the antenna is somewhat larger in the computation than in the measurement, leading to a general misalignment of the contours in this region. But the qualitative behavior is identical and good agreement can be claimed.

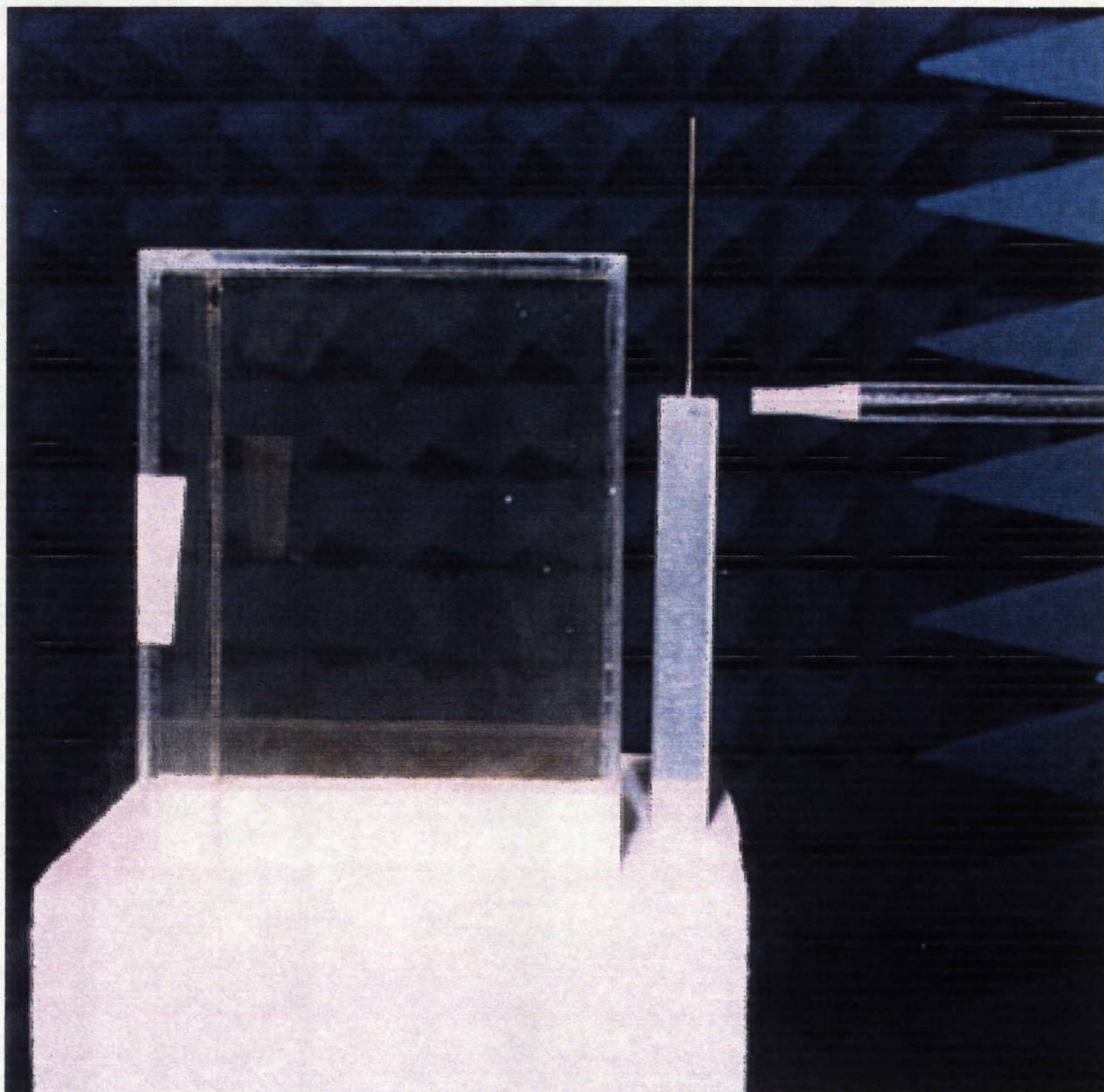


Fig. 3.1 The boxhead, the handset and the probe[17].



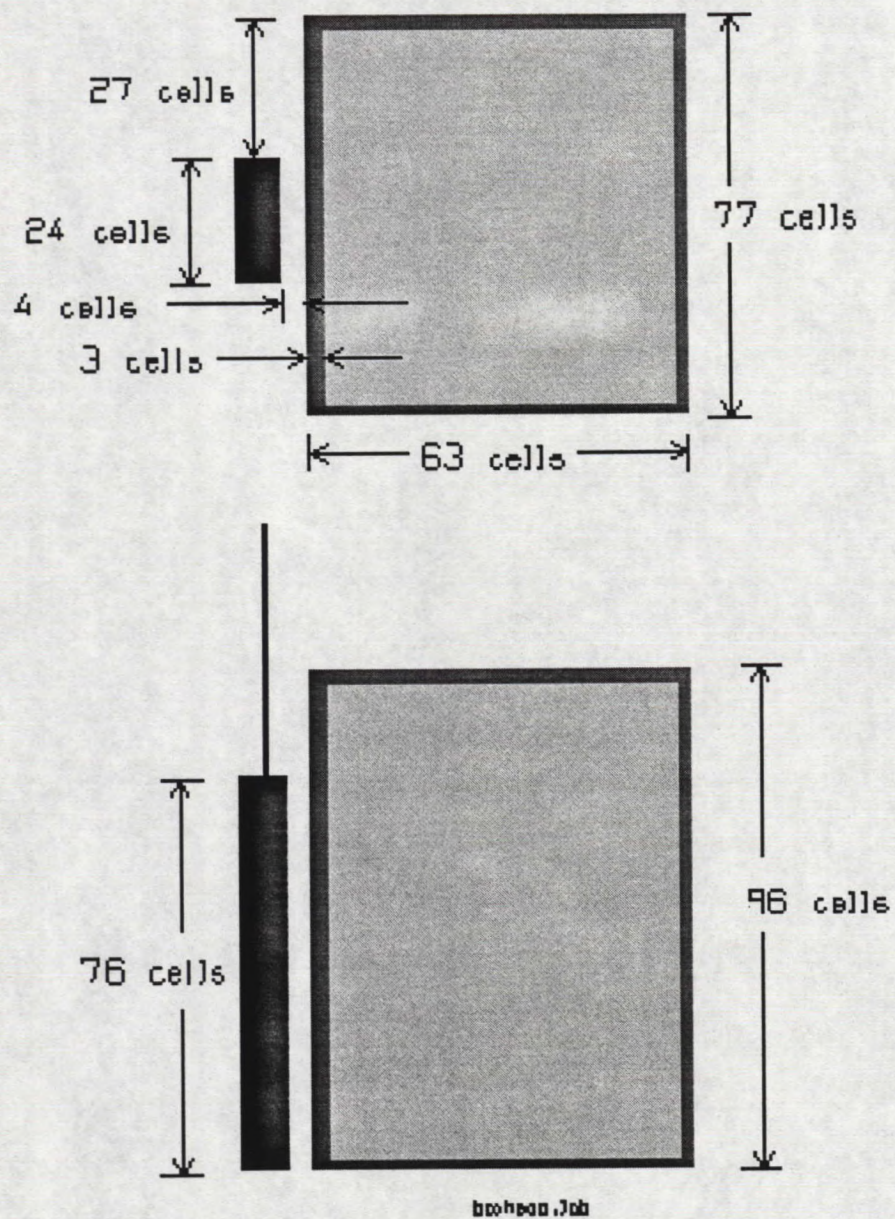


Fig. 3.2 The FDTD model of the handset and box head.



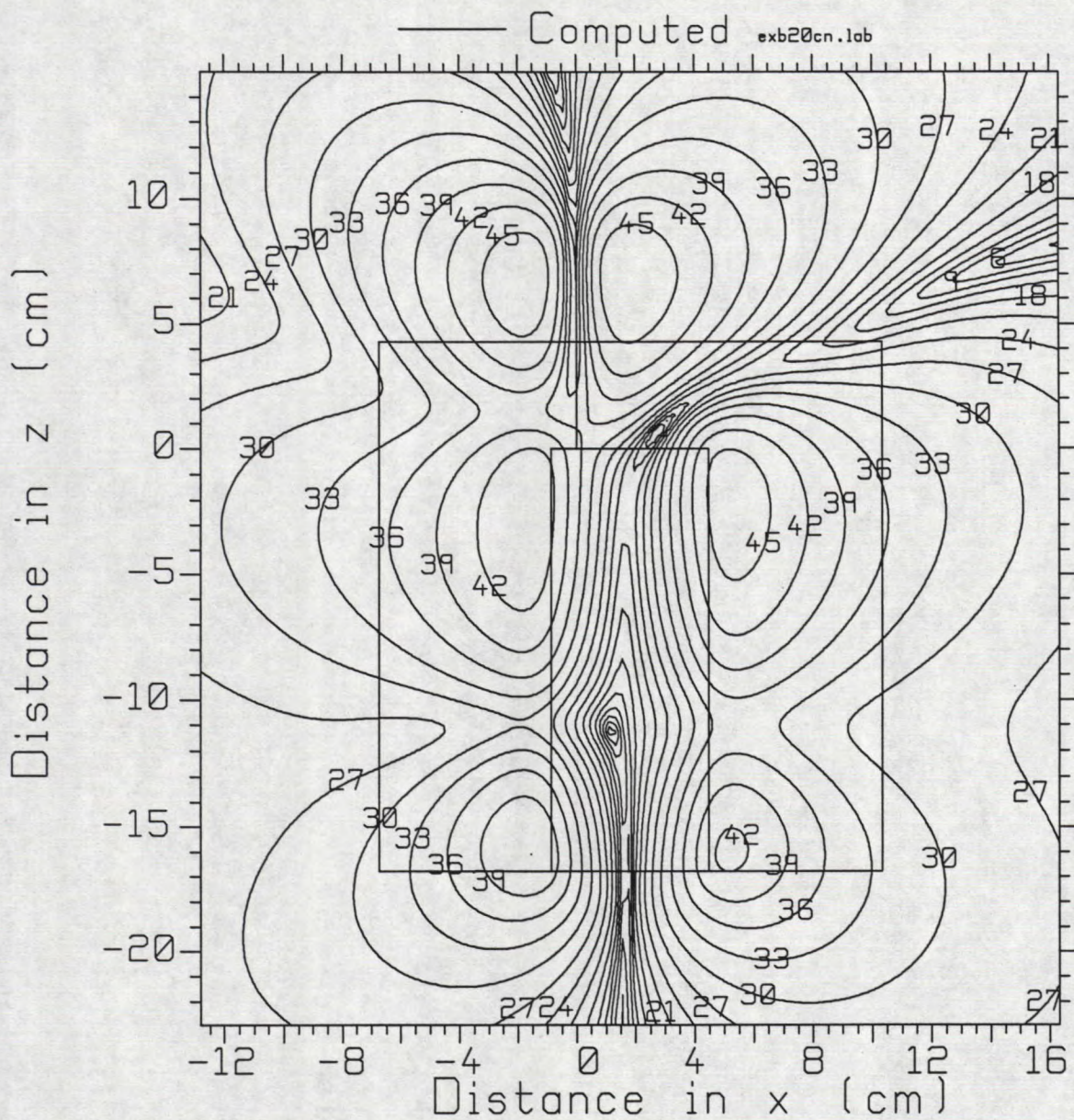


Fig. 3.3(a) The  $E_x$  component in an  $xz$  plane at 21.8 mm from the antenna.



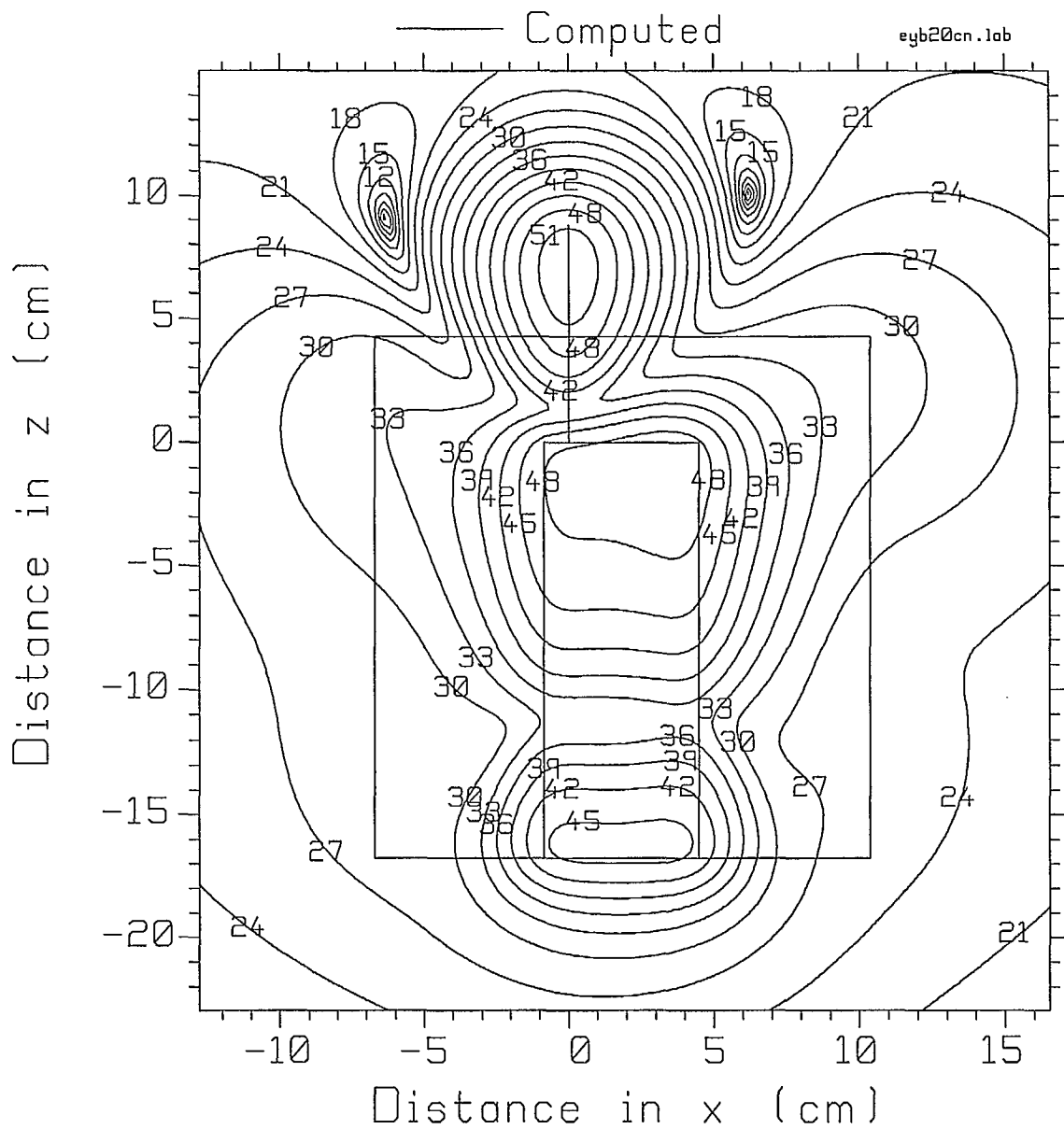


Fig. 3.3(b) The  $E_y$  component in an  $xz$  plane at 22.9 mm from the antenna.

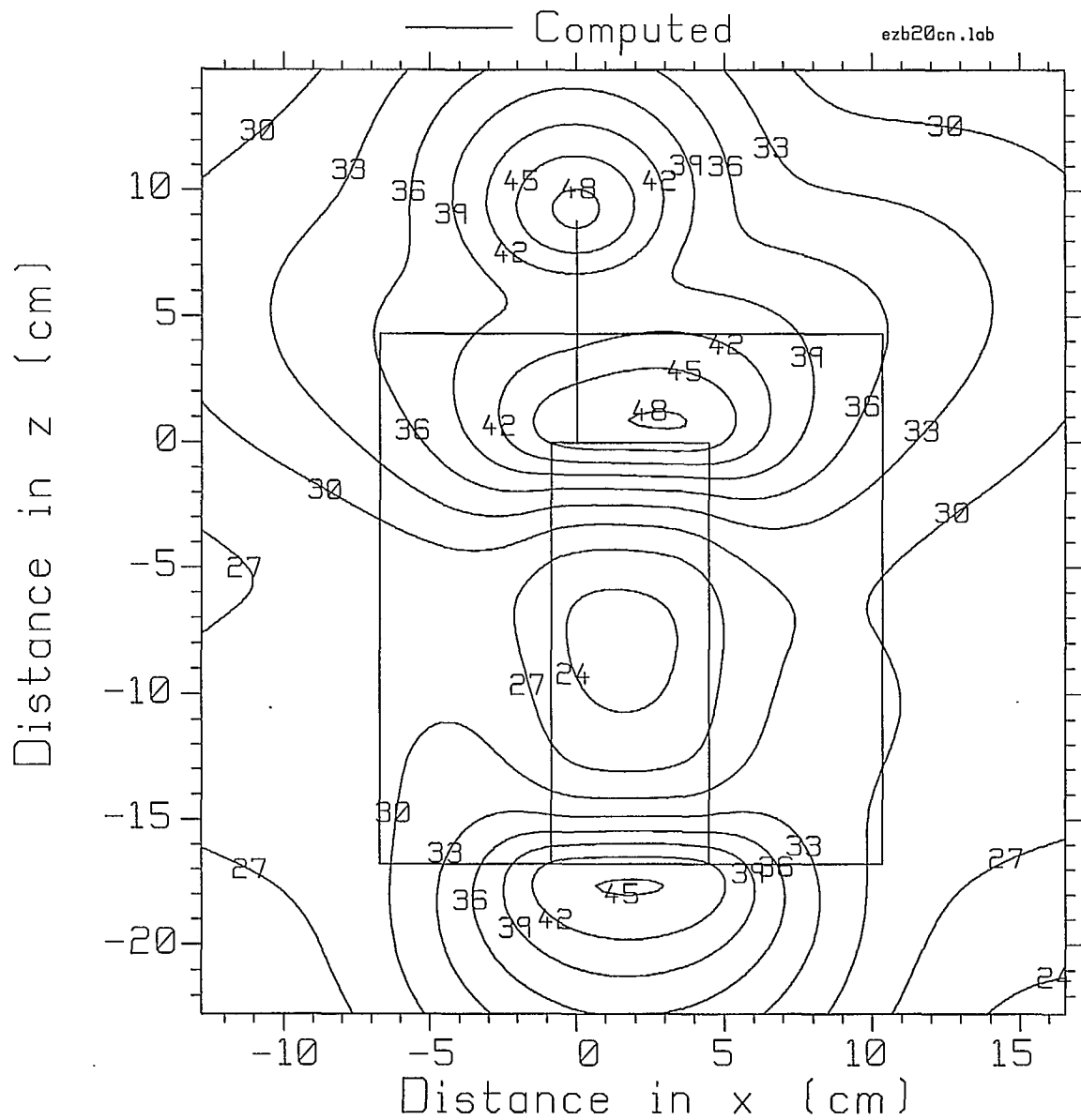


Fig. 3.3(c) The  $E_z$  component in an  $xz$  plane at 21.8 mm from the antenna.



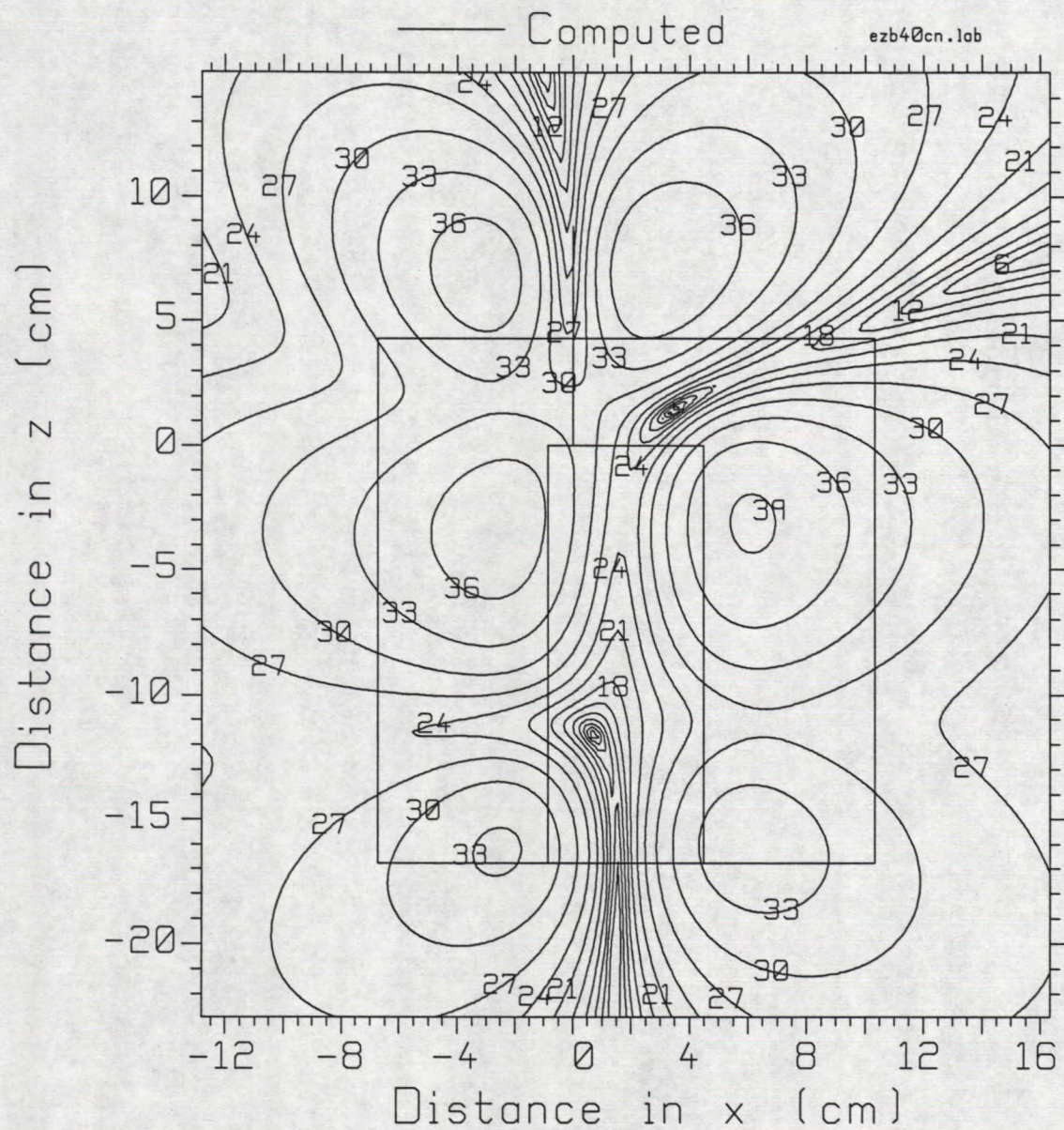


Fig. 3.4(a) The  $E_x$  component in an  $xz$  plane at 41.8 mm from the antenna.

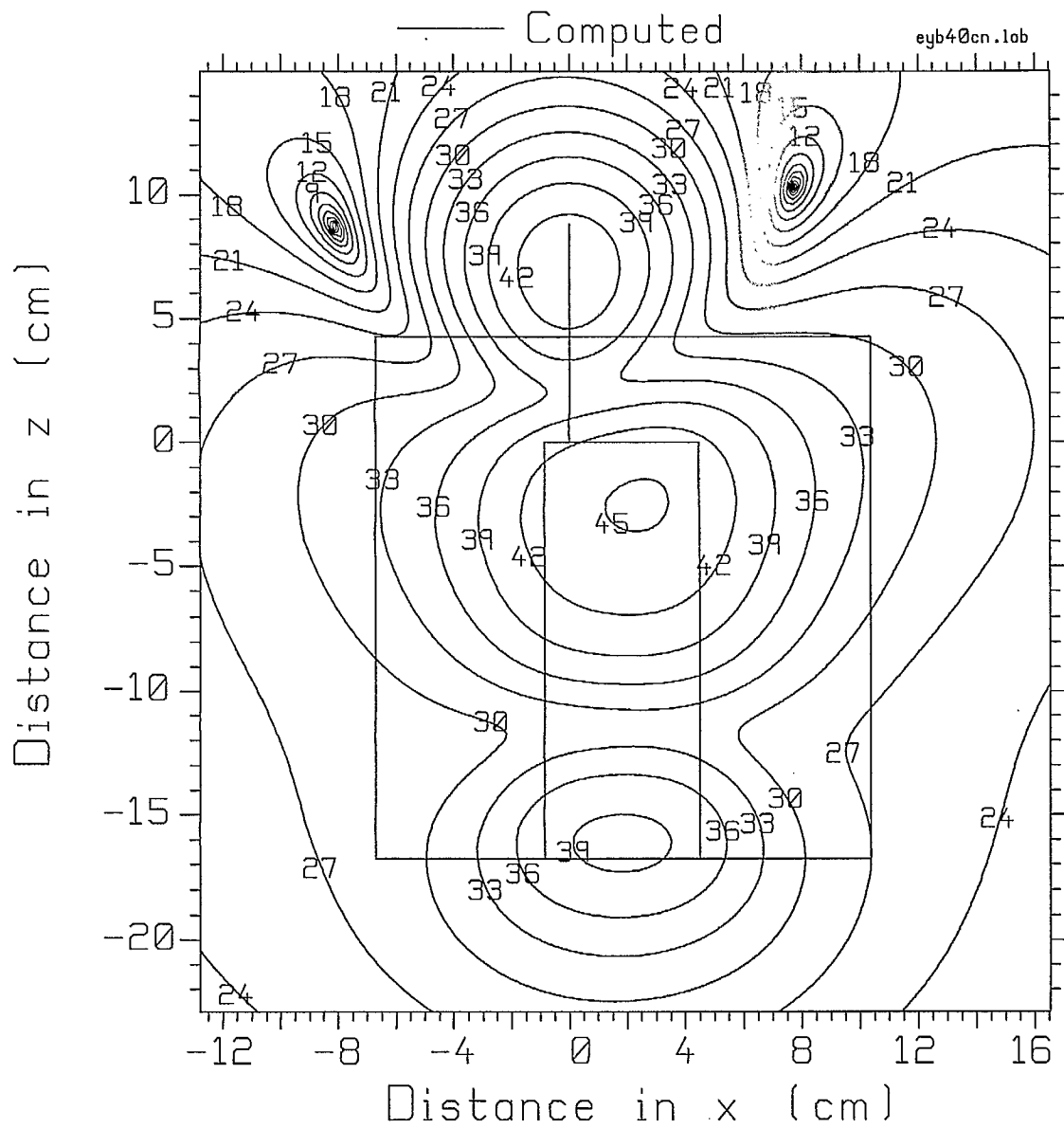


Fig. 3.4(b) The  $E_y$  component in an  $xz$  plane at 42.9 mm from the antenna.



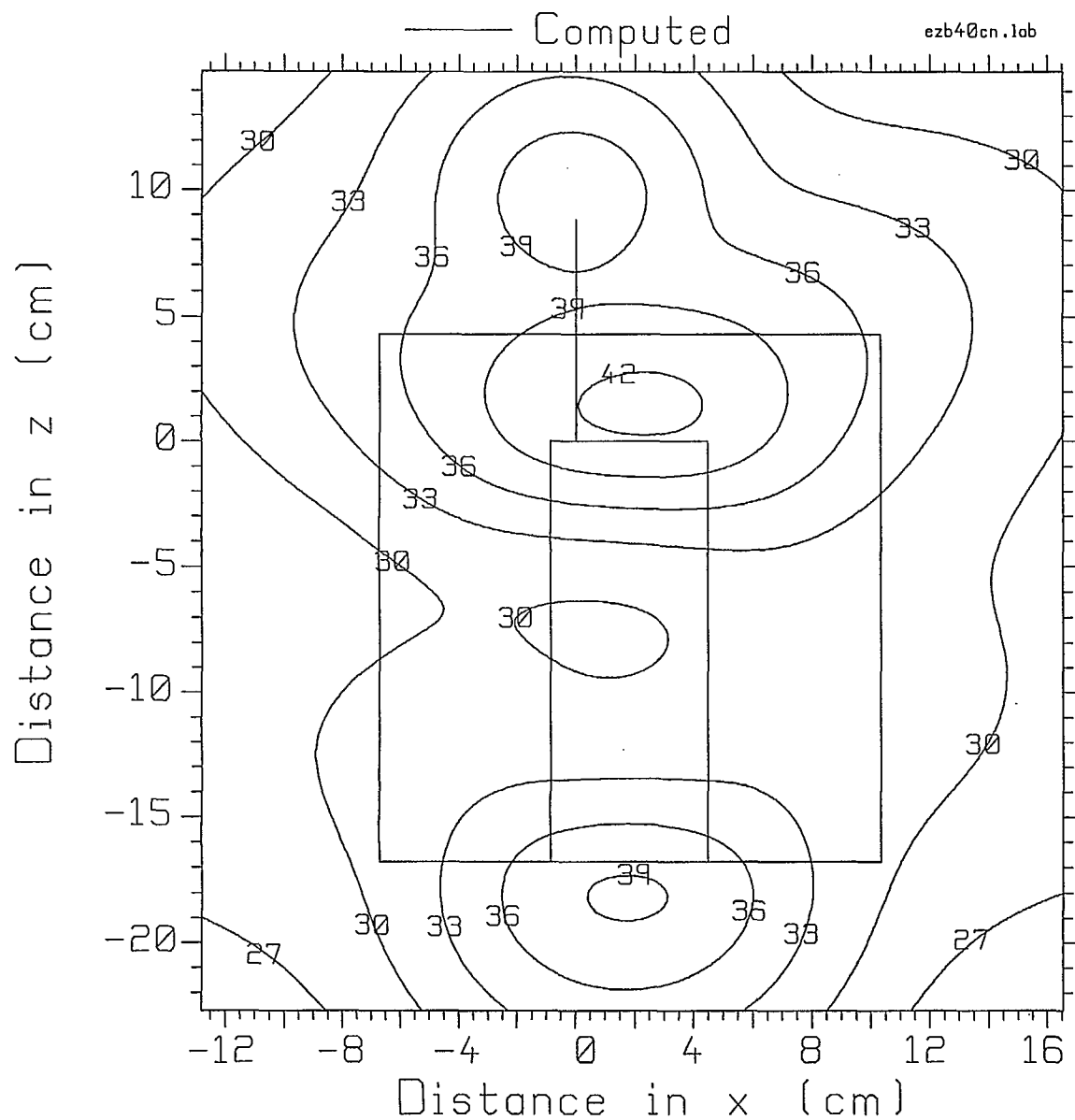


Fig. 3.4(c) The  $E_z$  component in an  $xz$  plane at 41.8 mm from the antenna.

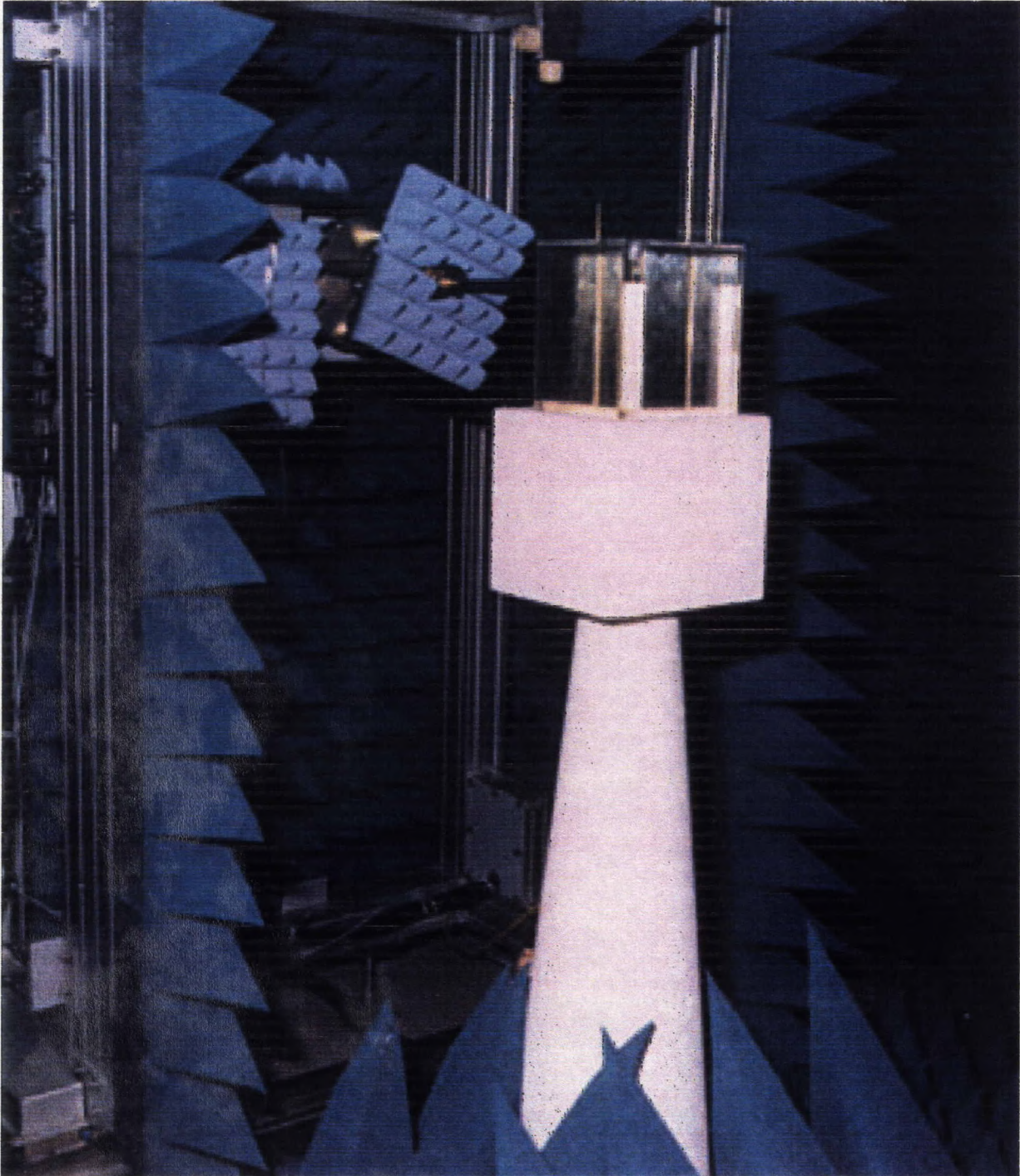


Fig. 3.5 The planar scanner holding the probe and measuring the near field of the handset and box head [17].



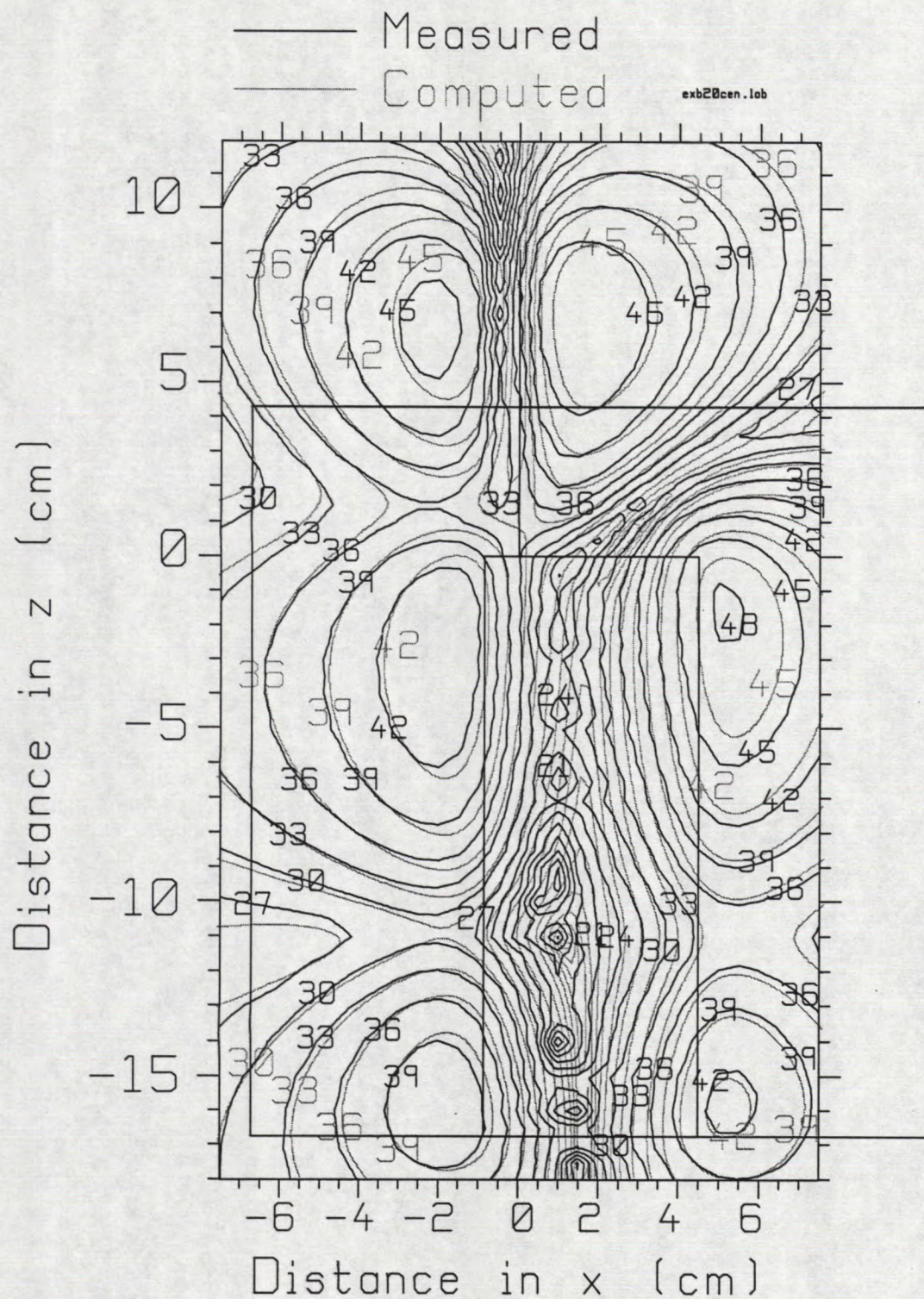


Fig. 3.6(a) Comparison of the measured and computed  $E_x$  component in an  $xz$  plane at 21.8 mm from the antenna.



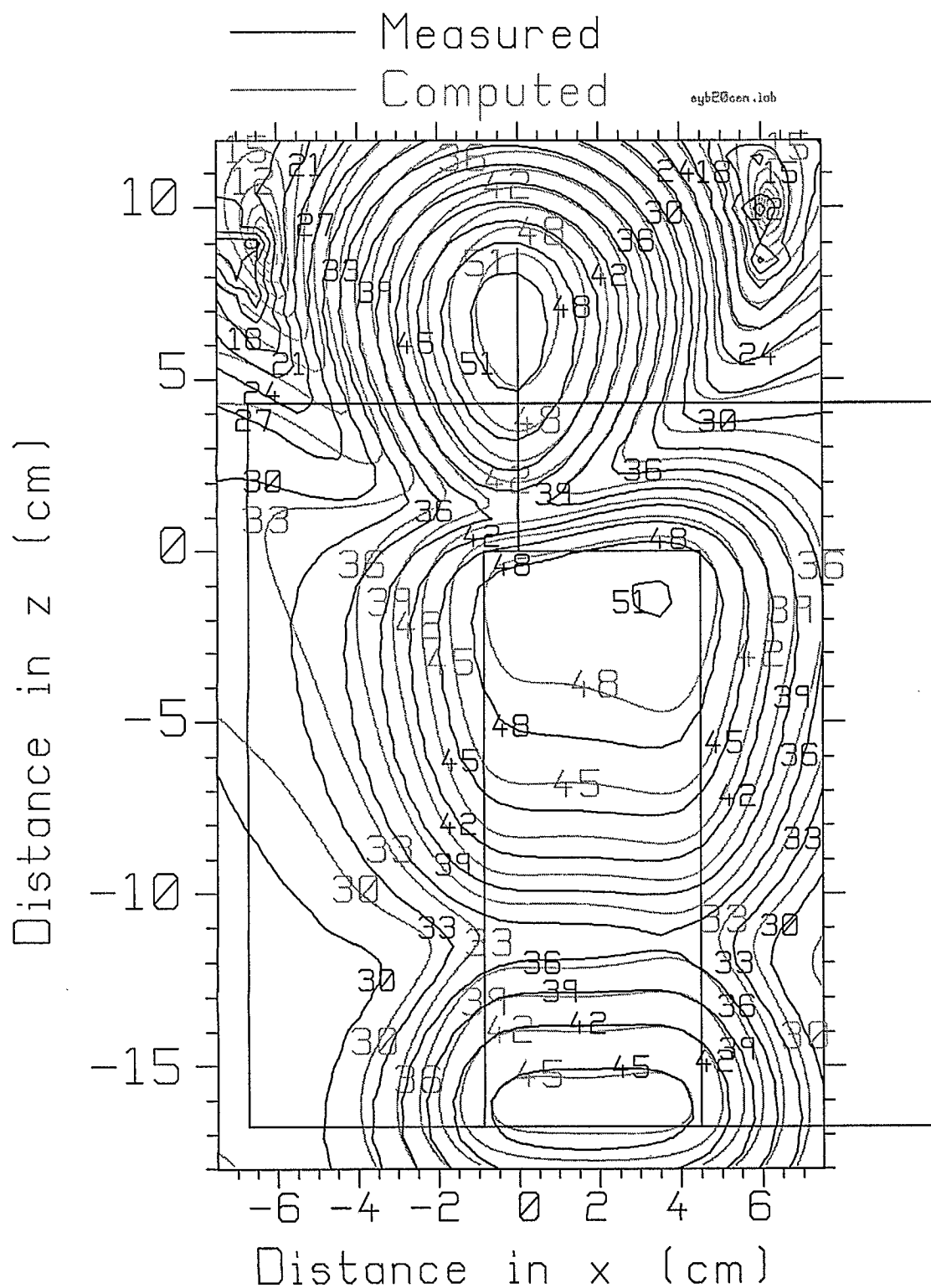


Fig. 3.6(b) Comparison of the measured and computed  $E_y$  component 22.9 mm from the antenna.



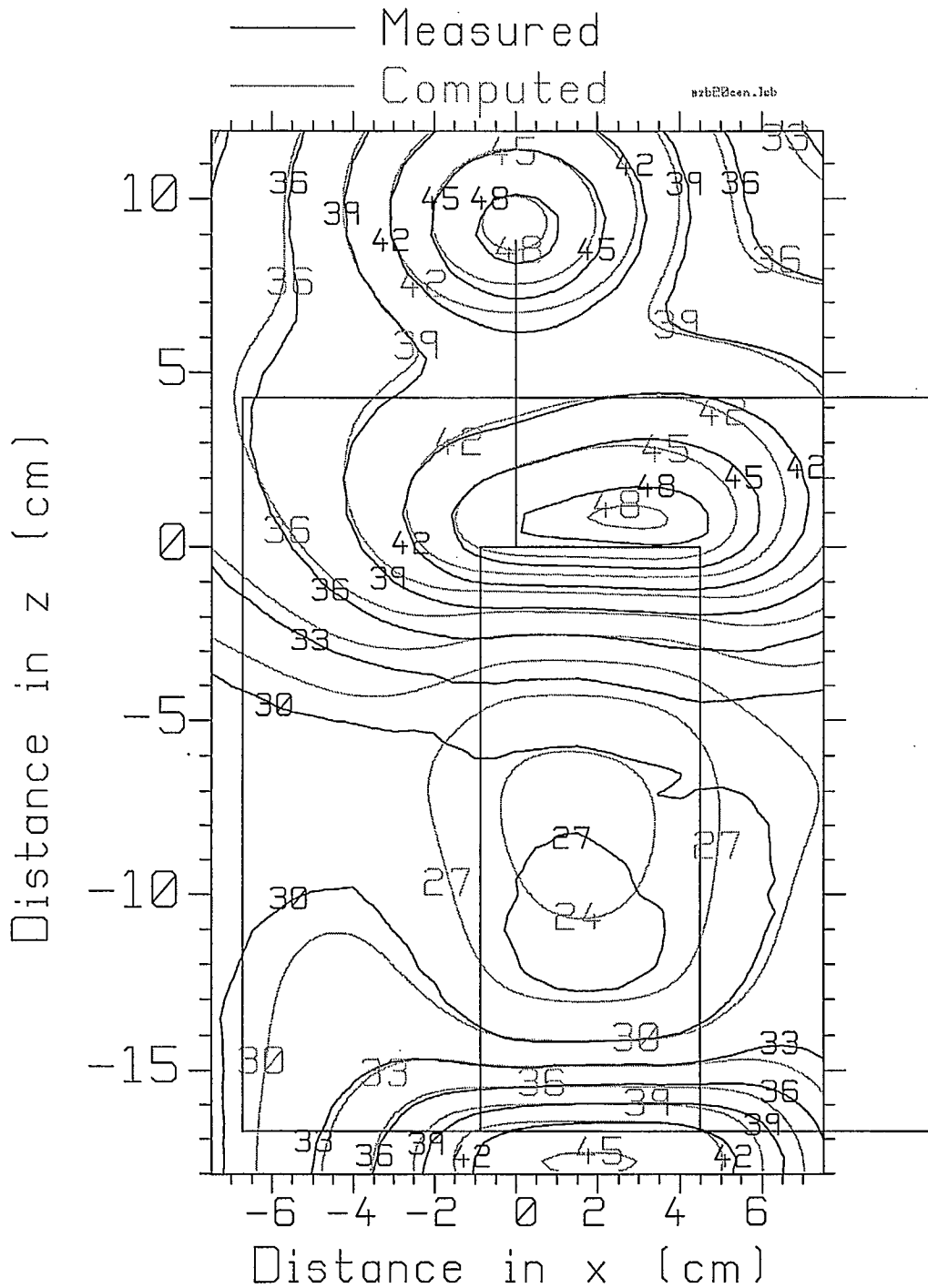


Fig. 3.6(c) Comparison of the measured and computed  $E_z$  component 21.8 mm from the antenna.



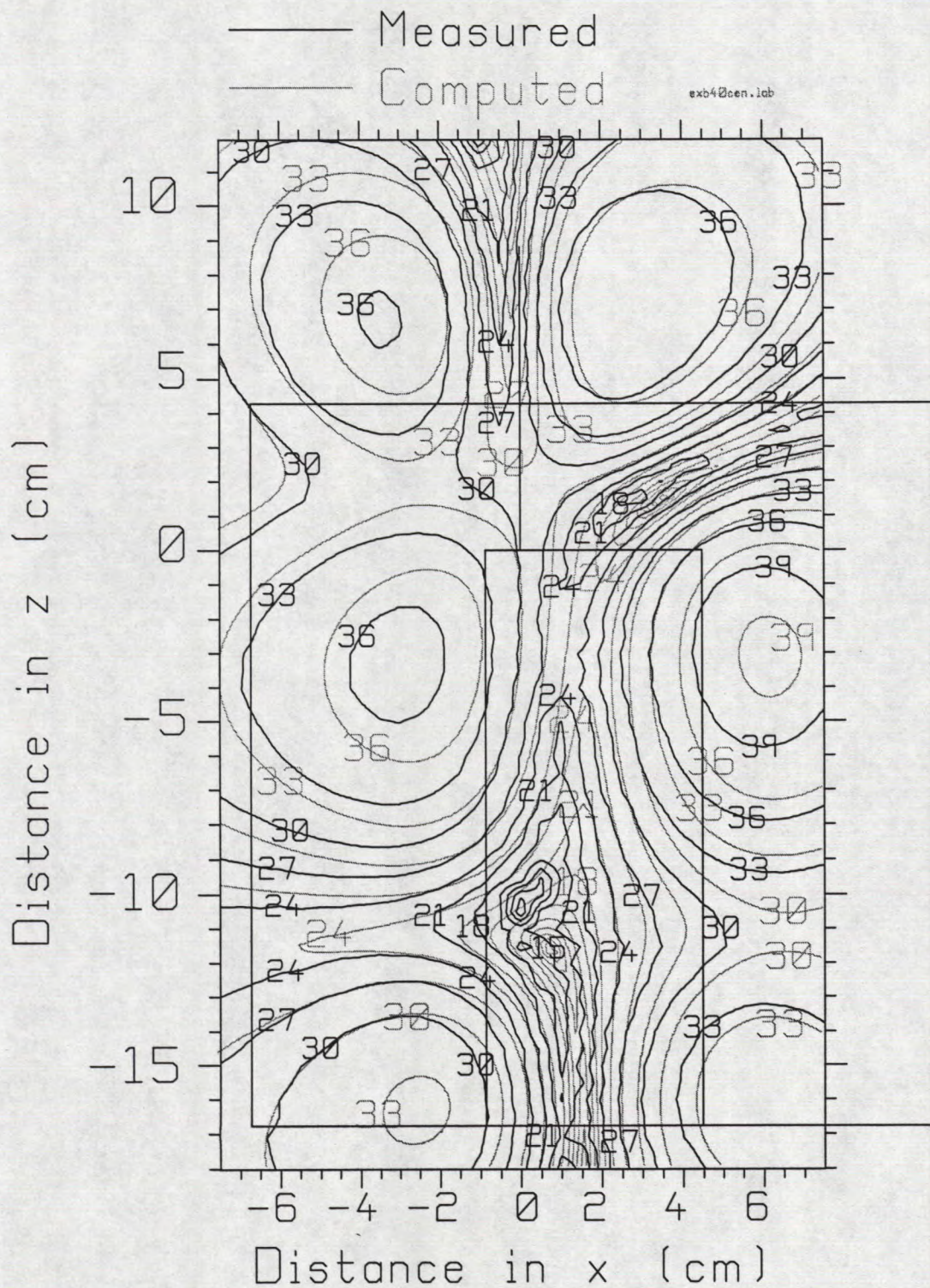


Fig. 3.7(a) Comparison of the measured and computed  $E_x$  component in an  $xz$  plane at 41.8 mm from the antenna.



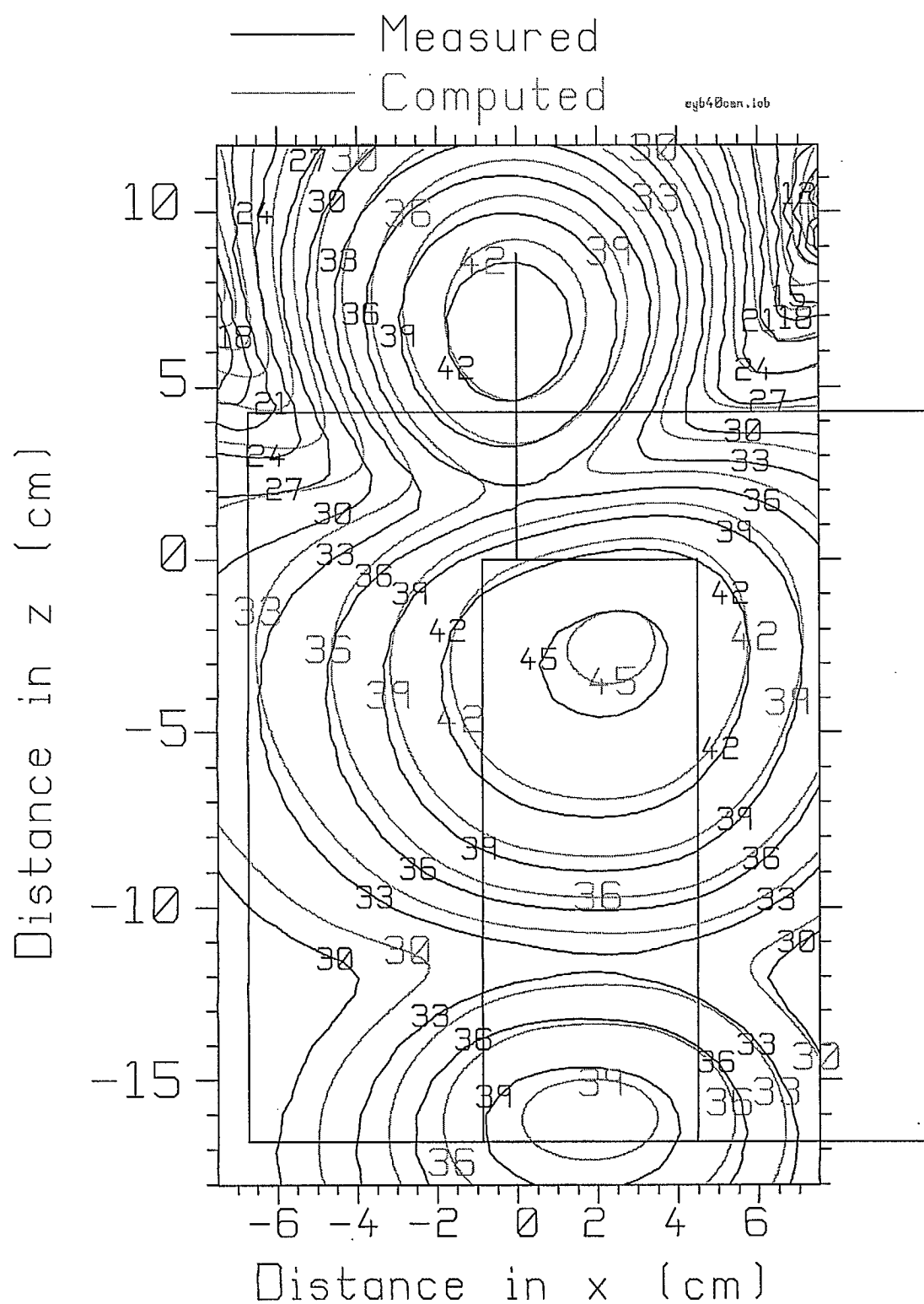


Fig. 3.7(b) Comparison of the  $E_y$  component at 42.9 mm from the antenna.

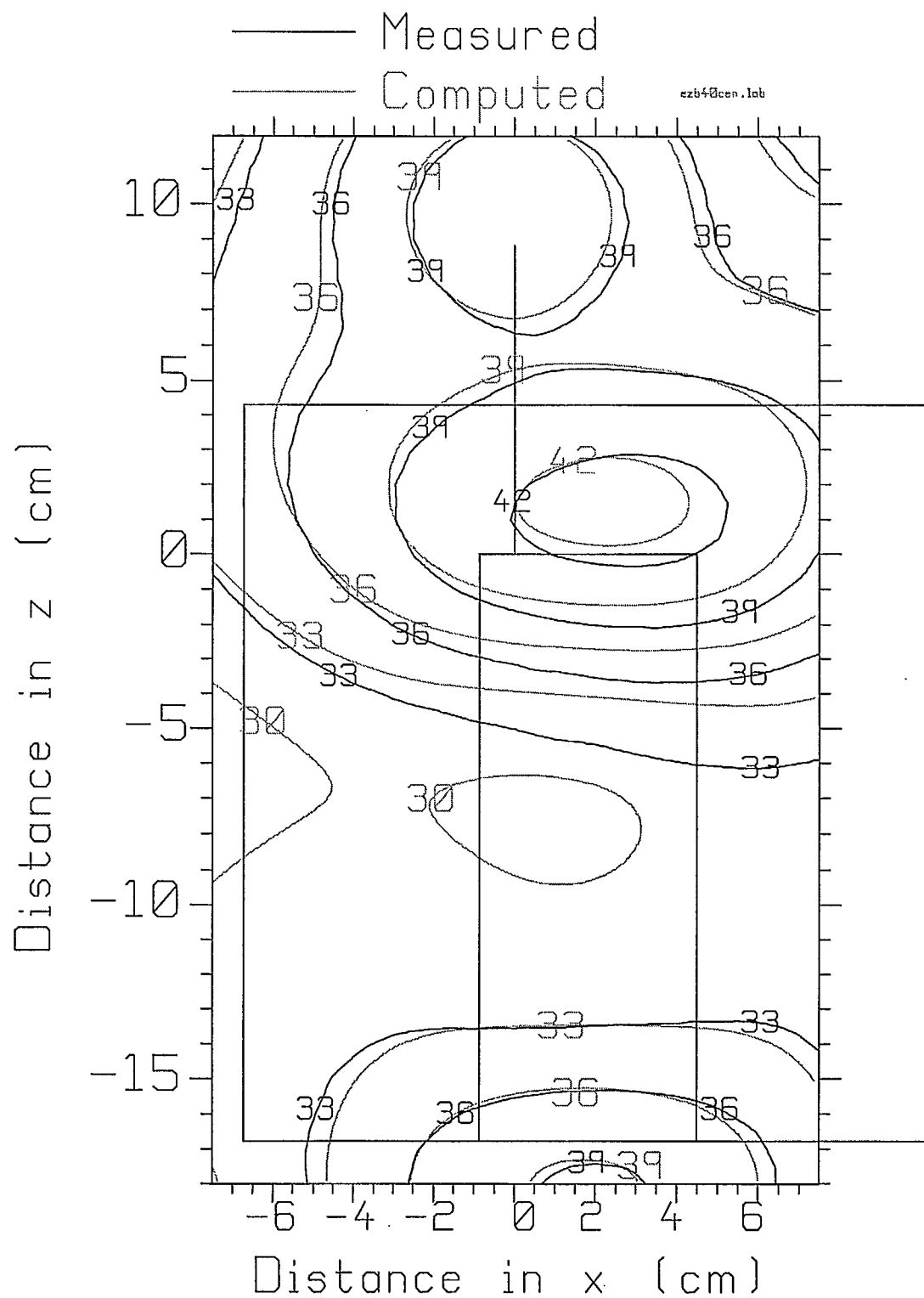


Fig. 3.7(c) Comparison of the  $E_z$  component at 41.8 mm from the antenna.



## Chapter 4

### Near Fields of the Handset and Sphere Head

A sphere is a much more realistic shape to represent the head than a box. This chapter investigates the near fields of the handset held vertically adjacent to a sphere modeling the head. The “sphere head” is a plexiglas sphere of outside diameter 20.68 cm and wall thickness 0.365 cm. The sphere is filled with “brain liquid” of conductivity  $\sigma = 1.064$  and relative permittivity  $\epsilon_r = 40.42$ . The plexiglas was modeled with  $\sigma = 0.0049$  and  $\epsilon_r = 3.45$ , which were taken from the literature[22] although measured values would be preferred. The handset is positioned 0.94 cm from the surface of the sphere. The near fields were measured with the probe tip 20 mm and 40 mm from the base of the antenna. This chapter presents the computed fields of the handset near the sphere head, and then compares the measured field maps with the computations.

#### 4.1 The FDTD Model of the Handset and Sphere Head

The handset and sphere head were modeled at 850 MHz with 2.205 mm cells as in the previous chapters. The handset was modeled with 24 by 8 by 76 cells with a 40 cell antenna, as before. Fig. 4.1 shows the handset and sphere head cell model schematically. Note that the bottom of the handset aligns with the bottom of the sphere. The sphere’s curved surface must be “staircased” with cubical FDTD cells to approximate its shape. The surface is smoothed by the averaging process that is built into the FDTD code, in which the permittivity used to update the field at the cell edges is the average of the permittivity values for the four adjacent cells. The same averaging process is used for the conductivity. The sphere is represented with 93 cells across its diameter, for a 20.51 cm sphere, close to the true diameter of 20.68 cm. The plexiglas wall is represented as 2 cells thick, or 4.4 mm, compared to the true thickness of 3.45 mm. The spacing from the handset surface to the sphere surface is modeled as 5 cells or 11.02 mm, where the true spacing is 9.4 mm. The relative position of the handset and the sphere were determined from the CRC mechanical drawings[17] and are as precise as can be represented with 2.205 mm cells.

The handset and sphere are embedded in an FDTD cell space of size 167 by 179 by 189 cells for a total of 5,649,777 cells. The 6 cells adjacent to the outer boundary of the cell space are used to implement the perfectly-matched layer absorbing boundary. The FDTD code is time-stepped for 4096 steps to reach steady state.

After FDTD PML was run for the sphere, the FARZONE code was used to compute the conical cut radiation pattern set. The power flow density over the surface of the radiation sphere was integrated to find the radiated power, and then the near fields of the handset and sphere were scaled to 600 mW of radiated power. In the following, the contour maps of the sphere’s near field are presented.

## 4.2 Computed Near Fields of the Handset and Sphere

Figs. 4.2 and 4.3 present the computed near fields of the handset and sphere at 20 mm and 40 mm distance from the antenna to the tip of the probe in the measurement setup. The region over which the near field was calculated is somewhat larger than that used for the measurements, and these figures give insight into the behavior of the field over this larger area. As before, the field is graphed in decibels with a reference level of 1 volt/meter.

An overall comparison of the fields of the handset and sphere head with those of the handset alone suggests that the sphere has much less effect on the handset patterns than does the box head. This is because the sphere's surface curves away from the handset. The handset has three regions of high field, at the tip of the antenna, at the top of the case and at the base of the case. Two of these regions, the antenna tip, and the base of the case, are quite far from the sphere in Fig. 4.1 hence are less influenced by the dielectric material making up the sphere. The third region, the top of the case, is further from the sphere surface that it is in the handset and box head case, and so once again the sphere's influence on the fields is less.

### 4.2.1 Computed Fields at 20 mm Distance

Fig. 4.2(a) shows the  $E_x$  component of the field of the handset and sphere head in an  $xz$  plane at 21.8 mm distance from the base of the handset's antenna. The field is similar to that of the handset alone in Fig. 2.7(a). For the handset near the sphere, this horizontal component of the field on either side of the antenna has 42 dB contours, whereas for the handset alone, the field to the left of the antenna never reaches 42 dB. The field to the left of the top of the handset case is 42 dB for the handset and sphere head, and is quite similar to that of the handset alone in Fig. 2.7(a). At the bottom of the case, both have a 39 dB contour, but for the handset and sphere the contour is larger in enclosed area, indicating that the field has a stronger maximum value. To the right of the top of the handset case, the handset and sphere field reaches 45 dB, and is very similar to the field of the handset alone. At the base of the case, there is a 42 dB contour for the handset and sphere, whereas for the handset alone, the field does not get as large as 42 dB.

Because the lossy dielectric sphere absorbs power, the handset must deliver more power to the handset and sphere system to *radiate* 600 mW than for the handset alone. Hence we find stronger fields near the handset when the head is present.

Fig. 4.2(b) shows the  $E_y$  component of the field, which is perpendicular to the plane of the paper. Over the antenna, the field has a 48 dB contour, which is quite similar to that for the handset alone in Fig. 2.7(b). There are two minima in the field on either side of the antenna, which are not seen in the handset alone fields, but are clearly seen in the handset and box head fields in Fig. 3.3(b). Also note that for the handset and box head, the field over the antenna is much larger, with a large 51 dB contour. The box head is much closer to the handset and couples more strongly to the fields at the top of and the

base of the case, hence absorbs much more power. Over the top of the case, there is a 48 dB contour for the handset and sphere, larger in area than for the handset alone in Fig. 2.7(b). Over the bottom of the case there is a 45 dB field contour, similar to that for the handset alone.

Fig. 4.2(c) shows the vertical component of the field at 21.8 mm from the base of the antenna. There is a 42 dB contour surrounding the tip of the antenna, similar to that for the handset alone in Fig. 2.7(c). At the top of the case the handset and sphere has a large 45 dB contour; for the handset alone there is a 45 dB contour that is “smaller”, meaning that it encloses less area. At the bottom of the case the handset and sphere has a small 45 dB contour, whereas for the handset alone the field here is never stronger than 45 dB so only a 42 dB contour is seen.

#### 4.2.2 Computed Fields at 40 mm Distance

Fig. 4.3 shows the computed field maps at 40 mm from the probe tip to the antenna. Part (a) shows the  $E_x$  component in an  $xz$  plane 41.8 mm from the base of the antenna. The field just to the left of the antenna has a small 33 dB contour, whereas to the right of the antenna the 33 dB contour is much larger. There is a sharp, deep minimum in the field just above the case, where the minimum contour is 9 dB. To both the left and right of the top of the handset case, there are large 36 dB contours. To the left of the bottom of the case there is a small 33 dB contour. The field to the right of the bottom of the case is stronger, with a larger-area 33 dB contour. There is a trough in the field towards the bottom center of the handset case, where the minimum field contour is 0 dB.

Fig. 4.3(b) shows the  $E_y$  component of the field at 22.9 mm from the base of the antenna. There is a 39 dB contour over the antenna. There are minima in the field to the left and right of the top of the case. The minimum field is -15 dB in the minimum at left, and is -6 dB in the minimum at right. The field near the top of the case has a small 45 dB contour. At the bottom of the case there is a larger 39 dB contour.

Part (c) shows the vertical component of the field at 41.8 mm from the base of the antenna. The tip of the antenna is enclosed by a 36 dB contour. The field strength at the top of the case has a small 42 dB contour. The field over the body of the handset has a 30 dB contour so falls below 30 dB. At the base of the case there is a 39 dB field contour.

#### 4.3 Comparison with the Measured Near Fields

The near fields of the handset and sphere head were measured using the near field system described in Chapter 2. Fig. 4.4 shows the handset and sphere head sitting on a styrofoam holder, with the near field probe nearby. The measured near fields were scaled to the level of the computed fields using the “tie-line” normalization method discussed in Chapter 2. The electric field strength is graphed in decibels with a reference level of one volt per meter.



#### 4.3.1 Comparison at 20 mm Separation

Fig. 4.5 compares the computed and measured near fields at a distance of 20 mm from the tip of the probe to the base of the antenna. Part (a) compares the measured and computed  $E_x$  component in an  $xz$  plane at  $y=-21.8$  mm. To the left of the antenna, near the border of the contour map, the 30, 33 and 36 dB contours correspond very well between the measurement and the computation. However, close to the antenna, the computed field is much stronger, with at 42 dB contour, whereas the measured field has a 39 dB maximum contour. Very close to the location of the antenna, the measured and computed contours do not correspond precisely. To the right of the antenna, the measured 42 dB contour is larger in area and shifted closer to the antenna compared to the computed 42 dB contour. Although the 39, 36 and 33 dB contours compare well in shape between the measurement and the computation, the measured contours are closer to the antenna. Near the top of the handset case, there is a trough in the field. The measured field falls to 21 dB in the trough, and the computed field to 15 dB at a nearby location.

To the left of the top of the handset case, the measured field has a 42 dB contour. The computed field has a 42 dB contour enclosing a larger area, hence the computed field rises to larger values in this region. The 39 and 36 dB contours are also larger in the computation than in the measurement. To the right of the top of the case, The computed 45 dB contour is much smaller than the measured contour. Hence the measured field has larger values than the computed field in this region. The measured 42 dB contour is also larger in area than the computed contour. At the bottom left corner of the case, the measured and computed fields both have a 39 dB contour, with the computed contour larger in area. To the right of the bottom of the case, the measured and computed data both have small 42 dB contours. The 39 dB contours are almost the same size and in the same location.

There is a trough in the field strength to the left of the centerline of the case in both the measurement and the computation. The measured field falls to -3 dB. The computed field has a minimum contour of 0 dB, at almost the same position.

Fig. 4.5(b) compares the measured and computed  $E_y$  component of the field at 22.9 mm from the base of the antenna. Both the measured and the computed fields have 48 dB contours over the antenna, but the computed contour is much larger in area. The measured and computed contours do not stay aligned in position on either side of the antenna. There is a minimum in the field both to the left and to the right of the antenna, near the edges of the contour map. At left, the measured field has a minimum contour of 12 dB, and the computed minimum contour is 3 dB, and the location of the minimum is substantially shifted in position compared to the measured minimum. To the right of the antenna, above and to the right of the top corner of the handset case, there is a minimum in the measured field of 12 dB. Very nearby there is a minimum in the computed field, of 3 dB.

Over the top of the handset case, both the measured field and the computed field have 45 dB contours. These are almost equal in enclosed area, but the measured contour is shifted downwards compared to the computed contour. To the right of the top of the handset, the 45, 42 and 39 dB contours correspond well. To the left of the top of the

handset case, the contours have the same general shape but do not correspond precisely in position.

At the bottom of the handset case both the measurement and the computation have a 45 dB contour, and they are similar in size and position. The 42, 39 and 36 dB contours correspond well over the bottom of the case. To the left of the case the computed fields are somewhat lower in value than the measured fields, with the measured 27 dB contour falling on the computed 24 dB contour. To the right of the bottom of the case the alignment of the contours is better.

Fig. 4.5(c) compares the measured and computed vertical component of the field at 21.8 mm from the base of the antenna. Around the tip of the antenna, the measured and computed fields both have 42 dB contours, and of almost the same enclosed area or "size". The 39 dB contours also correspond quite well, and indeed the 36 dB contours align well, too. At the top of the handset case both the measured and the computed data have 45 dB contours with the measured contour slightly larger in enclosed area. The measured data shows a very small region where the field is in excess of 48 dB. To the left of the top of the handset the 42, 39, 36 and 33 dB contours align very well, but to the right these contours are not well aligned between the measurement and the computation. Over the body of the handset case, the computed field has a 24 dB contour, but the measured field shows only a 27 dB contour and does not fall as low as 24 dB. At the bottom of the case the measured and computed fields have 42 dB contours, but the computed contour is larger and the computed field has a small 45 dB contour. The 39, 36 and 33 dB contours align quite well.

#### 4.3.2 Comparison at 40 mm Separation

Fig. 4.6 compares the measured and computed fields when the probe tip is 40 mm from the base of the antenna. Part (a) shows the  $x$  component of the field. To the left of the antenna, the computed field is stronger than the measured field, with a 33 dB contour. The 30 dB contour in the computation is also larger in area than the 30 dB contour in the measurement. To the right of the antenna, the measurement and the computation both have 33 dB contours, with the measured contour slightly larger in enclosed area. There is a minimum in the field above the tip of the antenna where the computed field falls to have an 18 dB contour. The measured field has a small 21 dB contour at a nearby location. Near the top of the case the measured field has a sharp minimum with a small 12 dB contour. Very nearby, the computed field has a sharp minimum of field strength 9 dB.

To the left of the top of the handset case there is a small 36 dB contour in the measurement, and a much larger 36 dB contour in the computed field. Evidently the computed field is much stronger in this region. To the right of the top of the handset case there is a 36 dB field strength contour that is larger in area in the measurement than in the computation. To the left of the bottom of the handset, there is a 33 dB contour in the computed field but the measured field is not this large. The 30 dB contour in the measurement corresponds to the 30 dB contour in the computation, but the measured contour is somewhat smaller in enclosed area. To the right of the bottom of the handset case there is a 33 dB contour that corresponds quite well between the measurement and the computation.

Near the bottom of the handset case, to the left of center, there is a trough in the field. The minimum contour in the measured data is 6 dB. The minimum computed contour is 0 dB. The general configuration of the trough is quite similar between the measurement and the computation but the precise location of the contours does not correspond well.

Fig. 4.6(b) compares the measured and computed  $E_y$  field component at 42.9 mm distance from the base of the antenna. Over the antenna, both the measured and the computed fields have 39 dB contours, with the measured contour smaller in enclosed area than the computed contour. The 36 and 33 dB contours correspond well.

The measured field has a local minimum to the left of the antenna near the edge of the contour map. The field falls to 9 dB. The computed field also has a local minimum of field strength -15 dB, at about 1.5 cm above the location of the measured minimum. The measured field also has a minimum above and to the right of the top of the handset case. The measured field falls to 12 dB, and at a nearby location the computed field has a sharper minimum, falling to -6 dB.

Near the top of the handset case both the measured field and the computed field have 45 dB contours. The 42 dB contours correspond very well. The 39 dB contours superimpose quite well except to the right of the top of the case. At the base of the case there is a 39 dB contour that is very similar in the measurement and computation, but slightly larger in enclosed area in the measurement. The 36 and 33 dB contours correspond reasonably well, especially over the handset case, and to the right of the bottom corner of the case.

Fig. 4.6(c) compares the measured and computed vertical component of the field at 41.8 mm from the base of the antenna. The tip of the antenna is surrounded by a large 36 dB contour that corresponds quite well between the measurement and the computation. Above the top of the case there is a 42 dB contour which is somewhat larger in enclosed area in the measured field than in the computed field. The 39 dB measured contour is also larger in area than the corresponding computed contour. Over the center of the case, the computed field falls below 30 dB but the measured field does not. Near the bottom of the case both the measured and the computed fields have 39 dB contours, but the computed contour is much larger. The computed 36 dB contour is only slightly larger in enclosed area than is the measured 36 dB contour. The 33 dB contours correspond reasonably well.

#### 4.4 Conclusion

This chapter has presented the near fields of the handset near the sphere model of the head. Because the surface of the sphere curves away from the bottom and the top of the handset, the sphere interacts less with the handset's fields than does the box head. Although the handset and sphere near fields resemble the handset and box near fields, the changes from the handset alone near fields are less marked for the sphere head than for the box head.

In general very good agreement has been achieved between the computed near fields and the measured near fields. The discussion presented above is intended to step through the field maps pointing out similarities and differences. Overall the measured



and computed field maps are very close to one another and the differences are in detail rather than in substance.

The concluding chapter of this report will comment on the degree of agreement obtained here between the measured and computed near fields compared to that in previous work.

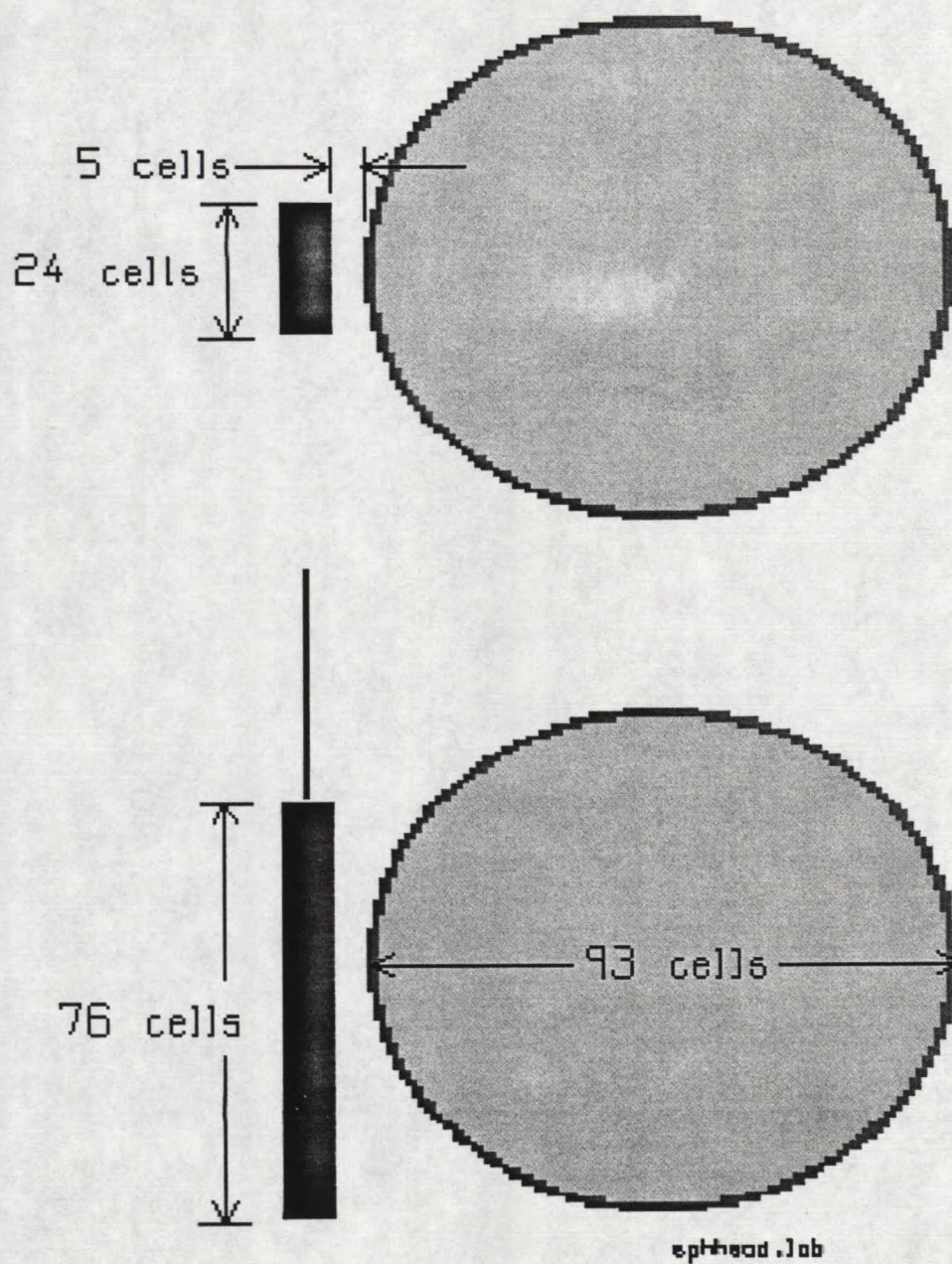


Fig. 4.1 The FDTD cell model of the handset and sphere.



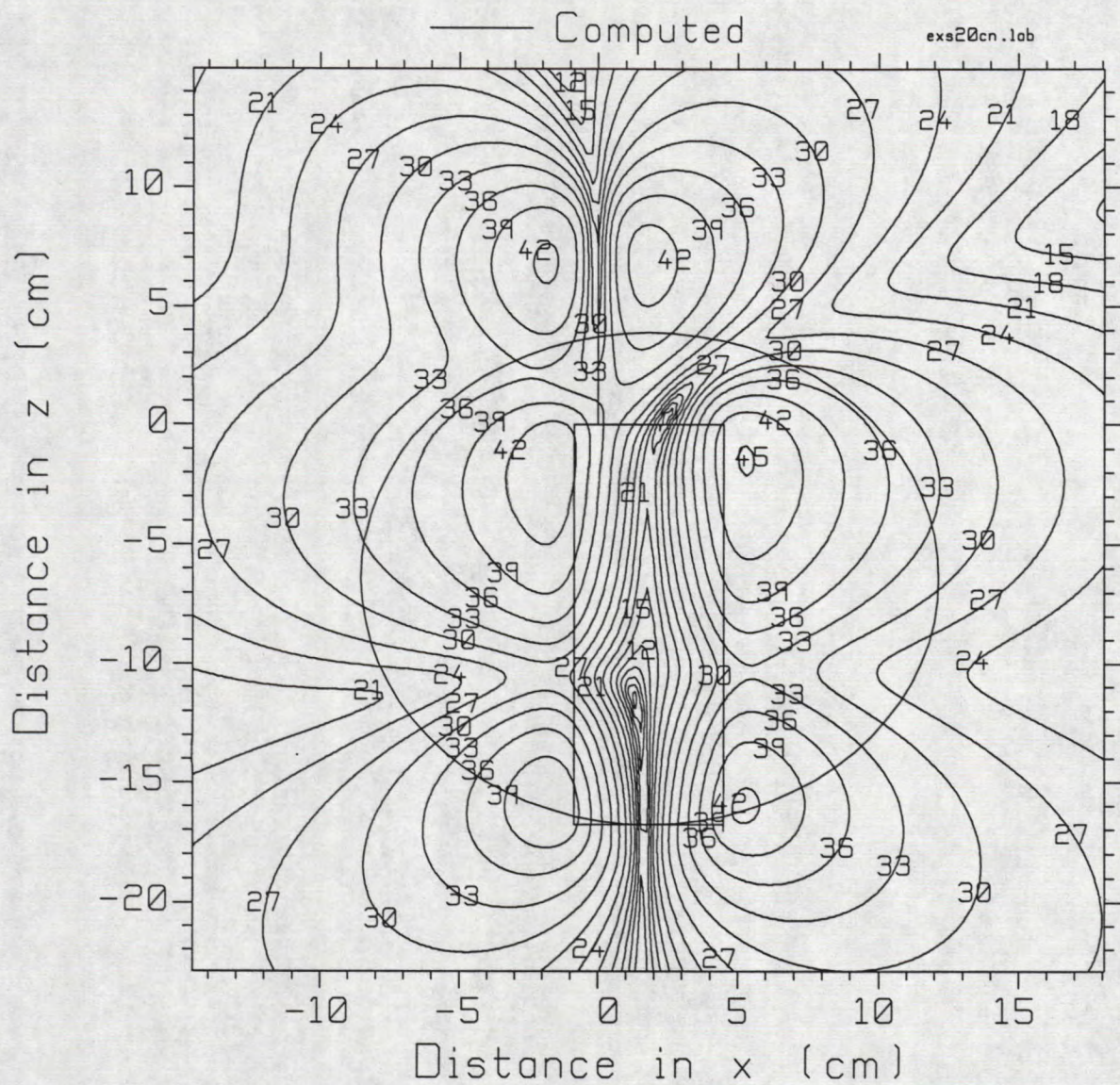


Fig. 4.2(a) The  $E_x$  component of the field for the handset and sphere in an  $xz$  plane at 21.8 mm from the antenna.



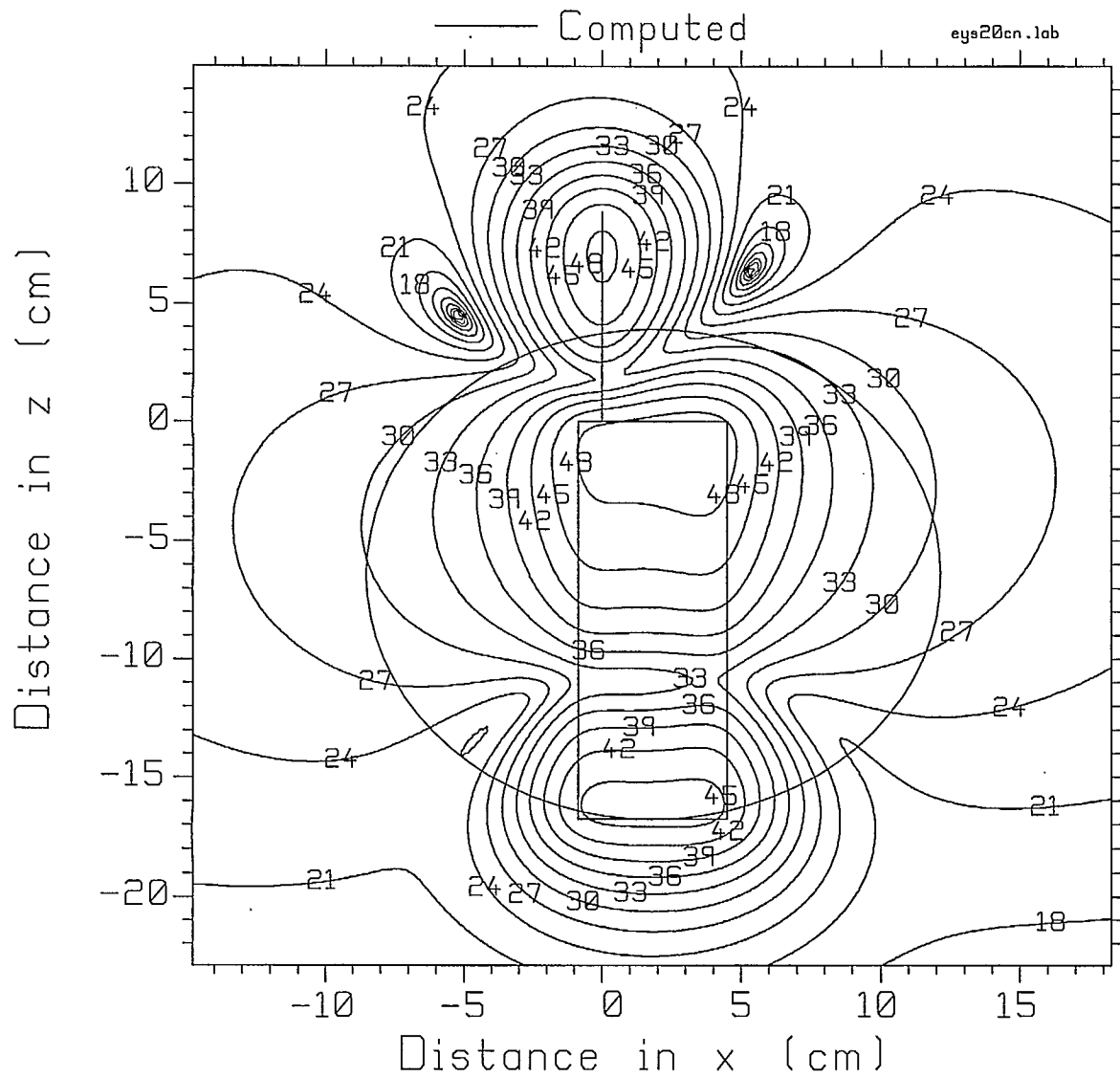


Fig. 4.2(b) The  $E_y$  component of the field for the handset and sphere 22.9 mm from the antenna.

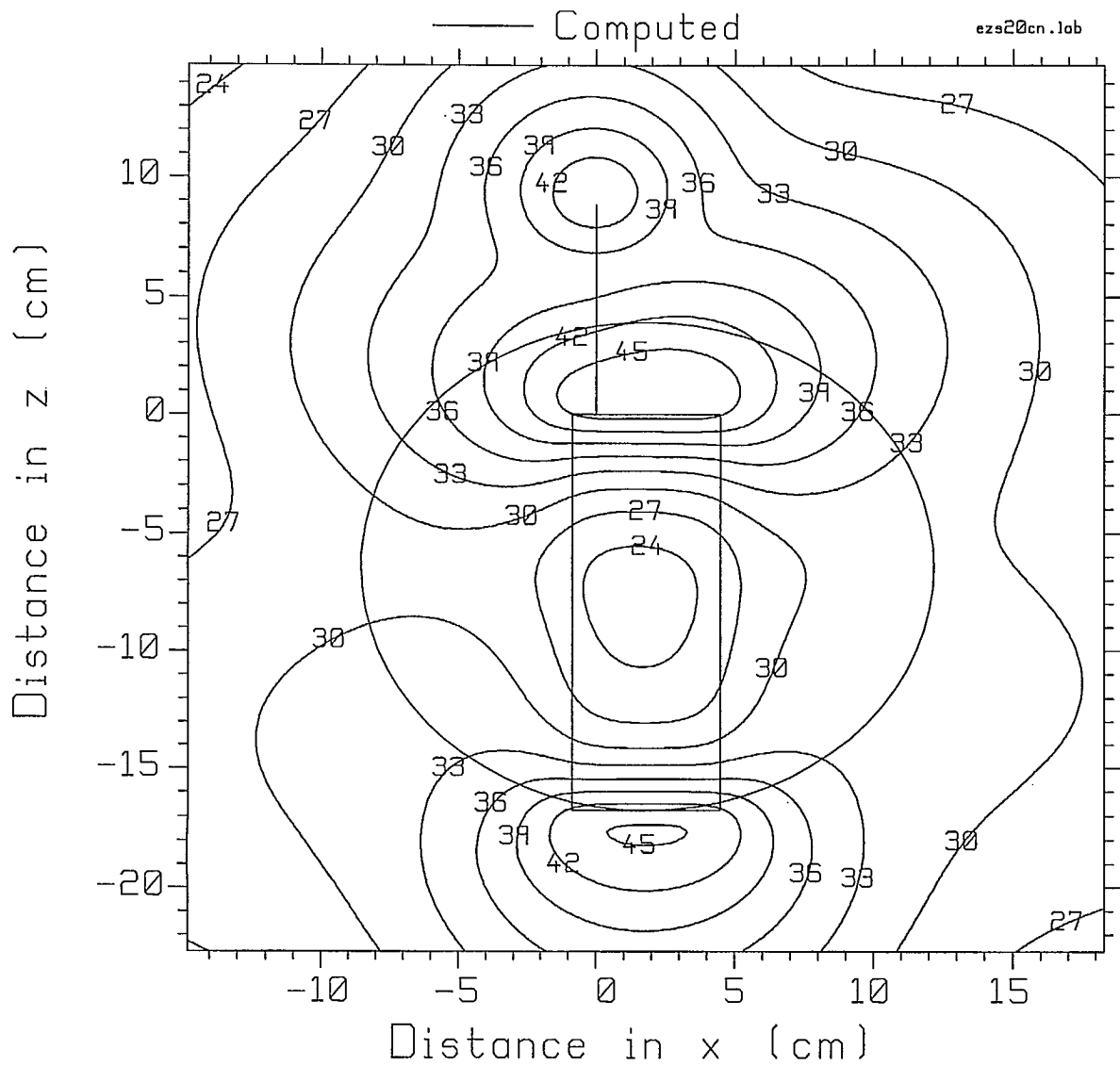


Fig. 4.2(c) The  $E_z$  component of the field for the handset and sphere 21.8 mm from the antenna.

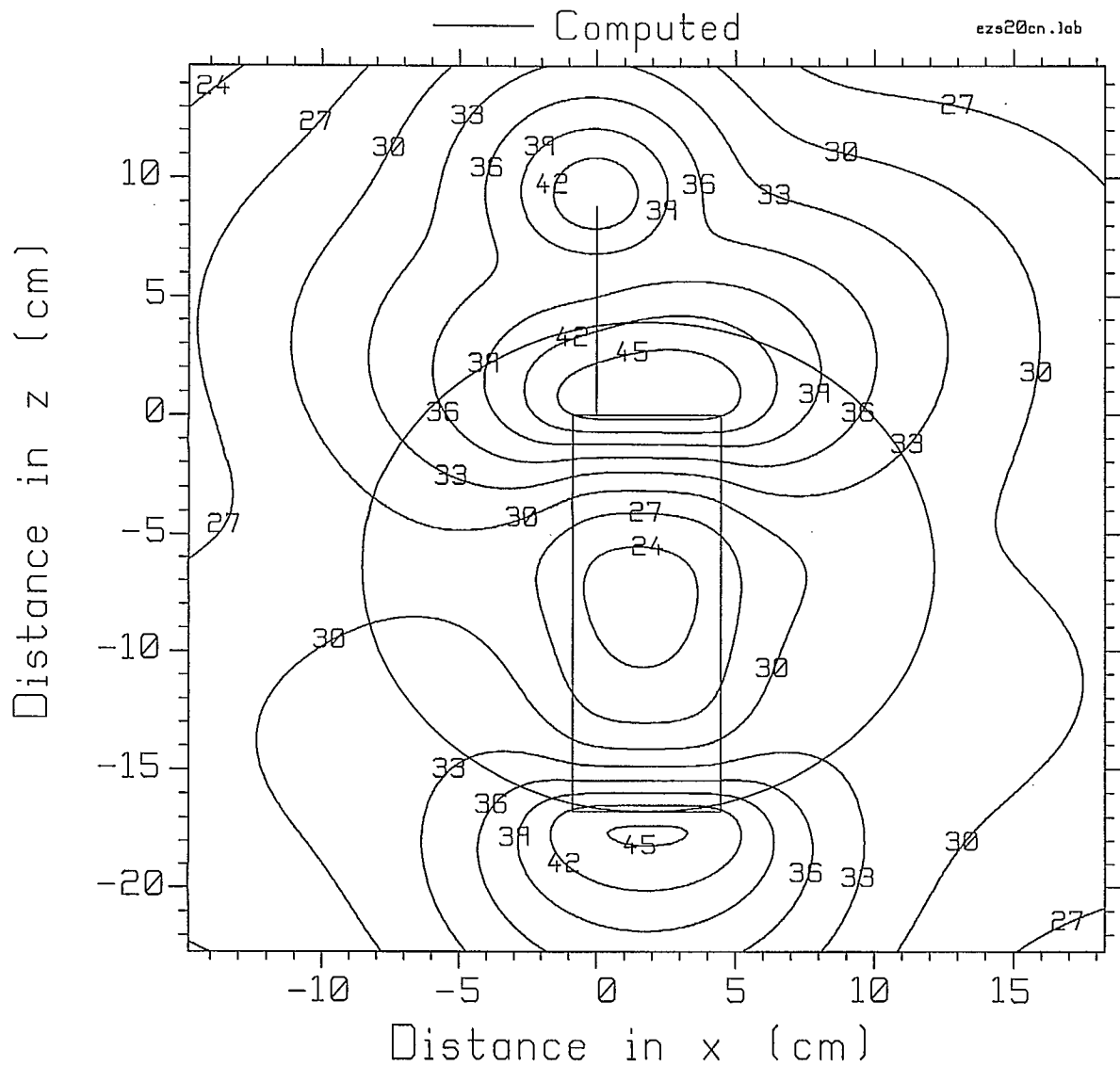


Fig. 4.3(a) The  $E_x$  component of the field for the handset and sphere 41.8 mm from the antenna.



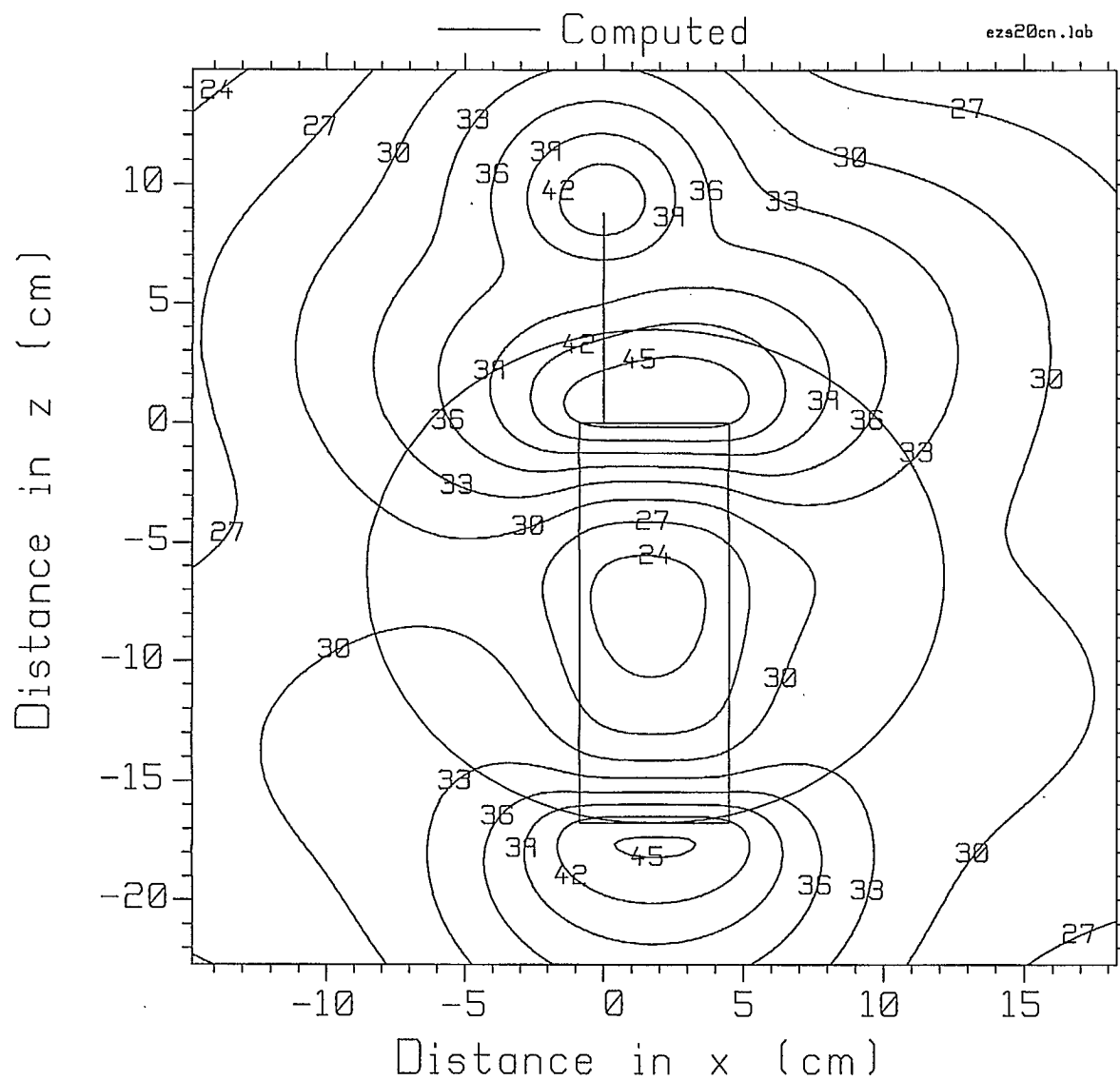


Fig. 4.3(b) The  $E_y$  component of the field for the handset and sphere 42.9 mm from the antenna.

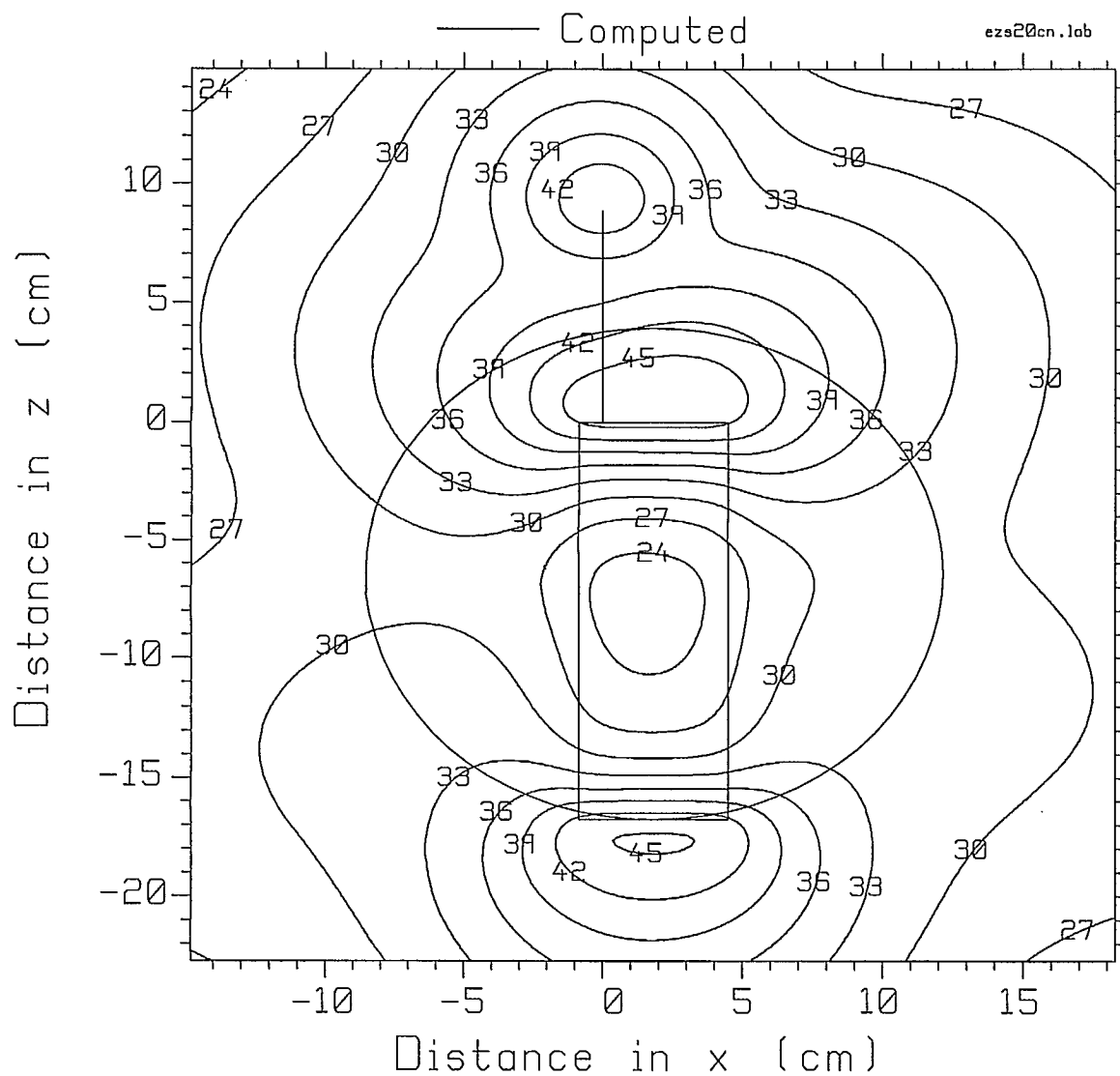


Fig. 4.3(c) The  $E_z$  component of the field for the handset and sphere 41.8 mm from the antenna.

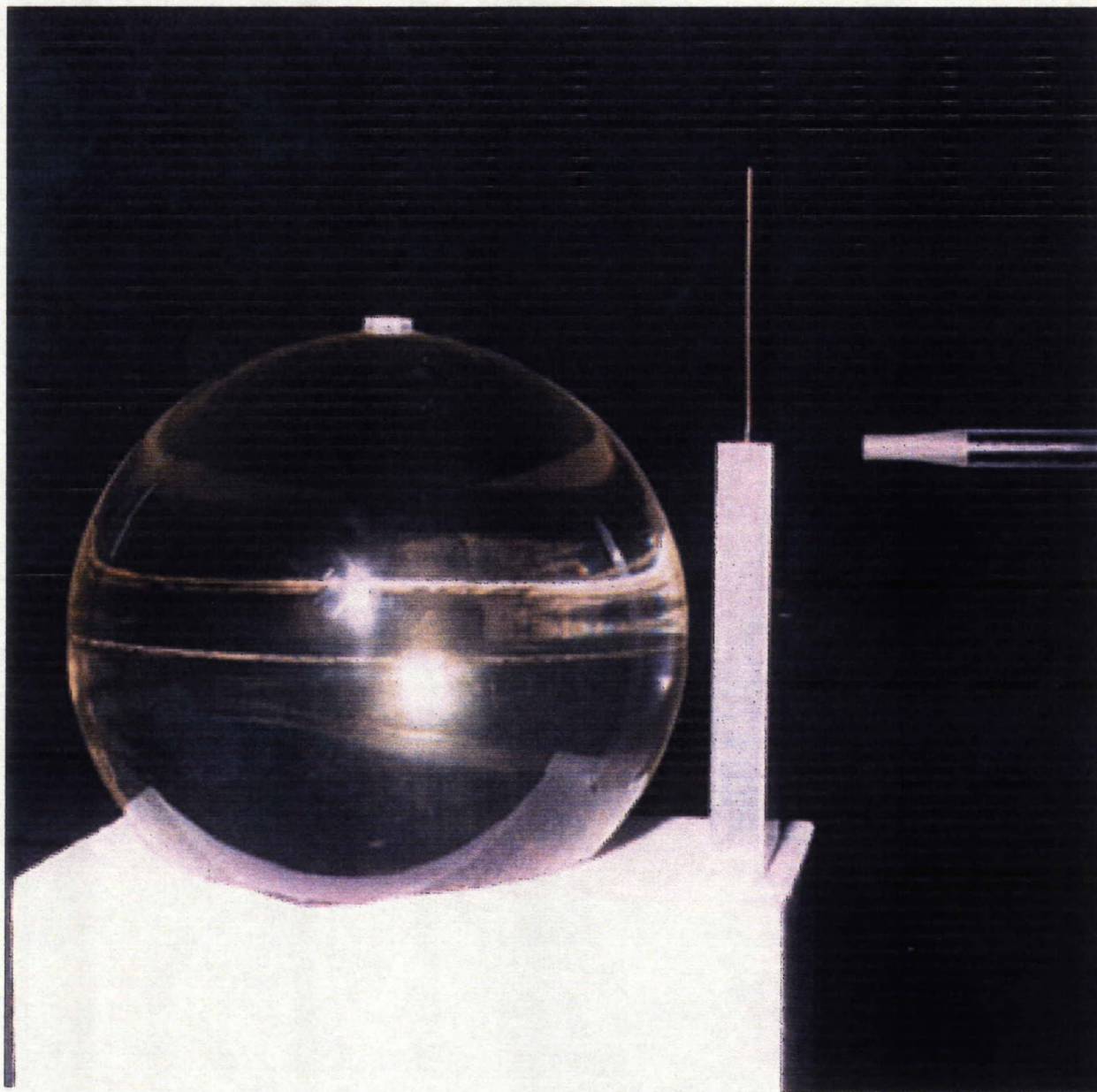


Fig. 4.4 The handset near the sphere head on top of the styrofoam support column, with the measurement probe adjacent to the handset.



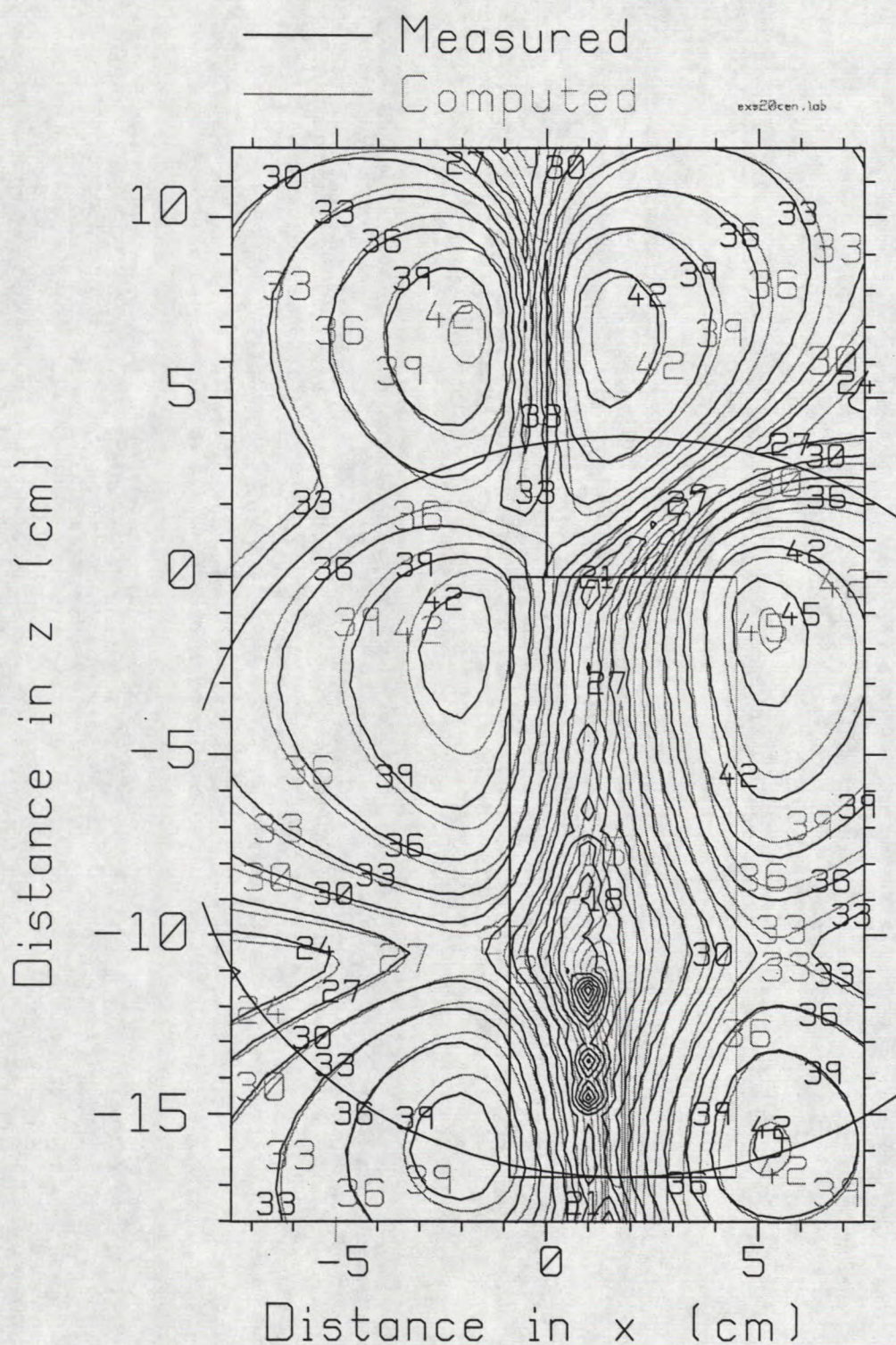


Fig. 4.5(a) Comparison of the measured and computed  $E_x$  component for the handset and sphere head, in an  $xz$  plane at a distance 21.8 mm from the antenna.



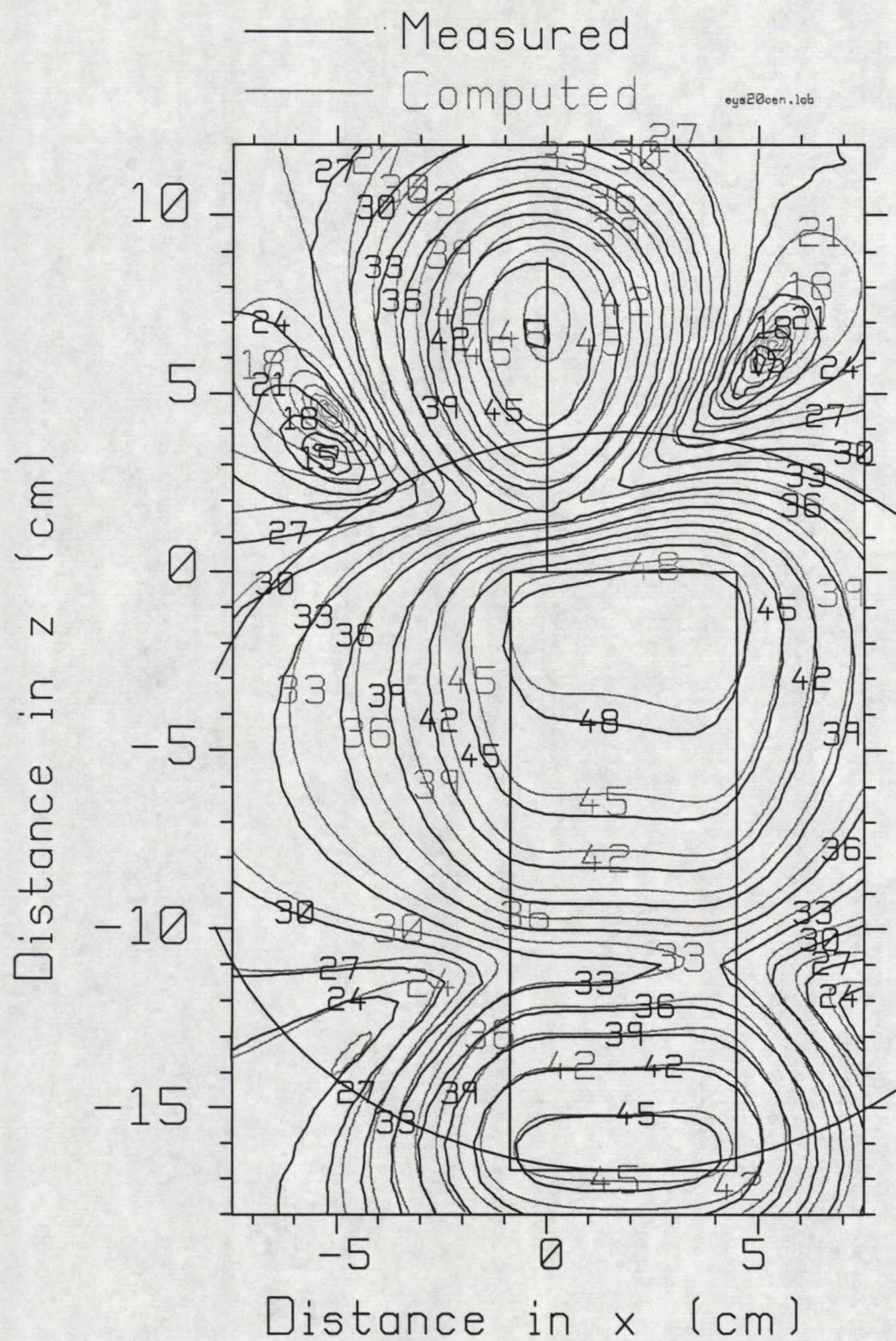


Fig. 4.5(b) Comparison of the measured and computed  $E_y$  component 22.9 mm from the antenna.



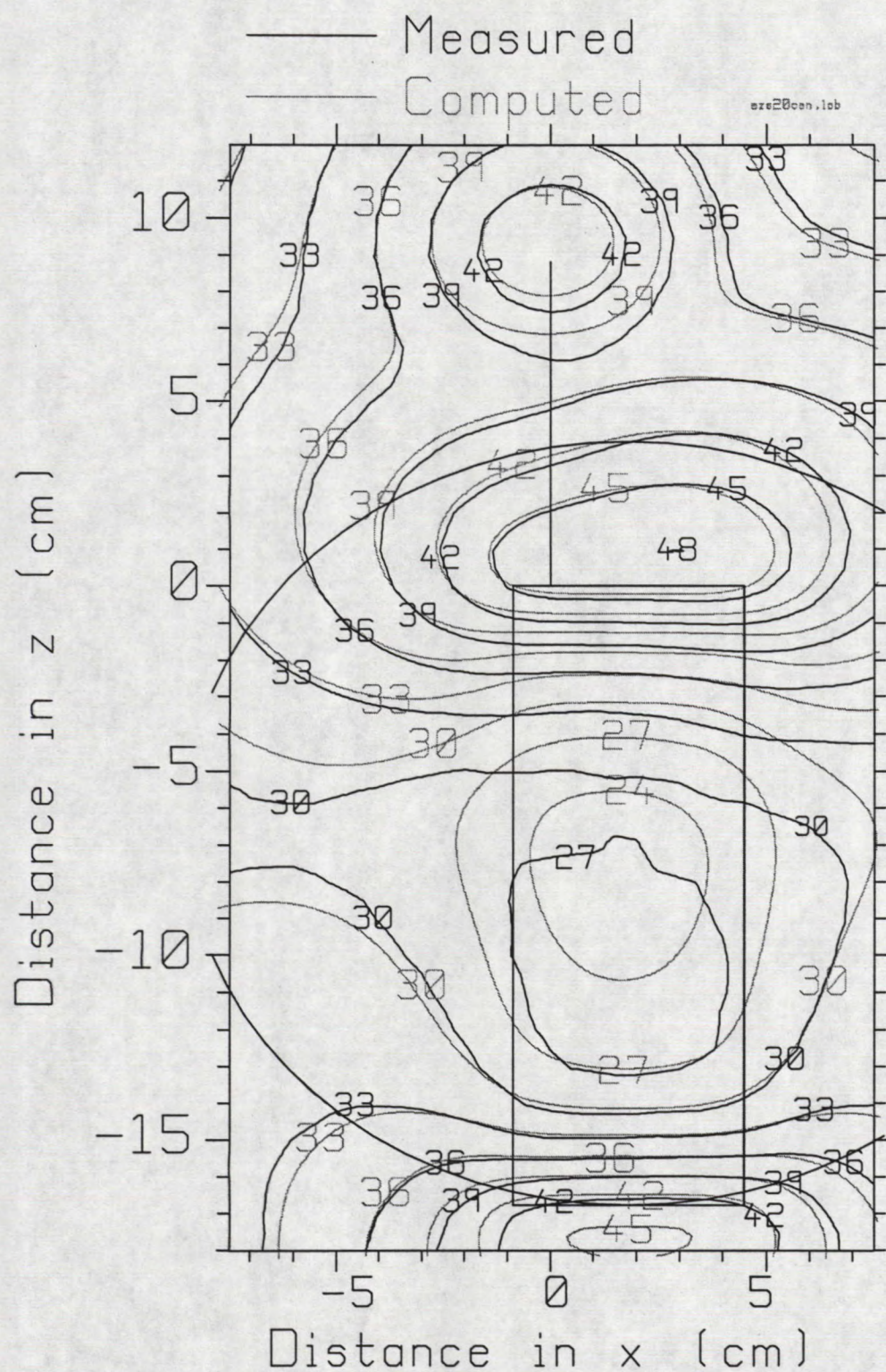


Fig. 4.5(c) Comparison of the measured and computed  $E_z$  component 21.8 mm from the antenna.



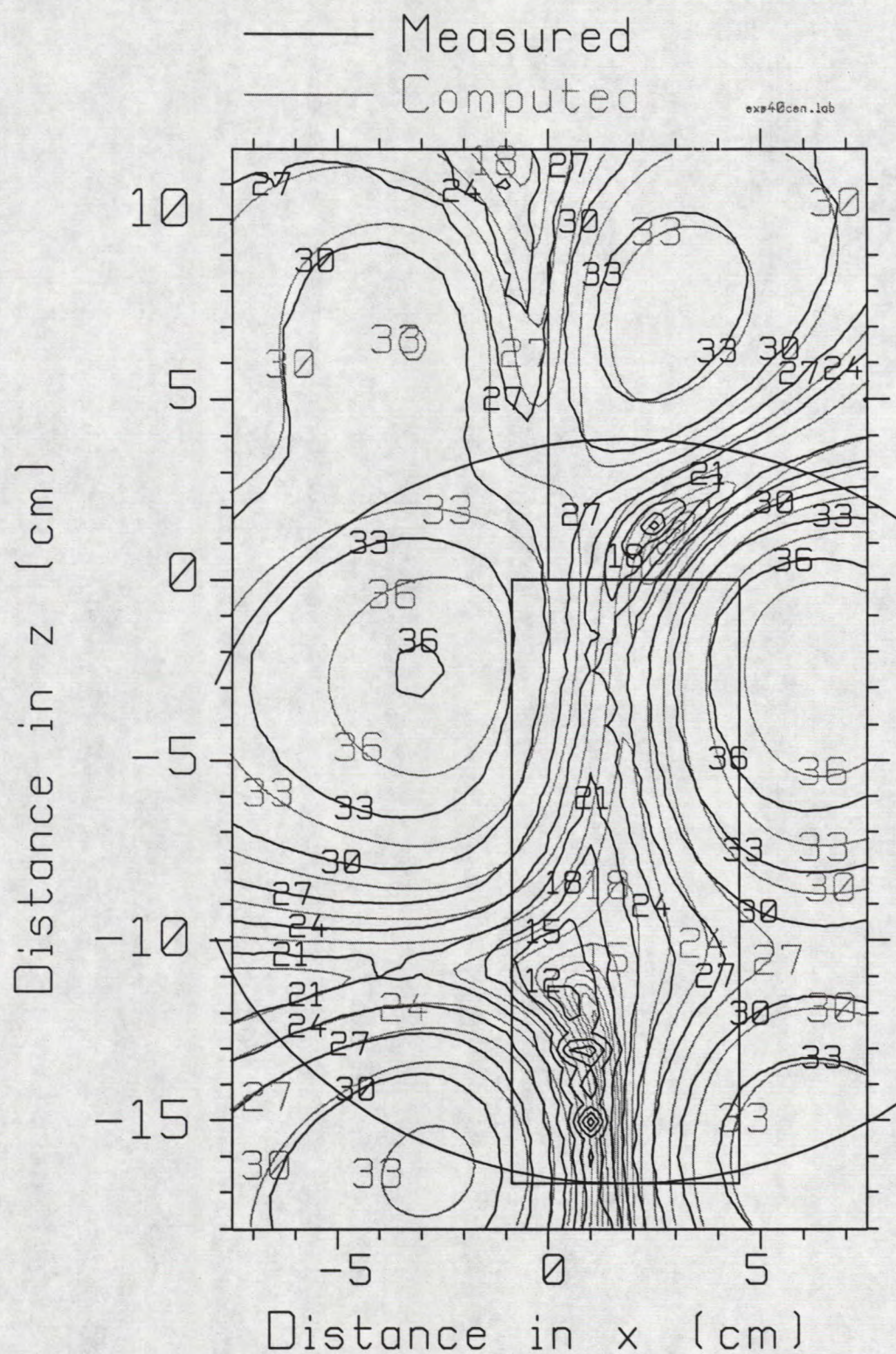


Fig. 4.6(a) Comparison of the measured and computed  $E_x$  component 41.8 mm from the antenna.



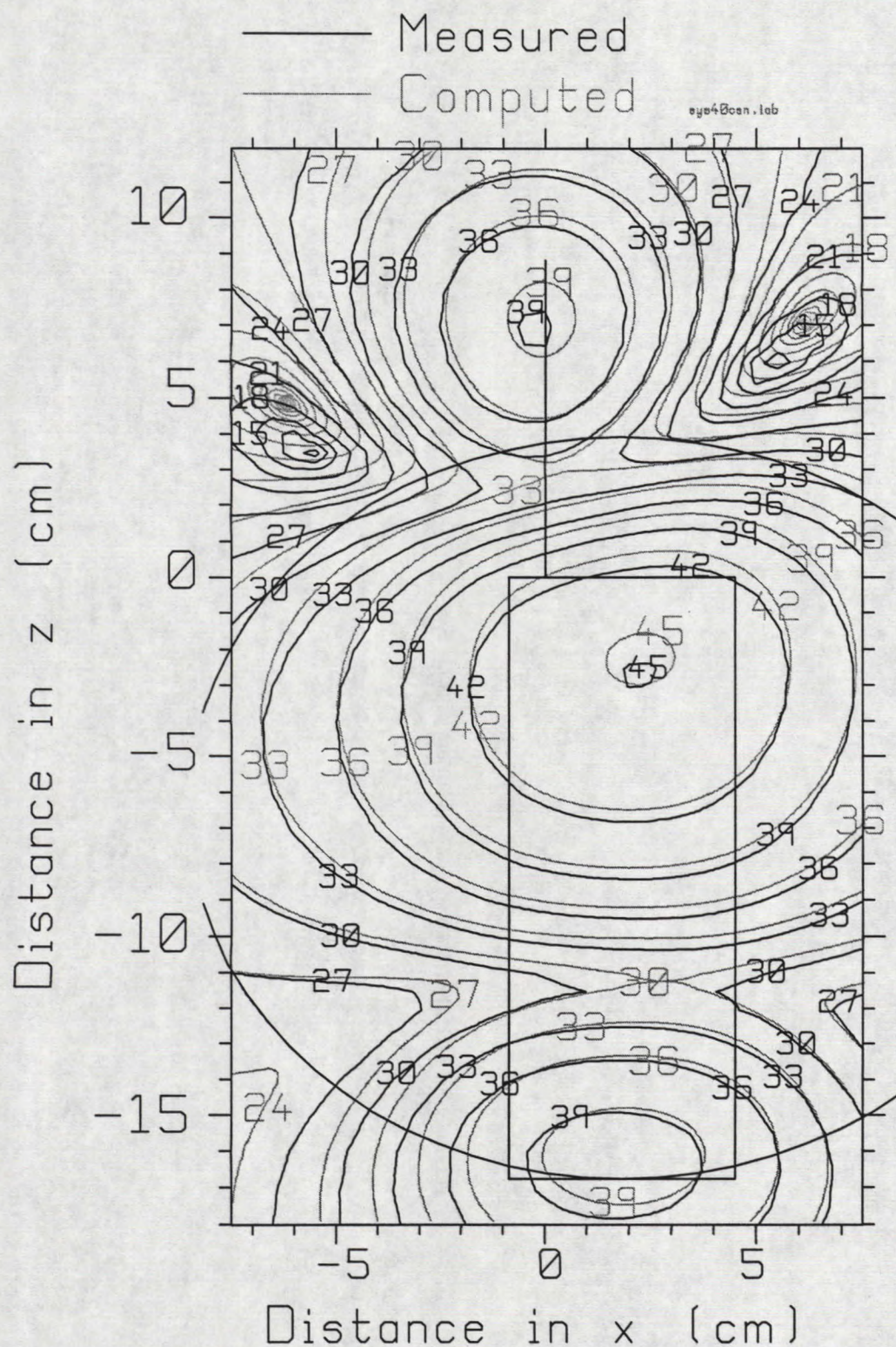


Fig. 4.6(b) Comparison of the measured and computed  $E_y$  component 42.9 mm from the antenna.

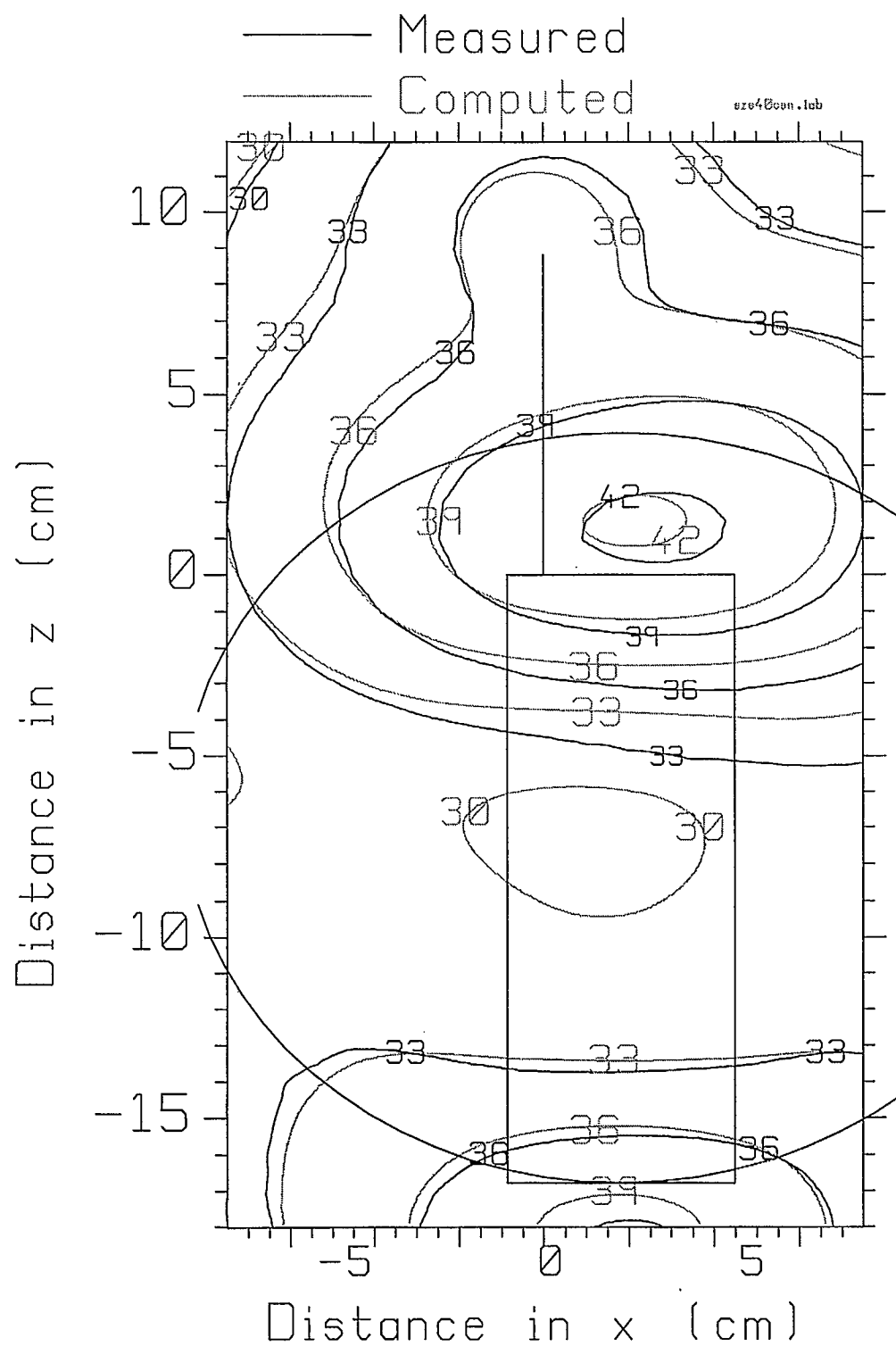


Fig. 4.6(c) Comparison of the measured and computed  $E_z$  component 41.8 mm from the antenna.



## Chapter 5

### Far Fields of the Handset Alone

The far field of the handset alone has been investigated previously in this project and is reported in Refs. [1,2,3,4]. Also, in Ref. [1] the far fields of the handset and sphere head and of the handset and box head have been computed with FDTD and compared with the measured principal plane patterns. The agreement has been very good. In this report, the far field of the handset, held at a realistic angle near the head will be investigated. This chapter compares the fields of the handset oriented vertically, computed with FDTD, to the measured far fields. The measurement is a new one done at CRC in the summer of 1998[18]. This chapter re-establishes confidence both in the measurement method and in the computation. The next chapter deals with the methods required to use FDTD to compute the far fields of the handset held at a realistic angle relative to the vertical axis. The computed principal plane patterns will be compared with the measured fields. A measurement model of the head called a "phantom" has been obtained for testing the performance of the handset near a realistic head. Chapter 7 develops a cell model of the phantom for analysis with FDTD. Chapter 8 compares the computed fields of the handset operating near the phantom head with the measured principal plane patterns.

#### 5.1 Cell Model of the Handset

In this chapter the handset is oriented vertically in the coordinate system, as shown in Fig. 1.4. The antenna lies along the  $z$  axis with its base at the origin. The broad faces of the case are parallel to the  $xz$  plane. The antenna is located at the  $-x$  side of the case. In later chapters, the user's head will be positioned in the positive  $y$  half space, facing in the  $+x$  direction.

The cell model of the handset is the same as that used in previous chapters for near field computations. The cell model uses 2.205 mm cells. The case is represented with 24 by 8 by 76 cells, and the antenna is 40 cells long. For the computation of the far field, the handset and antenna are surrounded by 10 cells of "whitespace". Of these 10 cells, the 4 cells adjacent to the handset are free space cells, and the 6 cells adjacent to the outer boundary of the cell space are used to implement the perfectly-matched layer absorbing boundary. The space size is 118,272 cells, which is a modest problem on a 200 MHz Pentium processor. The FDTD-PML code is run for 4096 time steps to obtain the field called SSSNZFZ.DAT, which contains the magnitude and phase of the electric and magnetic field over the six faces of an integration surface centered in the 4 cell free space zone just inside the PML layers. This file is the input to program FARZONE, which computes the radiation patterns of the handset using the data in the SSSNZFZ.DAT file.

The far field of the handset is obtained over the complete surface of the radiation sphere by calculating the "conical cut" set of radiation patterns described in Ref. [1]. This permits the power flow density to be computed over the surface of the radiation

sphere, and then integrated to find the radiated power of the antenna. In turn the radiated power is used to find the reference field strength called the “isotropic level”[1]. This is the field strength which, radiated uniformly in one polarization over the whole surface of the radiation sphere, obtains the same radiated power as the original antenna. The isotropic level field strength will be used as the reference level for graphing the field in decibels. Thus our radiation patterns will show the strength of the electric field above isotropic.

## 5.2 Wire-Grid Model vs. FDTD Cell Model

The Numerical Electromagnetics Code(NEC)[23] can be used to solve the handset problem by representing the handset with a wire-grid model[1]. This was done in Chapter 2 to verify that the FDTD code is functioning correctly for finding the handset’s near fields. Here, the far fields computed with the wire grid model will be compared with the FDTD computation, again as a basic confidence check that the FDTD PML and FARZONE codes are operating correctly.

Thus the NEC code was run with the wire grid model of the handset, which is presented in Ref. [1] and Appendices 2 and 3. As input, and the conical cut radiation patterns were computed. The radiated power and isotropic level were found so that the isotropic level can be used as the reference level for graphing radiation patterns. Similarly, FDTD was run to find the handset’s fields over the radiation sphere. Fig. 5.1 compares the NEC and FDTD far fields.

In the azimuth pattern, Fig. 5.1(a) the two computations are almost identical, both in  $E_\theta$  and in  $E_\phi$ . In the  $\phi=0$  elevation pattern, part (b), because of the symmetry of the handset about the  $xz$  plane, there is no  $E_\phi$  component. The wire-grid and FDTD patterns for  $E_\theta$  are almost identical, except in the minima. In the FDTD computation, there is a minimum at 60 degrees, -19.2 dB, whereas the wire-grid computation has a minimum at 60 degrees, -24.0 dB. In the FDTD model, there is a minimum at 283 degrees, -16.4 dB, whereas the wire-grid model gives a minimum at 283 degrees, -13.9 dB.

In the  $\phi=90$  elevation plane, Fig. 5.1(c), the  $E_\theta$  patterns are almost identical, except in the minimum. The FDTD model has minima at 67 and 293 degrees of field strength -20.0 dB. The wire-grid model has minima at the same angles, but of field strength -16.2 dB. The  $E_\phi$  patterns are almost identical.

The comparison in Fig. 5.1 gives confidence that the FDTD method is functioning correctly, and also shows that agreement of the field strength in the minima is hard to obtain between computational methods.

## 5.3 Scaling the Measured Patterns

The principal plane radiation patterns were measured at CRC[18] by the method described in Ref. [1]. The measurement of the patterns for the handset in isolation had been done in conjunction with the handset and box head and the handset and sphere head



measurements reported in Ref. [1] in the summer of 1997. The handset-alone measurement was repeated in the summer of 1998 in conjunction with the pattern measurement for the handset and the phantom head. This section summarizes the scaling procedure used for measured patterns, which is identical to that described in Ref. [1].

The measured data includes the  $E_\theta$  and  $E_\phi$  components in the three principal plane patterns. The measured data must be scaled to a level comparable to the computed data. As explained in Ref. [1], program FINDRMS is used to compute the RMS field strength account for both polarizations in all three principal plane patterns. FINDRMS is run on the computed pattern to find a reference level,  $E_{ref}$ . Then FINDRMS is run on the measured patterns to find the RMS field strength,  $E_{meas}$ , and the measured data is scaled by the ratio,  $E_{ref}/E_{meas}$ . In effect, this scales the measured patterns to have approximately the same radiated power as the computed patterns.

#### 5.4 Comparison of the Measured and Computed Patterns

Fig. 5.2 compares the measured and the computed principal plane patterns for the handset in the vertical orientation. In the azimuth pattern, part (a), the shape of the  $E_\theta$  curves is similar but the computed curve is at a higher level. The maximum computed field is 1.3 dB, and the minimum -5.2 dB. The maximum measured field is 0.7 dB, and the minimum -6.5 dB. The  $E_\phi$  patterns both have two lobes separated by minima at approximately 0 and 180 degrees. The measured data is not perfectly smooth as is the computed data. The measured pattern appears to be shifted a few degrees, having minima at 178 and 357 degrees, rather than 0 and 180 degrees. A laser beam was used to align the handset with the measurement horn to establish the zero degree position. However, no estimate in the error in the alignment procedure is available.

Part (b) of Fig. 5.2 shows the elevation pattern for  $\phi=0$  degrees. The measured pattern is remarkably smooth and very close to the computed data....

The computation has no  $E_\phi$  component due to the perfect symmetry of the computer model. The measured data has an  $E_\phi$  component with a maximum value of -25.8 dB. Any asymmetry in the measurement setup can introduce a cross-polarized component. To measure the  $\phi=0$  pattern, the handset is lain on its broad face on a styrofoam block. This introduces some asymmetry in the sense that there is free space on one side of the case, and styrofoam on the other. It has been suggested in Ref. [24] that the small holes in the case for the switch and the LED that are seen in Fig. 1.1 introduce sufficient asymmetry to raise the cross polarized field to levels of about -40 dB, not as large as that in Fig. 5.2(b). If the wire monopole becomes slightly bent in handling, then the wire may tilt away from the  $xz$  plane. Wire grid modeling was used in Ref. [25] to show that the slightly bent wire can lead to a cross-polarized field of about -41 dB.

Fig. 5.2(c) shows the elevation pattern for  $\phi=90$  degrees. The measured and computed patterns for the  $E_\theta$  component are in quite good agreement. There are differences in the depth of the minima, and the measured pattern shows asymmetry. The

$E_\phi$  pattern is nearly isotropic, and has about the same shape and level in the computation and in the measurement.

### 5.5 Conclusion

This chapter has presented a comparison of the measured and computed principal plane patterns of the handset oriented vertically. The degree of agreement in Fig. 5.2 is the best that has been achieved in this project, and sets the standard for comparisons of measured and computed patterns for the tilted handset in the next chapter, and for the tilted handset and phantom head in Chapter 8.



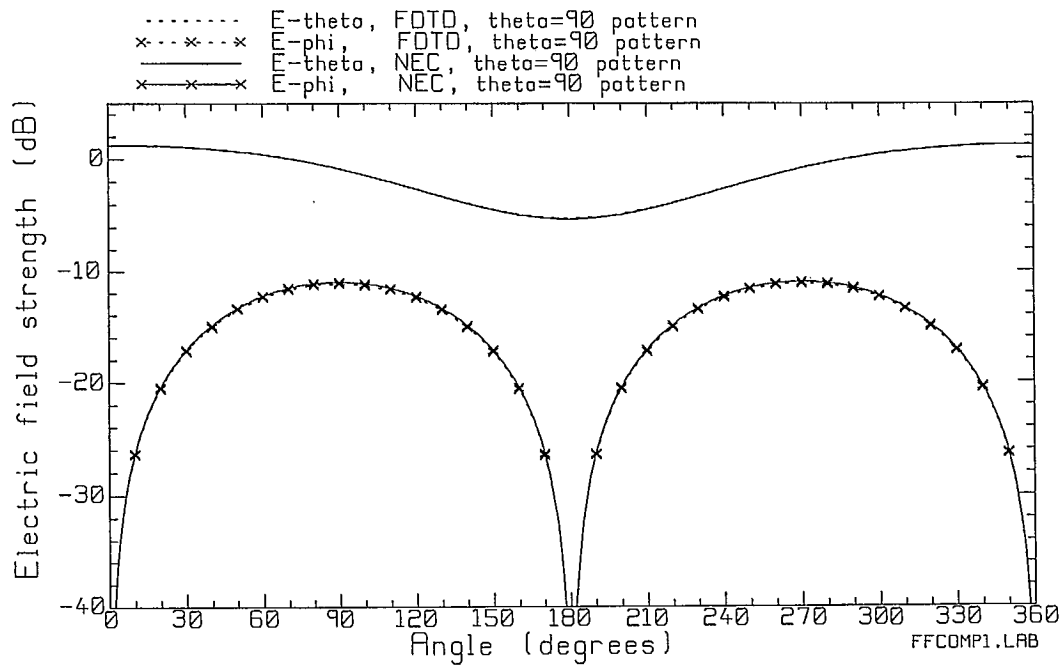


Fig. 5.1(a) The azimuth pattern of the vertical handset, computed with the wire-grid model and with the FDTD cell model.

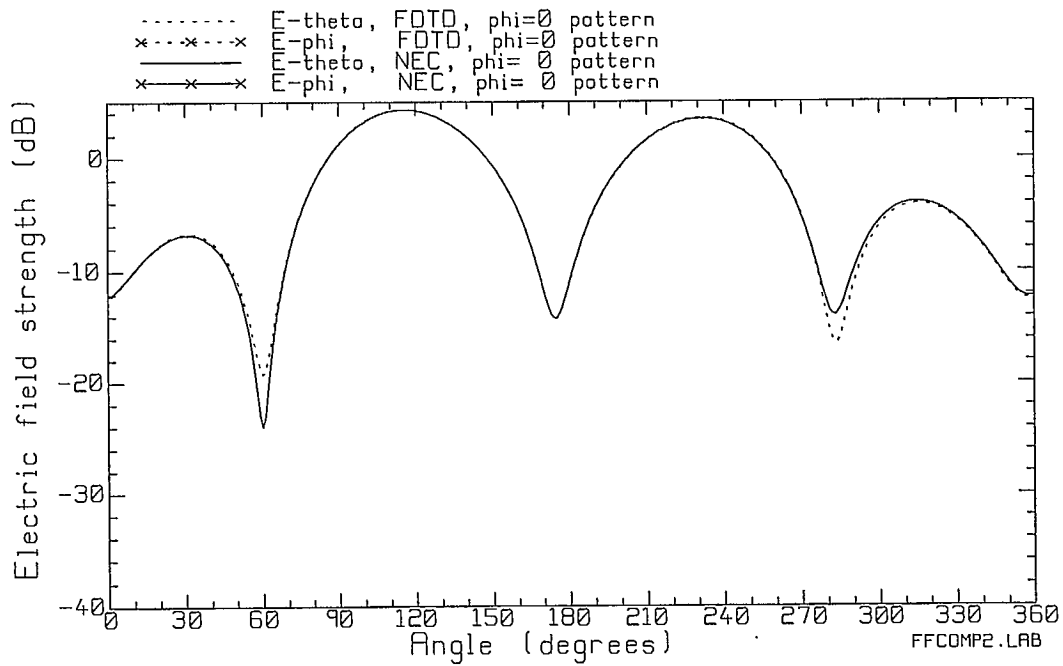


Fig. 5.1(b) The  $\phi=0$  elevation pattern.

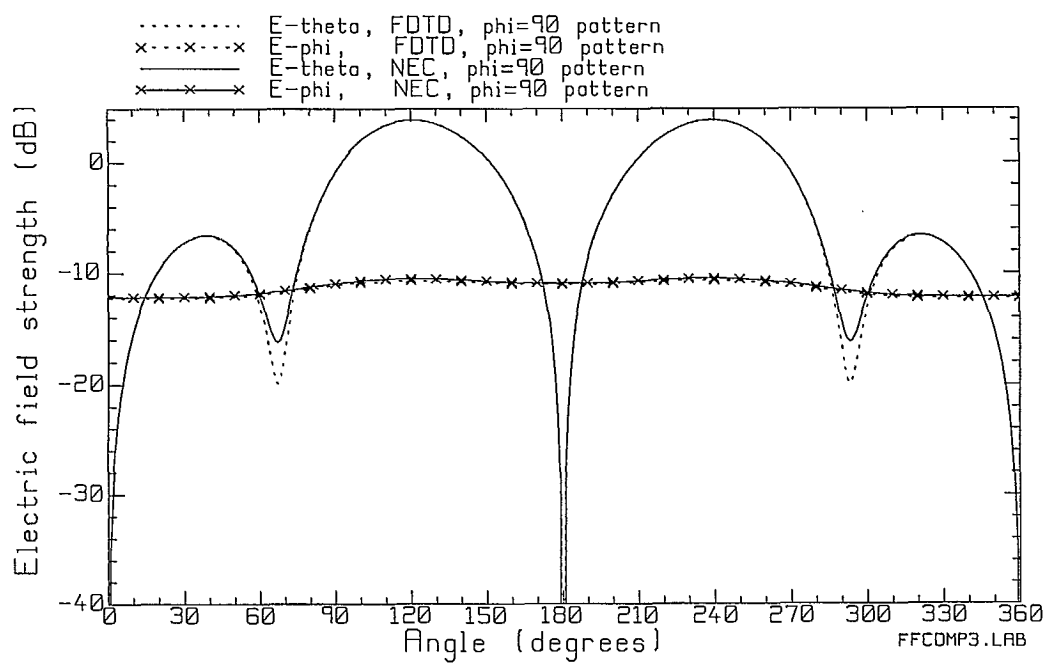


Fig. 5.1(c) The  $\phi=90$  elevation pattern.

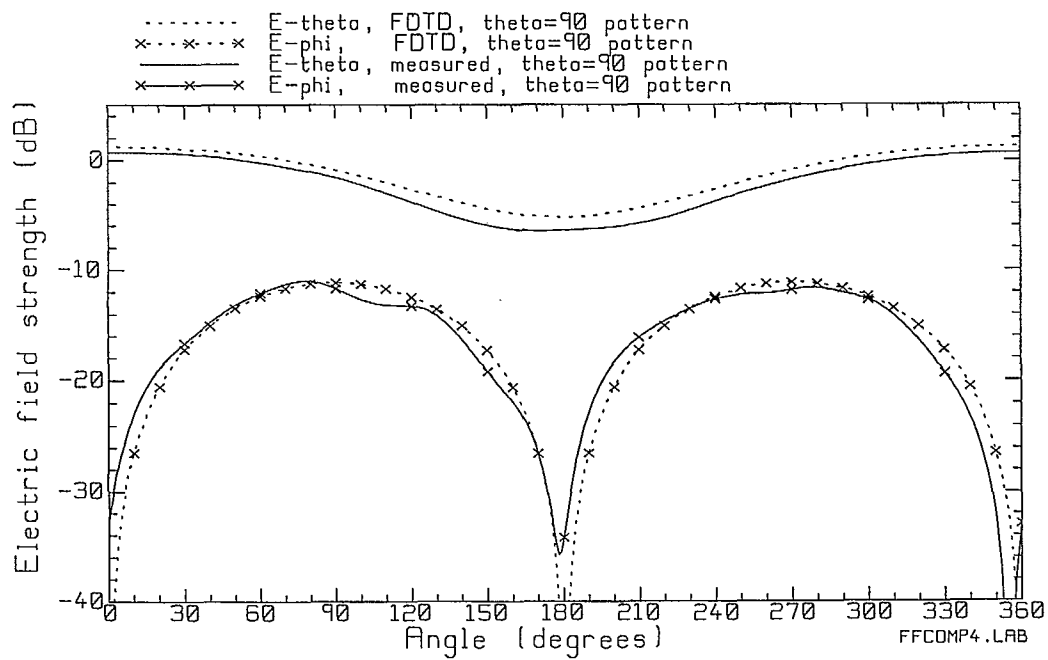
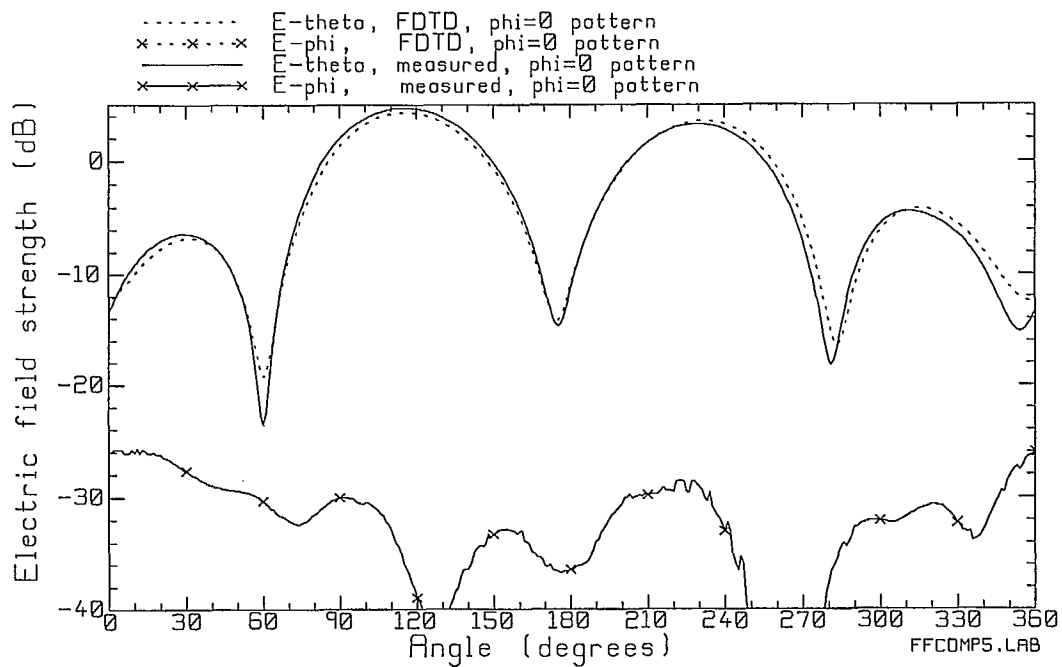


Fig. 5.2(a) Comparison of the computed and measured azimuth pattern.

Fig. 5.2(b) Comparison of the computed and measured  $\phi = 0^\circ$  elevation pattern.



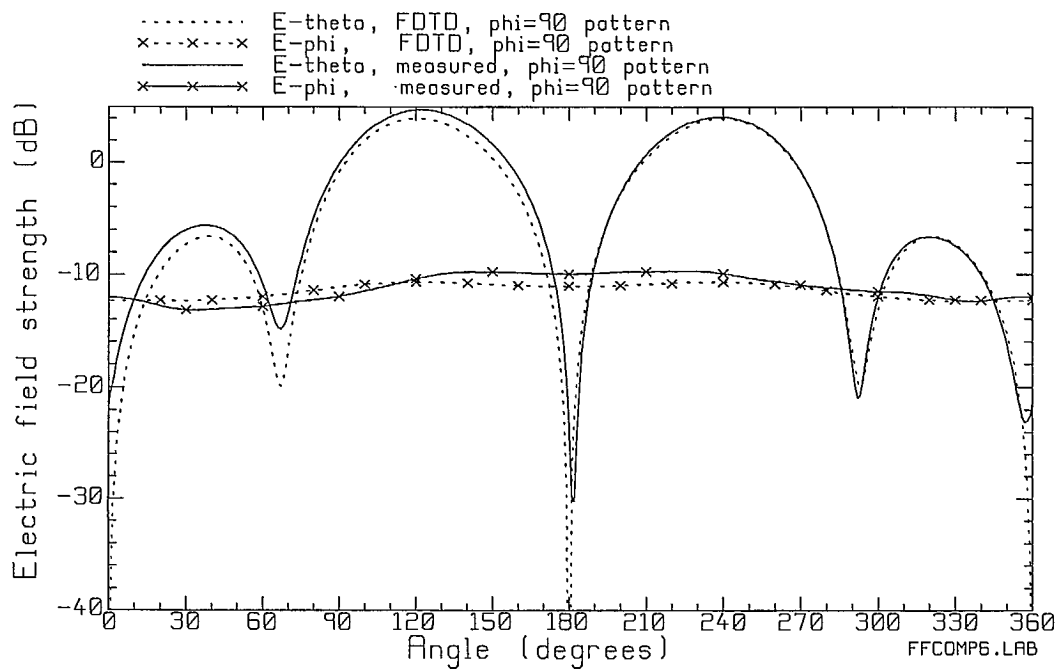


Fig. 5.2(c) Comparison of the computed and measured  $\phi=90$  elevation pattern.

## Chapter 6

### Far Fields of the Tilted Handset

The last chapter examined the radiation patterns of the handset oriented vertically, with the antenna aligned along the  $z$  axis. Good agreement was shown between the patterns computed with FDTD, and measured radiation patterns. However, the handset is normally held tilted relative to the head. For this project, a standard orientation of the handset has been adopted. In the “global” coordinate system, the vertical axis of the head lies along the  $z$  axis, and the head faces in the  $+x$  direction. The antenna is oriented in the direction  $\theta=64.42$  degrees,  $\phi=191.10$  degrees, where  $(\theta, \phi)$  are spherical angles in the global coordinate system. These angles are chosen to simulate the handset held in the right hand, with the antenna tilted towards the back of the head at roughly 65 degrees, and the bottom of the case turned so that the “mouthpiece” lies close to the mouth. The edges of the broad face of the case lie in vertical planes. We will call this handset position the “tilted” handset. This chapter considers the radiation patterns of the tilted handset, compared to those of the vertical handset, and compared to measurements.

For measurement of the radiation patterns, a jig was constructed at CRC[26] that holds the handset tilted at the desired angles, and the phantom head. The handset is held in a styrofoam block to maintain the tilt angles precisely, as shown in Fig. 6.1. Fig. 6.2 shows the handset in the measurement jig, but with no phantom head. The styrofoam blocks making up the jig are held together by four fiberglass bolts, each with a plexiglas washer and a fiberglass nut at each end. These are hidden inside the styrofoam blocks and are not seen in Fig. 6.2. In Fig. 6.2, the handset in the jig is sitting atop the styrofoam rotator column in the anechoic chamber, ready for the measurement of the azimuth pattern.

In solving the handset problem with FDTD, it is desirable to keep the antenna oriented along the  $z$ -axis in the FDTD coordinate system. Then the handset can be modeled in FDTD with a box of 24 by 8 by 76 cells of size 2.205 mm, with the surfaces of the box parallel to the coordinate planes. The coordinate system used in FDTD will be called the “local” coordinate system. The far fields are computed at “local” field angles  $(\theta_L, \phi_L)$  in “local” field components  $E_{\theta_L}, E_{\phi_L}$ . To compute radiation patterns in the global coordinate system, we must compile a list of spherical angle pairs  $(\theta, \phi)$  at which the field must be found, and then change each pair into the corresponding local spherical angles,  $(\theta_L, \phi_L)$ . The handset is then solved with FDTD-PML in the local coordinate system, and the components of the field at each angle pair are found in local coordinates,  $E_{\theta_L}, E_{\phi_L}$ . A coordinate transformation must then be done to convert the local field components into global field components,  $E_\theta, E_\phi$ . In the following, we describe this coordinate transformation process and verify its correct implementation.

### 6.1 Tilting the FDTD Model of the Handset

To rotate the handset from the global to the local coordinate system, three rotations are required in general. The antenna starts off in the global system with the antenna on the global  $z$  axis, with the broad face of the case parallel to the  $xz$  plane. First, the antenna is rotated about the  $y$  axis through angle  $\alpha$ , as shown in Fig. 6.3. The result is that the antenna lies in an  $xz$  plane at an angle  $\alpha$  to the global  $z$  axis. The second rotation is about the  $z$  axis, through angle  $\beta$ , as shown in Fig. 6.4. The last step is a rotation of the handset case about the axis of the antenna, through angle  $\gamma$ , as shown in Fig. 6.5.

The antenna in CRC measurement jig is positioned in direction  $\theta = 64.42$  degrees,  $\phi = 191.10$  degrees. No rotation of the case about the antenna axis is required to simulate the handset's position in the measurement jig. In the following, the details of the coordinate rotations are given.

### 6.2 Far Field Coordinate Transformation For Use With FDTD

To orient the handset in a general position, three rotations are required. The first is rotation about the  $y$  axis through an angle  $\alpha$ . This was done in the original version of the software setup described in Ref. [4]. Two further rotations are required: a rotation through angle  $\beta$  about the  $x$  axis to point the antenna in the desired direction; then a rotation through angle  $\gamma$  about the axis of the antenna to orient the case in the desired direction. To transform from "global"  $(x, y, z)$  to "local" coordinates  $(x_L, y_L, z_L)$ , two intermediate coordinate systems are used. After rotation through angle  $\alpha$  about the global  $y$  axis, the coordinates will be  $(x_1, y_1, z_1)$ . Then after a further rotation through angle  $\beta$  about the global  $x$  axis, the coordinates will be  $(x_2, y_2, z_2)$ . The final rotation through angle  $\gamma$  about the axis of the antenna changes  $(x_2, y_2, z_2)$  into  $(x_L, y_L, z_L)$ .

The coordinate change from global coordinates  $(x, y, z)$  to  $(x_1, y_1, z_1)$  is given by

$$\begin{aligned}x_1 &= x \cos \alpha + z \sin \alpha \\y_1 &= y \\z_1 &= -x \sin \alpha + z \cos \alpha\end{aligned}$$

The coordinate change from  $(x_1, y_1, z_1)$  to  $(x_2, y_2, z_2)$  is given by

$$\begin{aligned}x_2 &= x_1 \\y_2 &= y_1 \cos \beta - z_1 \sin \beta \\z_2 &= y_1 \sin \beta + z_1 \cos \beta\end{aligned}$$

The coordinate change from  $(x_2, y_2, z_2)$  to  $(x_L, y_L, z_L)$  is given by



$$\begin{aligned}
x_L &= x_2 \cos \gamma + y_2 \sin \gamma \\
y_L &= -x_2 \sin \gamma + y_2 \cos \gamma \\
z_L &= z_2
\end{aligned}$$

The inverse transformation from  $(x_L, y_L, z_L)$  to  $(x, y, z)$  is easily obtained by inverting the above transform matrices, to go from  $(x_L, y_L, z_L)$  to  $(x_2, y_2, z_2)$ , then from  $(x_2, y_2, z_2)$  to  $(x_1, y_1, z_1)$ , and finally from  $(x_1, y_1, z_1)$  to  $(x, y, z)$ .

To convert the global radiation pattern angles  $(\theta, \phi)$  into the local coordinate system angles  $(\theta_L, \phi_L)$ , we can imagine converting the vector  $(r=1, \theta, \phi)$  in global spherical coordinates to the corresponding vector in local spherical coordinates. Thus the global rectangular coordinates of the vector are given by

$$\begin{aligned}
x &= \sin \theta \cos \phi \\
y &= \sin \theta \sin \phi \\
z &= \cos \theta
\end{aligned}$$

These rectangular components are converted into local coordinates  $(x_L, y_L, z_L)$  using the transformations given above. Then the local spherical angles are found using

$$\tan \theta_L = \frac{z_L}{\sqrt{x_L^2 + y_L^2}}$$

and

$$\tan \phi_L = \frac{y_L}{x_L}$$

To convert the field components in the local coordinate system,  $E_{\theta_L}$  and  $E_{\phi_L}$  into global spherical field components requires some intermediate steps. First the local rectangular components of the field are found using

$$\begin{aligned}
E_{xL} &= E_{\theta_L} \cos \theta_L \cos \phi_L - E_{\phi_L} \sin \phi_L \\
E_{yL} &= E_{\theta_L} \cos \theta_L \sin \phi_L + E_{\phi_L} \cos \phi_L \\
\text{and} \\
E_{zL} &= -E_{\theta_L} \sin \theta_L
\end{aligned}$$

Then these local rectangular components are changed into global rectangular components by expressing each of the three local unit vectors in terms of the three global unit vectors in the form

$$\begin{aligned}
\hat{x}_L &= a_{11}\hat{x} + a_{12}\hat{y} + a_{13}\hat{z} \\
\hat{y}_L &= a_{21}\hat{x} + a_{22}\hat{y} + a_{23}\hat{z}
\end{aligned}$$

$$\hat{z}_L = a_{31}\hat{x} + a_{32}\hat{y} + a_{33}\hat{z}$$

where the coordinate transformations given above are used to find  $\{a_{ij}\}$ . Then the global rectangular components of the field are evaluated using

$$E_x = a_{11}E_{xL} + a_{21}E_{yL} + a_{31}E_{zL}$$

$$E_y = a_{12}E_{xL} + a_{22}E_{yL} + a_{32}E_{zL}$$

$$E_z = a_{13}E_{xL} + a_{23}E_{yL} + a_{33}E_{zL}$$

The global  $xyz$  components of the electric field are used to find the global  $(\theta, \phi)$  components using

$$E_\theta = E_x \cos \theta \cos \phi + E_y \cos \theta \sin \phi - E_z \sin \theta$$

$$E_\phi = -E_x \sin \phi + E_y \cos \phi$$

Note that all the arithmetic must be done using complex numbers to preserve the phase relationships of the various field components.

### 6.3 Software For Coordinate Transformations

The triple rotation including angles  $\alpha$ ,  $\beta$  and  $\gamma$  was implemented in a set of functions in a FORTRAN-90 module called "TILT\_TRANSFORM". The "module" is used by all programs requiring the axis rotations, including the program that derives the cell model of the phantom head, presented below in Chapter 8. The module is used as follows to implement the computation of the radiation patterns in global coordinates when the FDTD model of the handset is actually solved in local coordinates.

Program MAKERP accepts as input a list of the conical cut radiation patterns in the global coordinate system. MAKERP derives a list of all the global coordinate angle pairs  $\{\theta, \phi\}$  required for the set of radiation patterns. Then MAKERP produces a list of the corresponding set of angle pairs in the local coordinate system,  $\{\theta_L, \phi_L\}$ . MAKERP uses the "TILT\_TRANSFORM" module to do this angle transformation using the three-axis rotation with angles  $\alpha$ ,  $\beta$ , and  $\gamma$ . The output is a list of "RP cards" that are pasted into the "build" file describing the cell model for input to the FDTD PML program.

The next step is to run FDTD PML, which solves the handset cell model and produces the intermediate file called SSSNZFZ.DAT. This file gives the near field over all the surfaces of a parallelepiped enclosing the handset and the head model. Program FARZONE uses this near field data to derive equivalent surface currents over the parallelepiped, and integrates the equivalent currents to find the far field. This is done for each field angle pair  $\theta_L, \phi_L$  in local coordinates, leading to the complex values of the field components in local coordinates,  $E_{\theta_L}$  and  $E_{\phi_L}$ , which are written to an output file.

Program ECONVRT converts these electric field components from local to global coordinates. At each far field point, ECONVRT reads the magnitude and phase of the field components in the local coordinate system,  $E_{\theta_L}$  and  $E_{\phi_L}$ , and finds the  $x, y, z$  components of the field in the local system. The "TILT\_TRANSFORM" module is then used to express the three coordinate unit vectors in the local system in terms of the coordinate unit vectors in the global system. The unit-vector transformation is used to change the rectangular components of the field from the local coordinate system to the global coordinate system. Then the  $x, y, z$  components of the field in the global system are used to find the global spherical components,  $E_\theta$  and  $E_\phi$ . Note that all the arithmetic uses complex values to preserve the phase information. The final step is to take the magnitude of  $E_\theta$  and of  $E_\phi$  and to write these values to the output file.

Thus a three step process is required of the user. First, transform the global field pattern angles to local angles using MAKERP, and paste them into the "build" file. Then run FDTD PML and FARZONE. Then run ECONVRT to convert the local field components back to global components.

#### 6.4 Verification of the Angle Transform Software

The correctness of the conversion from local  $E_{\theta_L}$  and  $E_{\phi_L}$  components into global  $E_\theta$  and  $E_\phi$  field components was verified using the NEC program and the wire-grid model, as follows. The "direct" computation consists of tilting and rotating the wire-grid model of the handset that the antenna lies along the desired direction. Then the conical cut pattern set is computed *directly* with the NEC code. The handset is solved directly in global coordinates. In the "indirect" approach, which simulates the FDTD computation, the wire-grid model of the handset is maintained in the vertical position, and NEC is used to compute the local components of the field at the set of local field angles specified by program MAKERP. Then these "local" field components are converted into "global" components with ECONVRT. The far field patterns from the "indirect" computation are expected to be identical with those from the "direct" computation. This was achieved after a considerable effort in removing errors from the programs!

The direct and indirect computation with the wire-grid model were carried out using rotation angles of  $\theta=64.4238$ ,  $\phi=191.0994$ , and  $\gamma=5.5825$  degrees. Fig. 6.6 compares the "direct" calculation using the wire grid model positioned at  $\theta=64.4238$ ,  $\phi=191.0994$ , and  $\gamma=5.5825$  degrees in the global system with the "indirect" calculation using the wire-grid model positioned with the antenna on the "local"  $z$  axis. The radiation patterns found from the "direct" and "indirect" calculation are identical. This gives considerable confidence that the angle transformation has been implemented correctly.

#### 6.5 Tilted Handset Solved with FDTD

The procedure described above was used to compute the radiation patterns of the handset tilted at  $\theta=64.4238$ ,  $\phi=191.0994$  degrees, but with no rotation,  $\gamma=0$  degrees,



corresponding to the handset's position in the CRC measurement jig. The full set of conical cut radiation patterns are computed in each case[1], and the radiated power is calculated by integrating the power flow density over the radiation sphere. The radiation patterns are then presented on a dB scale, with the isotropic level field strength[1] as the zero dB reference. This is a convenient basis for the comparison of radiated patterns computed by different methods, or of computed and measured patterns.

As a further validation that the angle transformation process is being correctly executed, the FDTD computation was compared with the NEC computation for the same tilt angles, shown in Fig. 6.7. Since we are now comparing a wire-grid model with an FDTD cell model, we do not expect the patterns to be identical. In part (a), we see that the azimuth pattern is very similar in the wire-grid and in the FDTD computation. The main differences lie in the depth of the minima. The  $E_\theta$  pattern has shallow minima, which are about 0.8 dB deeper in the FDTD calculation. The  $E_\phi$  pattern has sharp, deep minima, which are much deeper in the FDTD computation, except for that at 256 degrees, which agrees well between the two methods.

Fig. 6.7(b) shows the elevation pattern for  $\phi = 0$  degrees. The  $E_\theta$  curve is almost identical, with some differences in the minima at 219 and 356 degrees. The  $E_\phi$  pattern is very similar. The minima at 221 and 356 degrees are much deeper in the FDTD calculation than in the wire-grid computation. Fig. 6.7(c) shows the elevation pattern for  $\phi = 90$  degrees. Again the  $E_\theta$  patterns are very similar. The minimum near 156 degrees is deeper in the wire-grid calculation than in the FDTD case. The minimum found at 351 degrees in the wire-grid model shifts to 357 degrees in the FDTD computation, and is much shallower. The  $E_\phi$  patterns are very alike. The wire-grid model has a deeper minimum at 332 degrees than does the FDTD model.

Fig 6.7 gives confidence that the patterns are being correctly computed by the FDTD method. The differences in the minima are consistent with previous experience with FDTD. The depth of the minima tend to depend on the cell size and other factors.

## 6.6 Tilted Handset Patterns Compared with Vertical Handset Patterns

Much of the previous work in this project[1,2,3,4] has oriented the handset vertically in the coordinate system and examined the principal plane patterns of the vertical handset near various head representations. In the present work the emphasis is on the handset held at a realistic angle relative to the head. This section investigates the changes in the radiation pattern that arise due to tilting the handset. Fig. 6.8 compares the radiation patterns of the vertical handset with those of the tilted handset, both found with FDTD.

For the vertical handset, we can speak  $E_\theta$  as the "principal" polarization, and  $E_\phi$  as the cross-polarized field, because the handset radiated primarily  $E_\theta$ . Thus in the azimuth plane, Fig. 6.8(a), for the vertical handset, the  $E_\theta$  pattern is approximately circular with a maximum value of 1.2 dB and a minimum of -5.2 dB. The cross-polarized field has a figure-eight pattern with maximum field strength -11.1 dB. When

we tilt the handset to about 65 degrees from the vertical, the handset becomes an efficient radiator of  $E_\phi$  and it is no longer reasonable to speak of a principal polarization. The  $E_\theta$  pattern for the tilted handset is also very roughly circular, with a maximum of -2.1 dB, and a minimum of -11.0 dB. The  $E_\phi$  pattern has four lobes for the tilted handset. The main lobes fall at 70 and 310 degrees, and have field strength about 3.5 dB, larger than  $E_\theta$ . The minor lobes fall at 153 and 229 degrees, and have field strength about -8.1 dB.

In the  $\phi=0$  elevation pattern, Fig. 6.8 (b), rotating the handset by 65 degrees in  $\theta$ , with no rotation in  $\phi$ , would simply rotate the  $E_\theta$  pattern by 65 degrees. In the present case there is also rotation in  $\phi$ , which destroys the symmetry about the  $xz$  plane and so introduces an  $E_\phi$  component. The pattern for  $E_\theta$  the tilted handset is very similar to the vertical handset's pattern rotated by 65 degrees. If we shift the dashed curve in Fig. 6.8(b) to the left by 65 degrees we get a curve similar to the solid curve. But the tilted handset radiates  $E_\phi$  with a broad lobe of field strength -8.6 dB centered at 107 degrees, and a minor lobe of field strength -15.0 dB centered at 284 degrees.

Fig. 6.8(c) shows that tilting the handset introduces major changes into the elevation pattern for  $\phi=90$  degrees. In  $E_\theta$ , the vertical handset pattern has two major lobes of field strength about 4 dB, and two minor lobes. For the tilted handset,  $E_\theta$  has two broad lobes with a maximum field strength of about -5.7 dB. In  $E_\phi$ , the vertical handset has an almost circular pattern of field strength about -11 dB. The tilted handset has a broadly directional pattern of maximum field strength 3.3 dB at 148 degrees and minimum field -19.4 dB at 328 degrees. For the vertical handset, most of the energy is in  $E_\theta$  in this pattern, whereas for the tilted handset, most of the energy is in  $E_\phi$ .

In summary, the vertical handset primarily radiates  $E_\theta$ , but the tilted handset radiates  $E_\phi$  efficiently, with  $E_\phi$  larger than  $E_\theta$  in two of the principal plane patterns.

## 6.7 Tilted Handset: Computed vs. Measured Radiation Patterns

The principal plane patterns of the handset were measured at CRC[18] with the handset mounted in the jig intended to hold the handset and phantom head, as shown in Fig. 6.1, with no head present. The jig holds the handset at the desired tilt angles of  $\theta = 64.4238$  and  $\phi = 191.0994$  degrees. The measurement thus includes the tilted handset, the styrofoam blocks making up the jig, and the four fiberglass bolts used to hold the jig together. This section compares these measured patterns with the computed patterns for the tilted handset, but with no styrofoam blocks nor fiberglass bolts.

The measured data consists of the values of  $E_\theta$  and  $E_\phi$  in the three principal plane patterns. The measured data was scaled to a level comparable to the computed data using the procedure described above in Section 5.3.

Fig. 6.9 compares the measured and the computed radiation patterns for the tilted handset. In part (a) we see that in the azimuth plane, the  $E_\theta$  polarization is very similar between the measurement and the computation. The broad lobe roughly centered around

zero degrees corresponds quite well between the measurement and the computation. The minima at 119 and 258 degrees are about  $-1.2$  dB deeper in the measurement. The main difference is that the measured pattern has a lobe at 202 degrees of  $-4.8$  dB, whereas the computed pattern's lobe falls at 185 degrees, of field strength  $-6.3$  dB. In  $E_\phi$ , the four lobes of the computed pattern correspond very well to the lobes of the measured pattern. The minima are sharper and deeper in the computation than in the measurement.

In the elevation pattern for  $\phi=0$  degrees, Fig. 6.9(b), the  $E_\theta$  polarization corresponds very well between the measurement and the computation. There is some disagreement in the depth of the minima. In  $E_\phi$ , the major lobe centered at 105 degrees corresponds quite well between the measurement and the computation, with about 1 dB strong field in the computation. However, the minor lobe at 286 degrees corresponds poorly. The computation has a field strength of  $-15.1$  dB. The measurement has the lobe at 277 degrees of field  $-11.8$  dB.

In the elevation pattern for  $\phi=90$  degrees, Fig. 6.9(c), the  $E_\theta$  polarization corresponds quite well between the measurement and the computation. Both patterns have two broad major lobes. There is some difference in the minimum. In the computation, there is a minimum of  $-32$  dB at 356 degrees, while in the measurement the minimum is about  $-40$  dB at 354 degrees. The  $E_\phi$  patterns are also very similar. There is a very broad lobe at 143 degrees, with 0.2 dB larger field strength in the computation than in the measurement. The computation has a minimum of  $-19.4$  dB at 328 degrees, whereas the measurement falls to  $-16.4$  dB at 356 degrees.

## 6.8 Conclusion

This chapter has presented the principal plane patterns of the handset when it is held at a realistic angle, tilted at about 65 degrees relative to the vertical axis of the head. The mechanics of computing radiation patterns in the global coordinate system based on solving the problem with FDTD in a local coordinate system in which the antenna is aligned with the local  $z$  axis have been presented. The wire-grid model of the handset was used to verify that the radiation patterns are computed correctly.

The patterns of the tilted handset were compared with those of the vertical handset. Whereas the  $E_\theta$  component of the field is dominant in the patterns of the vertical handset, tilting the handset introduces a strong  $E_\phi$  component into the radiation patterns.

The computed principal plane patterns of the tilted handset were compared with the measured patterns. The measurement includes the styrofoam jig which holds the handset, and its fiberglass bolts, whereas the computation does not. There is quite good agreement between the measured patterns and the computed patterns. The main differences are in the minima of the patterns.



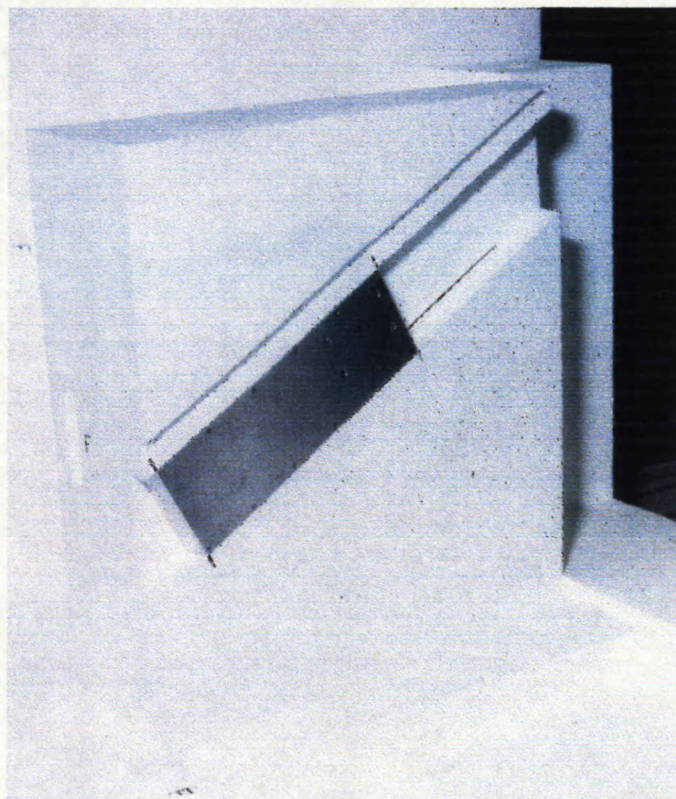


Fig. 6.1 The handset in the jig, held at the desired "tilt" angles.

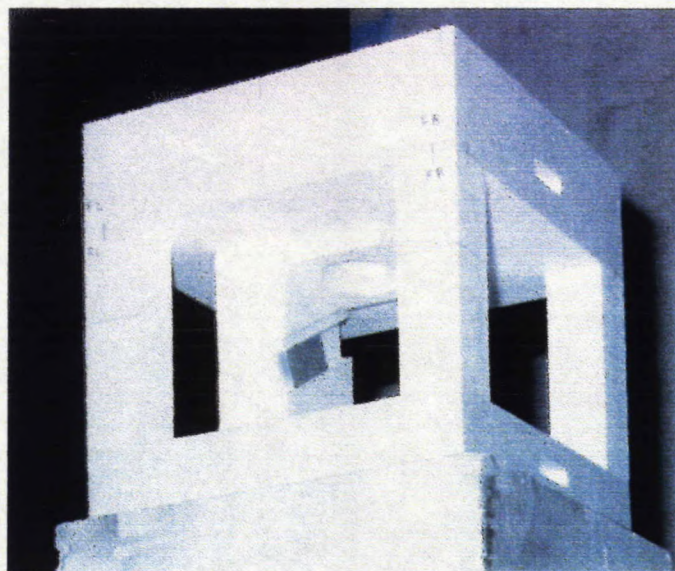


Fig. 6.2 The handset in the jig atop the rotator column in the anechoic chamber, for measurement of the azimuth pattern.



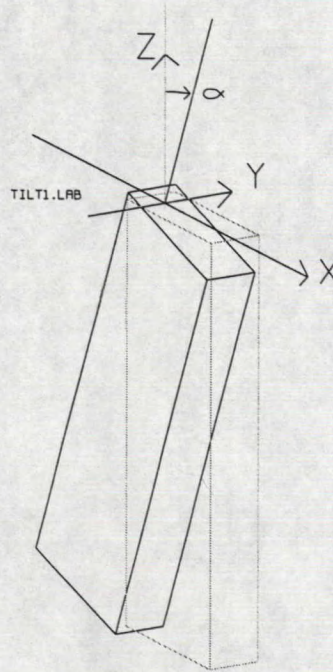


Fig. 6.3 The handset after rotation through angle  $\alpha$  about the global y axis.

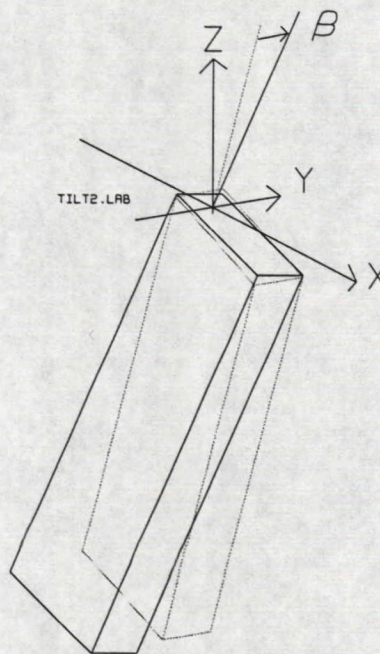


Fig. 6.4 The handset after a second rotation, through angle  $\beta$  about the global x axis.



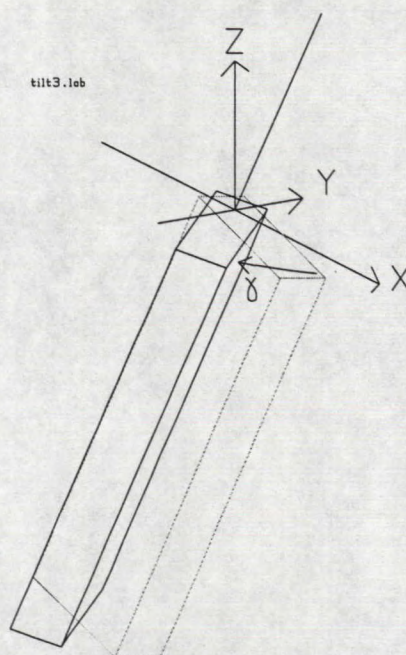


Fig. 6.5 The handset after rotation through angle  $\gamma$  about the axis of the antenna.



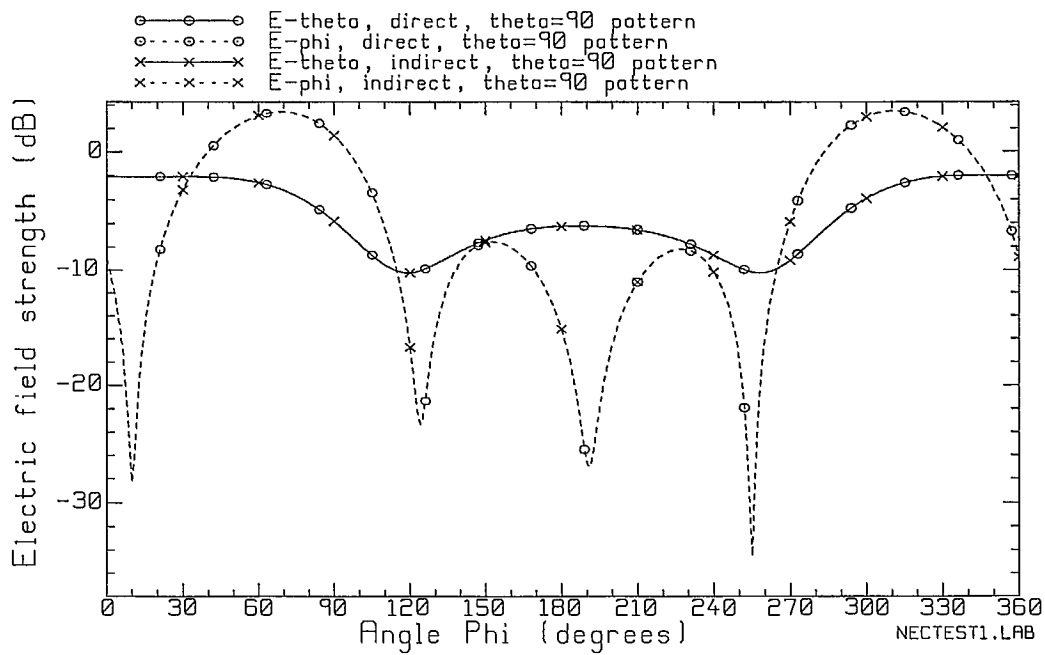


Fig. 6.6(a) The tilted handset's azimuth pattern computed with NEC using the "direct" and the "indirect" method.

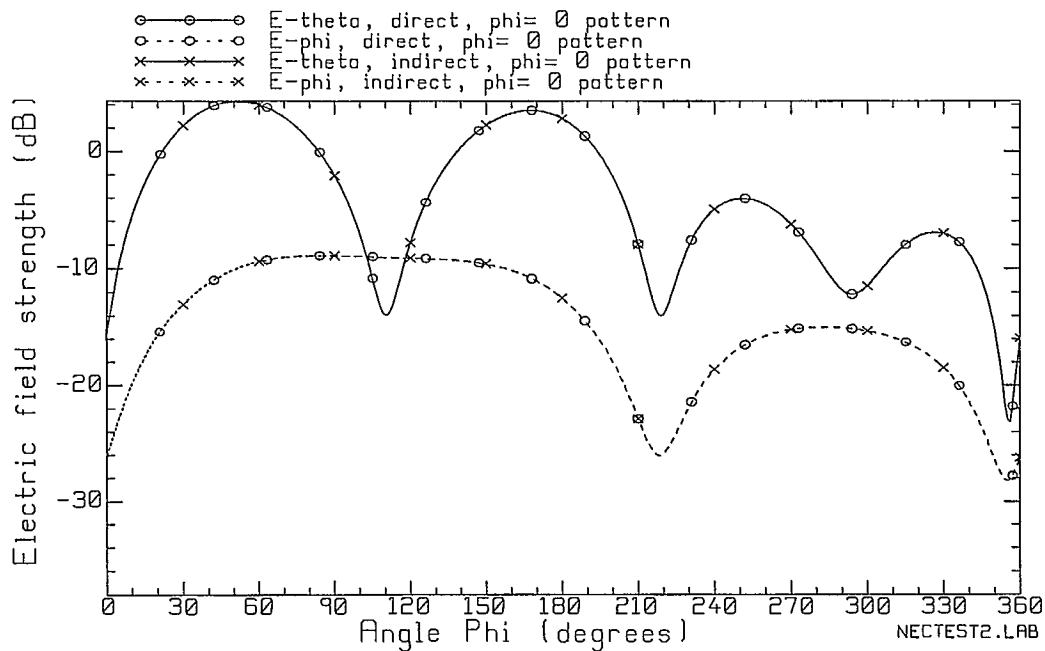


Fig. 6.6(b) The  $\phi=0$  elevation pattern by the "direct" and the "indirect" method.

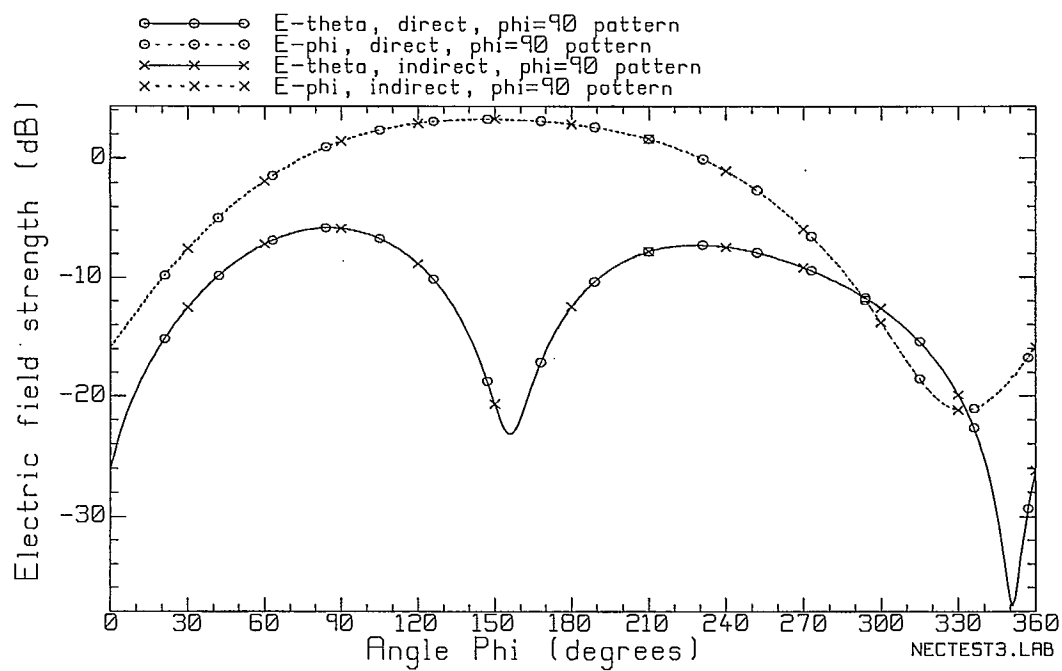


Fig. 6.6(c) The  $\phi=90$  elevation pattern by the “direct” and the “indirect” method.

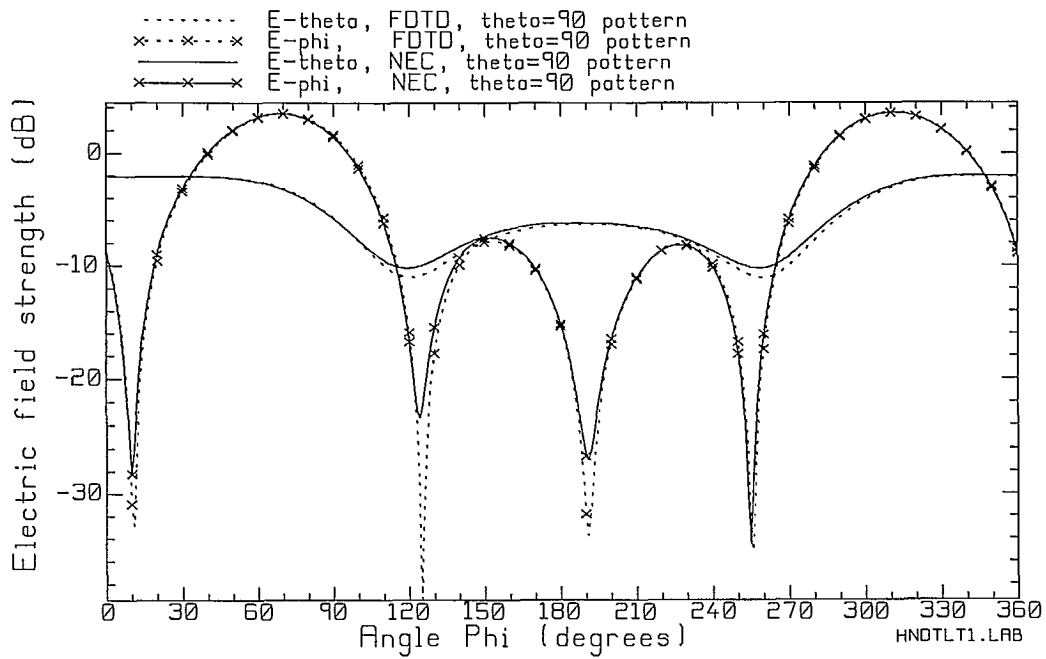
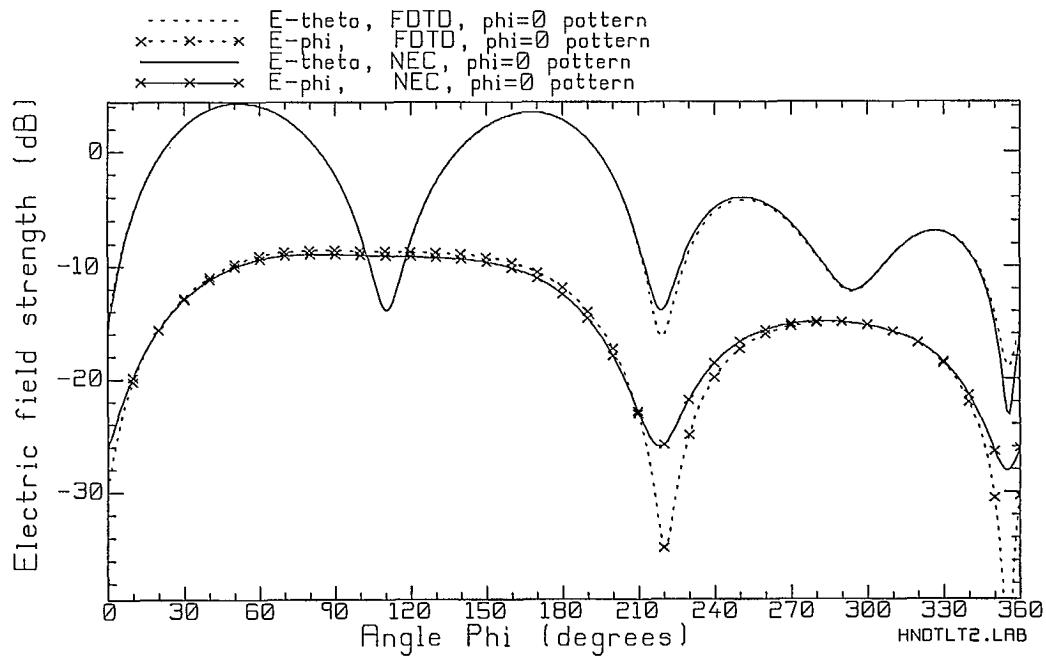


Fig. 6.7 (a) The azimuth pattern, NEC vs. FDTD.

Fig. 6.7 (b) The  $\phi = 0$  elevation pattern, NEC vs. FDTD.



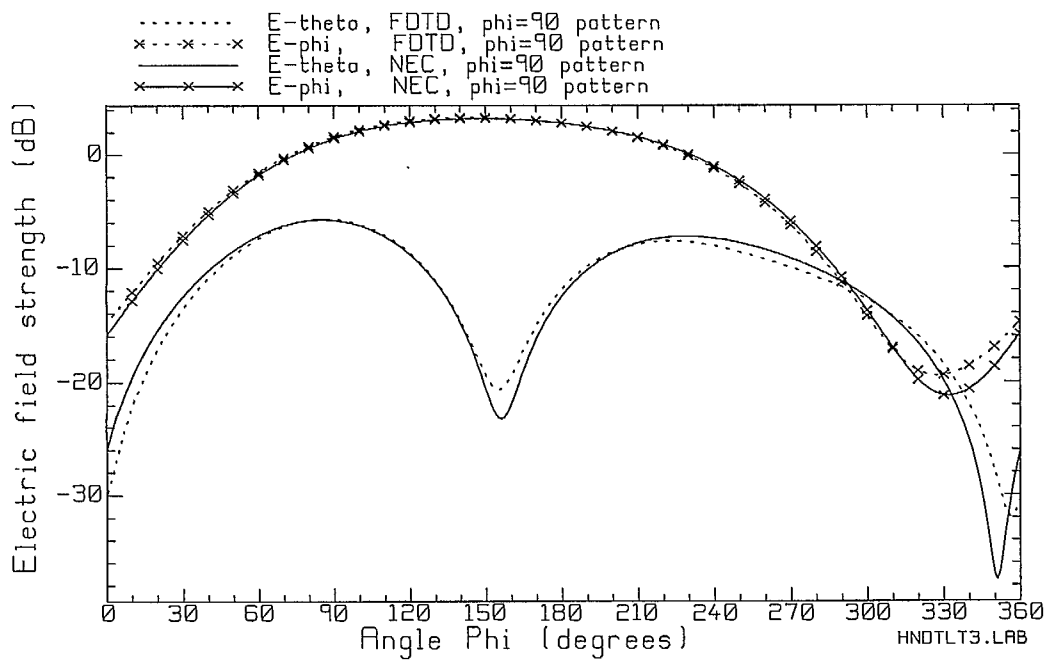


Fig. 6.7 (b) The  $\phi = 90$  elevation pattern, NEC vs. FDTD.

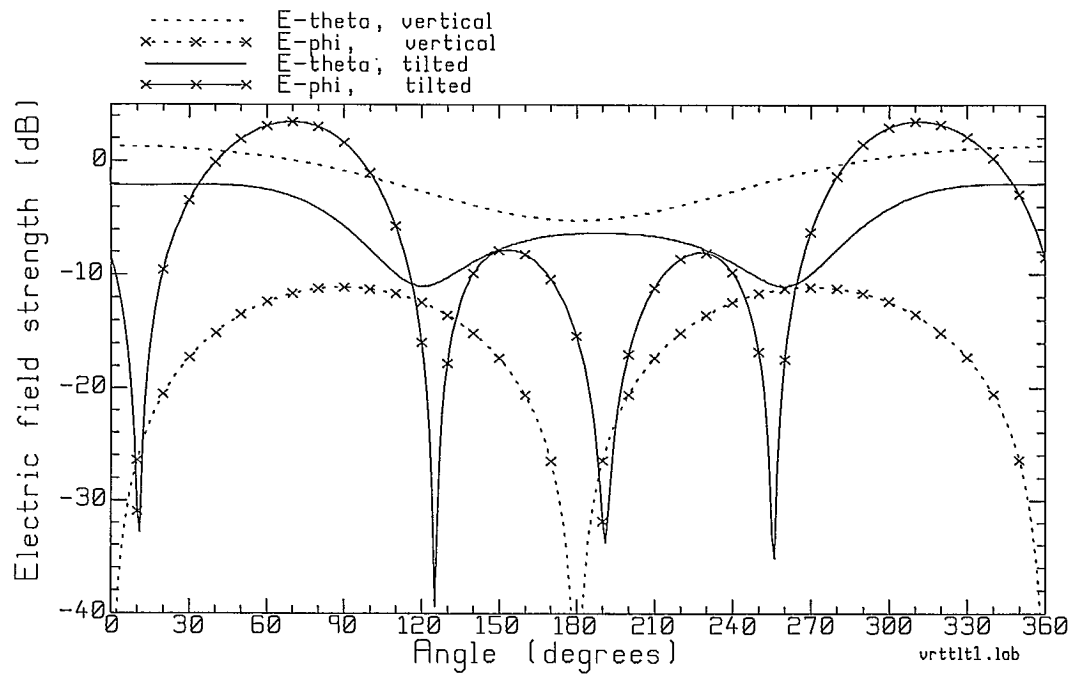


Fig. 6.8(a) Comparison of the azimuth pattern of the vertical handset and of the titled handset.

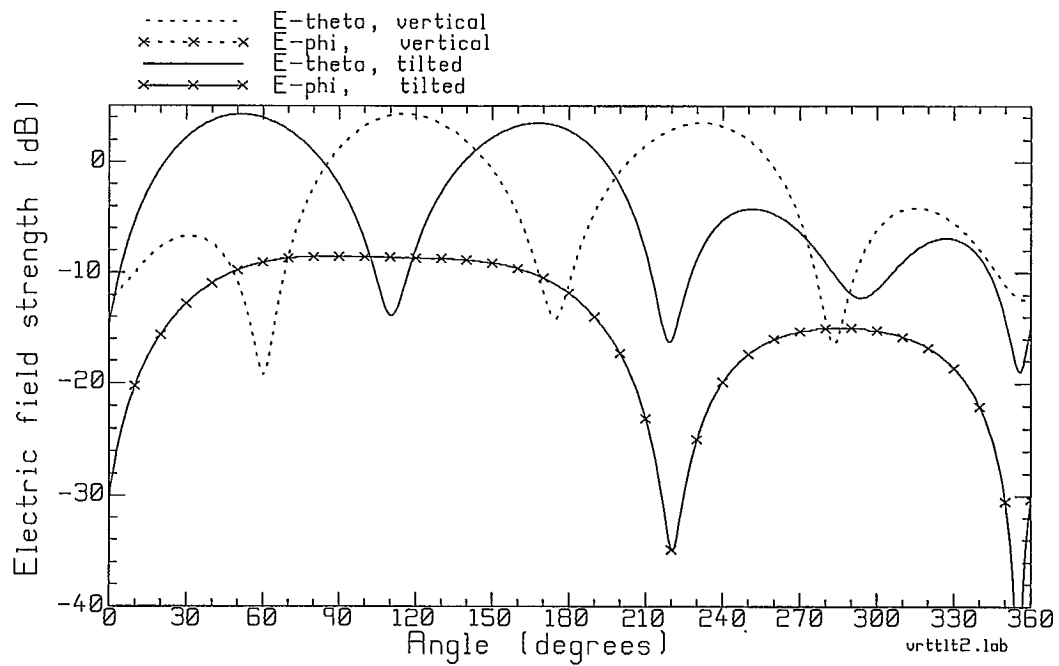


Fig. 6.8(b) The  $\phi=0$  elevation pattern.

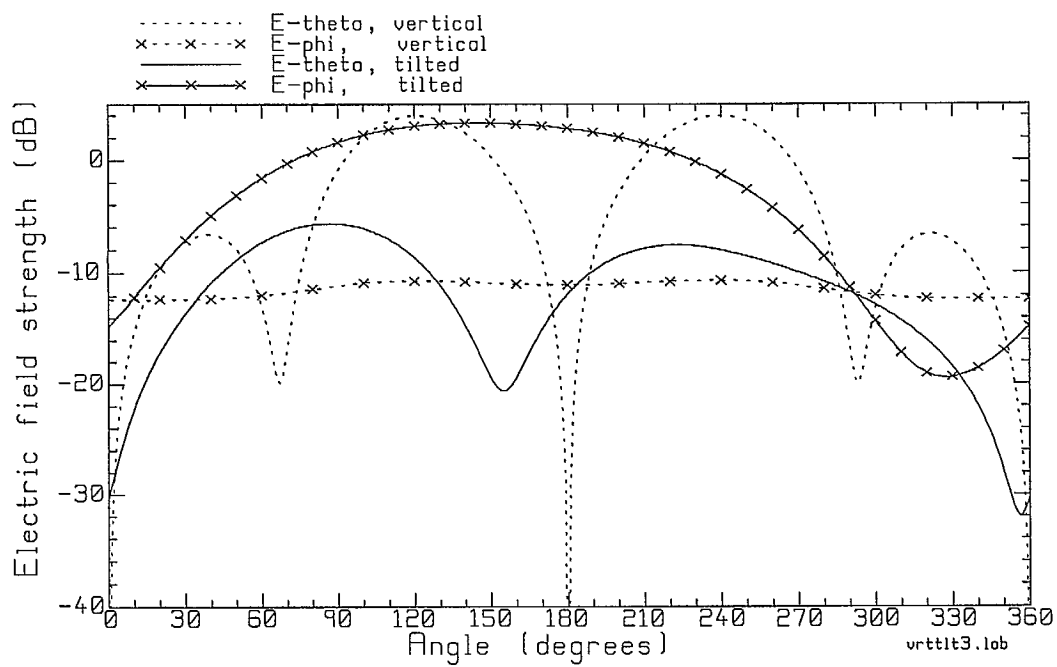


Fig. 6.8(b) The  $\phi=90$  elevation pattern.



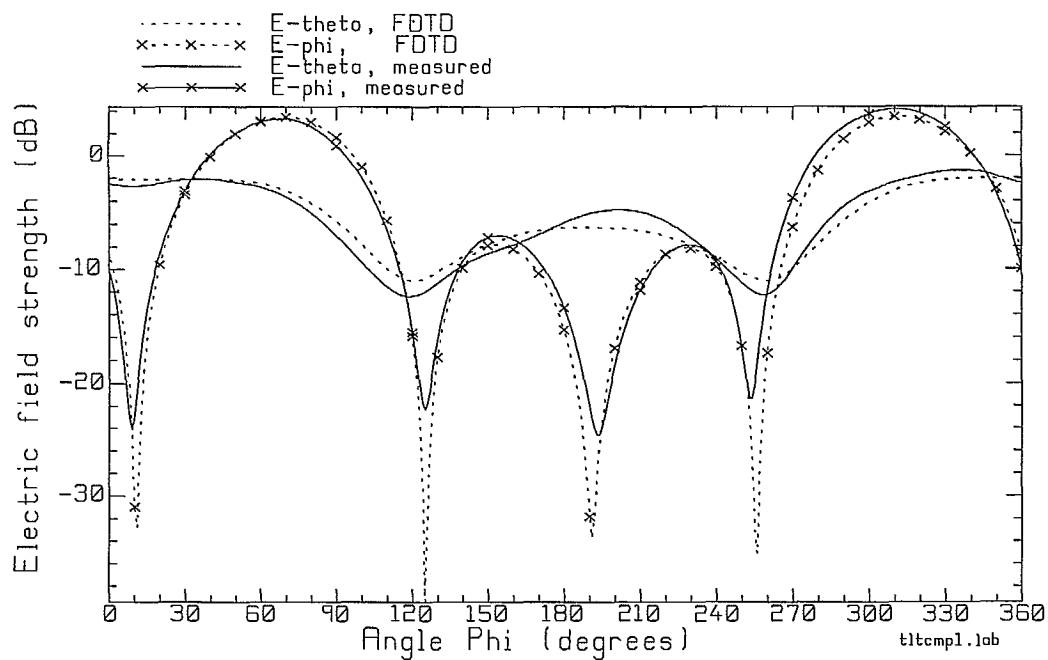
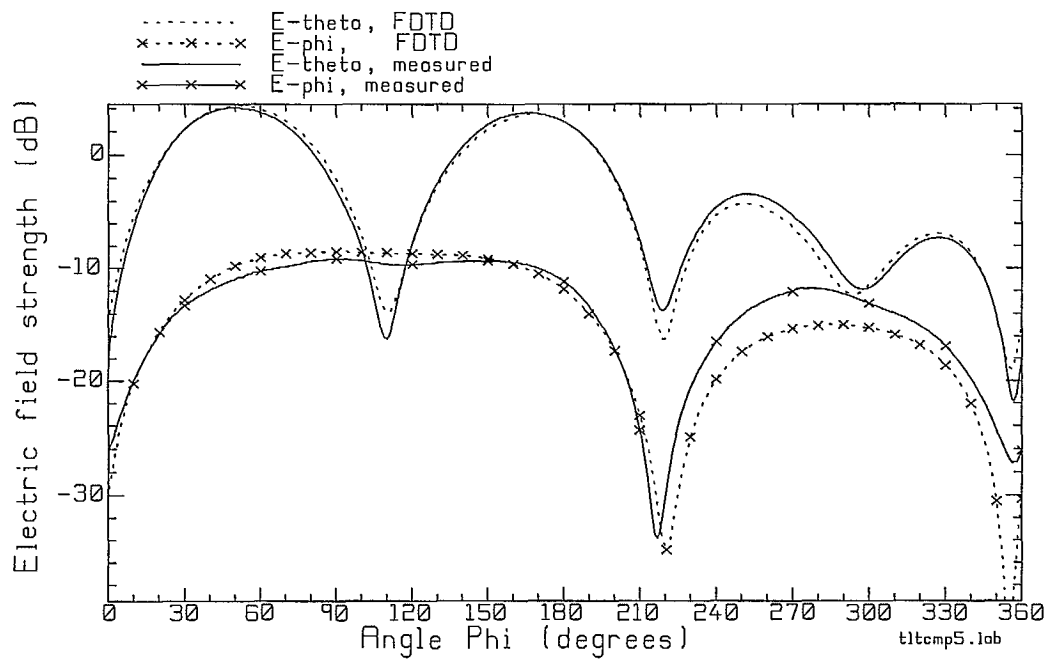


Fig. 6.9(a) The azimuth pattern, FDTD compared with measurement.

Fig. 6.9(b) The elevation pattern for  $\phi = 0$  degrees.

mottled appearance than the skin layer near the surface. In part (b) it is not easy to distinguish skin and muscle regions in the cheeks, nor in the back of the head. The same problem exists in part (c). In part (d), towards the top of the head, the muscle layer is thin and muscle and skin are not clearly distinguished. Part (b) shows that the ears are not clearly defined in some of the CT scans, whereas in others, part (c), the ears are much more clearly seen.

To assemble a cell model for analysis with FDTD, the tissue types in each of the CT scans must be unambiguously identified.

## 7.2 Identifying Tissue Types

To use the CT scan cross-sections as the basis for an FDTD cell model, the regions of skin, muscle and bone must be clearly identified. Each scan is 512 by 512 pixels, including the white regions surrounding the head. Ref. [28] suggests that the material type of each pixel can be identified from how gray the pixel is. Hence the gray scale is subdivided into bands, and each band associated with a particular tissue type. The reference suggests an orderly progression from very white regions for bone, through grayer regions for skin, to a darker gray for muscle, and so forth. This was attempted with the CT scan data. However the results were entirely unsatisfactory. The streaks in the regions outside the head are dark enough to be confused with the skin layer. The white regions representing the bone are liberally streaked with dark black, causing misidentification of the dark areas as muscle within the bone. A fully automatic tissue identification based on gray levels alone is not possible with this noisy data set.

It is necessary to process each of the 116 CT scans manually, to mark each pixel as free space, skin, muscle, bone or brain tissue. An interactive graphics program was created to aid in this process, called EDITMAP. Using EDITMAP to mark the tissue types in one of the CT scan sections was described in detail in Ref. [1] and is summarized in the following.

In EDITMAP all the pixels start out as "raw" pixels, having grey-scale values. The central idea in EDITMAP is to change "raw" pixels to "material" pixels representing tissue types. This is done by selecting a "current" tissue with the "choose a material" function, and then outlining a region with pixels of that tissue type, and then using the "area fill" function to change all the pixels within that area to the selected tissue type. Thus we can outline the bone regions with pixels marked as "bone", and then fill the interior with "bone" by changing all the pixels within the outline to "bone" pixels.

Fig. 7.3 shows the same set of four cross-sections as in Fig. 7.2, but after processing with EDITMAP. The program provides a variety of "tools" to aid in marking pixels by tissue type, listed at the right side of the display in Fig. 7.3. The program converts pixels to the "current" material being edited, which can be selected with the "choose a material" function.

The first step in processing each cross-section is to select "bone" as the current material and then use the "slope filter" to identify transitions from free-space to tissue. This function looks for large changes in grey-scale value from one pixel to the next, and marks such pixels as "bone". Since the bone regions appear largely in white on the CT scans, the surface of the bone is quite well identified by this step. But this step has the side effect of outlining the surface of the skin with "bone" pixels. This "error" is easily repaired, later in the process.

The next step is to carefully examine the outline of the spine drawn by the "slope filter", and use the "draw line" function to close any gaps in the outline. Then "area fill" is used to change all the enclosed "raw" pixels to "bone".

The next step is to separate the skin and muscle regions. This is done with the "range filter". The user selects "skin" as the tissue to be edited, and then selects "range filter". This changes "raw" pixels that lie in the gray-scale range from 0.28 to 0.40 to "skin" pixels. Because the CT scan data is quite noisy, this will change some regions that, to the eye, are clearly "muscle", into "skin" pixels. This must be repaired manually, later in the process.

The fourth processing step is to clean up the regions of muscle tissue so that all the pixels in these areas are marked as "muscle". The user selects "muscle" with "Choose a Material". "Zoom" is used to enlarge small regions of the map to fill the screen and then the "Draw a Line" function is used to enclose muscle regions with an unbroken line of red muscle pixels. Then "Area Fill" is used to change "raw" pixels within these regions to muscle. This does not change pixels marked as "skin". Then the "Revise Area" function is used to modify pixels incorrectly identified as "skin" to become muscle pixels. This step is time consuming and represents the bulk of the work needed on each cross-section.

The next processing step is to choose "skin" as the material to be edited and then use the "Revise Area" function to change the "bone" pixels at the surface to "skin". This is quick because the "Revise Area" function is able to follow the contour of pixels all around the surface and change them to "skin" in one operation. Some small regions of "raw" pixels within the skin region usually remain, and must be changed to "skin" with "Area Fill". The "Join Filter" is useful for changing the great many "raw" pixels just beneath the surface of the neck into "skin" pixels.

Finally, "wood" is selected as the current material and "Area Fill" is used to change the "raw" pixels of the neck support post to "wood" pixels, in cross-sections where the post is present. If the editing process in the foregoing has been carefully carried out, there will be few "raw" pixels at this stage. Any "raw" pixels are identified and removed with the "Clean Up" function. This searches the entire map for "raw" pixels and changes each to the tissue type of the majority of the neighbors. The result of the editorial process is maps such as those in Fig. 7.3, which should be compared with the input data, Fig. 7.2.

We note in Fig. 7.3 that in part (a), the void clearly seen in the CT scans at the surface of the muscle tissue was maintained in the tissue data base. In part (b), section #57, the region behind the nose is filled with skin tissue. There are no nasal cavities. The photos of the phantom do not show any muscle tissue in this area. Part (c) shows that in identifying tissue types in the cross-sections, the eye sockets were filled with a tissue labeled "eye". This was done in case it was desired to ask whether a different material type in the eye sockets would affect the far fields or near fields. To use the phantom data base, this "eye" material is made to have the same electrical parameters as the "skin" material.

The EDITMAP program took about 8 months to develop into a relatively efficient, easy to use editor for the CT scan cross sections. But still, there is a very significant amount of labor required to process 117 CT scan cross sections as described above. Also, in many cross-sections the boundaries between skin and muscle are not very clear, and some judgement must be used to identify muscle where it is seen in the photographs of the phantom. Also, the ears are vaguely defined in many of the CT scans, especially the right ear, and some imagination was used to create an ear similar to the left ear. Fig. 7.3 (b) and (c) show the ear that was created from the vague data in Fig. 7.2.

We are grateful to research assistant Najma Khalili for diligently and patiently processing each of the 117 cross-sections.



Once the 117 CT scan cross-sections had been processed to identify tissue types, it was discovered that from one cross section to the next, tissue boundaries sometimes changed position quite radically. This was fundamentally due to the noisy nature of the CT scan data. Where the surface of the skin was ill-defined in the CT scan data, processed cross-section positioned the surface somewhat arbitrarily, for instance.

Thus it was necessary to compare each cross-section with the neighboring sections to ensure continuity from one section to the next. The functions called "previous outline" and "next outline" were added to the EDITMAP program. When displaying cross-section #I, "previous outline" draws the surfaces of the tissue regions of section #(I-1) superimposed on section #I. Then adjustments can be made to section #I for continuity. Similarly, "next outline" draws the surfaces of the tissues in section #(I+1) on section #I, and changes can be made to section #I. This was very useful for cases where the CT scans for sections #(I-1) and #(I+1) identified the skin surface well, but not the scan for section #I. These functions allowed surfaces to be adjusted for section #I to ensure consistency with the neighboring sections.

This adjustment process was very tedious and took two weeks of effort on the part of our research assistant. The result is a data set for creating FDTD cell models that leads to fairly good continuity in the tissue surfaces throughout the cell model.

### 7.3 Creating an FDTD Cell Model from the CT Scan Data Set

The CT scan data, after processing with EDITMAP, provides a 512 by 512 pixel template for each of 117 cross sections of the phantom head, as a basis for creating FDTD cell models. We need to be able to create a cell model based on a specific cell size, such as 2.205 mm.

In the coordinate system used in this report, the head faces in the +x direction and the handset is held against the right side of the head. In the simplest case, the handset is positioned vertically, with the antenna parallel to the z axis, and the planes of the broad faces of the case are parallel to the yz plane.

But the user normally holds the handset with the antenna inclined at about 60 degrees to the vertical axis of the head. In addition the handset is often rotated so that the planes of the broad faces of the case are not parallel to the yz plane. In FDTD the handset can be modeled precisely when the case is positioned with the surfaces parallel to the coordinate planes and the antenna parallel to the z axis. Thus it is convenient to define an FDTD coordinate system with the handset positioned in this way, and the head tilted and rotated to its correct position relative to the vertical handset.

In Ref. [3] a program called MKHEAD was described for assembling a cell model from a database of sections based on anatomical data. In this program, the user specifies the cell size, and the rotation of the handset about the y axis, and the program assembles a cell model of a "tilted" head. For the present purpose the MKHEAD program was renamed MKPHANT and was re-engineered to use the phantom data set, and to permit two angles of rotation of the head relative to the handset. The user specifies the cell size, and the direction in which the antenna of the handset is pointing as angles  $(\theta, \phi)$  in spherical coordinates relative to the global coordinate axes. A third rotation angle called  $\gamma$  was included in the MKPHANT program to make the rotation general. This angle is a rotation about the axis of the antenna, and is not needed to model the handset in the CRC measurement jig. The program then assembles a cell model at the desired cell size, with the head oriented appropriately relative to the direction of the antenna. With the head tilted and rotated to the desired angles relative to the direction of the handset

antenna, we must ensure that the position of the handset is correct relative to the head. By this is meant that the distance from the handset surface to the ear must be correct. Also the handset must be positioned correctly relative to the head in the back-to-front and up-and-down sense.

#### 7.4 Cell Model of the Handset and Head in the Measurement Jig

The measurements of the radiation patterns of the handset and the phantom head are done by mounting the handset and head in the measurement jig shown in Fig. 7.4. The jig holds the handset at a well-known, reproducible position relative to the head[26]. The handset antenna is aligned relative to the head's vertical axis at  $\theta=64.42$  degrees,  $\phi=191.10$  degrees. A special-purpose version of the MKPHANT program was created that positions the handset correctly, both in terms of these rotation angles and of the position, back-to-front, side-to-side and up-and-down. The program adds the wood base to the phantom model, positioned correctly relative to the head. It adds the white column seen in Fig. 7.1 that supports the base of the neck, and extends the wood post supporting the chin down to the wood base.

The CRC measurement jig is held together by four long fiberglass bolts, with a plexiglas washer and a fiberglass nut at each end of each bolt. These too were included in the output of the MKPHANT program. However, the styrofoam blocks making up the jig were not included in the model.

A cell model of the head is created by running MKPHANT. For each cell in the FDTD cell space, MKPHANT changes the cell center coordinates from the FDTD coordinate system, in which the handset antenna lies along the  $z$  axis, to the global system in which the  $z$  axis is the vertical axis of the head. Then MKPHANT searches the head phantom data base to find the nearest pixel on any of the 117 cross sections. The material of that pixel is assigned to the cell. The output of the MKPHANT program is a "build" file for input to the FDTD PML program.

A display and edit program for cell models, described in "build" files, has been created and is called "EDITCEL". This program displays cell models in the format shown in Fig. 7.5. Each material is assigned a name and a color. This is done in the build file to give the user control over the color selection. The program permits the user to step through the model by cross-section in  $xy$ ,  $xz$ , or  $yz$  planes. The user can zoom the display to examine regions in detail. The material composition of individual cells can be modified with the mouse. In addition to these graphical functions, the EDITCEL program can change the amount of whitespace surrounding the model. This is usually adjusted, using EDITCEL, to 10 cells, prior to running the FDTD PML code to find the radiation patterns of the model.

#### 7.5 The FDTD Model of the Phantom Head Oriented Vertically

The MKPHANT program was used to create an FDTD model of the phantom head with the handset held vertically alongside the head, at cell size 2.205 mm. An  $xz$  section through the head at the location of the hole for filling the brain cavity is shown shown in Fig. 7.5. We see that the model includes the wood base, the neck support post between the base and the bottom of the head, the chin support post, and the head itself. The bone material, shown in yellow in Fig. 7.5, includes the neck support post, the spine, the skull, and the jaw. The muscle layers are clearly seen in red in the neck, and throughout the mouth. The skin material covers the outside of the phantom and fills the nose and sinus region.

Fig. 7.6 shows sections of the cell model of the head phantom. The color key for the material types is given in Fig. 7.5. Fig. 7.6(a) shows an  $xy$  plane section through the wood base. The four fiberglass bolts are seen in the four corners of the section. Part (b) shows a section through the neck support column and the chin support post, and again the four fiberglass bolts appear in the corners. Part (c) shows a section through the neck. The small airspace at the muscle to skin interface is clearly seen. A handset case has been included in the figure to show the relative size of the handset to the phantom head. Part (d) shows a section through the jaw of the phantom. Part (e) shows a section near the base of the brain cavity and shows a peculiarity of the phantom head. That is, near the right ear there is a hole in the bone layer that allows the brain material to come through the skull to touch the muscle material. This was verified in the corresponding CT scan cross section of the phantom. Part (f) is a section at the height of the nose and ears. Part (g) shows a section through the eye sockets, which are filled with skin material. Part (h) is a  $yz$  cut through the handset case and head. The handset case is more than half the height of the phantom head. The section shows the bones in the neck and skull, the brain cavity, the muscle layers in the neck, and the skin layers including the ears. The phantom is not very symmetric internally. Thus the brain cavity clearly lacks symmetry.

This cell model was not analyzed with the FDTD PML code. It is instructive to look at the size of the cell space for comparison with the tilted head in the next chapter. The model in Fig. 7.6 uses a cell space of 246 by 246 by 260 cells, and includes only 4 cells of whitespace. Increasing this to 10 cells would add 16 cells for a space size of 262 by 262 by 276 cells. This space size includes the full length of the four fiberglass bolts. The total number of cells is 18,945,744. This is a very large FDTD model.

## 7.6 Conclusion

This chapter described the development of a data base of 117 cross sections of the head phantom that was created from CT scans of the phantom. Each section is a map of 512 by 512 pixels, and identifies the material of each pixel as free space, skin, bone, muscle, brain or wood. The sections are used to assemble FDTD cell models of the head with a user-specified cell size. A cell model using 2.205 mm cells was created for the case of the handset held vertically beside the head. Then the axis of the antenna is parallel to the vertical axis of the head. The cell model includes the wood base of the head phantom and the four fiberglass bolts used to assemble the measurement jig.

In the next chapter a cell model is created of the handset and head with the handset held at a realistic angle against the head. The radiation patterns are computed and compared with measured patterns.



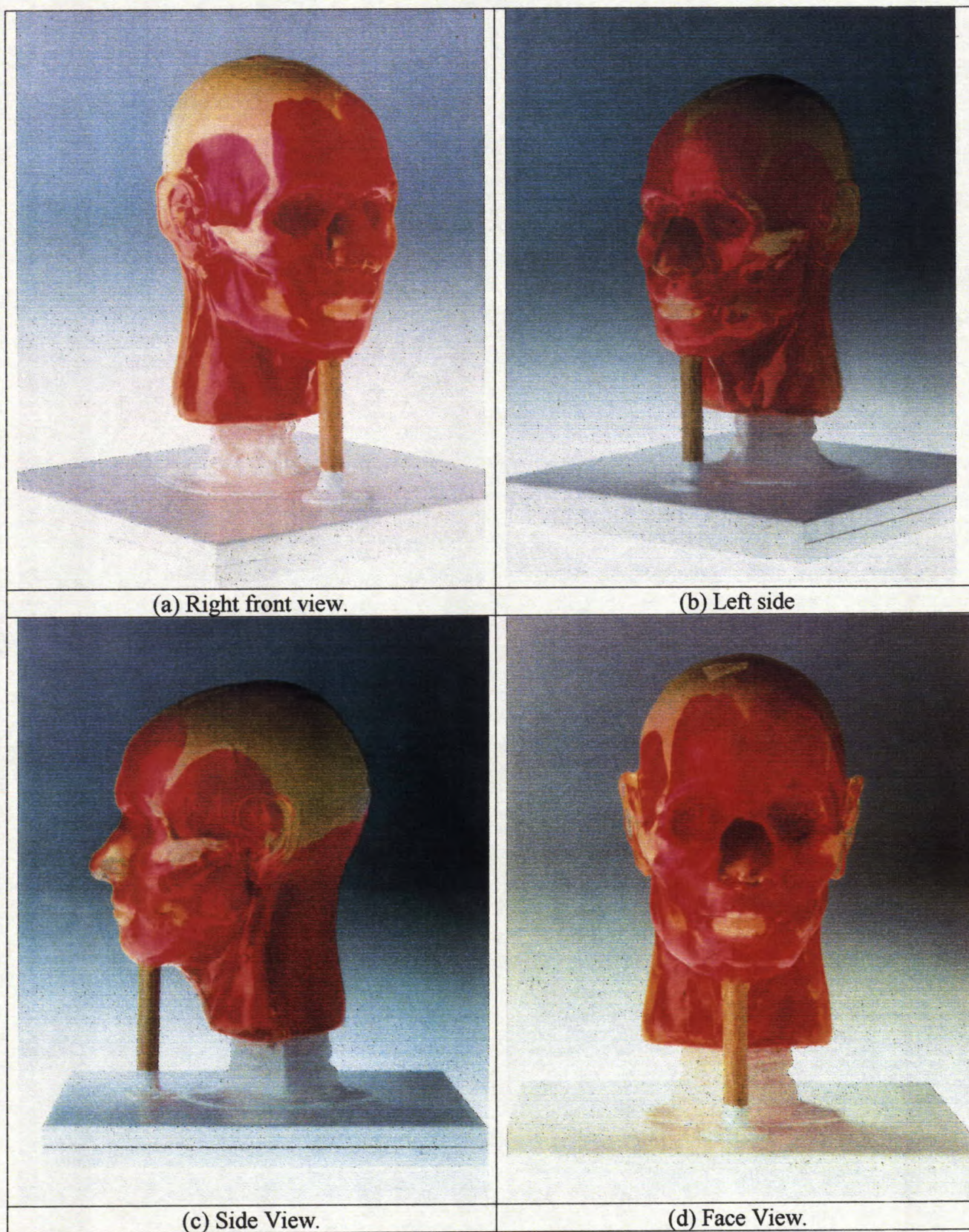


Fig. 7.1 Four views of the phantom head.



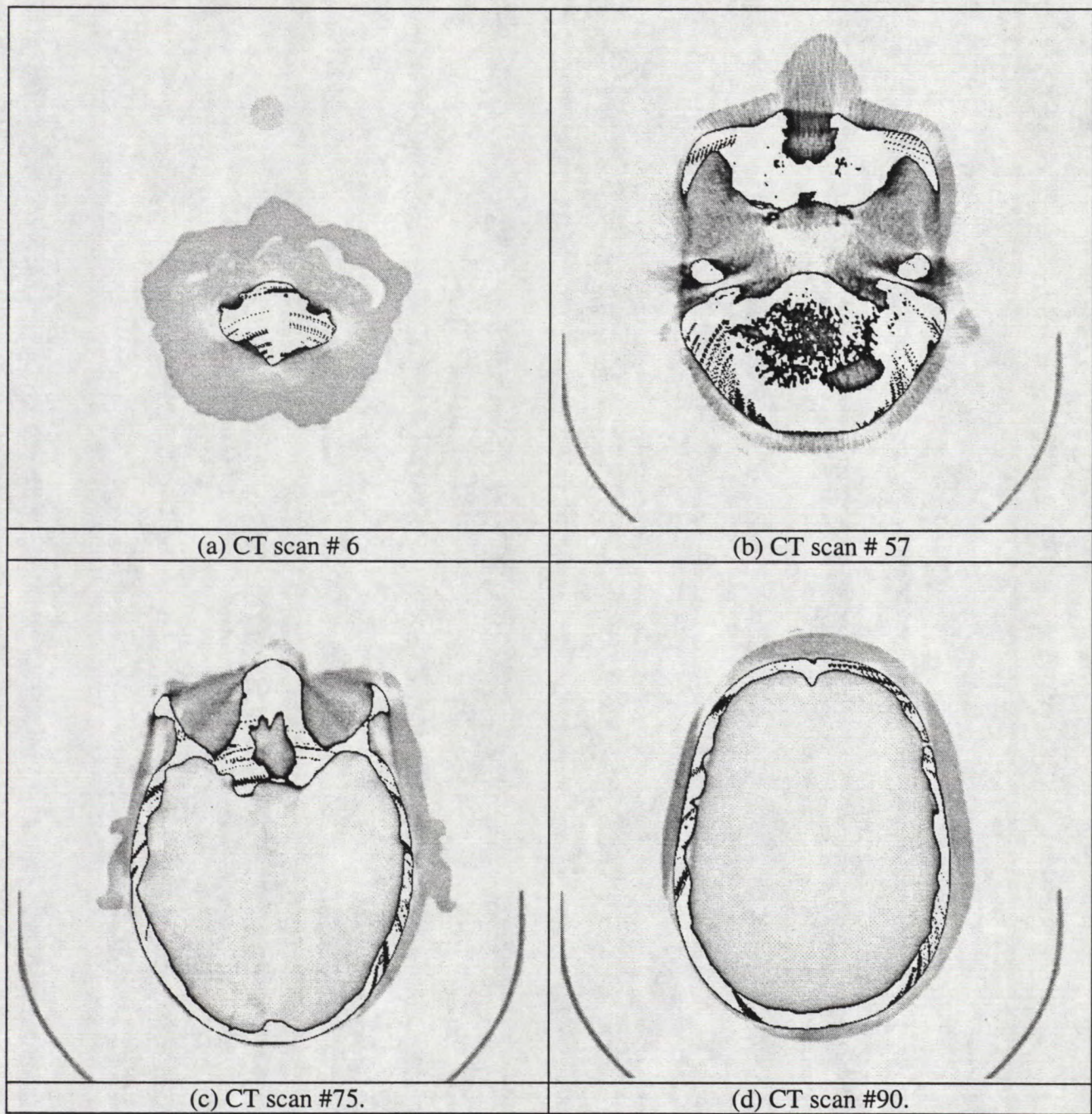


Fig. 7.2 Some CT scan cross sections of the head phantom.



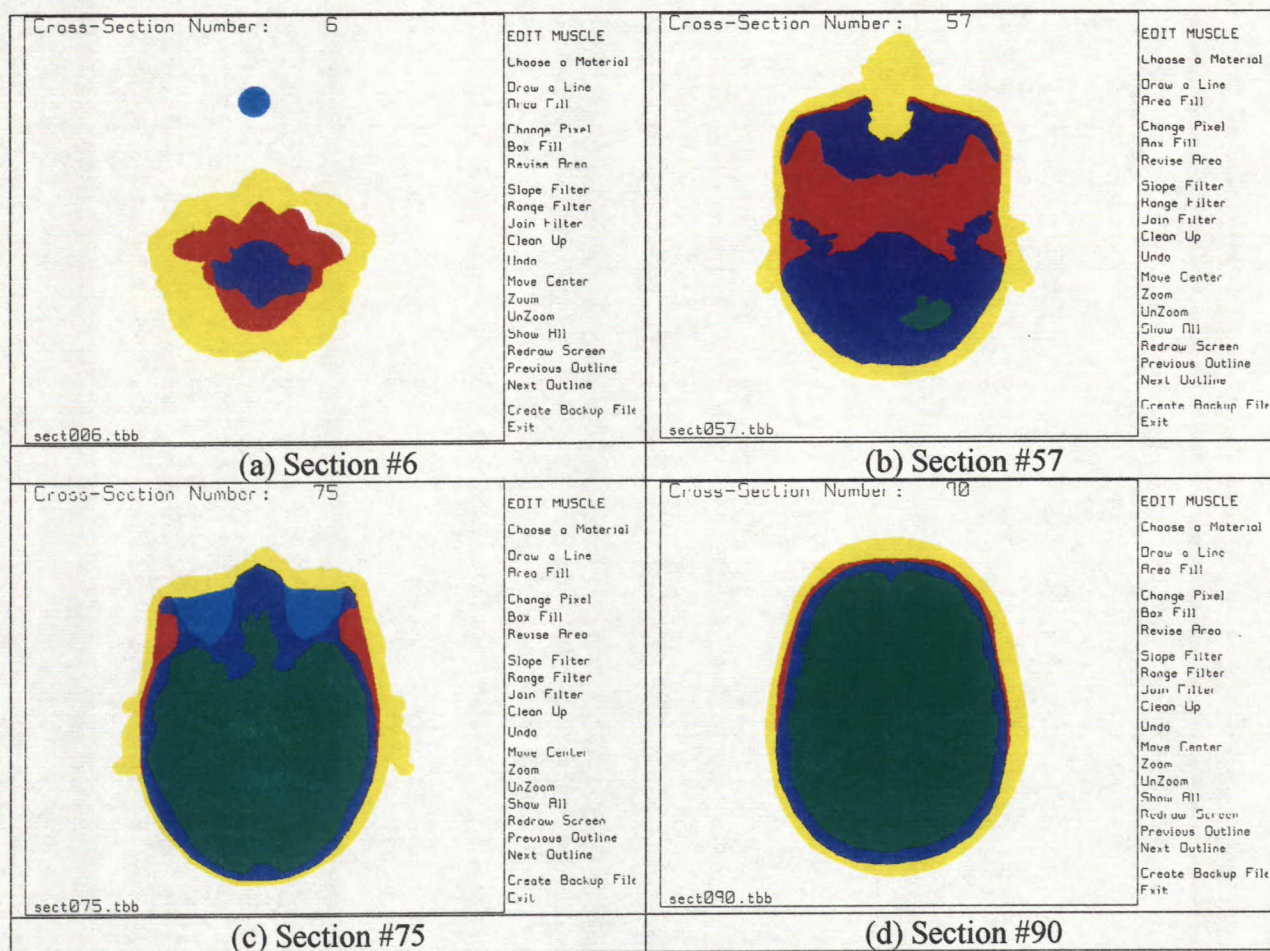


Fig. 7.3 Cross-sections of the phantom head identifying the tissues.

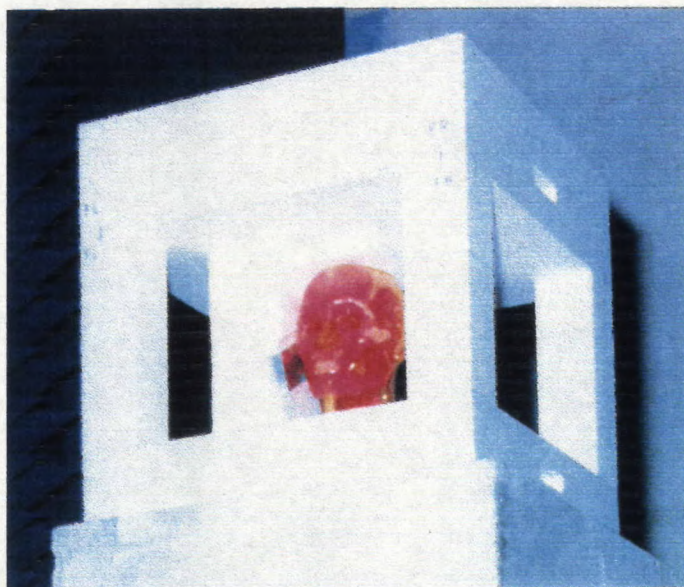


Fig. 7.4 The measurement jig holding the handset and the phantom head.



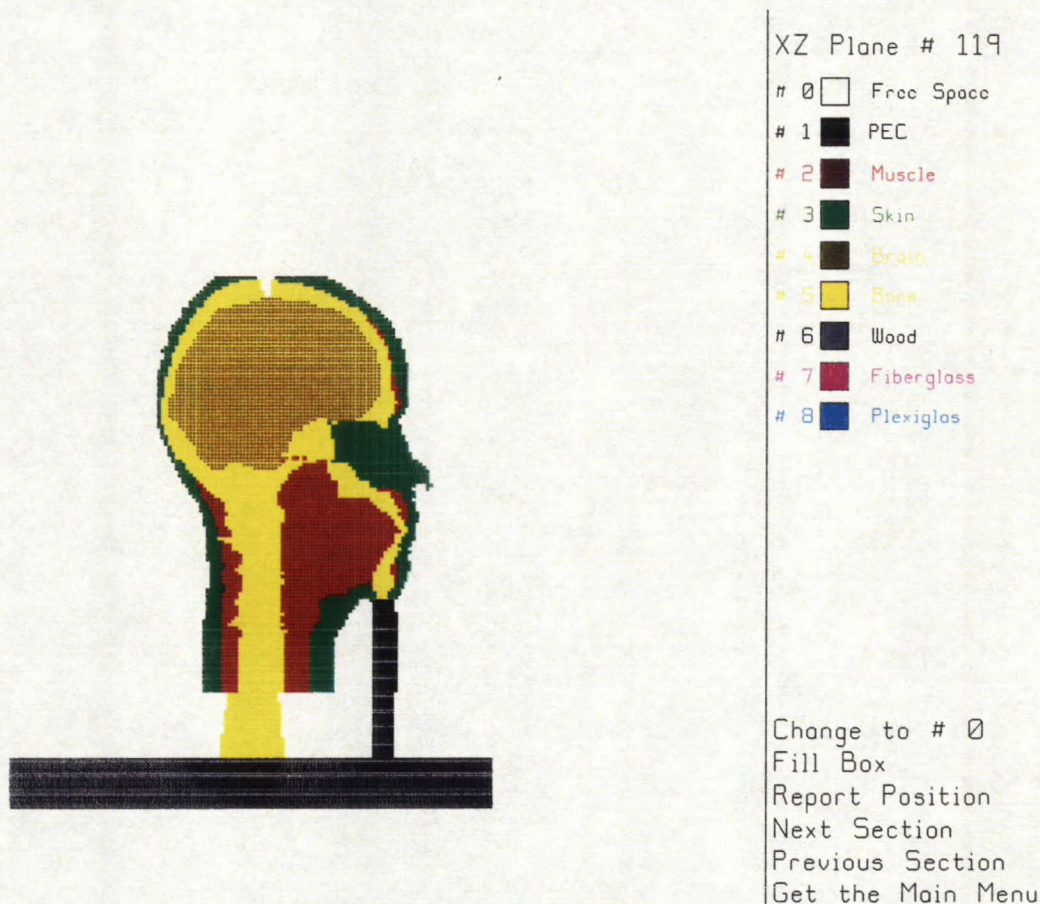


Fig. 7.5 An  $xz$  plane cut through the phantom head when it is oriented vertically in the FDTD cell space. This cut shows wood base, the column supporting the base of the neck, the wooden post supporting the chin, and the hole in the top of the head used to fill the brain cavity. The right-hand column gives the color key used in subsequent figures to identify materials.



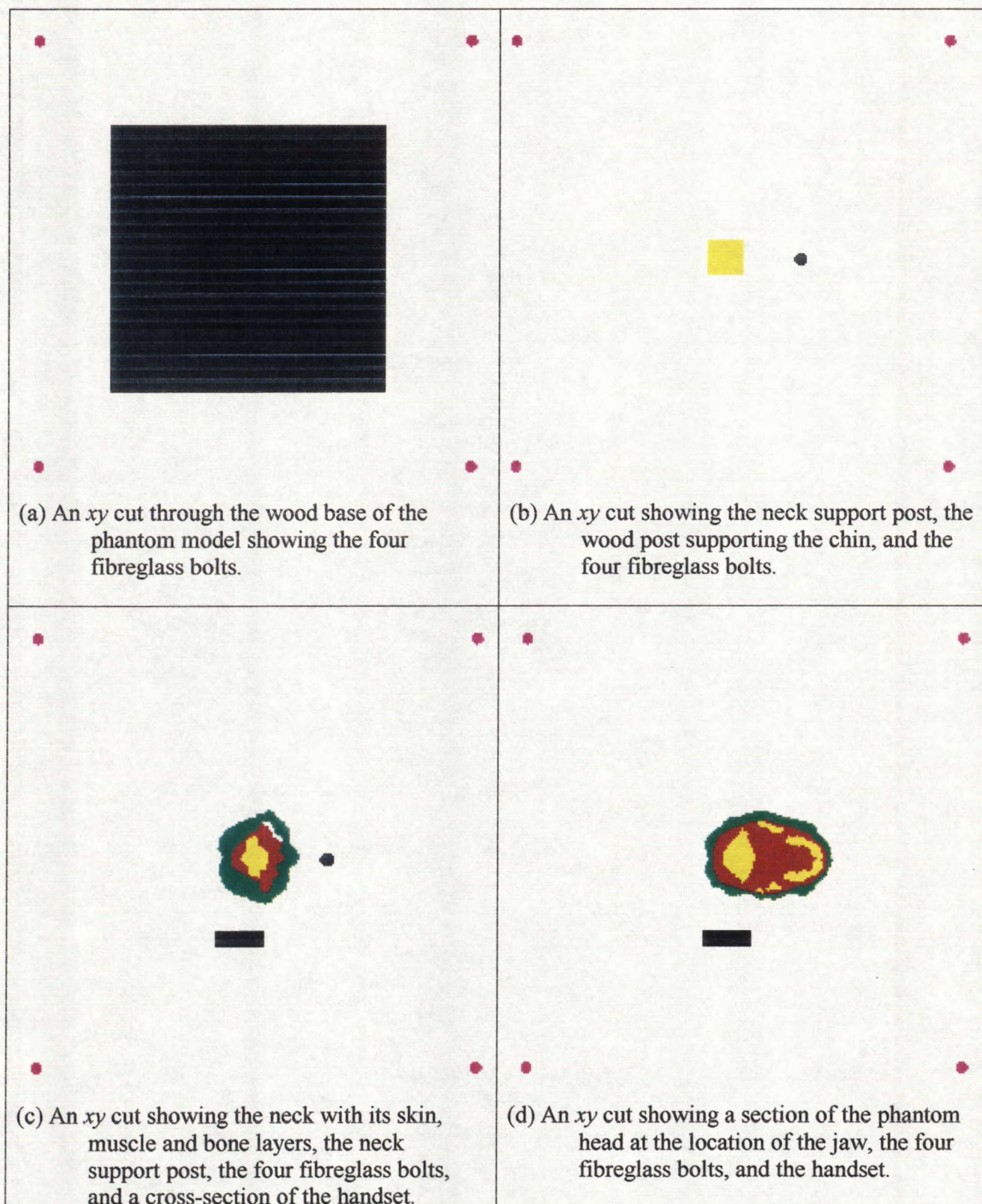


Fig. 7.6 Four sections of the head phantom FDTD model oriented vertically.



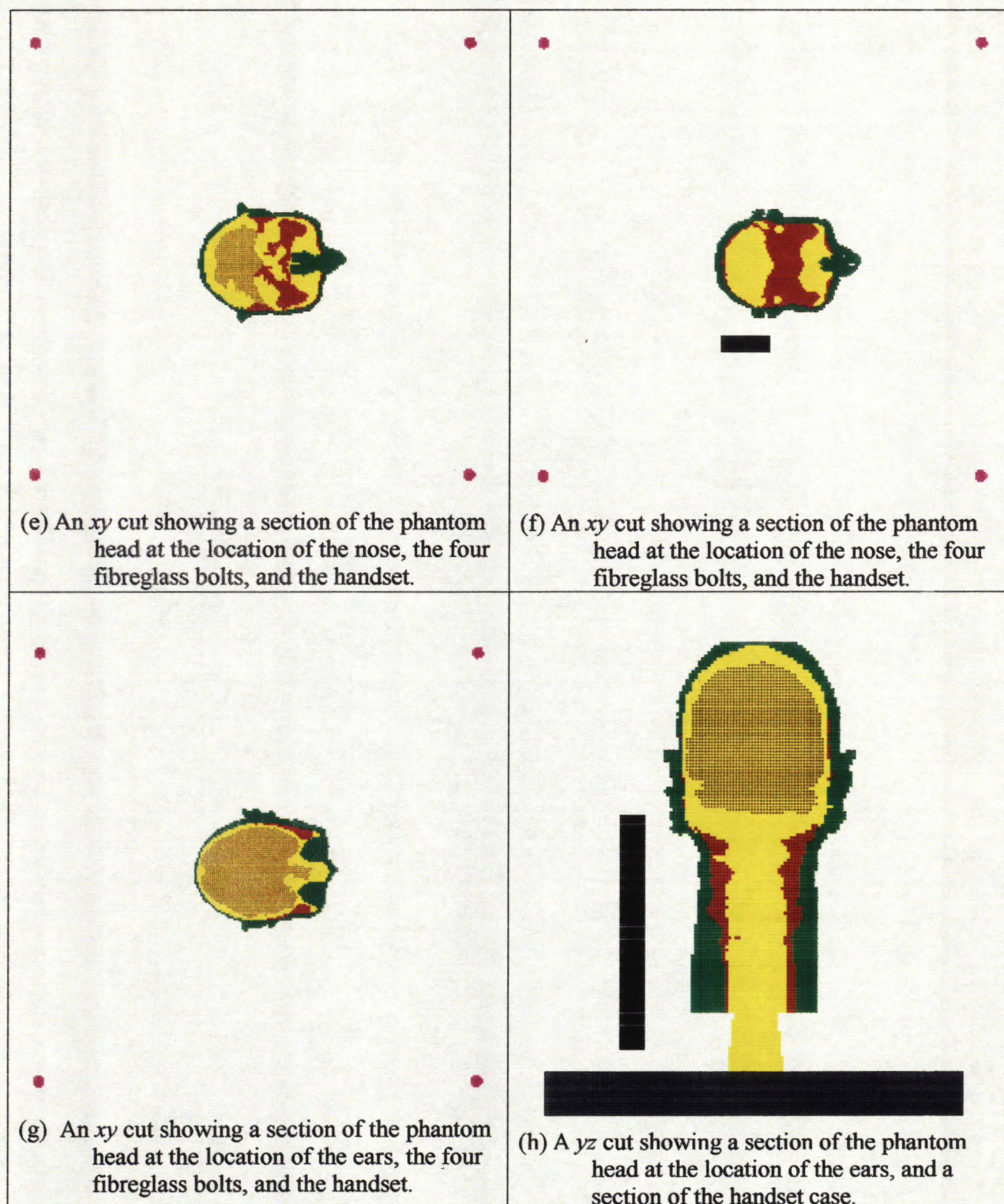


Fig. 7.6, continued.



## Chapter 8

### Far Fields of the Handset and Phantom Head

The data base of 117 cross sections of the phantom head described in the last chapter can be used to create a cell model of the phantom head in any orientation relative to the handset. The measurements of the far field of the handset and head done at CRC[18] use a jig[26] to hold the handset and head. Fig. 8.1 shows the partially-assembled jig and displays the relationship of the handset to the phantom head. The handset is positioned as if it were held in the right hand, tilted back at an angle of about 60 degrees and rotated towards the mouth. The antenna is aligned along the direction  $\theta=64.42$  degrees,  $\phi=191.10$  degrees in a spherical coordinate system, in which the axis of the head is vertical. Drawings of the handset and head mount jig[26] were used to determine the exact position and spacing of the handset to the head, and this was coded into the MKPHANT program. Also, the drawings were used to determine the size and position of the wood base of the head relative to the handset, and of the four fiberglass bolts which hold the jig together. This chapter presents the full cell model of the handset, head phantom, and the fiberglass bolts of the head mounting jig. The radiation patterns of the handset and head computed with FDTD PML will be compared to those measured at CRC.

#### 8.1 FDTD Model of the Tilted Head

Fig. 8.2 shows a cross-section of the FDTD cell model of the handset and head in an  $xy$  plane in the FDTD coordinate system. In these coordinates the handset antenna is aligned along the  $z$  axis with the broad faces of the case parallel to  $yz$  planes. The cell size is our standard size of 2.205 mm, permitting the handset case to be represented with good fidelity with 24 by 8 by 76 cells, and 40 cell edges for the antenna. Fig. 8.2 shows a section of the handset case and of the head through the ears and jaw. The four fiberglass bolts that are used to assemble the measurement jig are seen as well. Including a whitespace of 10 cells all around, the cell model occupies a space of 344 by 302 by 365 cells, or 37,919,120 cells. For the cell model of the vertical head in Chapter 7, the space size was 262 by 262 by 276 cells or 18,945,744 cells in total. We note that the increase in the size of the cell space is large in the  $x$  sense, modest in the  $y$  sense, and large in the  $z$  sense. The model of the head tilted relative to the handset is much larger in  $x$  and  $z$  because the diagonal size of the "box" defined by the four mounting bolts must be accommodated by the cell space in  $x$  and  $z$ .

At the time that this report is being written, a cell space of about 38 million cells is too large for the available computer resources and the full model including the four mounting bolts cannot be solved. By deleting the mounting bolts we can considerably reduce the size of the cell space.

#### 8.2 Handset and Head Model Without the Bolts

Figs. 8.3, 8.4 and 8.5 shows sections of the cell model of the handset and head with the four fiberglass bolts removed from the model. The space size required, including 10 cells of

whitespace all around the model, is now 196 x 175 x 195 cells, for a total of 6,688,500 cells. This model can be executed for 4096 time steps on a 450 MHz Pentium computer using about 192 megabytes of memory.

Fig. 8.3(a) shows an  $xy$  section of the FDTD cell space through the bottom of the handset case. We see a section of the wood base of the phantom, and a slice through the wood post supporting the phantom's chin. Part (b) shows a section through the neck support column, and the lower part of the face of the phantom. Part (c) shows an  $xy$  section at the height of the ear. The relative position of the handset case to the ear can be seen. Part of the wood base is seen. Part (d) is a section through the top of the handset case, showing a slice through the back of the head, and a section of the wood base.

Fig. 8.4(a) shows an  $xz$  plane section through the wood base of the phantom and the handset case. Part (b) shows an  $xz$  section through the phantom head, showing the wood base, the neck support column, the chin support post, and a section through the head. Part (c) is a section clearly displaying the spine, the muscles in the lower part of the head, and the nose region. Part (d) is a  $yz$  plane section through the neck of the phantom. We see the phantom's wood base, the chin support column, and the skin, muscle and bone layers in the neck.

Fig. 8.5(a) shows more  $yz$  plane sections. Part (a) shows a section through the back of the handset case, and through the head showing the jaw. Part (b) shows the position of the handset case to the ear. Part (c) is a section through the front of the handset case, showing the ear and the bottom of the nose. Part (d) is a section through the phantom's nose.

### 8.3 Material Properties of the Phantom Cell Model

Table 8.1 lists the relative permittivity and the conductivity of each of the materials making up the phantom head model. The parameters for muscle, skin and bone are those listed by the phantom head's manufacturer for these materials near 850 MHz. The parameters for brain are those measured for the brain liquid mixture used at CRC. The parameters for wood were taken from a reference book[22].

**Table 8.1**  
**Material Properties for the Phantom Head Model**

Material	Relative Permittivity	Conductivity (mS/m)
Muscle	51.73	1.108
Skin	42.230	0.777
Brain	40.420	1.064
Bone	14.770	0.144
Wood	2.5	0.00118

### 8.4 Bandwidth of the Cell Model

The bandwidth of an FDTD cell model is taken to be the frequency where the cell size equals one-tenth of the wavelength in one of the materials making up the model. In the lossy materials, the wavelength depends both on the relative permittivity and on the conductivity. The EDITCEL program includes a function for finding the frequency where the cell size equals a tenth wavelength for each of the materials making up the model, and the result is shown in Table 8.2.

For the handset alone in free space, with 2.205 mm cells, the maximum frequency at which the FDTD simulation is valid is 13, 598 MHz, more than 10 times greater than our operating frequency of 850 MHz. However, when the high permittivity, lossy materials making up the phantom head are present in the problem, the frequency limit is much lower. Table 8.2 shows that the material with the shortest wavelength is muscle. For muscle, the 2.205 mm cell size is equal to the tenth wavelength at 1881 MHz. Our operating frequency of 850 MHz is thus less than half the maximum frequency at which our FDTD model would be expected to obtain useful results.

**Table 8.2**  
**Material Properties for the Phantom Head Model**

Material	Maximum Frequency MHz
Free Space	13598
Muscle	1881
Skin	2086
Brain	2126
Bone	3537
Wood	8598

### 8.5 Handset Alone Patterns Compared to Handset and Head Patterns

In a previous chapter, the radiation patterns of the handset in free space were computed, tilted such that the antenna is oriented along the direction  $\theta = 64.42$  degrees,  $\phi = 191.10$  degrees. The FDTD cell model described above was used to compute the principal plane patterns of the handset positioned near the head. Recall that the radiation patterns are required in the global coordinate system in which the head is vertical and the handset is tilted back. Program MAKERP takes the specific  $(\theta, \phi)$  angles at which far field values are required, in global coordinates, and computes the corresponding  $(\theta_{FDTD}, \phi_{FDTD})$  angles in the FDTD coordinate system. The FDTD PML program is run to solve the handset and head problem and create the data file of field values over a closed surface, SSSNZFZ.DAT, required for the near to far zone program, FARZONE, to compute the far fields. FARZONE is then run and computes the far field at the desired set of angles,  $(\theta_{FDTD}, \phi_{FDTD})$ , in the FDTD coordinate system. Program ECONVRT is used to convert the field components in the FDTD coordinate system to field components in the global coordinate system, and thus assemble the radiation patterns in global



coordinates. This is how the handset alone and also the handset and phantom head patterns in Fig. 8.6 are constructed.

It is instructive to compare the radiation patterns of the handset in free space with the patterns of the handset near the phantom head. Fig. 8.6 shows the principal plane patterns. The comparison is made on the basis of equal *radiated* power. As discussed in Ref. [1], in each case the full set of "conical cut" radiation patterns is computed using FDTD, and then the power flow density over the surface of the radiation sphere is calculated. Radiation patterns are then displayed in dB relative to the "isotropic level" field strength[1]. This is defined as the field strength, in one polarization, radiated uniformly over the entire radiation sphere, that would radiate the same power as the original antenna.

Fig. 8.6 compares the principal plane patterns of the handset alone, solid curves, to those of the handset and phantom head, dashed curves. In the azimuth pattern, part (a), the  $E_\theta$  polarization for the handset alone has a broad maximum of -2.1 dB at zero degrees, and shallow minima of -11.0 dB at 120 and 260 degrees. With the head the pattern is roughly similar. The broad maximum at zero degrees is lower in level, with the largest field strength at -3.8 dB. The minima are at about the same angular locations, but are deeper, with the minimum field strength at -15.5 dB.

In  $E_\phi$ , the handset alone pattern has two large lobes of field strength about 3.5 dB at 70 and 310 degrees, and minor lobes of about -8 dB at 153 and 228 degrees. There are four very deep, sharp minima in the pattern with the field strength falling to -39 dB. With the head, the pattern is roughly similar. There is a lobe of field strength 4.2 dB at 303 degrees similar to the handset-alone lobe at 310 degrees. There is a lobe at 71 degrees, but the field is much lower at -1 dB than for the handset alone. The field strength in the region of the minor lobes rises to about -2 dB. There are only two sharp, deep minima in the pattern of the handset and head.

Fig. 8.6(b) shows the elevation pattern for  $\phi=0$  degrees. In  $E_\theta$ , the pattern for the handset alone and the handset with the head are very similar. Both have major lobes near 50 and 170 degrees. Both have two minor lobes. The field strength is generally comparable between the two patterns. In  $E_\phi$ , with no head the pattern is roughly circular with a maximum level of about -2 dB. But with the head the field strength is generally much lower, with a maximum of -8.5 dB. The pattern has a broad main lobe centered at about  $\theta=106$  degrees, and a minor lobe centered at  $\theta=287$  degrees (that is, for  $\phi=180$  degrees and  $\theta=73$  degrees). The minima separating these lobes are quite deep.

Fig. 8.6(c) shows the elevation pattern for  $\phi=90$  degrees. In  $E_\theta$ , the pattern with no head is quite different from the pattern with a head. With no head there are two broad lobes, at 88 and 223 degrees. The maximum field strength is -5.7 dB. The lobes are separated by broad minima, with a minimum field strength of -32 dB. With the head, there are three lobes. The largest has maximum field 0.3 dB at 128 degrees. There is a lobe at -2.3 dB, 337 degrees, and a narrower lobe at -4.8 dB, 73 degrees. The deepest minimum is -22.3 dB. In  $E_\phi$  the patterns are quite similar. For the handset alone, there is a very broad lobe of maximum 3.3 dB centered at 149 degrees. The pattern has one broad minimum, of field -19.4 dB at 328 degrees. For the handset and head, this minimum becomes deeper at -34.8 dB, and quite sharp, centered at 8 degrees. The broad lobe is less smooth. The maximum field strength is slightly less, 2.6 dB at 151 degrees.

Fig. 8.6 has compared the fields of the handset alone, held with the antenna oriented in the direction  $\theta=64.42$  degrees,  $\phi=191.10$  degrees, to the patterns of the handset and head. In many cases the patterns are quite similar and the head changes the details but not the general character of the radiation pattern.  $E_\theta$  in the azimuth plane is not greatly changed.  $E_\phi$  drops in level but is similar in shape.  $E_\theta$  is similar in the  $\phi=0$  elevation pattern, but  $E_\phi$  changes shape and drops in level.  $E_\theta$  is changed considerably in pattern shape and level in the  $\phi=90$  elevation pattern, but  $E_\phi$  is not much changed.

### 8.6 Measured Patterns Compared with the FDTD Computation

The principal plane patterns were measured at CRC[18] by the method described in Ref. [1]. The handset and head were held in the styrofoam jig shown in Figs. 7.4 and 8.1. Figs. 7.4 and 8.7 show the handset, head, and measurement jig atop the rotator column in the anechoic chamber. In Fig. 7.4 the head is oriented vertically so that the azimuth plane pattern can be measured. In Fig. 8.7(a) the  $\phi=0$  elevation pattern is being measured, and in part (b) the  $\phi=0$  elevation pattern.

To compare the measured principal plane patterns with the computed patterns, the measured data must be scaled to approximately the same level as the computed data. The scaling method was explained in Ref. [1]. The RMS field strength of the fields in the three measured patterns is computed as 0.09487921 V/m. Similarly the RMS field strength of the computed principal plane patterns is 0.6853019 V/m. The measured data is scaled by the ratio of these two RMS fields, 7.2228879. This process compares the computed and measured data approximately on the basis of equal radiated power.

Fig. 8.8 compares the measured and computed radiation patterns. Part (a) shows the azimuth pattern. In  $E_\theta$ , the measured and computed patterns are quite similar, with maxima near 60 degrees, 210 degrees and 300 degrees. The computed pattern has a minimum of -15.5 dB at 265 degrees. The measured data has a sharper, deeper minimum of -37.1 dB at 269 degrees. The patterns are also quite similar, with lobes at 140 degrees and 304 degrees. The computed field strength in these lobes is about 1 dB greater than the measured. In the region from 0 to 120 degrees, the computed  $E_\phi$  pattern has two sharp deep minima, at 33 and 107 degrees. These are separated by a lobe of field strength -0.9 dB at 73 degrees. The measured pattern has only one sharp deep minimum, at 45 degrees. There is a lobe of field -4 dB at 78 degrees. The minimum expected at 107 degrees is a shallow trough in the measured data, of field strength -6.1 dB at 103 degrees.

Fig. 8.8(b) shows the elevation pattern for  $\phi=0$  degrees. In  $E_\theta$ , the measured and computed patterns are again quite similar. Both have lobes near 45 degrees and 170 degrees. The computed field strength is about 1.5 dB greater in these lobes than the measured field strength. Both patterns have a minimum near zero degrees, but the computed data has a much deeper minimum. Both have minima near 125 degrees, but here the measured pattern has the much deeper minimum. The  $E_\phi$  patterns are both approximately circular. The computed pattern is rather smoother than the measured pattern, with a computed maximum of -2.1 dB and minimum of -5.9 dB. The measured pattern has a maximum of 0.8 dB and a minimum of -9.3 dB.

Fig. 8.8(c) shows the elevation pattern for  $\phi=90$  degrees. In  $E_\theta$ , the computed and the measured patterns are quite similar. Both have lobes near zero degrees, 80 degrees, and 210 degrees. Both have minima near 110 and 270 degrees, though the measured minima are considerably deeper than in the computation. In  $E_\phi$ , the minimum near zero degrees differs between the measurement and the computation. In the computed pattern there is a minimum of -34.8 dB at 8 degrees, whereas the measurement has a much shallower minimum of -18.5 dB at 18 degrees.

## 8.7 Conclusion

The comparison of the measured and computed radiation patterns in Fig. 8.7 invites further analysis. When compared to comparisons in the literature such as Ref. [30], our results include both polarizations and show good correspondence of the main features of the computed and measured patterns. The good agreement achieved between the computation and the measurement for the tilted handset in Fig. 6.9 is not seen in Fig. 8.7. The agreement is not of the quality achieved for the handset and box and sphere head in Ref. [1]. It is clear that the general nature of the changes introduced by the head into the handset is similar for the computations and for the measurements. But the detailed, point-by-point agreement is less good than we would like. The obvious shift of the minima signals a need for careful scrutiny of the factors that might produce it.

The cause of such differences is usually associated with geometric errors in the cell model compared to the physical structure being measured. The geometrical differences between the computation and the measurement should be explored.

In the present case the styrofoam blocks and fiberglass bolts of the measurement jig have been omitted from the computer model. Experiments without and with fiberglass bolts for the box head in Ref. [1] suggest that their effect would be minor and so they are not likely the cause of the disagreement in Fig. 8.7. It might be of interest to embed the entire handset and head system in styrofoam as a medium, to look for gross changes in the patterns due to the presence of styrofoam. If significant changes are seen, then a more realistic representation of the styrofoam geometry could be developed. But the good agreement between the measured and computed patterns of the handset alone in Fig. 6.9 suggest that the styrofoam and the fiberglass bolts mainly affect the minima in the radiation patterns and are not the primary causes of the differences in Fig. 8.7.

The most obvious source of geometric differences between the measurement setup and the computer model would be the positioning of the handset relative to the phantom head. The tilt angles of the handset are most likely to be correct because they are identical to those used for Fig. 6.9, which leads to good agreement. There may be a translation error in the position of the handset relative to the phantom head. Thus the handset may be too close or too far, or too high or low. Considerable care has been taken in reading the CRC drawings[24] and incorporating the location of the handset relative to the head into the cell model. Nevertheless, the first step in trying to improve the agreement would be to verify the handset position.

Care has been taken to ensure that the internal structure of the phantom head cell model is a good representation of the real phantom head, as described in Chapter 7. It is possible that the electrical parameters reported by the manufacturer for the materials are somewhat in error. Some numerical experiments with close by values might be of interest.



Comparing the photos of the phantom head, such as Fig. 8.1, to the cell model shows that the neck support column in the cell model is in the wrong shape. The CT scan cross-sections did not extend to the bottom of the neck; nor did they include the support column. Thus in the cell model the neck has been terminated quite squarely, unlike the real phantom, and a simple approximate shape used for the support column. Improving these details is not likely to have a major effect on the computed patterns, however.

It would be of interest to use the computer model to explore the changes in the handset and head patterns that are due to the wood base of the phantom head. Since the wood base is such a large structure, it is possible that the electrical parameters of wood could significantly change the overall radiation patterns. Also, the permittivity and conductivity of the wood were taken from the literature rather than measured. Some exploratory calculations with different but plausible values of the electrical parameters of wood might be of interest. Also, the gross effect of the base could be judged by removing it from the FDTD cell model and repeating the computation.

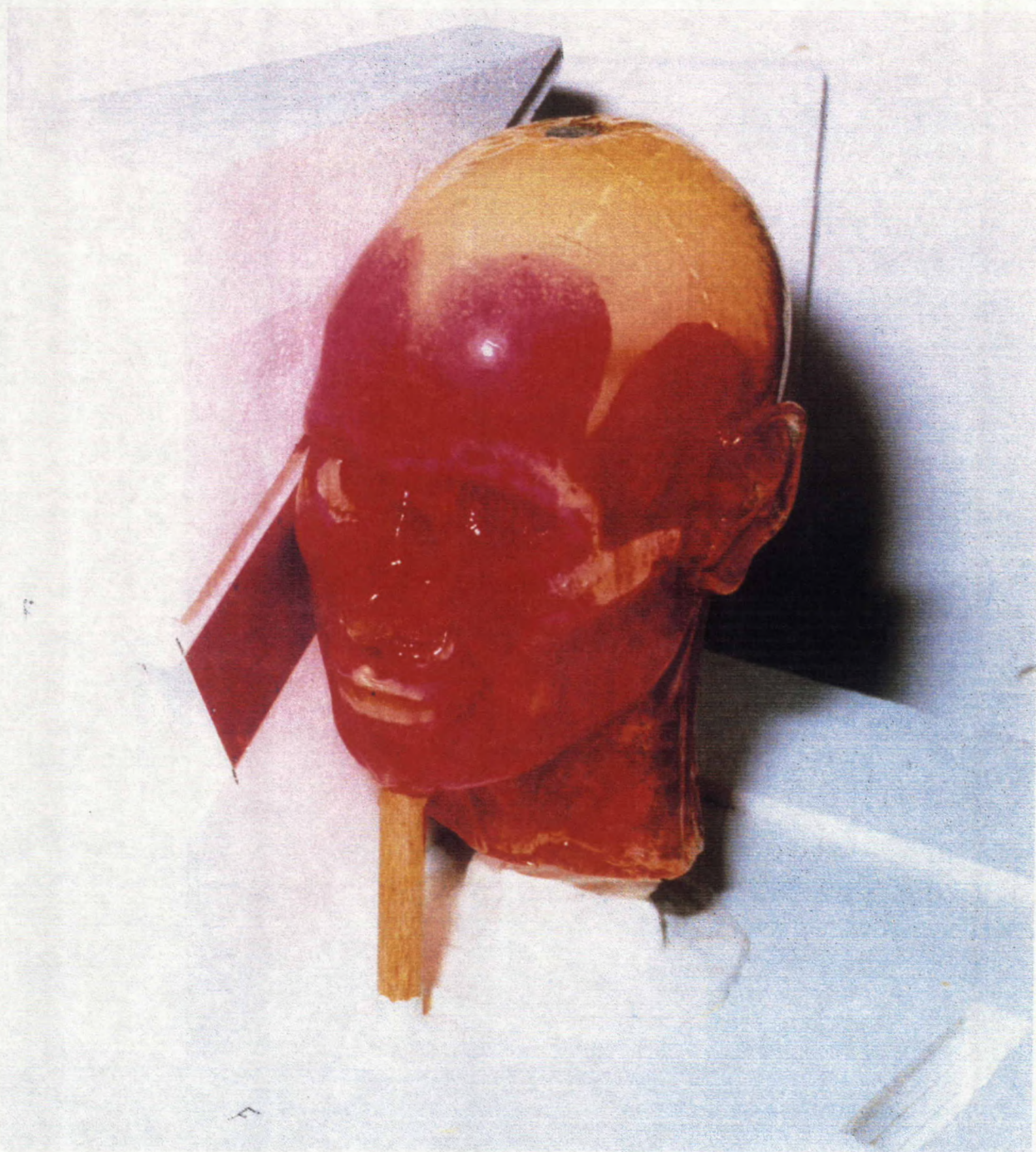


Fig. 8.1 The handset and the phantom head in the partially-assembled mounting jig.





YZ Plane # 170

- # 0 ☐ Free Space
- # 1 ☐ PEC
- # 2 ☐ Muscle
- # 3 ☐ Skin
- # 4 ☐ Bone
- # 5 ☐ Bone
- # 6 ☐ Wood
- # 7 ☐ Fiberglass
- # 8 ☐ Plexiglas

Change to # 0  
 Fill Box  
 Report Position  
 Next Section  
 Previous Section  
 Get the Main Menu

Fig. 8.2 A yz plane cut through the handset and phantom head, when the head is tilted relative to the handset.



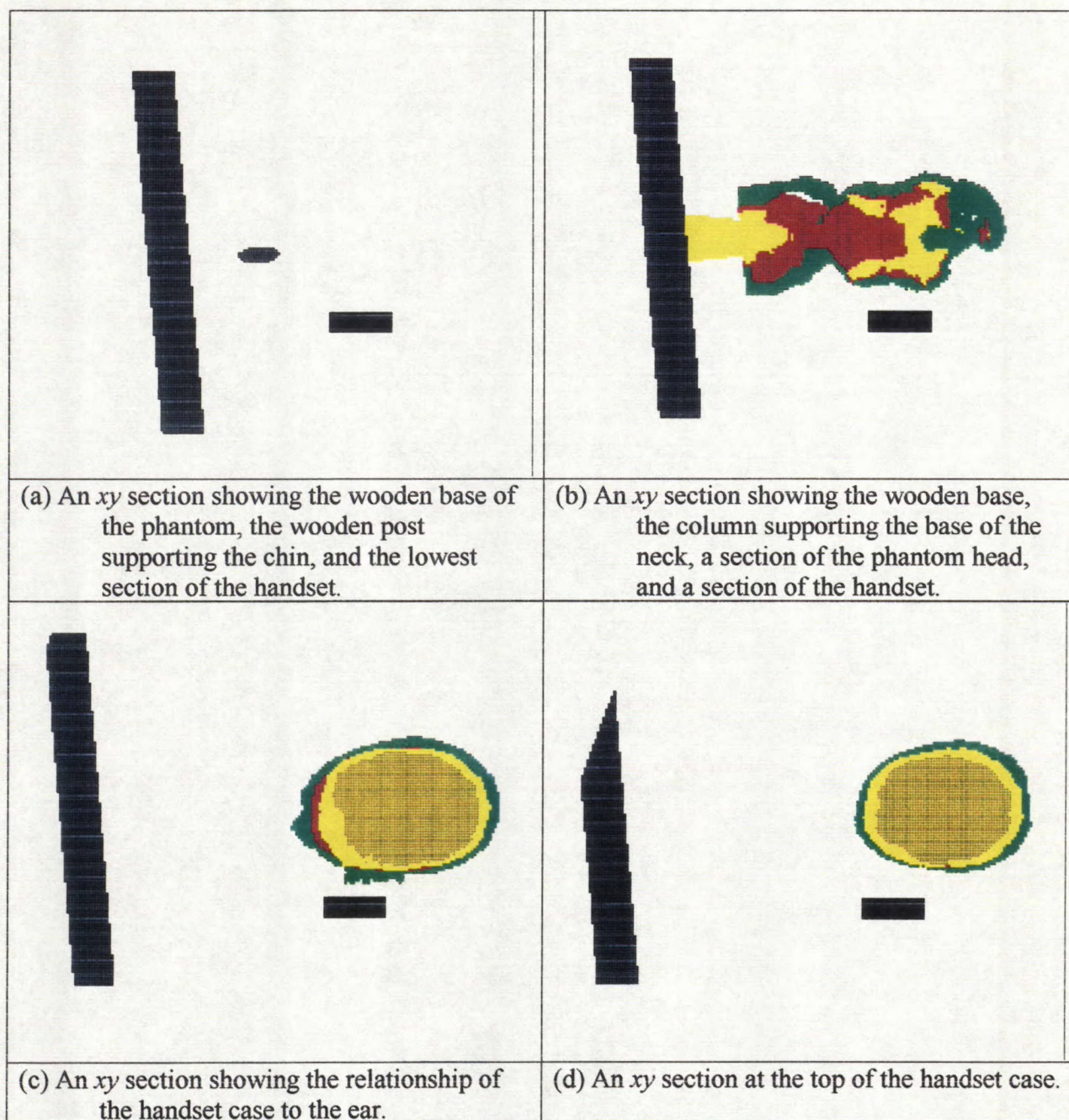


Fig. 8.3 Sections of the handset and phantom head model.



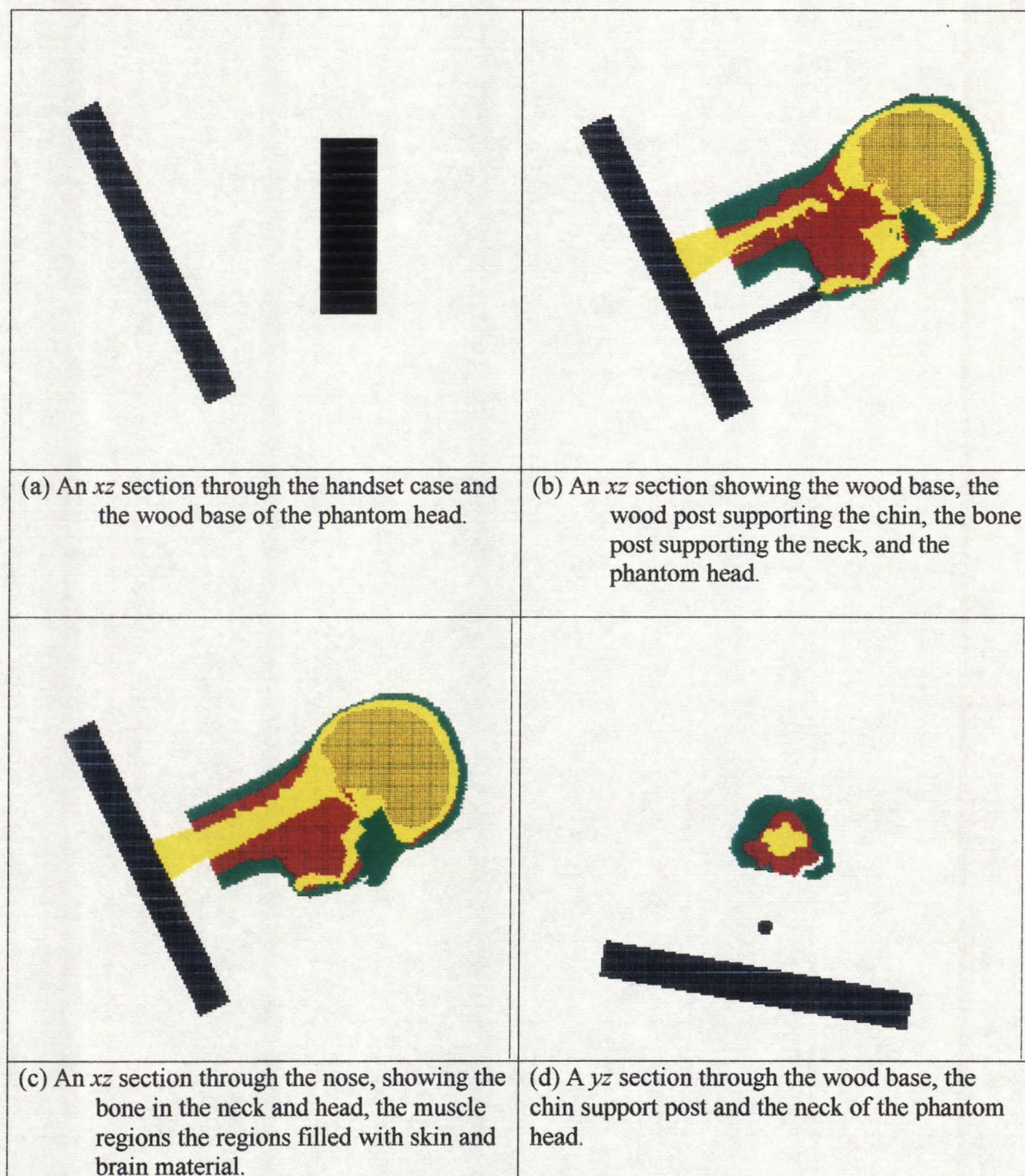


Fig. 8.4 Sections of the handset and phantom head model.



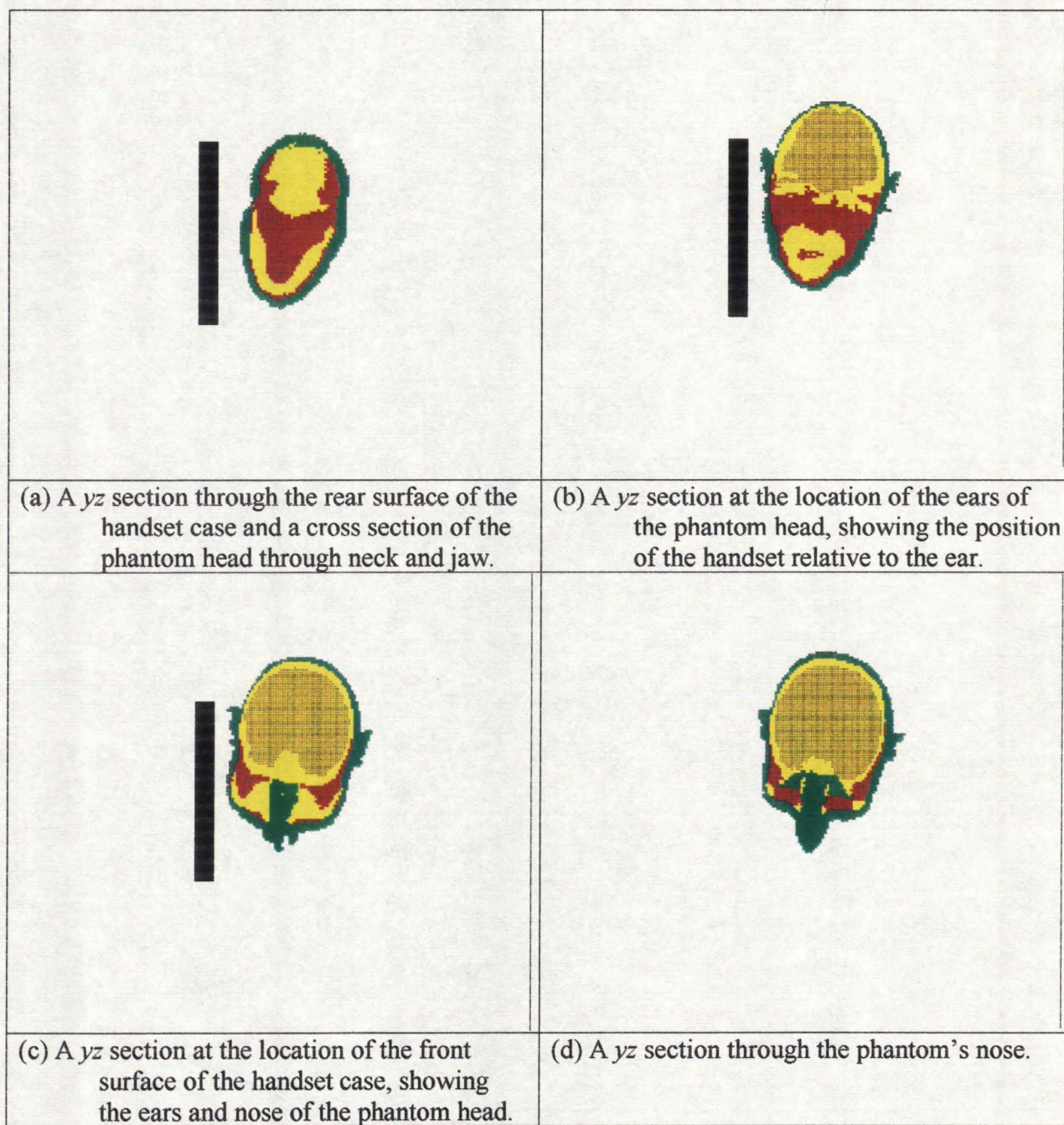


Fig. 8.5 Sections of the handset and phantom head model.



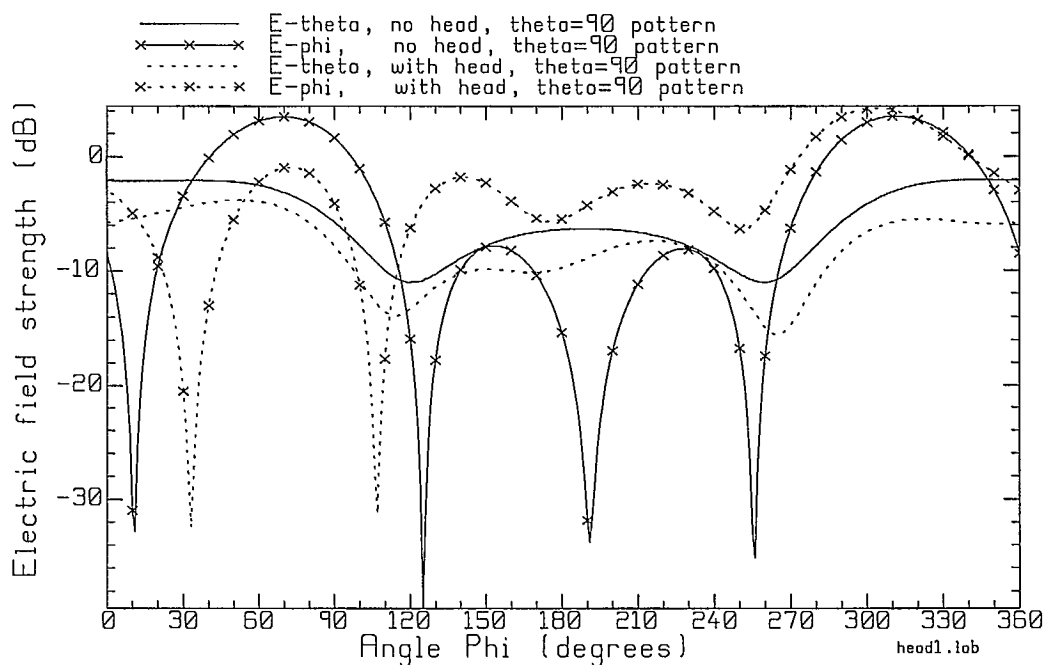
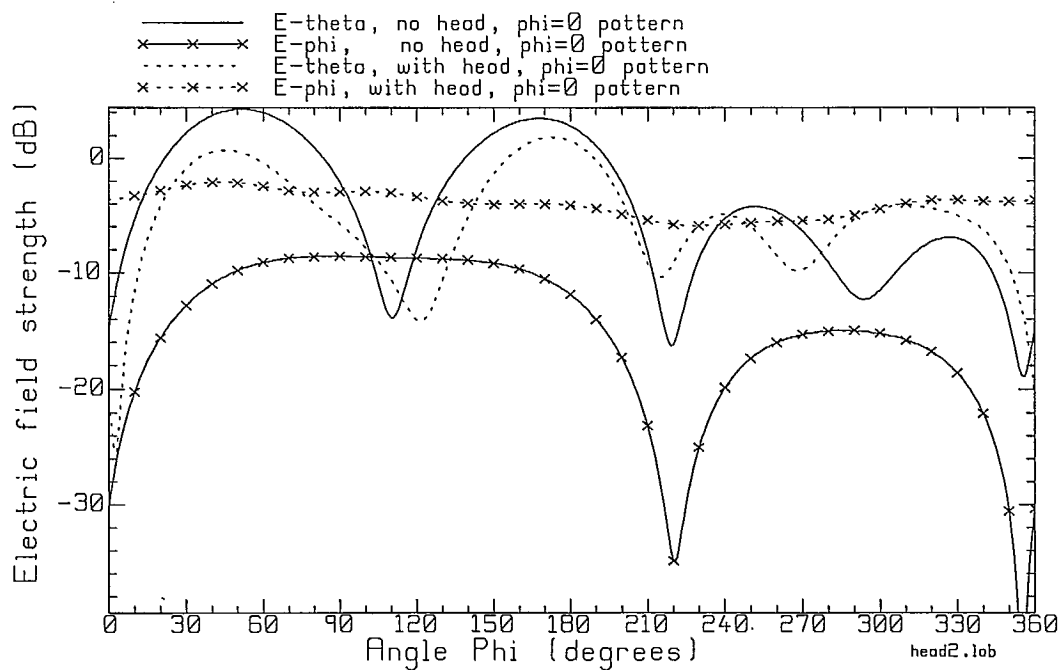


Fig. 8.6(a) Azimuth pattern, handset alone vs. handset and head.

Fig. 8.6(b) Elevation pattern for  $\phi=0$  degrees, handset alone vs. handset and head.

## Handset Radiation Patterns

No head/with head

Azimuth Pattern

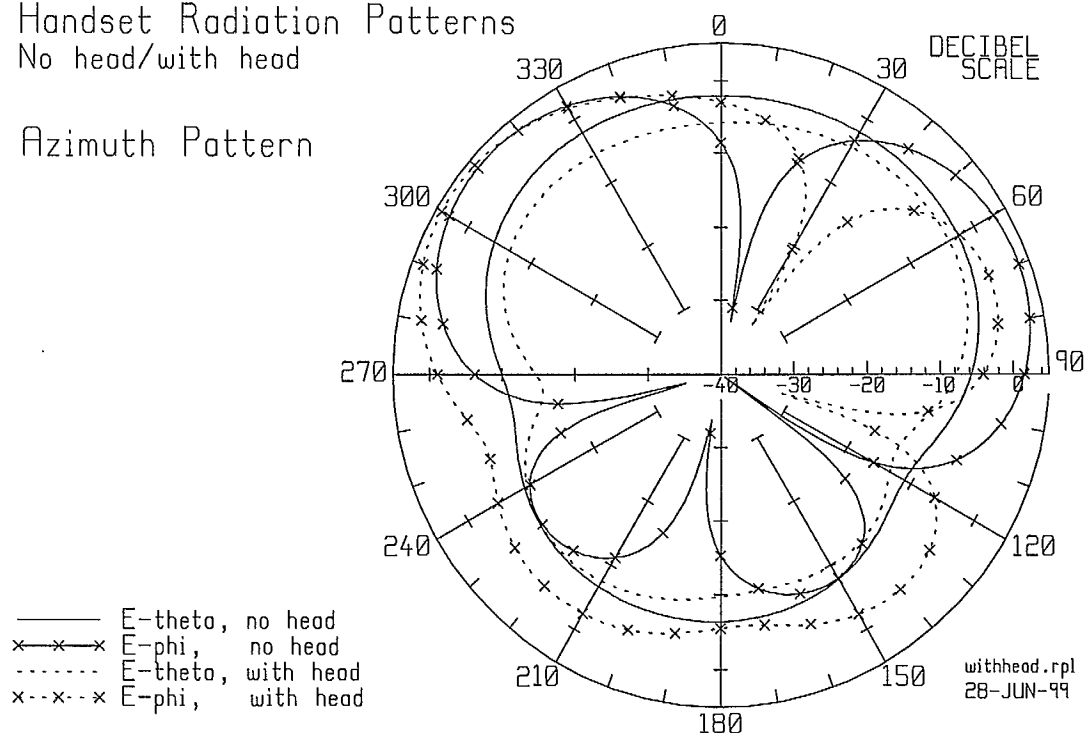
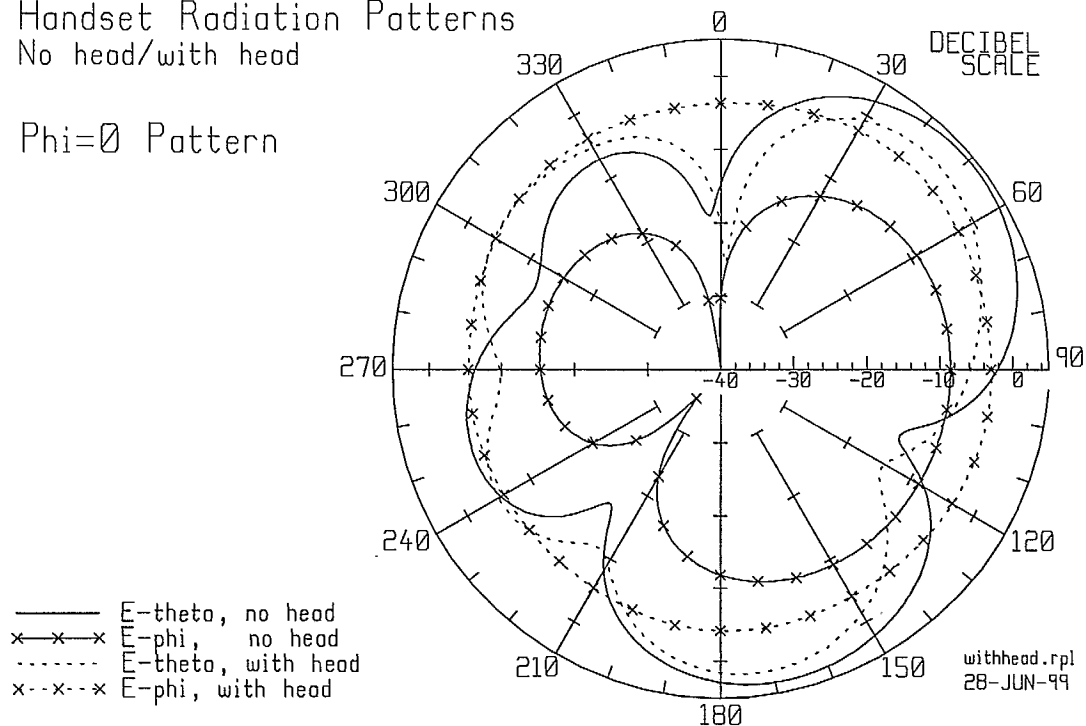


Fig. 8.6(a) Azimuth Pattern

## Handset Radiation Patterns

No head/with head

 $\Phi=0$  PatternFig 8.6(b)  $\phi=0$  elevation pattern.

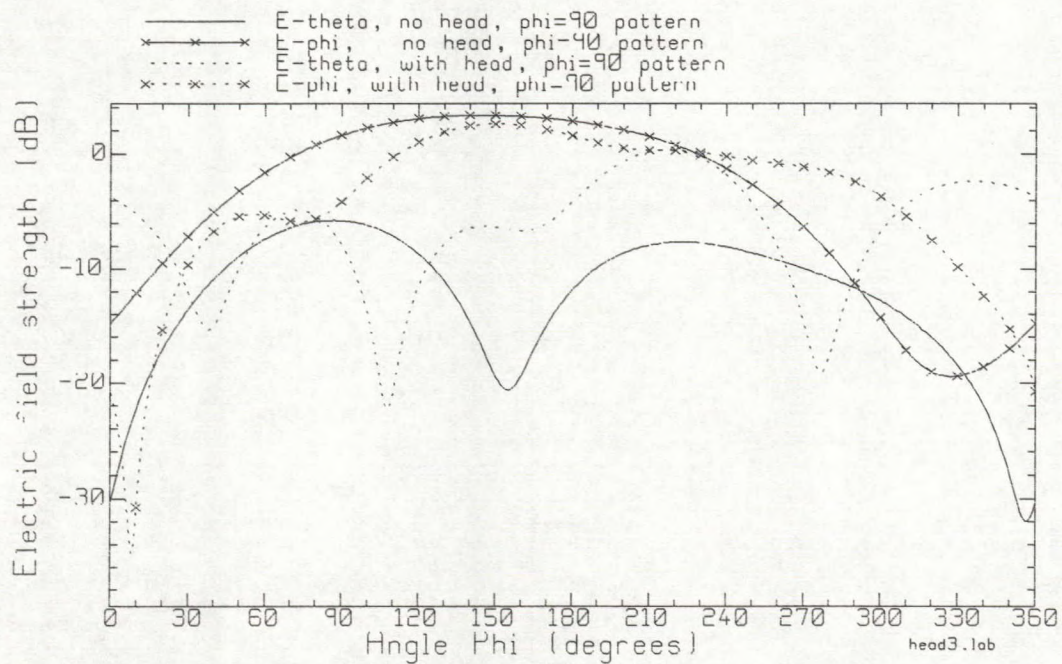


Fig. 8.6(c) Elevation pattern for  $\phi=90$  degrees, handset alone vs. handset and head.

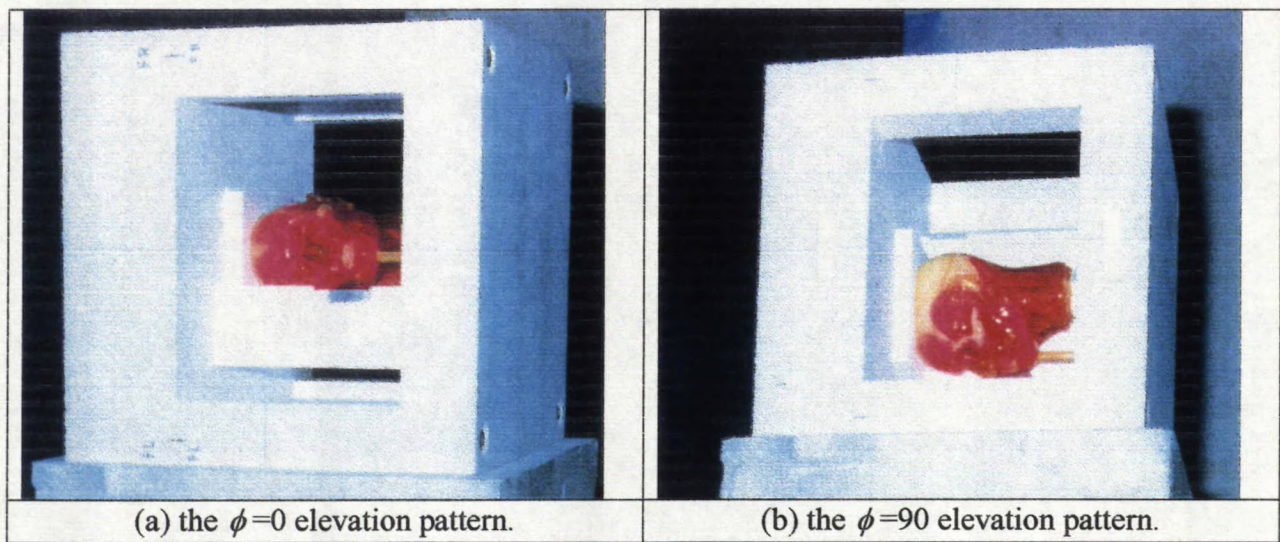


Fig. 8.7 The handset, head and mounting atop the rotator column for measurement of two of the principal plane patterns.



# Handset Radiation Patterns

No head/with head

Phi=90 Pattern

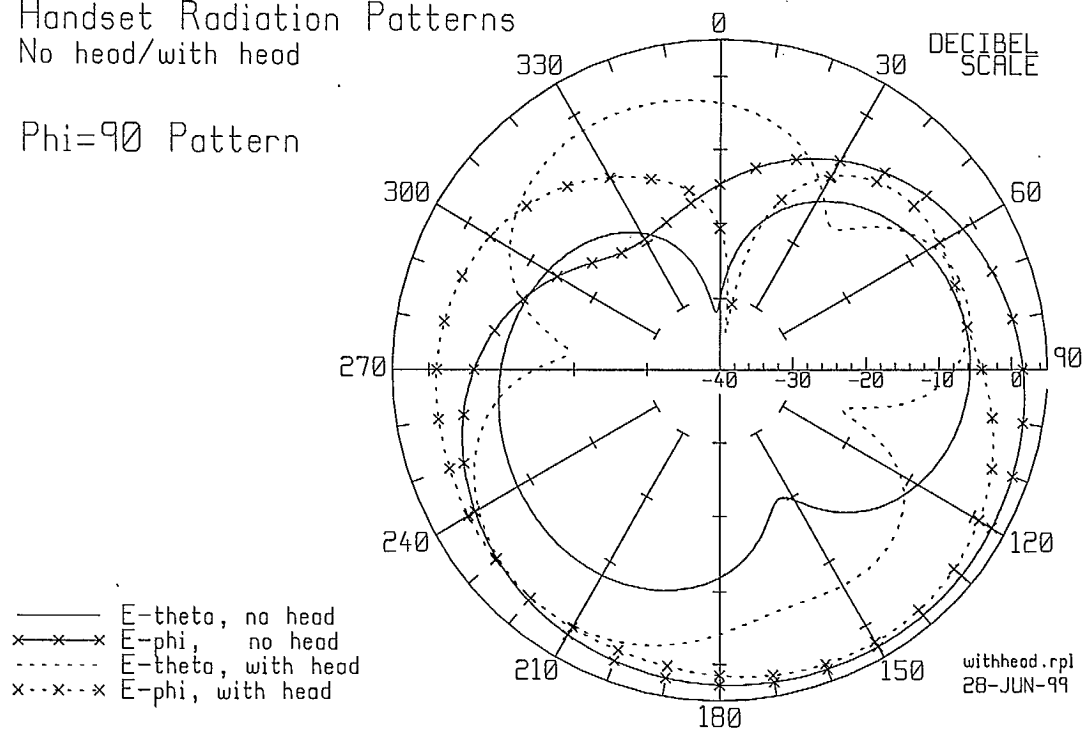


Fig 8.6(c)  $\phi=90$  elevation pattern.

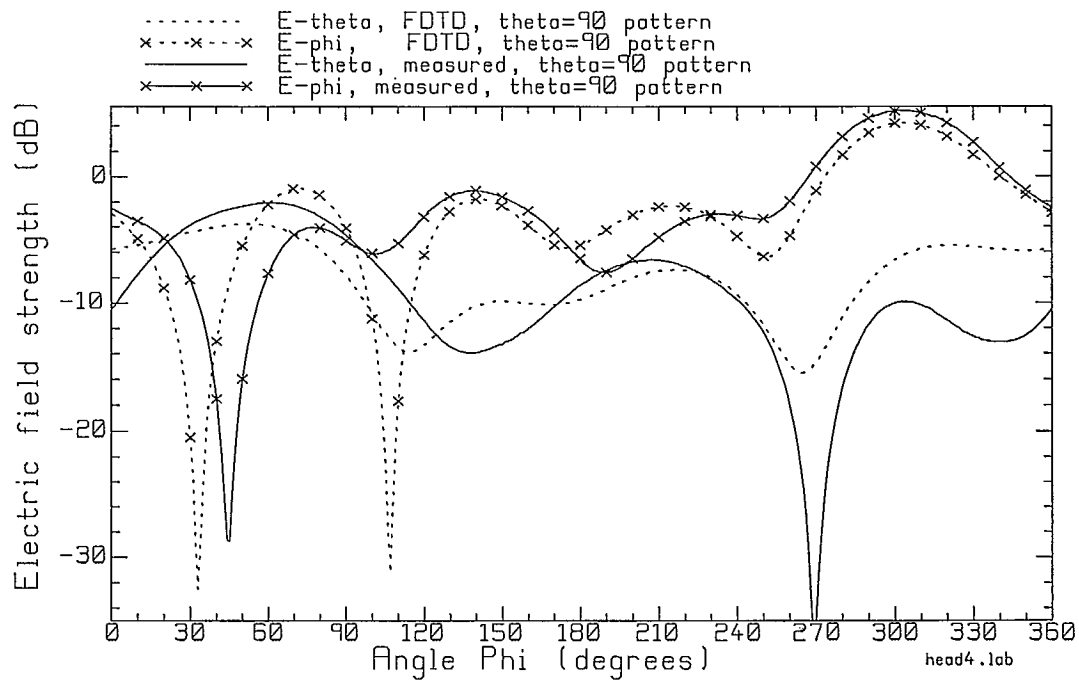
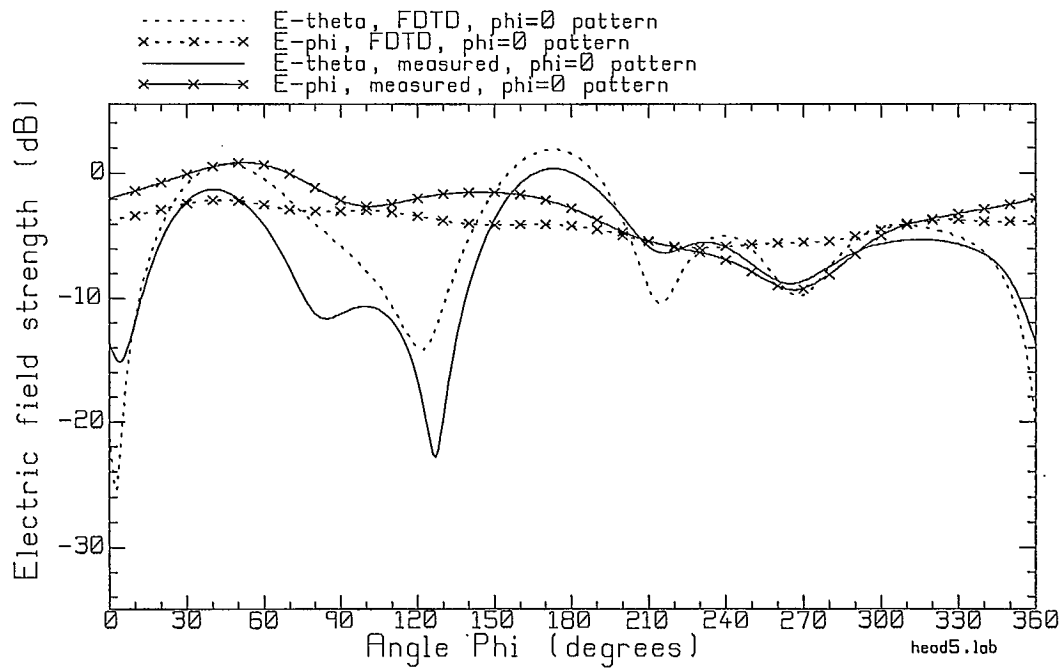


Fig. 8.8 (a) The azimuth pattern of the handset and phantom head.

Fig. 8.8 (b) The  $\phi=0$  elevation pattern of the handset and phantom head.

Handset Radiation Patterns  
Computed vs. Measured

Azimuth Pattern

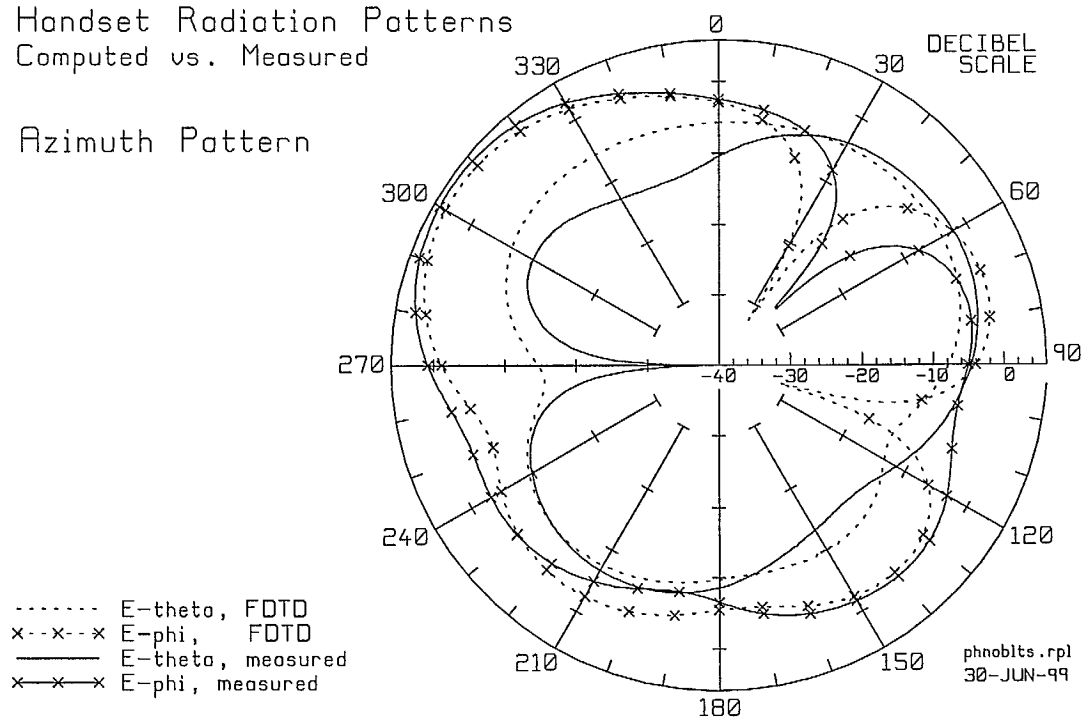


Fig. 8.8(a) Azimuth Pattern

Handset Radiation Patterns  
Computed vs. Measured

Phi=0 Pattern

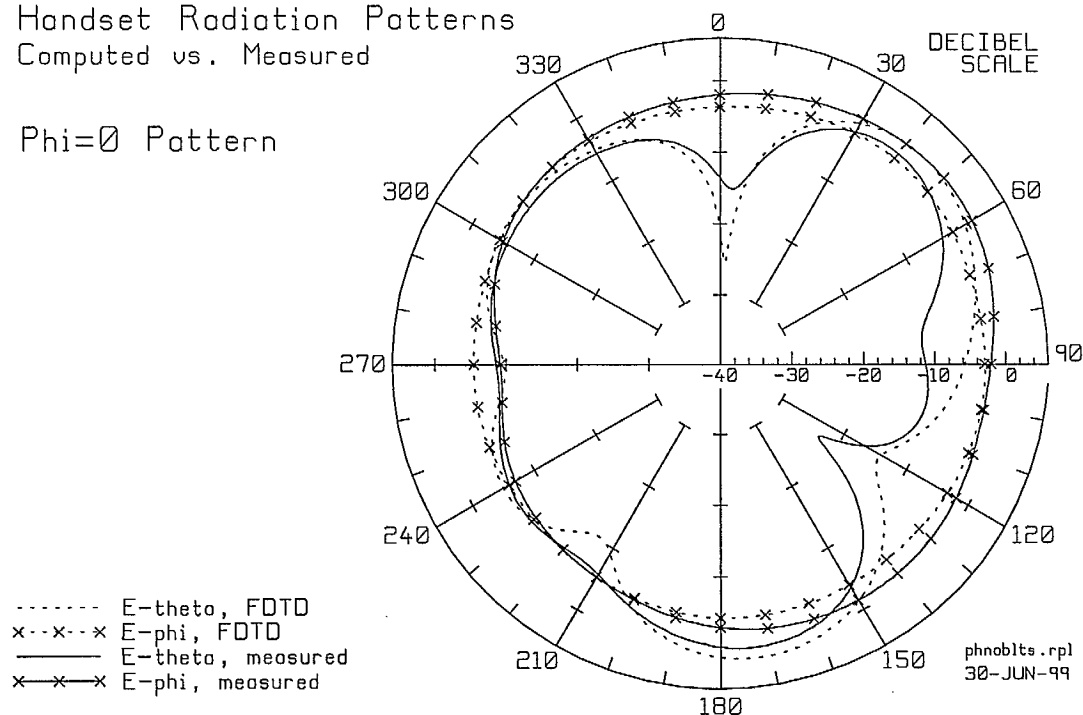


Fig 8.8(b)  $\phi=0$  elevation pattern.



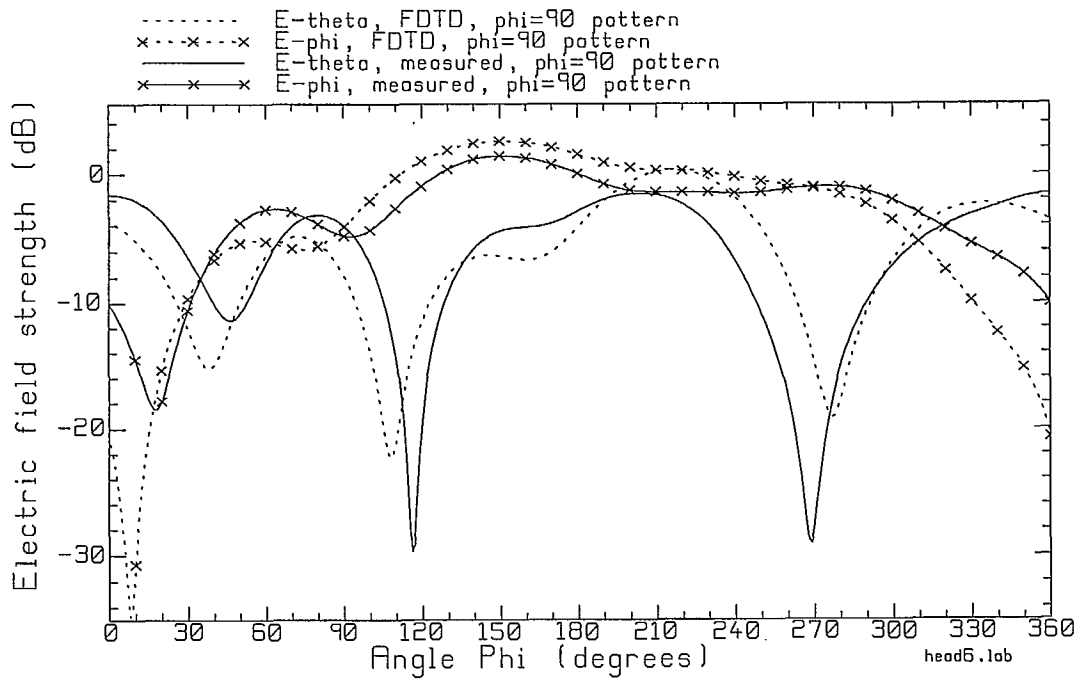


Fig. 8.8 (c) The  $\phi=90$  elevation pattern of the handset and phantom head.

# Handset Radiation Patterns Computed vs. Measured

Phi=90 Pattern

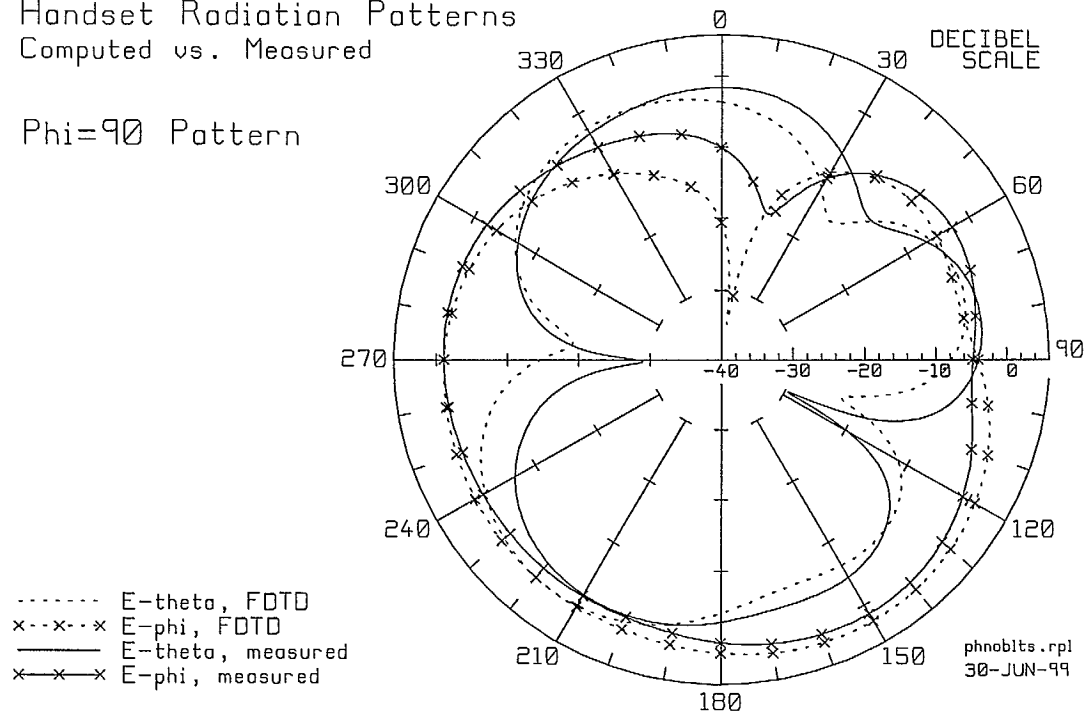


Fig 8.8(c)  $\phi=90$  elevation pattern.

## Chapter 9

### Conclusions and Recommendations

This chapter summarizes the work presented in this report in relation to previous work, and makes recommendations for further work.

#### 9.1 Conclusions and Comparisons with Previous Results

This section compares previous work in this project to the results presented in this report.

##### 9.1.1 Near Field Measurements and Computations

Chapters 2, 3 and 4 of this report presented computations and measurements of the near fields of the handset and the simple head models.

##### 9.1.1.1 The Measurement System

Previous measurements of the near fields and comparisons with computations were reported in Ref. [3]. The measurement system used a cable entering the handset at the bottom to power the handset's monopole antenna. The vertical component of the field was measured using a probe intended for wideband EMC measurements, that averaged the field over a significant volume of space. Each measurements were done over a region roughly 50 by 50 cm. For the handset alone, the field was measured in  $xz$  and  $yz$  planes adjacent to the handset. For the handset and head models, the field was measured in  $xz$  planes adjacent to the handset, in  $yz$  planes in front of the head, and in  $xz$  planes on the opposite side of the head from the handset.

In the present work, the measurement setup has been improved as follows. The feed cable has been eliminated by using a battery-operated oscillator inside the handset. The field is measured with a probe intended for near field measurement, consisting of short dipole antennas. The dipoles average the field over a much smaller region of space than in the previous work. The probe measures all three components of the field,  $E_x$ ,  $E_y$  and the vertical component,  $E_z$ . However, the life of the battery limits the measurement region to an area of approximately 15 by 30 cm, much smaller than in the previous measurement. In the present work only  $xz$  planes adjacent to the handset have been measured.

##### 9.1.1.2 The FDTD Computation

The computation in Ref. [3] was flawed in two ways. The cell size was too large to respect the tenth-wavelength size limit at 850 MHz in the dielectric materials. The handset and head models were permitted to be too close to the Liao 2<sup>nd</sup> order absorbing boundary, which can reduce the accuracy due to reflections from the boundary. In the present work 2.205 mm cells have been used, generously satisfying the tenth-wavelength



rule. The perfectly-matched layer absorbing boundary has been used, and the handset and head model have been kept farther from the absorbing boundary than in Ref. [3].

### 9.1.1.3 The Scaling Method

To prepare comparisons between the measured and computed near field maps, Ref. [3] computed the RMS field strength over an area centered on the antenna. This “area normalization” scheme tends to align the measured and computed contours of large field strength in the region of the antenna and the top of the handset case. This is inherently flawed in that the EMC probe used in Ref. [3] smoothes out the large peaks in the field found particularly at the tip of the antenna for the vertical component. The RMS field as a measure tends to emphasize large field strengths unduly because it is an integral of the square of the field strength. “Area normalization” tends to align the measured and computed field contours where the field is large in value, at the expense of the alignment in regions of small field. The field is large near the antenna and the top of the case so area normalization makes the agreement look better in these regions. But then the agreement towards the edges of the contour map will be poor. This tended to compensate for the averaging effect of the EMC probe to a certain extent.

Ref. [3] recognized that there was a problem but did not fully explain it. Fig. 2.18 of Ref. [3] plots the field as a function of distance  $x$  through the top of the handset case. The scaling process for the measured data has shifted the measured curve upwards so that it agrees with the computed curve on the shoulders of the peak. Then at the peak the computed field is clearly stronger than the measured field, because the EMC probe has smoothed out the peak. But at the edges of the graph, for  $x$  near  $-25$  and near  $+20$ , the measured data is considerably larger than the computed data.

In the present report the “area normalization” method has been replaced with “tie line normalization”. In this method, the measured and computed data are aligned as well as possible at the left hand edge of the field map, as far as possible from the regions of high field strength. Then the data is permitted to fall where it may in the regions of high field strength. Fig. 9.1 compares the measured and computed fields in a format similar to [3] Fig. 2.18. Fig. 9.1 plots the vertical component of the field strength for the handset alone at  $y=-21.8$  mm as a function of distance  $x$ , for heights of  $z=0$ , at the base of the antenna, and  $z=8.82$  cm, through the tip of the antenna. In Fig. 9.1, at the base of the antenna the measured and computed curves align almost perfectly right across the graph. Both at the edges of the graph, where the field is less than 35 dB, and in the center of the graph, where the field is more than 45 dB, there is excellent agreement. Through the tip of the antenna, the curves agree somewhat less well. In this case the computed field is uniformly below the measured field across the whole width of the graph.

For data sets in perfect agreement, it would not matter whether area normalization or tie line normalization were used. For data sets with imperfect agreement, the tie line method encourages a more objective assessment of the agreement.

### 9.1.1.4 Format For Comparing the Measurements and The Computations

In Ref. [3], Fig. 2.8 compares the measured and the computed contour maps of the vertical component of the field at 17 mm from the handset surface. The format used is to plot the measured contour map at the top of the page and the computed contour map at

the bottom. The reader must compare the values and locations of contours by switching back and forth between the two maps. In the present report, the software was advanced to permit the graphing of the two contour maps on the same axes, as in Fig. 2.13. The measured contours are drawn in black, and the computed contours in gray, or in green on a color monitor or color printer. This encourages a much more quantitative and precise comparison of the position of the contours between the measurement and the computation.

#### 9.1.1.5 Improvement in the Agreement

Is the agreement between the measured and computed data in Ref. [3] poorer than that in the present work? Fig. 9.1 compares the measured and computed vertical component for two "cuts" across the field map of Fig. 2.13(c), through the base of the antenna and through the tip of the antenna. The agreement is clearly superior to that in Fig. 2.18 of Ref. [3].

Consider Ref. [3] Fig. 2.8, which compares  $E_z$  at 17 mm from the handset surface, compared to Fig. 2.13(c), for 21.8 mm from the antenna or 13.1 mm from the case. The area normalization method used for [3] Fig. 2.8 aligns the contours where the field well in regions where the field is 3 to 5 dB below the peak value. Thus right at the tip of the antenna the computed field has a -18 dB contour not seen in the measured data, and a -21 dB contour surrounds the tip, also not seen in the measurement. But the -24 and -27 dB contours are very similar between the measurement and the computation. This clearly shows that the averaging effect of the EMC probe used in Ref. [3] is spoiling the agreement of the fields near the tip of the antenna. Near the top of the handset case, the measured data has a -18 dB contour. The computed data has a -18 dB contour enclosing a much larger area, suggesting the field attains higher values near the top of the case. This is seen in [3] Fig. 2.18. Thus the main flaw of the measurement in Ref. [3] is the tendency of the EMC probe to smooth the peaks in the field.

The agreement in Fig. 2.13(c) between the measured and computed contours at the tip of the antenna and the top of the case is much, much better than in Ref. [3].

The contours to the left of the top of the handset case in [3] Fig. 2.8 agree poorly between the measurement and the computation. The -30 dB contour in the region of the feed cable to the bottom left of the handset case in [3] Fig. 2.8 is quite different between the measurement and the computation.

It is interesting to note that the field contours over the surface of the case in [3] Fig. 2.8 agree very well between the measurement and the computation. Both show contours of -36 dB field strength and in approximately the same position. The probe used in this report has problems close to the handset surface at least for the vertical component. Thus in Fig. 2.13(c) the minimum measured contour is 27 dB and corresponds poorly to the computed 27 dB contour. The computation has a 24 dB contour not seen in the measured data.

Consider Ref. [3] Fig. 3.19, which shows measured and computed contour maps for the handset and the box head. The differences between the measured and computed contours near the antenna tip and the top of the handset clearly show the averaging effect of the EMC probe. Fig. 3.6(c) of this report shows much better agreement in these regions. Fig. 3.19 of Ref. [3] clearly shows distorted field contours in the region of the

feed cable, to the left of the bottom of the handset case. The agreement is spoiled. Fig. 3.6(c) shows quite good agreement in this region, though it would be more satisfying to have measured data over a much larger area.

Similarly, for the handset and sphere, [3] Fig. 4.19 shows the vertical component at 17.5 mm from the handset case. Again the agreement of the field near the tip of the antenna is poor. The contours in the measured data are clearly distorted to the left of the bottom of the handset case, due to the feed cable. The agreement in Fig. 4.6 is much superior, both at the tip of the antenna, at the top of the case and to the left of the base of the case.

### 9.1.2 Far Field Measurements and Computations

This section comments on the far field measurements and computations in this and previous years of the project.

#### 9.1.2.1 Vertical Handset

This report contains the measured and computed far fields of the vertical handset in isolation, but did not repeat the measurement or computation for the box head or sphere head with the vertical handset. Fig. 3.9 in Ref. [1] compares the measured and computed fields of the handset with 2.205 mm cells. In the present work the measurement was repeated, to obtain the fields in Fig. 5.2. We can note that the computation was also repeated, and we are not simply re-graphing the same data file as in [1]. Comparing [1] Fig. 3.9 with Fig. 5.2 shows that the process used to scale the measured data puts the measured slightly below the computed curve in Ref. [1], and further below in Fig. 5.2. Recall that the normalization process uses both polarizations in all three principal plane patterns, so changes in the measured field in all three patterns can effect the position of the  $E_\phi$  curve in the azimuth pattern. In the  $E_\phi$  polarization, the measured data in [1] deviates further from the computation near 60 degrees than in Fig. 5.2(a). The "new" measured curve is similar to the old between 90 and 180 degrees, and between 300 and 360 degrees. These features of the measured curve appear to reflect some real feature of the measurement setup. The holes for the switch and LED in the handset case may be associated with this problem, or the presence of styrofoam at the base of the handset, or some other geometric difference between the measurement and the computation.

Comparing the elevation patterns for  $\phi = 0$  degrees in [3] Fig. 3.9(b) and Fig. 5.2 (b) shows that the agreement between the  $E_\theta$  measured and computed curves is not much changed in the minima near 60 and 290 degrees. The shape of the  $E_\phi$  curve is quite different, suggesting that this curve is much more sensitive than  $E_\theta$  to small changes in the measurement setup. Once again, differences such as the presence of styrofoam below the broad face of the case, the holes for the switch and the LED, and the straightness of the wire antenna may significantly affect this curve.

Comparing the elevation patterns for  $\phi = 90$  degrees in [3] Fig. 3.9(c) and Fig. 5.2 (c) shows similar differences between the measured and computed  $E_\theta$  fields in the



minima near 60 and 300 degrees. The  $E_{\phi}$  measured curve in [3] and in Fig. 5.2(c) are different in detail, with better agreement in the present measurement.

### 9.1.2.2 Handset at a Realistic Angle

This report has presented a comparison of the measured and computed principal plane patterns for the handset held at a realistic angle for actual use, both without and with the phantom head. With no head, the handset patterns were measured in the jig that holds the handset and head, including the four fiberglass bolts. The agreement with the computed patterns is quite good. The computation of the patterns of the tilted handset with the phantom head that is reported in Chapter 8 is regarded as preliminary. The agreement between the measurement and the computation is not as good as is desired. Time did not permit any verification of the relative position of the handset to the phantom head beyond that done in the initial effort to set up the model. Thus we are reasonably sure that the tilt angles of the handset are correct but less certain that the handset is positioned correctly relative to the head in a translational sense. It may be too close, or too high, for example. This needs to be carefully verified with a second look at the drawings and their coding into a cell model, to increase our confidence in the computation.

## 9.2 Recommendations for Further Work

This section makes some recommendations for further work in this project. Suggestions will be made for the continuation and completion of the on-going near and far field measurement portions, and then for some new directions in the project.

### 9.2.1 Near Fields

The extent of the area over which near field data was measured was limited in the present work by the battery life of the handset. The measured maps do not include the whole area near the box head or the sphere head. It might be possible to measure over a wider region by scanning the probe over the lower half, then recharging the battery and scanning the probe over the upper half. This is much more inconvenient of course. The two measurements would need to be compensated separately for battery life, and then assembled into a single data set. Care would be required to align the two data sets. Difficulties might be had with repositioning the handset precisely after charging the battery.

#### 9.2.1.1 Contour Maps In Front of and on the Far Side of the Head

Ref. [3] contained measured maps for the field in front of the face, for instance in Fig. 4.21 for the handset and sphere head. This data contains an interesting trough in the field near the surface of the sphere. The agreement between the computation and the measurement in Fig. 4.21 is very approximate. It would be of considerable interest to repeat this measurement. Fig. 4.23 of Ref. [3] shows the field on the opposite side of the sphere head to the handset. Here the measurements and computations show very poor agreement. This is a more difficult problem from the computational point of view. There are two mechanisms for the propagation to the far side of the sphere. The field can travel

through the sphere. Maps of the computed field strength inside the sphere show that the field attenuates quite rapidly with distance from the surface, due to the conductivity of the brain liquid filling the sphere. Also, the field inside the sphere might be characterized as a standing wave. Propagation directly through the sphere is thus not the principal mechanism. The field can propagate around the surface of the sphere as a creeping wave, and maps of the field suggest this is the primary means of propagation. The field on the far side is thus formed by the wave that arrives "clockwise" from the antenna and that arriving "counterclockwise". These give rise to an interference pattern. This is suggested in Fig. 4.23 of [3] by the deep minimum seen in the field on the far side of the sphere in the both the measurement and the computation. But the measured and computed field contours agree poorly in Fig. 4.23.

It would be of interest to repeat the measurement of the field on the far side of the box head and sphere head, to provide reference data for evaluating the computed field.

#### 9.2.1.2 Near Fields with the Phantom Head

It is straightforward to measure the near fields of the handset and phantom head for the handset oriented vertically near the head. A very simple styrofoam slab with a slot for the base of the handset could be made. The slab would lie on the phantom's wood base against the neck and chin support post posts, and hold the handset at a well known position relative to the phantom head. The measured near field would be of interest adjacent to the handset, in front of the head, and on the opposite side of the head from the handset. This measurement is relatively quick to set up because of the simple nature of the styrofoam holder. It would provide an "easy" geometry to model with FDTD and a significant validation of the cell model of the phantom head.

A more elaborate styrofoam block is required to hold the handset in the "realistic" orientation to the head that was used in Chapter 8. If we are content to rotate the handset about the y axis through 65 degrees, but keep the handset's broad surface parallel to the xz plane, then a relatively simple vertical styrofoam slab could be devised, having a cutout to hold the handset. If we also wish to accommodate the approximately 11 degree rotation of the handset about the z axis, then a styrofoam wedge could be made to hold the vertical slab at 11 degrees to the edge of the wood base. Positioning the handset realistically relative to the head increases the interaction between the handset and head and might lead to more interesting comparisons of the near field.

It has been noted in the literature that the coupling of a handset's fields into the head is greatly increased if the handset is pressed against the ear. It would be of interest to position the handset as close as possible to the head to increase the interaction.

#### 9.2.1.3 Scaling the Computed Near Field

In this report the near fields of the handset alone, the handset and box head, and the handset and sphere head were compared on the basis of equal radiated power. The radiated power is found by determining the far fields over the full radiation sphere, and then integrating the power flow density through the sphere to find the radiated power. The near fields are then scaled to 600 mW of *radiated* power. Since the head models are

lossy and so absorb power, the handset supplies more than 600 mW to the system. This leads to a stronger source field around the handset for the handset and head models than for the handset alone.

An alternative procedure would be to compare the near fields of the handset alone and of the handset and the head models on the basis of equal *input* power. At present, the FDTD code does not permit the computation of the input power to the antenna. There are three methods possible for computing the input power. The first is to improve the fidelity of the generator model in the FDTD code, thus permitting an accurate determination of the antenna impedance, and hence the input power due to a 1 volt generator. The second is to determine the power flowing away from the handset itself by enclosing the handset in a parallelepiped and then integrating the power flow density over the surface of the parallelepiped. The third method is to determine the power absorbed in each cell of the head model, sum up to find the total absorbed power, and then use conservation of power to compute the input power as the dissipated power plus the radiated power. Each method involves some degree of approximation. It is not obvious a priori which would offer the best accuracy. The computation of input power should be implemented in the FDTD code.

## 9.2.2 Far Fields

This section suggests further work on the far field pattern comparison between the computations and the measurements.

### 9.2.2.1 Error Bounds on the Measurements

It is common practice in measurement to include error bounds on measured data. The handset is aligned with the measurement horn to establish the zero degree angular direction. What is the error associated with the alignment? The handset must rotate in a horizontal plane. Is the surface of the handset level within 0.1 degree, or to within one degree? The anechoic chamber is not large enough for the measurement to be truly "far field". The range from the handset to the measurement horn is about 330 cm, whereas the handset size is about 25 cm, and the wavelength is about 35 cm. In Ref. [1], Fig. 3.7 used the wire-grid model to explore the effect of the range to the horn on the elevation pattern for  $\phi = 0$  degrees. It was found that, indeed, the true far field pattern and the "near field" pattern computed at 330 cm agree very well in the maxima. But in the sharp minimum at 60 degrees, a difference of 3.9 dB was found. It is clear that the distance to the horn is sufficient for good accuracy in the maxima of the radiation patterns, but too close for accuracy in the sharp minima. What is the expected error in the maxima? In the minima? Error bounds would help to establish whether the differences between computed and measured patterns are significant or lies within experimental error.

### 9.2.2.2 Differences Between Measurements and Computations

Ref. [1] compared computed and measured principal plane patterns for the vertical handset alone, and for the vertical handset and the box head or the sphere head. Although the agreement was good, the lack of error bounds on the measured data does not permit us to assess whether the differences are within "experimental error". In the paper given in



Appendix 1, we cannot put limits on the experimental error and judge whether the agreement is within the error bound, and so the argument is weakened considerably.

Assuming that the differences between the measured and computed patterns exceed the error bound on the measurement, it may be worthwhile to explore geometrical differences between the real handset and the computational model. One difference is that the antenna on the real handset is not perfectly straight nor perpendicular to the top of the handset. Some initial investigations were done in Ref. [25] using the wire-grid model, and these could be extended and written up formally for the next contract period. Small deviations of the antenna from perfectly straight and perpendicular are not possible to incorporate into the FDTD computation. The changes in the handset's patterns due to the holes in the case for the switch and the LED were explored at CRC[24]. A more precise model including the case thickness, the body of the switch filling the hole, the switch lever which protrudes beyond the case surface, and the body of the LED should be looked at. Also the presence of the styrofoam holding the handset may affect the patterns and this could be investigated numerically. If the handset is not perfectly level when it is rotated to measure a radiation pattern, this may introduce small errors and asymmetries. This could also be explored by computation.

### 9.2.2.3 Computed Patterns at Finite Range

At present the FDTD code is not able to calculate "near field" radiation patterns accounting accurately for the 330 cm range. It is possible to add this capability, albeit with considerable programming effort. This project was assigned to a graduate student, but he has made little progress. Comparing computations and measurements at the same range would remove one of the sources of error in the comparison.

### 9.2.2.4 Measurement of the Volumetric Radiation Patterns

The initial objective of the measurement phase of the project was to measure the "volumetric" patterns of the handset with various head models. By this is meant the measurement of the full set of conical cut radiation patterns over the surface of the radiation sphere. An initial attempt was made in 1996 and reported in Ref. [2]. The mechanical arrangement for moving the handset was awkward and did not lead to a straightforward relationship between the angles associated with the measurement setup and the spherical angles ( $\theta, \phi$ ) in which the far fields are normally expressed. Nor was it possible to extract the  $E_\theta$  and the  $E_\phi$  spherical components of the field from the measured amplitude of the horizontal and vertical field. The coordinate transformations must be done with complex numbers representing both the amplitude and the phase of the field, and this requires the measurement of the phase as well as the amplitude.

Since good success has been obtained with the measurement of the principal plane patterns, a second attempt should be made to measure  $E_\theta$  and  $E_\phi$  in the conical cut pattern set over the whole radiation sphere. This permits a complete characterization of the radiation characteristics of the handset in three-dimensional space. Also, given the full set of measured conical cut patterns, the radiated power could be computed by the same method used with the far fields found from FDTD. Then a comparison could be made based on true radiated power.

### 9.2.2.5 Material Parameters of the Phantom Head

The phantom cell model uses values for the permittivity and conductivity of the wood base taken from the literature. There is some variation in the values reported for “wood”, and it is clear that various materials that can be classified as “wood” behave differently electrically. The cell model would more precisely represent the actual base of the phantom if the permittivity and conductivity of the wood base were measured. The same technique used to measure the parameters of the brain liquid mixture might be used.

The cell model of the phantom head is readily used to explore the differences in the far fields and the near fields due to changes in the brain material parameters. The current model at 850 MHz uses  $\epsilon_r=40.40$  and  $\sigma=1.064$  S/m. These were the values measured for the brain liquid mixture with which the phantom was filled[21]. Ref. [1] discussed the values for various materials cited in the literature and summarized them in Table 7.1. Average brain is cited as having a relative permittivity of about 41 and a conductivity of between 0.86 and 1.22 S/m. It has been suggested[29] that more accurate values would be  $\epsilon_r=46$  and  $\sigma=0.74$ . The table of parameter values supplied with phantom head[1] cites  $\epsilon_r=41.54$  and  $\sigma=0.759$  S/m at 881 MHz. Evidently there is some disagreement in the proper values for “average brain” material. In fact [1] Table 7.1 cites values for “white matter” and “gray matter” that are different from “average brain”.

### 9.2.2.6 Explorations of the Radiation Patterns of the Handset near the Phantom

The cell model of the handset and phantom head can be used for a variety of investigations that may be of interest to this project. The effect on the radiation patterns of the handset and phantom head of the rather large wood base might be studied. The base is an integral part of the phantom head and is not easily removed, nor should it be. But the base is readily deleted from the cell model, and the radiation patterns without and with the base could be compared.

A further exploration might involve the effect of the position of the handset relative to the head on the radiation patterns. The handset can be moved closer to or farther away from the head in the cell model quite readily. With the handset very close to the head, perhaps in contact with the ear or cheek, then the coupling between the handset and the head is substantially increased and the changes in the radiation patterns would be expected to be larger. The cell model can readily be used to explore such changes.

### 9.2.2.7 Effect of the Hand

The head phantom comes equipped with a matching hand. The presence of the lossy dielectric material of the hand changes the current flow over the surface of the handset and would be expected to change the radiation patterns and near fields. It would be of interest to explore the effects of the hand on the radiation patterns of the handset. Perhaps the measurement jig used to hold the handset and head could be modified to

permit the hand to be wrapped around the handset in a realistic way. The hand may not be suitable to "hold" the project's handset; it may be necessary to create a new handset shaped to fit in the hand. Certainly our computations and measurements would have more credibility and relevance to the community if the hand were included.

Modeling the hand with FDTD is very challenging. The phantom hand would need to be CT-scanned. Its individual cross-sections would have to be processed to identify the material types as was done for the phantom head, which is a lengthy and tedious procedure. Then the MKPHANT program would need to be modified to create cell models of the hand in any desired orientation.

#### **9.2.2.8 Realism of the Phantom Head**

This project has developed a cell model of the phantom head, and two different cell models of real heads based on anatomical data. Ref. [13] used a vertical handset near an anatomical head and near the phantom head to ask if the phantom does reasonably represent an anatomical head for the purposes of radiation pattern computation. It might be of interest to peruse this comparison. A version of the anatomical head model could be created by scaling the geometrical data that is comparable in volume to the cell model of the phantom head. Care could be taken to position the handset in reasonably equivalent positions relative to the two head models, and the radiation patterns computed and compared. It might be of interest to do this for both anatomical head models, because the two are quite different in shape. Does a phantom reasonably represent a real head?

Another possibility is to use scaling to investigate the effect of the size of the head on the radiation patterns of the handset. The phantom could be scaled up or down by 10 or 20 percent, and the radiation patterns computed with the handset in approximately equivalent positions for the various sizes. It has been argued in the literature that an anatomically-based model of the head should not simply be scaled in size. Thus a small person's head has a somewhat different internal structure from a large person's head. Scaling might provide a first approximation to the effect of size but should not be used to judge changes in the internal field in local regions of the head.

### **9.3 New Directions**

This section suggests some new investigations that might be of interest in this project.

#### **9.3.1 PCS Frequencies**

Newer cellular telephone handsets are based on digital technology and operate in the "PCS" frequency band at approximately 1900 MHz. Also, new handsets are considerably smaller than the handset that is studied in this report. It may be of interest to construct a representative handset at 1900 MHz, and to investigate the near fields and far fields as has been done for the 850 MHz handset in this and previous reports. A simple quarter-wave monopole antenna might be used on the new handset. Or, a more complex antenna design could be incorporated. Some recent antenna designs are difficult to model precisely with FDTD.



The cell model of the phantom head uses cells of 2.205 mm size, and this could be somewhat reduced without exceeding the resolution of the data base of cross-sections of the phantom head. The permittivity and conductivity of the real biological materials changes with frequency, as do the material parameters of the skin, muscle and bone in the phantom head. The correspondence between the parameters of the phantom's materials and real materials at 1900 MHz should be verified. Scanning the table of values for the phantom given in Ref. [1] shows that for muscle,  $\epsilon_r$  declines from about 52 to about 50 from 850 to 1900 MHz, and  $\sigma$  increases from 1.1 to about 1.6. For the skin material,  $\epsilon_r$  declines from about 42 to about 31, and  $\sigma$  increases from 0.8 to about 2.2. For bone,  $\epsilon_r$  declines from about 15 to about 13, and  $\sigma$  increases from 0.14 to about 0.35. The brain liquid mixture can be prepared to have the desired permittivity and conductivity at 1900 MHz; the table suggests that  $\epsilon_r$  declines from about 41 to about 32, and  $\sigma$  increases from 0.8 to about 1.8. Thus the relative permittivity declines but the conductivity increases substantially for these materials. The frequency at which 2.205 mm cells are a tenth of a wavelength in size was computed for each material. The material limiting the bandwidth of the model is muscle, which has a maximum frequency of 1895 MHz. Thus the phantom with 2.205 mm cells is at the top of its frequency range at 1900 MHz. The cell size could be reduced to 2 mm to generate a model that is valid to 2093 MHz, and could thus be used for computations at the PCS frequency.

### 9.3.2 Real Cellular Telephone Handsets

It might be of considerable interest to investigate the modeling of one or more real cellular telephone handsets with FDTD. The objective would be to compare measured principal plane patterns with those computed with the best FDTD model of a handset that we are able to develop. Perhaps the cooperation of a manufacturer could be solicited, including the donation of a handset and some information about what is inside the plastic case. Development of a cell model of a handset requires knowledge of the internal structure. The material layers, the presence of conductors on circuit boards, of an internal ground plane, of metallized layers or foil included for shielding, of metallic objects such as batteries, and so forth all contribute to the cell model. It is not a trivial task to develop a realistic cell model of a handset. Engineering drawings of a handset would be a good guide, or a "scrap" handset that could be disassembled to discover the internal parts.

An assessment of the accuracy of FDTD to predict the radiation patterns of a real handset might be of interest to those using computational methods to design handset antennas. Predictions of the radiation patterns of a real handset near the phantom and comparisons with measured patterns might be of interest as phantoms are extensively used in the industry to assess handset performance.

A good knowledge of the radiation patterns of a real handset is of considerable interest in the associated problem of assessing electromagnetic compatibility between the handset and other electrical equipment. This is particularly important in a hospital environment where interference with some equipment could be life threatening. Studies of the fields in an indoor environment aimed at assessing the risk to equipment would be better based on a realistic model of the radiation characteristics of a real handset than on

simple dipole antenna patterns. This project has demonstrated very effectively that a simple dipole is a poor model of a real handset.

### 9.3.3 Other Applications

Cellular telephones and walkie-talkies are not the only application for portable radios. In the near future, laptop computers will carry miniature antennas for wireless communication using the internet, in offices, public places and aircraft. Such antennas will operate at about 2.5 GHz, not far above the PCS frequency. Determining the performance of antennas for wireless applications such as this can be done either by measurement or by computation. It may be of interest to investigate representative antennas as an extension of this project.

### 9.4 Conclusion

This project has developed both a computational tool and a measurement tool for determining the performance of handset antennas, in the near field and in the far field. The capability includes realistic models of the head. Good agreement has been demonstrated for both near fields and far fields. But a tool without work for it to do is of little use. The project needs a revisiting of its original primary objectives to provide it with renewed impetus. The effectiveness of the standardized computational and measurement methods developed in this project could be demonstrated by solving problems of interest to the community.

### Postscript

After this report was written it was learned that the Microwave Consultants Head Phantom includes eye material in the eye sockets. This material is not seen in the CT scans of the phantom presented in Chapter 7. The computations reported in Chapter 8 and discussed in Chapter 9 filled the eye sockets with skin material, with  $\epsilon_r=42.23$  and  $\sigma=0.777$ , instead of eye material with  $\epsilon_r=69.45$  and  $\sigma=1.610$ . Also it was learned that the measurement of the radiation patterns of the handset with the phantom head were done with a brain liquid mixture having  $\epsilon_r=41.54$  and  $\sigma=0.759$ ; whereas the computation used  $\epsilon_r=40.42$  and  $\sigma=1.064$ . These differences in the brain and eye materials have an unknown impact on the radiation patterns of the handset and head. It would be desirable to repeat the computation including the eye material and using the correct electrical parameters for the brain material.

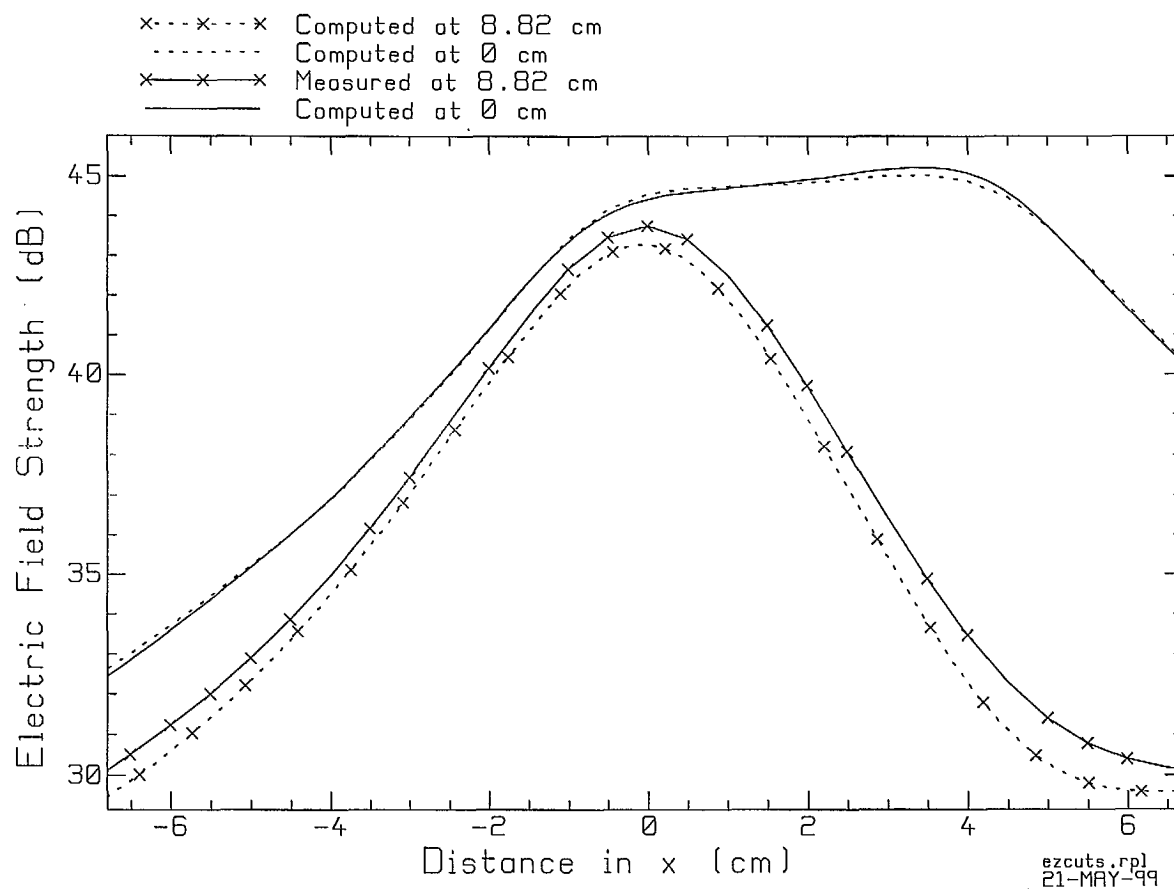


Fig. 9.1 The  $E_z$  component for the handset at  $y=-21.8$  mm as a function of distance  $x$  for  $z=0$  cm and  $z=8.82$  cm.



## References

- [1] C.W. Trueman and S.J. Kubina, "A Research Study on Electromagnetic (EM) Fields Produced by Portable Transceivers", Final Report in Contract Number U68000-7-0726/001/ST, Technical Note No. TN-EMC-94-01, Dept. of Electrical and Computer Engineering, Concordia University, March 31, 1998.
- [2] C.W. Trueman, S.J. Kubina, D. Gaudine and B. Lorkovic, "A Research Study on Electromagnetic Fields Produced by Portable Transceivers", Final Report, Public Works and Government Services Canada, Communications Research Centre, Contract #PWGSC/CRC U68000-6-0755/001/ST, Technical Note TN-EMC-97-01, ECE Dept., Concordia University, March 31, 1997.
- [3] C.W. Trueman, S.J. Kubina and M. Danesh, "Fields of a Portable Radio Handset Near the Human Head", Final Report, Public Works and Government Services Canada, Communications Research Centre, Contract #PWGSC/CRC 67CRC-5-0850/01-ST, Technical Note TN-EMC-96-01, ECE Dept., Concordia University, March 31, 1996.
- [4] C.W. Trueman and S.J. Kubina, "Characteristics of Electromagnetic Fields Produced by Portable Handheld Transceivers", Final Report prepared for the Communications Research Centre, Ottawa, Contract No. PWGSC/CRC 36001-4-0395/01-ST, Technical Note No. TN-EMC-95-01, Electromagnetic Compatibility Laboratory, Concordia University, March 31, 1995.
- [5] S.J. Kubina and C.W. Trueman, "Computational Studies for Prediction of Energy Deposition in Humans Exposed to RF Fields from Cellular Phones", Final Report, Ministry of Industry, Science and Technology, Communications Research Centre, Contract # MIST/CRC 36001-3-3603, Technical Note No. TN-EMC-94-01, Dept. of Electrical and Computer Engineering, Concordia University, March 31, 1994.
- [6] K.S. Kunz and R.J. Luebbers, "The Finite-Difference Time-Domain Method for Electromagnetics", CRC Press, 1993.
- [7] A. Taflove, "Computational Electrodynamics, The Finite-Difference Time-Domain Method", Artech House, 1995.
- [8] J.M. Bertrand and W.R. Lauber, "CRC Model Transmitter", Technical Memorandum, Communications Research Centre, Industry Canada, May, 1997.
- [9] "TX Handset", CRC Drawing Number 96364-01A3.
- [10] J.H. Beggs, R.J. Luebbers, D. Steich, S. Scott Langdon, and K.S. Kunz, "User's Manual for Three Dimensional FDTD Version C Code for Scattering from Frequency-Independent Dielectric and Magnetic Materials", Electrical and Computer Engineering Department, The Pennsylvania State University, University Park, Pennsylvania, June 16, 1992.
- [11] J. P. Bérenger, "Improved PML for the FDTD Solution of Wave-Structure Interaction Problems", *IEEE Trans. Antennas and Propagation*, Vol. 45, No. 3, pp. 466-473, March 1997.
- [12] M. Vall-llossera and C.W. Trueman, "Comparison of the Performance of the and the Liao Absorbing Boundary Formulation", Conference Proceedings, 14th Annual Review of Progress of the Applied Computational Electromagnetics Society, pp. 523-530, Monterey, California, March 16-20, 1998.

- [13] C.W. Trueman, S.J. Kubina, J.E. Roy and W.R. Lauber, "Portable Radio Handset Patterns in the Presence of a Model of the Head", Symposium on Antenna Technology and Applied Electromagnetics, Ottawa, August 9-12, 1998.
- [14] "The Visible Human Project", National Library of Medicine, [http://www.nlm.nih.gov/research/visible/visible\\_human.html](http://www.nlm.nih.gov/research/visible/visible_human.html)
- [15] C.W. Trueman, S.J. Kubina, J.E. Roy and W.R. Lauber, "Validation of FDTD Handset and Head Patterns by Measurement", 1998 IEEE APS Conference on Antennas and Propagation for Wireless Communications, Watham, Mass., Nov. 1-4, 1998
- [16] C.W. Trueman, S.J. Kubina, D. Cule and W.R. Lauber, "Validation of the FDTD Near Fields of a Portable Radio Handset and a Simple Head", Conference Proceedings, 15th Annual Review of Progress of the Applied Computational Electromagnetics Society, pp. 660-667, Monterey, California, March 16-28, 1999.
- [17] D. Cule and J. Bertrand, "Measurements of the Electromagnetic Near-Fields Produced by a Portable Radio Transmitter", CRC Technical Memorandum VPRB-02-98, August, 1998.
- [18] J.R. Roy, private communication, far field pattern measurements, Dec. 24, 1999.
- [19] Probe ER3DV4, SN:2201, Schmid and Partner Engineering AG, Oberer Deutweg 59, CH-8400 Winterthur, Switzerland.
- [20] G. Hartsgrrove, A. Kraszewski and A. Surowiec, "Simulated Biological Materials for Electromagnetic Radiation Absorption Studies", *Bioelectromagnetics*, Vol. 8, pp. 29-36, 1987.
- [21] CRC, private communication, measured values for the relative permittivity and conductivity of the brain liquid mixture by Joe Seregelyi, September 11, 1997.
- [22] C.A. Balanis, "Advanced Engineering Electromagnetics", Wiley, New York, 1989.
- [23] G.J. Burke, A.J. Poggio, J.C. Logan and J.W. Rockway, "NEC - Numerical Electromagnetics Code for Antennas and Scattering", 1979 IEEE International Symposium on Antennas and Propagation Digest, IEEE Publication No. 79CH1456-3AP, Seattle, Washington, June, 1979.
- [24] J.R. Roy, private communication, handset radiation patterns, October 9, 1998.
- [25] C.W. Trueman, "Changes in the Handset Patterns Due to a Bent Antenna", private communication to J. Roy, Oct. 30, 1998.
- [26] "Mount For EM Field Measurements With TX and Phantom Head", CRC drawing set 98020, July 14, 1998.
- [27] Head Phantom manufactured by Microwave Consultants Limited, 17B Wooford Road, London E18 2E1, United Kingdom.
- [28] Y. Rahmat-Samii and M.A. Jensen, "Personal Communications Antennas: Modern Design and Analysis Techniques Including Human Interaction", Short Course presented at the IEEE Antennas and Propagation Society International Symposium, Montreal, Quebec July 18, 1997.
- [29] W. Lauber, electrical parameters of brain tissue, private communication to C.W. Trueman, February 26, 1999.
- [30] G. Lazzi, S.S. Pattnaik, and O.P. Gandhi, "Experimental and FDTD-Computed Radiation Patterns of Cellular Telephones Held in a Slanted Operational Position", *IEEE Trans. On Electromagnetic Compatibility*, Vol. 41, No. 2, pp. 141-144, May, 1999.

## **Appendix 1**

### **“Portable Radio Handset Patterns in the Presence of a Model of the Head”**

**by**

**C.W. Trueman, S.J. Kubina, J.E. Roy and W.R. Lauber**

Symposium on Antenna Technology and Applied Electromagnetics,  
Ottawa, August 9-12, 1998.



# Portable Radio Handset Patterns in the Presence of a Model of the Head

C. W. Trueman

S.J. Kubina

Electromagnetic Compatibility Laboratory,  
Concordia University,  
Montreal

J.E. Roy

W.R. Lauber

Communications Research Centre,  
Ottawa

**Abstract**-This paper examines the principal plane radiation patterns of a portable radio handset at 850 MHz operating near a model of the human head. The handset and head are solved by the finite-difference time-domain method. To validate the computed patterns, they are compared with measured radiation patterns, with excellent agreement for the handset alone and very good agreement for both the handset near the box model of the head, and the handset near the sphere head model. FDTD is then used to find the principal plane patterns of the handset near a realistic model of the head based on anatomical cross-sections. The principal plane patterns of the handset and anatomical head are shown to be very similar to those of the handset near a sphere of size comparable to the head.

## Introduction

Fig. 1 shows a portable radio "handset"[1,2] comprised of an aluminum box 5.35 by 1.74 by 16.77 cm, with an antenna 8.82 cm in length, located 0.87 cm from three adjacent edges of the case. The antenna is a quarter-wave monopole operating at 850 MHz. In this paper we investigate the radiation patterns of this simple handset operating near box, sphere and anatomical models of the human head. The principal plane radiation patterns are found using the finite-difference time-domain (FDTD) method[3]. FDTD has been used extensively in the literature[4] to find the radiation patterns and near fields of portable radio handsets operating near head models. This paper provides a validation by comparing computed radiation patterns against measured patterns, using box and sphere models of the head. The patterns of the handset near an anatomically-based model of the head are then found, and are shown to be remarkably similar to those of the handset near a sphere of similar size.

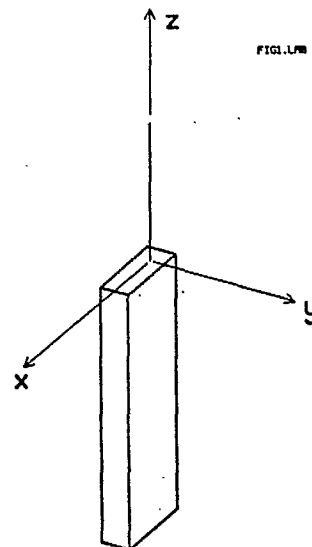


Fig. 1 The portable radio handset in the  $xyz$  coordinate system.

## Measurement of the Radiation Patterns

The radiation patterns were measured[5] with the head model and the handset held in the mounting jig of Fig. 2, consisting of styrofoam blocks and fiberglass bolts. The jig holds the handset in a well-known, reproducible position relative to the head. The jig sits atop a styrofoam rotator column in a 6x6x6 meter anechoic chamber. Fig. 2 shows the jig positioned for rotation in the  $yz$  plane in



Fig. 1, for measurement of the  $\phi = 90$  degree elevation pattern. The jig was aligned with the column's axis of rotation as accurately as possible using a laser beam.

The handset contains a battery-operated oscillator at 850 MHz. An open-ended waveguide was mounted near the base of the rotator column to sample the field to provide a reference signal to phase-lock a network analyzer. The horizontal and vertical components of the field were measured by a dual-polarized ridged waveguide horn mounted about 330 cm from the handset. Considerable care was taken to optimize the quality of the measured data. Unwanted reflections in the anechoic chamber were identified and reduced with absorber. However, the absorber in the chamber is designed for best performance above 1.5 GHz. The relatively short range from the handset to the horns incurs errors approaching one degree in the angle from the antenna feed point to the horn, compared to the true "far field" angle. These errors will primarily affect the measured patterns in the minima.

The computations and measurements in this paper are compared on the basis of equal radiated power. The three principal plane patterns are obtained from the measurement. The radiated power in each pattern is found by integrating the power density

$$S_{av} = \frac{E_{\theta}^2 + E_{\phi}^2}{2\eta}$$

over the pattern, and then the total radiated power is estimated by summing the radiated power in the three principal plane patterns. The radiated power in the computed patterns is estimated in the same way, and then measured data are scaled to have the same estimated radiated power as the computations.

### Radiation Patterns of the Handset Alone

Fig. 3 compares the measured and computed radiation patterns of the handset oriented vertically as shown in Fig. 1. Using a cell size of 2.205 cm, the handset case is very close to 24 by 8 by 76 cells, and the antenna is 40 cell edges in length. The perfectly-matched layer (PML) absorbing boundary[6] is used, 6 cells in thickness with a surface reflection coefficient of 0.001 and parabolic evolution of the conductivity. The surfaces of the handset and the tip of the antenna are separated from the first layer of the PML by 4 cells of free space or "whitespace". The FDTD computation is run for 4096 time steps with a sinusoidal generator at 850 MHz at the base of the monopole. The patterns have been scaled to have an "isotropic level" field strength[1] of 0 dB.

The agreement between the measurement and the computation in Fig. 3 is the best we have been able to obtain. In the azimuth pattern, at  $\phi = 0$  degrees the computed field is 1.3 dB

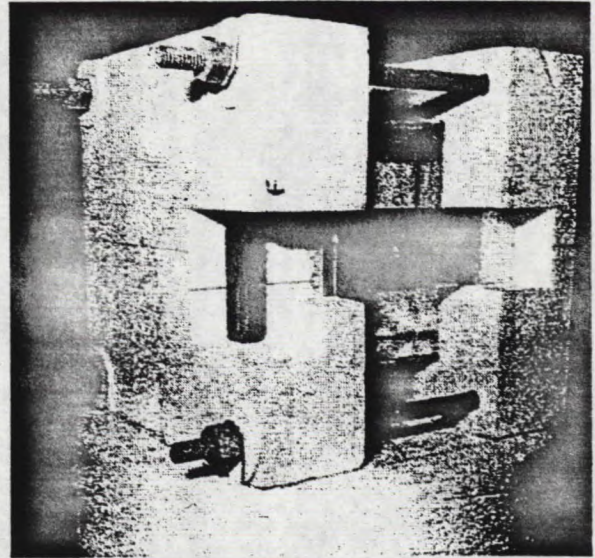


Fig. 2 The handset and box head mounted in the styrofoam jig, positioned on top of the rotator in the anechoic chamber.



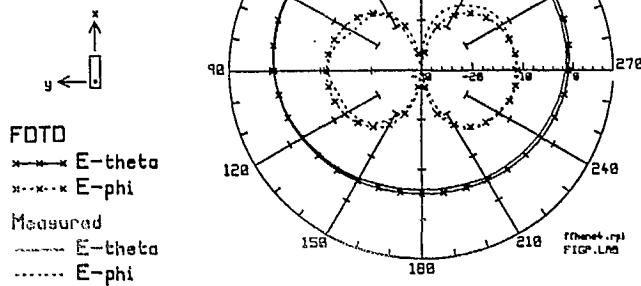
compared with 0.8 dB in the measurement. In the elevation pattern for  $\phi = 0$ , the computed field at 115 degrees is 4.3 dB compared to the measured value of 4.8 dB. In the  $\phi = 90$  pattern the lobe at 119 degrees has a measured and a computed field strength of 4.0 dB.

### The Handset and the Box Head

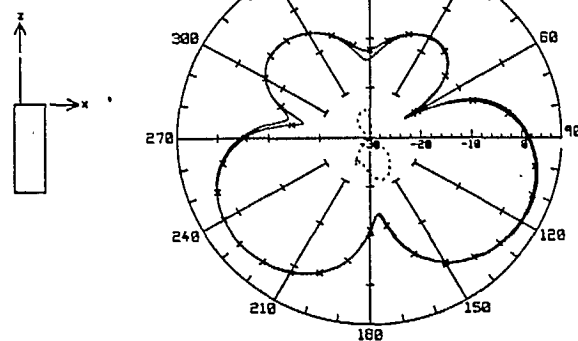
The "box head" is a plexiglas box 17.07 by 13.89 by 21.06 cm, with a wall thickness of 0.51 cm. The box is filled with "brain liquid", a sugar, salt and water mixture having the electrical parameters of brain matter[7]. The relative permittivity and conductivity of the brain liquid were measured[8] to be 40.42 and 1.064 S/m, respectively, and these values were used in the computations. Using 2.205 mm cells, the box is modeled in FDTD with 78 by 63 by 95 cells, and the plexiglas wall is two cells thick. The computation includes the four fiberglass bolts of the mounting jig of Fig. 2, but not the styrofoam blocks. The 2.205 mm cell size corresponds to one-tenth wavelength in the brain liquid at 2125 MHz. This small cell size was used to allow the curvature of the bolts to be reasonably well defined. The FDTD cell space was terminated with a PML as described above. The FDTD model was run for 4096 time steps.

Fig. 4 compares the measured and computed radiation patterns of the vertical handset operating near the boxhead. The figure shows very good agreement between the measurement and the computation for the handset and box head. In the azimuth pattern, the maximum measured  $E_\theta$  is 3.0 dB at 295 degrees, and the maximum computed field is 2.4 at 303 degrees. The cross-polarized field  $E_\phi$  has a maximum in the measured pattern of -4.1 dB at 128 degrees, compared to -4.4 dB at 129 degrees in the computation. Both the principal polarization and the cross polarization agree well in all three principal plane patterns. The computed patterns were examined in Ref. [1] without and with the four bolts used to hold the jig together. The bolts have only a minor effect on the patterns.

Handset Alone  
Azimuth Pattern



Phi=0 Elevation Pattern



Phi=90 Elevation Pattern

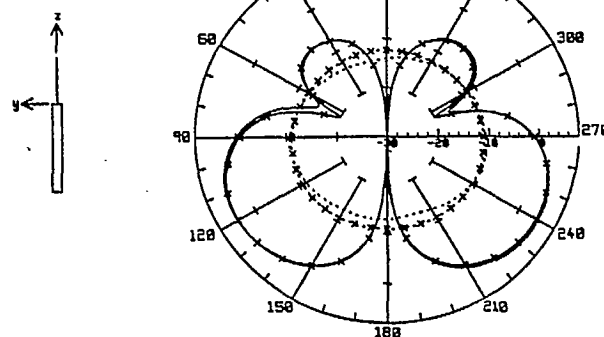


Fig. 3 The principal plane patterns of the handset alone.



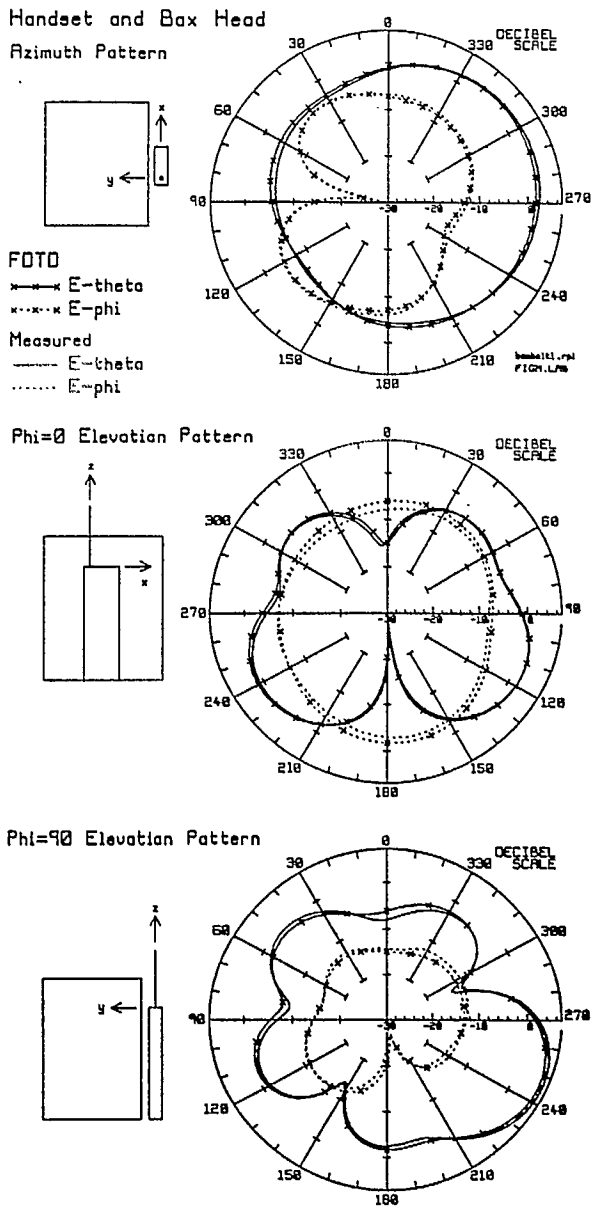


Fig. 4 The principal plane patterns of the handset and box head.

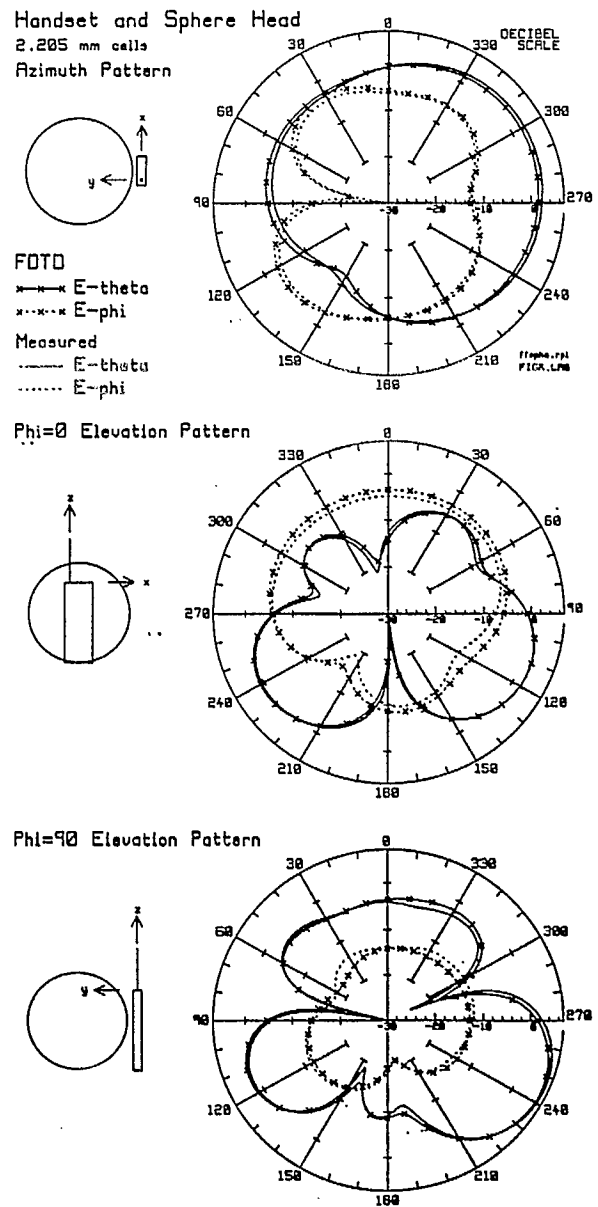


Fig. 5 The principal plane patterns of the handset and sphere head.

### The Handset and Sphere Head

The "sphere head" is 20.68 cm in diameter with a wall thickness of 3.65 mm. The sphere's curved surface was approximated with a "staircase" of 2.205 mm cells. The 3.65 mm plexiglas wall thickness is about 1.65 cells thick; it was approximated as either one cell or two cells thick, being the difference between the staircase modeling the outer sphere and the inner sphere defining the plexiglas wall. The fiberglass bolts of the mounting jig were not included in the FDTD model for the sphere. The sphere is 94 cells or 20.73 cm in diameter, a reasonable approximation of the true 20.68 cm diameter.

Fig. 5 compares the principal plane patterns of the handset and sphere with the measured patterns. In the azimuth pattern, the maximum measured  $E_\theta$  is 2.9 dB at 298 degrees, compared to a maximum computed field of 2.1 dB at 300 degrees. The cross-polarized field  $E_\phi$  has a maximum in the measured pattern of -3.3 dB at 135 degrees, compared to -2.5 dB at 133 degrees in the computation. Both the principal polarization and the cross polarization agree well in all three principal plane patterns. The agreement between the measurements and the computations is about as good for the handset and sphere head as it is for the handset and box head, even though the fiberglass bolts were omitted for the sphere head calculation. The agreement for the sphere case was improved considerably by reducing the cell size used to model the sphere from 4.41 mm[1,2] to 2.205 mm.

Figs. 4 and 5 have been presented side-by-side to encourage a comparison of the principal plane patterns of the handset and box head with those of the handset and sphere head. The box volume is 5023 ml, and the sphere 4631 ml, making the two "heads" similar in size. Comparing Figs. 4 and 5 shows that the azimuth patterns are similar but not identical. The sphere head  $E_\theta$  polarization has a more pronounced minimum near 150 degrees. The elevation pattern for  $\phi=0$  degrees is more symmetric for the handset and box head than for the handset and sphere head. In the sphere case the minor lobe near 315 degrees in  $E_\theta$  is much smaller. In  $E_\phi$ , the field has minima near 120 and 210 degrees with the sphere that are not seen in the box patterns. The elevation pattern for  $\phi=90$  degrees is more directional with the sphere head than with the box head. There are much sharper minima near 85 degrees, 160 degrees, and 300 degrees. The fields in  $E_\phi$  are similar between the two cases.

### Handset and the Anatomical Head

Ref. [9] presents a set of 19 anatomical sections of half of the head, roughly from the nose to the top of the skull, and 8 full sections from nose level to neck level. The sections are not in parallel planes, but instead are inclined to one another, as shown in Fig. 6. The sections are approximately 1 cm apart. The sections were made by dissecting a male cadaver. The sections are well labeled with tissue types, in Latin. To construct an FDTD cell model, each anatomical section was "digitized" by overlaying it with a grid of 3.3 mm square cells, and identifying the predominant material in each cell[1]. Then a computer program was used to create an FDTD cell model from the cross-sectional data, using 2.205 mm FDTD cells. For each FDTD cell the nearest cell on any of the anatomical sections was found and the material type of that cell was assigned. The wide spacing of the anatomical sections leads to unacceptable errors in assigning materials to cells when a full-size

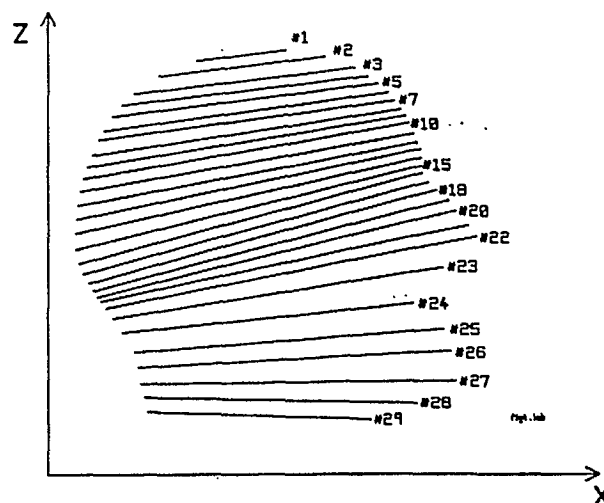


Fig. 6 The location of cross-sectional planes for constructing the anatomical model of the head.

head is made with 2.205 mm cells. It was found that a good model of a small head 60 cells or 13.23 cm across the ears could be made at this cell size.

The anatomical head[1] uses 12 different tissue types: bone, nerve, white matter, grey matter, average brain, skin, cartilage, gland, blood, muscle, eye and cerebral spinal fluid(CSF). Fat was treated as having the same electrical properties as bone. Values for the relative permittivity and conductivity of the various tissues were taken from Refs. [7], [10] and [11] and are given in Table 1. The material with the shortest wavelength is CSF, with a relative permittivity of 79.1 and a conductivity of 2.14 S/m. The cells of CSF are a tenth-wavelength at 1500 MHz, so our model is conservative when run at 850 MHz. The surface of the head is "coated" with a one-cell thick layer of skin, except over the bottom of the neck. The head was solved with FDTD with the handset vertical, parallel to the vertical axis of the head. The cell space was terminated with a PML as described above, and FDTD was run for 4096 time steps.

Fig. 7 shows the radiation patterns of the vertical handset near the anatomical head. When these patterns were compared with those in Fig. 5 for the handset and sphere, great similarity was seen, even though the sphere is much larger than the anatomical head. A smaller sphere model was prepared having a diameter of 60 cells or 13.23 cm, the same size as the ear-to-ear dimension of the anatomical head. The sphere has a "skin" layer one cell thick at the surface and is filled with average brain material. The schematics of the handset and head alongside each pattern were drawn to scale and so compare the relative size of the sphere and the anatomical head. All three patterns in Fig. 7 are very similar for the two cases. The azimuth pattern

shows a maximum  $E_\theta$  for the handset and sphere of 0.9 dB at 60 degrees, compared to -2.1 dB for the handset and head at the same angle. This is on the opposite side of the head to the handset. The handset and head has a maximum field of 0.7 dB at 290 degrees, compared to -1.6 dB for the handset and sphere. This is an angle where the observer sees the head behind the handset. The  $E_\phi$  component has a maximum of -2.1 dB for the handset and head at 145 degrees, compared to -2.4 dB for the handset and sphere. In the elevation pattern for  $\phi=0$  degrees, the main lobes in  $E_\theta$  correspond very well. The minor lobe at 40 degrees, -3.5 dB for the head falls at 35 degrees, -5.9 dB for the sphere. In  $E_\phi$ , the pattern is almost circular. For the handset and head the maximum is at 49 degrees, -2.2 dB and the minimum at 217 degrees, -7.1 dB. For the handset and sphere the range of values is smaller, with the maximum at 44 degrees, -2.6 dB, and the minimum at 248 degrees, -4.9 dB. The elevation pattern for  $\phi=90$  degrees is again very similar between the two cases.

**Table 1**  
Material Parameters of the Biological Materials used  
in the Anatomical Head Model

Material	Relative Permittivity	Conductivity S/m
Free Space	1.00	0.
Bone	20.9	0.33
Nerve	33.4	0.60
Average Brain	41.0	0.86
White Matter	34.5	0.59
Grey Matter	53.8	1.17
Muscle	57.4	0.82
Eye	67.9	1.68
Cartilage	41.9	0.83
Gland	45.3	0.92
Blood	55.0	1.86
CSF	79.1	2.14
Skin	40.7	0.65



## Conclusion

This paper has presented a validation of FDTD computations of principal plane radiation patterns for a handset operating near box and sphere models of the head. Excellent agreement between the measured patterns and the computations was found for the handset alone, and very good agreement for the handset and the box head, or sphere head.

Comparing Fig. 3 with either Fig. 4 or Fig. 5 shows that operating the handset near the head leads to major changes in the radiation patterns. The  $E_\theta$  polarization becomes more directional, with larger field strengths in directions where the head lies behind the handset and smaller fields where the head is between the handset and the observer. The  $E_\phi$  polarization rises substantially in value when the head is present. In the  $\phi=0$  elevation pattern, the  $E_\theta$  polarization is similar without and with the head, but the head introduces an  $E_\phi$  component which is comparable in strength to  $E_\theta$ . The  $\phi=90$  elevation pattern has smaller  $E_\theta$  field strengths with the head between the observer and the handset, and below the head, than for the handset alone. The  $E_\phi$  polarization is similar in level but more directional.

This paper compared the fields of the handset operating near an anatomically-based model of the head with those of the handset near a sphere of size similar to the anatomical head. The patterns of the handset and head are quite similar to those of the handset and sphere; indeed the sphere may be a useful simple model of the head. The similarity is not greatly sensitive to the composition of the sphere, nor to the size of the sphere, nor to the exact position of the handset.

In this paper the handset is oriented vertically. A cellular telephone user typically tilts the handset at about 60 degrees to the vertical; thus our handset position is not realistic. Ref. [1] investigated the patterns of the handset tipped 60 degrees to the vertical. In that case, the handset alone radiates  $E_\theta$  and  $E_\phi$  more nearly equally than in Fig. 3. Again, the head has a major effect

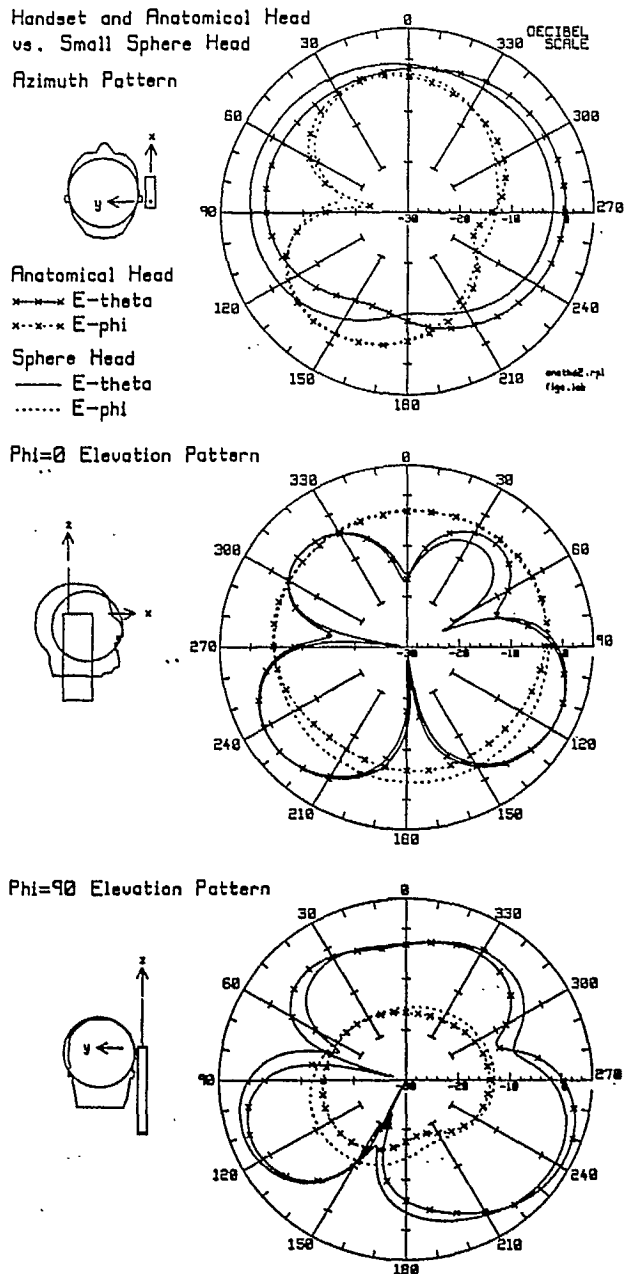


Fig. 7 Comparison of the principal plane patterns of the handset and sphere head, and the handset and anatomical head.

on the handset patterns. This paper does not consider the hand. The user's hand represents a high-permittivity lossy dielectric coating over part of the handset surface. It is expected that the hand will influence the radiation patterns of the handset[4].

Further work in this project will compute and measure radiation patterns for the handset operating near a realistic "phantom" of the head, including the hand.

## References

- [1] C.W. Trueman and S.J. Kubina, "A Research Study on Electromagnetic (EM) Fields Produced by Portable Transceivers", Final Report in Contract Number U68000-7-0726/001/ST, Technical Note No. TN-EMC-94-01, Dept. of Electrical and Computer Engineering, Concordia University, March 31, 1998.
- [2] C.W. Trueman, S.J. Kubina, J.E. Roy, W.R. Lauber, and M. Vall-Ilossera, "Validation of FDTD-Computed Handset Patterns by Measurement", Conference Proceedings, 14th Annual Review of Progress of the Applied Computational Electromagnetics Society, pp. 93-98, Monterey, California, March 16-20, 1998.
- [3] K.S. Yee, "Numerical Solution of Initial Value Problems Involving Maxwell's Equations in Isotropic Media", IEEE Trans. on Antennas and Propagation, Vol. AP-14, No. 3, pp. 302-307, May, 1966
- [4] Y. Rahmat-Samii and M.A. Jensen, "Personal Communications Antennas: Modern Design and Analysis Techniques Including Human Interaction", Short Course presented at the IEEE Antennas and Propagation Society International Symposium, Montreal, Quebec July 18, 1997.
- [5] J.E. Roy, W.R. Lauber and J.M. Bertrand, "Measurements of the Electromagnetic Far Field Produced by a Portable Transmitter(Principal Planes)", CRC Report # CRC-RP-98-002, Communications Research Centre, Ottawa, February, 1998.
- [6] J.P. Berenger, "A Perfectly-Matched Layer for the Absorption of Electromagnetic Waves", Journal of Computational Physics, Vol. 114, pp. 185-200, 1994.
- [7] G. Hartsgrrove, A. Kraszewski and A. Surowiec, "Simulated Biological Materials for Electromagnetic Radiation Absorption Studies", *Bioelectromagnetics*, Vol. 8, pp. 29-36, 1987.
- [8] CRC, private communication, measured values for the relative permittivity and conductivity of the brain liquid mixture by Joe Seregelyi, September 11, 1997.
- [9] A.C. Eycleshymer and D.M. Schoemaker, "A Cross-Sectional Anatomy", D. Appleton and Co., New York, 1911.
- [10] V. Homback, K. Meier, M. Burkhardt, E. Kuhn and N. Kuster, "The Dependence of EM Energy Absorption Upon Human Head Modeling at 900 MHz", IEEE Trans. on Microwave Theory and Techniques, Vol. MTT-44, No. 10, pp. 1865-1873, October, 1996.
- [11] G. Lazzi and O.P. Gandhi, "Realistically Tilted and Truncated Anatomically Based Models of the Human Head for Dosimetry of Mobile Telephones", IEEE Trans. on Electromagnetic Compatibility, Vol. 39, No. 1, pp. 55-61, February, 1997.

## **Appendix 2**

### **“Validation of FDTD Handset and Head Patterns by Measurement”**

**by**

**C.W. Trueman, S.J. Kubina, J.E. Roy and W.R. Lauber**

1998 IEEE APS Conference on Antennas and Propagation for Wireless Communications  
Waltham, Mass., Nov. 1-4, 1998



# Validation of FDTD Handset and Head Patterns by Measurement

C. W. Trueman  
S.J. Kubina

Electromagnetic Compatibility Laboratory,  
Concordia University,  
Montreal

J.E. Roy  
W.R. Lauber

Communications Research Centre,  
Ottawa

**Abstract**-This paper compares the principal plane radiation patterns of a portable radio handset at 850 MHz computed with the finite difference time domain method with measured radiation patterns. The agreement for the handset in isolation is excellent. The computed patterns of the handset operating near a box model of the head are compared with measured patterns with very good agreement. Finally the computed patterns of the handset operating near a sphere model of the head are compared with measured patterns, with very good agreement, but not quite as good as for the box. The comparisons demonstrate the effect of simple head models on the radiation patterns of a vertical handset, and provide a validation of the FDTD computations.

## Introduction

Fig. 1 shows a simple portable radio[1] using a quarter-wave monopole antenna, at 850 MHz. This "handset" is an aluminum box 5.35 by 1.74 by 16.77 cm, with an antenna 8.82 cm in length, located 0.87 cm from three adjacent edges of the case. In this paper, the handset is operated near simplified head models[1,2] that are easy to build and straightforward to model with FDTD, as a preliminary step to studying a full head phantom. The "box head" is a plexiglas box 17.07 by 13.89 by 21.06 cm, with a wall thickness of 0.51 cm. The box is filled with "brain liquid", a sugar, salt and water mixture having the electrical parameters of brain matter[3]. The permittivity and conductivity of the brain liquid were measured and the measured values were used in the computations. The "sphere head" is 20.68 cm in diameter with a wall thickness of 3.65 mm. The finite-difference time-domain(FDTD) method has been used extensively to evaluate the radiation patterns and near fields of portable radio handsets operating near head models[1] and this paper tests such computations against measurements.

## Measurement of the Radiation Patterns

The radiation patterns were measured with the head and handset in the mounting jig of Fig. 2, consisting of styrofoam blocks and fiberglass bolts, which holds the handset in a well-known, reproducible position relative to the head. The jig sits atop a styrofoam rotator column in a 6x6x6 meter anechoic chamber[1,2]. Fig. 2 shows the jig positioned

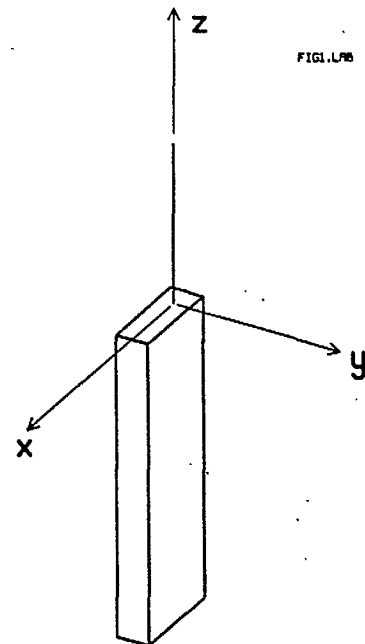


Fig. 1 The portable radio handset in the xyz coordinate system.



for rotation in the  $yz$  plane in Fig. 1, for measurement of the  $\phi = 90$  degree elevation pattern. The handset in the jig was aligned with the column's axis of rotation as accurately as possible using a laser beam. The handset contains a battery-operated oscillator at 850 MHz. An open-ended waveguide was mounted near the base of the rotator column to sample the field to provide a reference signal to phase-lock a network analyzer. The horizontal and vertical components of the field were measured by a dual-polarized ridged waveguide horn mounted about 330 cm from the handset. Considerable care was taken to optimize the quality of the measured data. Unwanted reflections in the anechoic chamber were identified and reduced with absorber. However, the

absorber in the chamber is designed for best performance above 1.5 GHz. The relatively short range from the handset to the horns incurs errors approaching one degree in the angle from the antenna feed point to the horn, compared to the true "far field" angle. These errors will primarily affect the measured patterns in the minima.

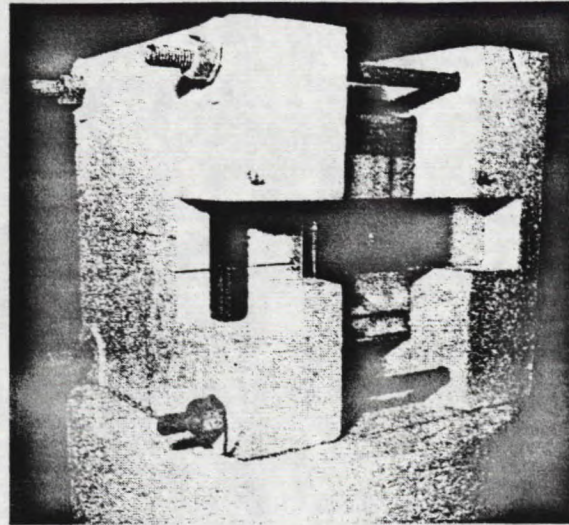


Fig. 2 The handset and box head mounted in the styrofoam jig, positioned on top of the rotator in the anechoic chamber.

### Patterns of the Handset Alone

Fig. 3 compares the measured and computed radiation patterns of the handset oriented vertically as shown in Fig. 1. Using a cell size of 2.205 cm, the handset case is very close to 24 by 8 by 76 cells with a 40 cell antenna. The FDTD code uses a PML 6 cells in thickness with a surface reflection coefficient of 0.001 and parabolic evolution of the conductivity. The surfaces of the handset and the tip of the antenna were separated from the first layer of the PML by 4 cells of free space or "whitespace". The FDTD computation was run for 4096 time steps with a sinusoidal generator at 850 MHz at the base of the monopole. The computed patterns were scaled to have an "isotropic level" field strength[1] of 0 dB.

The computations and measurements in Figs. 3, 4 and 5 are compared on the basis of equal radiated power. The three principal plane patterns were obtained from the measurement, and the radiated power was estimated from the RMS field strength summed over these three patterns. The measured data were scaled to have the same RMS field strength as the computations, estimated in the same way from the three principal plane patterns.

The agreement between the measurement and the computation in Fig. 3 is the best we have been able to obtain. In the azimuth pattern, at  $\phi = 0$  degrees the computed field is 1.3 dB compared with 0.8 dB in the measurement. In the elevation pattern for  $\phi = 0$ , the computed field at 130 degrees is 4.3 dB compared to the measured value of 4.8 dB. In the  $\phi = 90$  pattern at 116 degrees, the computed field is 4.8 dB compared to a measured field of 4.3 dB.



### The Handset and the Box Head

Fig. 4 compares the measured and computed radiation patterns of the vertical handset operating near the boxhead. With 2.205 mm cells, the box is modeled with 78 by 63 by 95 cells, with the box wall two cells thick. The computation includes the four fiberglass bolts of the mounting jig, but not the styrofoam blocks.

Fig. 4 shows very good agreement between the measurement and the computation for the handset and box head. The maximum measured  $E_\theta$  is 3.0 dB at 297 degrees, and the maximum computed field is 2.4 at 304 degrees. The cross-polarized field  $E_\phi$  has a maximum in the measured pattern of -4.1 dB at 129 degrees, compared to -4.4 dB at 128 degrees in the computation. Both the principal polarization and the cross polarization agree well in all three principal plane patterns.

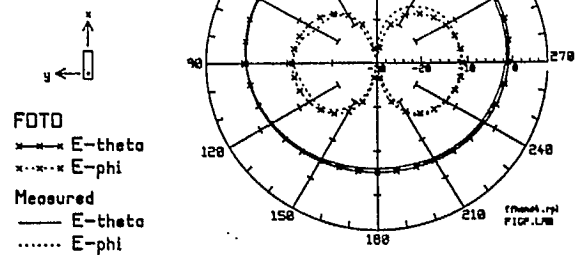
The computed patterns were examined in Ref. [1] without and with the four bolts used to hold the jig together. The bolts have only a minor effect on the patterns.

### The Handset and Sphere Head

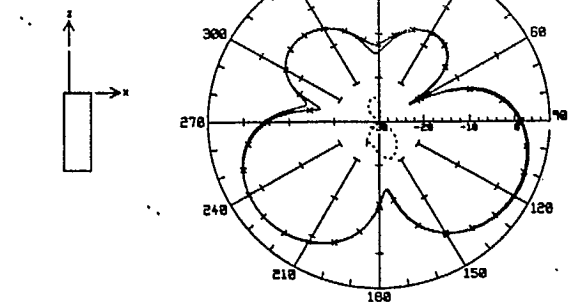
The sphere was solved without the bolts, and with a larger cell size of 4.41 mm. This will introduce more "staircasing" error into the sphere computation compared to that with a 2.205 mm cell. The 3.65 mm plexiglas wall thickness is modeled with one 4.41 mm cell. The sphere is 47 cells or 20.73 cm in diameter, compared to a true diameter of 20.68 cm.

The agreement of the sphere patterns with the measurement is not quite as good as that for the box. In the azimuth pattern the maximum computed field strength is 2.0 dB at 300 degrees, compared to 2.9 dB in the measured pattern. We note that the agreement in the

Handset Alone  
Azimuth Pattern



$\Phi=0$  Elevation Pattern



$\Phi=90$  Elevation Pattern

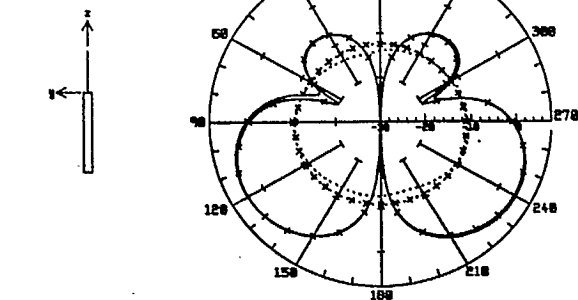
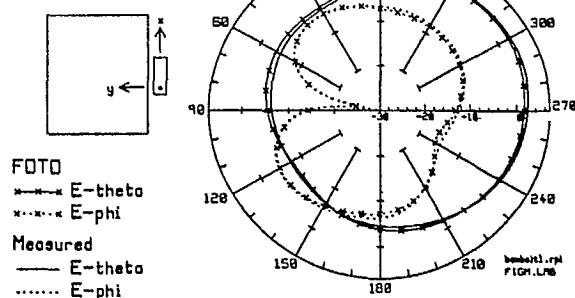


Fig. 3 The principal plane patterns of the handset alone.

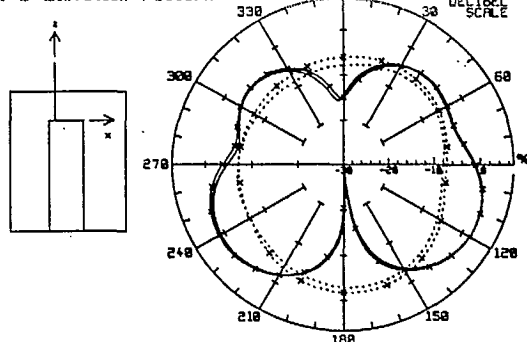
cross-polarized field in the  $\phi = 0$  pattern is not quite as good for the handset and sphere as for the handset and box. The larger difference may be due to the coarser cell size used in the sphere computation, or may be inherent to the staircased approximation of the curved surface. The author plans to explore this difference further.



Handset and Box Head  
Azimuth Pattern



Phi=0 Elevation Pattern



Phi=90 Elevation Pattern

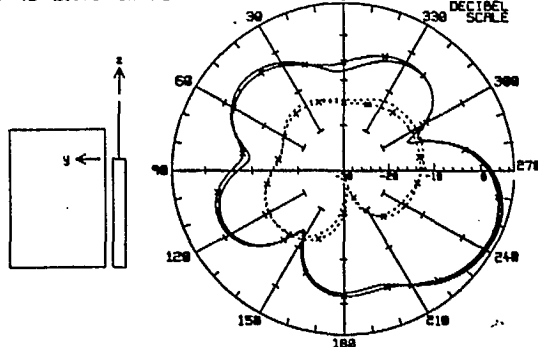
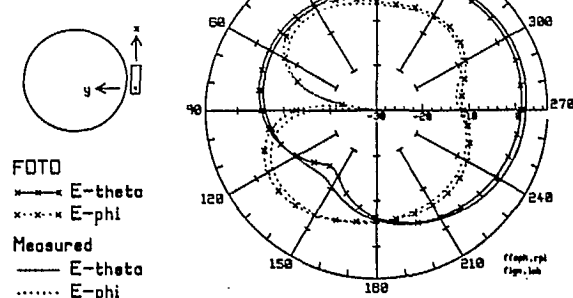
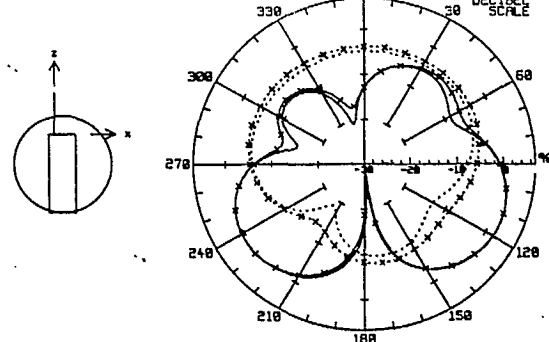


Fig. 4 The principal plane patterns of the handset and box head.

Handset and Sphere Head  
Azimuth Pattern



Phi=0 Elevation Pattern



Phi=90 Elevation Pattern

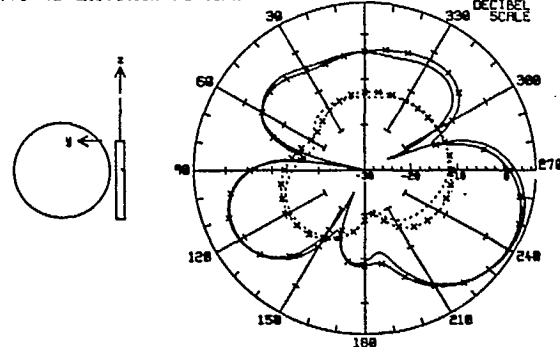


Fig. 5 The principal plane patterns of the handset and sphere head.

## References

1. C.W. Trueman and S.J. Kubina, "A Research Study on Electromagnetic (EM) Fields Produced by Portable Transceivers", Technical Note No. TN-EMC-94-01, ECE Dept. Concordia University, March 31, 1998.
2. C.W. Trueman, S.J. Kubina, J.E. Roy, W.R. Lauber, and M. Vall-Ilossera, "Validation of FDTD-Computed Handset Patterns by Measurement", Conference Proceedings, ACES Symposium, Monterey, California, March 16-20, 1998.
3. G. Hartsgrrove, A. Kraszewski and A. Surowiec, "Simulated Biological Materials for Electromagnetic Radiation Absorption Studies", *Bioelectromagnetics*, Vol. 8, pp. 29-36, 1987.

## **Appendix 3**

### **“Validation of the FDTD Near Fields of a Portable Radio Handset and a Simple Head”**

**by**

**C.W. Trueman, S.J. Kubina, D. Cule and W.R. Lauber**

Conference Proceedings, 15th Annual Review of Progress of the Applied Computational  
Electromagnetics Society  
Monterey, California, March 16-28, 1999.

# Validation of the FDTD Near Fields of a Portable Radio Handset and Simple Head

C. W. Trueman  
S.J. Kubina

Electromagnetic Compatibility Laboratory,  
Concordia University,  
Montreal

D. Cule  
W.R. Lauber

Communications Research Centre,  
Ottawa

**Abstract**-This paper examines the near field of a portable radio handset at 850 MHz operating near a model of the human head. The handset and head are solved by the finite-difference time-domain method. For the handset in isolation, the near field computed with FDTD is compared with that computed with the Numerical Electromagnetics Code, with excellent agreement. The near field was measured using a three-axis probe positioned with a planar scanner system in an anechoic chamber. The FDTD computation is compared with the measured near field and very good agreement is shown. Introducing a box or sphere model of the head changes the field of the handset. The measured near field of the handset and box head, and of the handset and sphere head are shown to be in good agreement with the FDTD computation.

## Introduction

Fig. 1 shows a portable radio "handset"[1] comprised of an aluminum box 5.35 by 1.74 by 16.77 cm, with an antenna 8.82 cm in length, located 0.87 cm from three adjacent edges of the case. The antenna is a quarter-wave monopole operating at 850 MHz. In this paper we investigate the vertical component of the near field of the handset in an  $xz$  plane located at  $y = -21.8$  mm in Fig. 1, where the base of the antenna is at the origin. The objective is to validate computations of the near field done with the finite-difference time-domain(FDTD) method[1,2].

## Near Field of the Handset Alone

Using a cell size of 2.205 cm, the handset case is very close to 24 by 8 by 76 cells, and the antenna is 40 cell edges in length. The perfectly-matched layer(PML) absorbing boundary[2] is used, 6 cells in thickness with a surface reflection coefficient of 0.001 and parabolic evolution of the conductivity. The handset is embedded in a cell space 96 by 88 by 188 cells with the base of the antenna on cell edge 41, 41, 113. The surfaces of the handset and the tip of the antenna are separated from the first layer of the PML by 30 cells of free space or "whitespace". In all cases in this paper the FDTD computation is

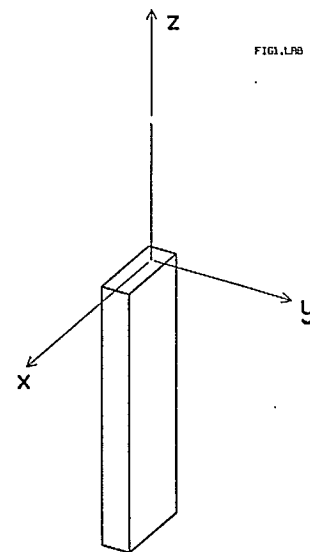


Fig. 1 The portable radio handset in the  $xyz$  coordinate system.



run for 4096 time steps with a sinusoidal generator at 850 MHz at the base of the monopole. The FDTD code is used to compute a set of "conical cut" radiation patterns[1] that cover the surface of the radiation sphere. The radiated power is computed from the patterns as

$$P_{rad} = \frac{1}{2\eta} \int_{\theta=0}^{\pi} \int_{\phi=0}^{2\pi} (E_{\theta}^2 + E_{\phi}^2) \sin \theta d\phi d\theta$$

and the fields presented in this paper are scaled to correspond to a radiated power of 600 mW.

An initial validation of the FDTD computation was obtained by comparing the near field of the handset computed with FDTD with that found using a wire-grid model of the handset[1] solved with the Numerical Electromagnetics Code(NEC)[3]. Fig. 2 shows the vertical component  $E_z$  of the near field of the handset in an  $xz$  plane in Fig. 1 at  $y=-21.8$  mm. The field is shown in decibels with 1 volt per meter as the 0 dB reference. The black contours were computed with FDTD. The region of space around the edges of the map corresponding to the PML layers were removed from the FDTD data. In Fig. 2, the FDTD-computed contours are superimposed on the near field computed with the wire-grid model of the handset, shown in gray. There is excellent agreement between the two computations. The near field is large surrounding the tip of the antenna, the top of the case and the base of the case. At the surface of the case the  $E_z$  component of the field would be zero. At our  $xz$  plane, 13.1 mm from the case surface, the near field falls to values below 24 dB over the center of the case. The frequency-domain, moment-method based NEC computation obtains almost the identical near fields to the time-domain FDTD method.

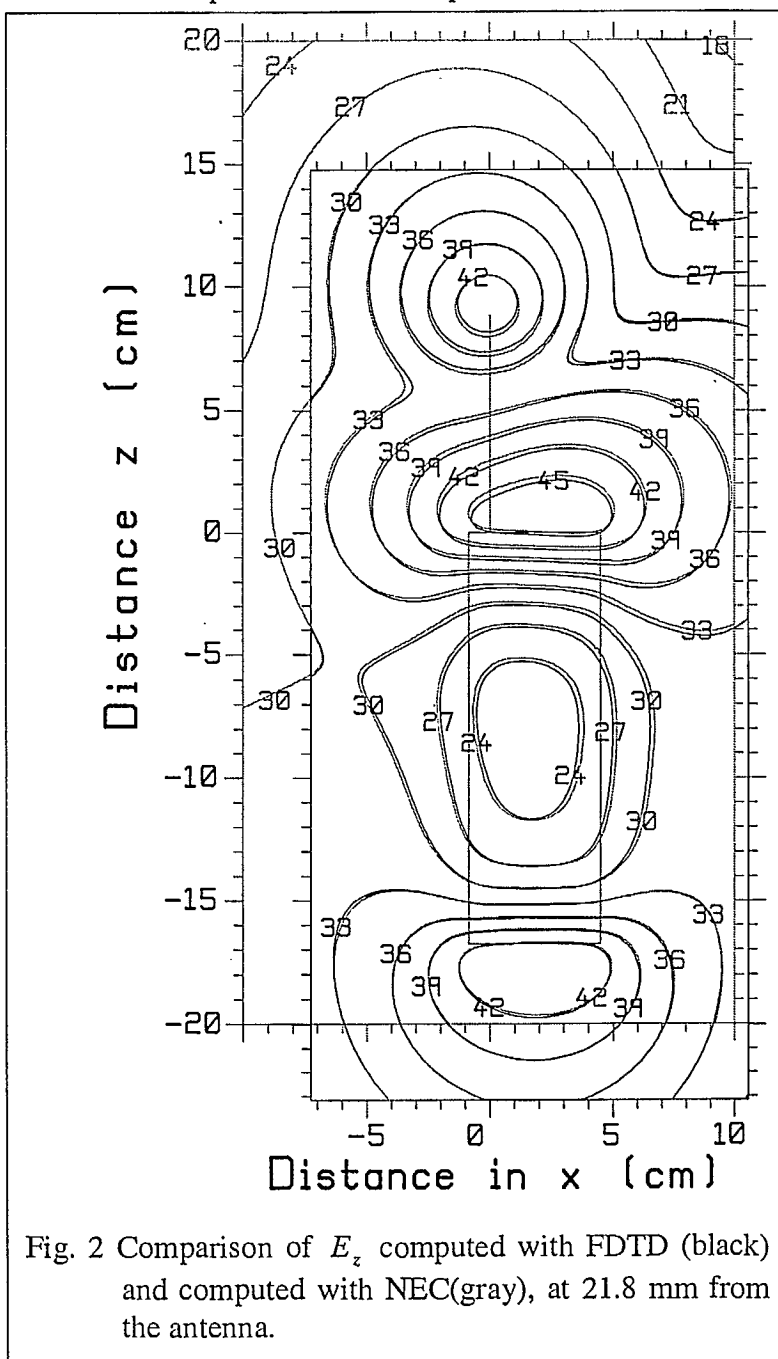


Fig. 2 Comparison of  $E_z$  computed with FDTD (black) and computed with NEC(gray), at 21.8 mm from the antenna.

### Measurement of the Near Field

The near field of the handset was measured[4] in an anechoic chamber 2.5 m in height and 3.74 m in width and depth. The ceiling and walls were lined with 12 inch thick absorber. The probe was moved over the measurement plane using an Orbit Advanced Technologies planar scanner. The scanner was covered with 12 inch absorber as much as possible. The positioning mechanism was covered with three-inch absorber.

A "DASY-2" three-axis probe[5] uses three small, orthogonal dipoles to measure the magnitude of each of the three components of the near field. The dipoles are terminated with Schottky diodes, which are connected with high-resistance lines to a battery-operated data acquisition unit at the base of the probe. The signals are then sent via a fiber-optic cable to a computer plug-in card. We note that the probe does not measure  $E_x$ ,  $E_y$ , and  $E_z$  at exactly the same point. Components  $E_x$  and  $E_z$  are measured at slightly offset points in the same  $xz$  plane; whereas  $E_y$  is measured in an  $xz$  plane 1.1 millimeters further from the tip of the probe.

The 850 MHz oscillator in the handset is powered by a rechargeable battery, with a life of about 2 hours, sufficient to measure a plane of the size presented in Figs. 3, 4 and 5. The oscillator output declines over the course of a measurement. The change in field strength over time was monitored and recorded, and the measured data presented in this paper has been compensated to account for declining battery power.

Fig. 3 compares the FDTD-computed(black) and measured(gray) contours for the handset alone at  $y=-21.8$  mm. The measured fields must be scaled to correspond in level to the computation. This was done by computing the RMS

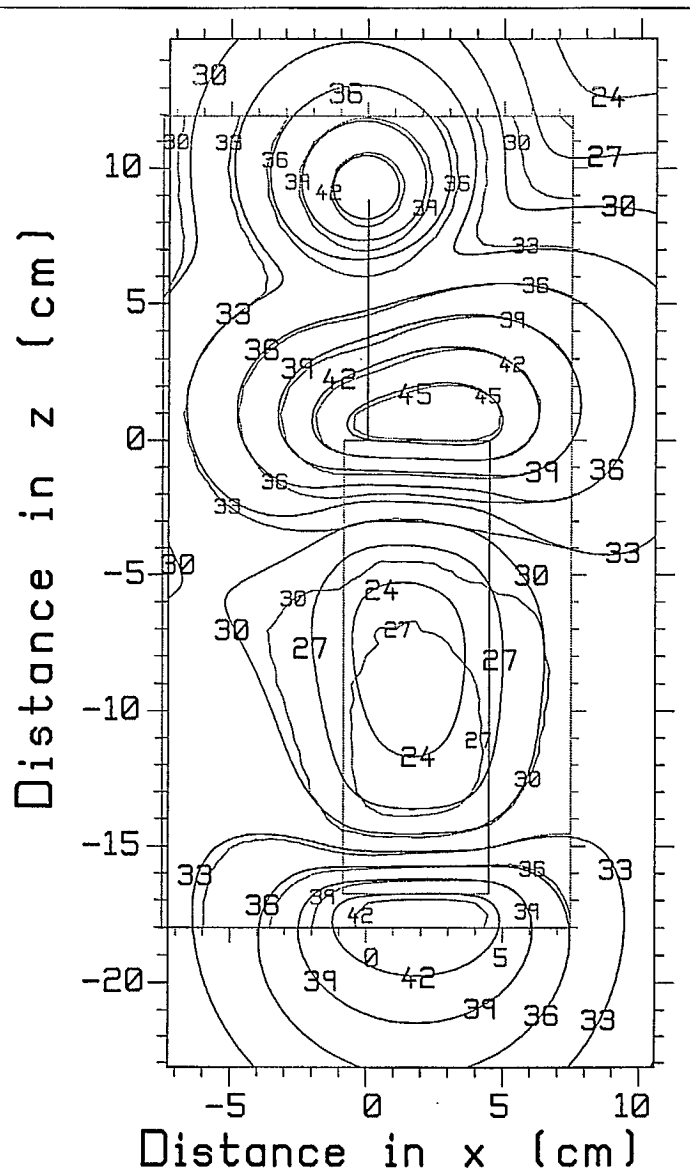


Fig. 3 Comparison of  $E_z$  computed with FDTD (black) and the measured field(gray), at 21.8 mm from the antenna.

field strength along a "tie line",

$$E_{RMS} = \sqrt{\frac{1}{L} \int E^2 dz}$$

where  $L$  is the length of the tie line. The tie line was chosen as the left-hand edge of the computed contour map in Fig. 3, at  $x=-7.277$  cm, from  $z=-18.01$  cm to  $z=11.95$  cm. If  $E_c$  is the RMS field along the tie line in the computation, and  $E_m$  the RMS field in the measurement, then the measured data is scaled by  $E_c/E_m$ . Tie-line normalization aligns the measured and computed contours to approximately the same level at the left edge of the contour map. If the maps are in good agreement, the remaining contours will then align well.

In Fig. 3 the computed contours (black) align very well with the measured contours (gray) around the tip of the antenna and the top of the handset case. At the base of the case the 42 dB contour is smaller in the measurement than in the computation. Over the surface of the case there is a large computed contour at 24 dB; whereas the measured contour over the case is 27 dB. The measured field is about 3 dB stronger over the case. The contours to the left of the antenna and handset case align quite well, particularly near the top of the handset case. In the top right-hand corner of the contour map, we note that the measured contours tend to lie somewhat further from the antenna than do the computed contours.

### The Handset and the Box Head

The "box head" is a plexiglas box 17.07 by 13.89 by 21.06 cm, with a wall thickness of 0.51 cm. The box is filled with "brain liquid", a sugar, salt and water mixture having the electrical parameters of brain matter [6]. The relative permittivity and conductivity of the brain liquid were measured to be 40.42 and 1.064 S/m, respectively, and these values were used in the computations. With the base of the antenna in Fig. 1 at the origin, the box head is located in the +y halfspace with one corner at  $x=-6.73$ ,  $y=1.81$  and  $z=-16.77$  cm. The bottom of the handset is at the same height as the bottom of the box head. Using 2.205 mm cells, the box is modeled in FDTD with 78 by 63 by 95 cells, and the plexiglas wall is two cells thick. The 2.205 mm cell size corresponds to one-tenth wavelength in the brain liquid at 2125 MHz. To find the coefficients for updating the electric field on each cell edge, the FDTD code averages the permittivity and conductivity of the four adjacent cells. The FDTD cell space was terminated with a PML as described above. A bigger cell space was used for the box head problem, 149 by 147 by 188 cells, which puts the base of the antenna on cell edge 67, 41, 113. The FDTD model was run for 4096 time steps, more than adequate to reach the sinusoidal steady state.

Fig. 4 shows the computed (black) field contours for the vertical component of the near field at  $y=-21.8$  mm. This  $xz$  plane is on the opposite side of the handset from the box head. Comparing Figs. 3 and 4 shows a 42 dB contour surrounding the tip of the antenna for both the handset alone and the handset and box head. The tip is well above the top of the box head. However, the contour for the handset alone near the top of the handset is at 45 dB, but only 42 dB for the handset and box head. Similarly, the contour at the bottom of the handset is 42 dB for the handset alone but only 39 dB for the handset and box head. The computed field over the surface of the handset falls to values less than 18 dB in Fig. 4, much less than the field of 24 dB for the handset alone in Fig. 3.

Fig. 4 compares the computed (black) and measured (gray) contours for the vertical component of the field. The measurement was scaled to match the level of the computation along a



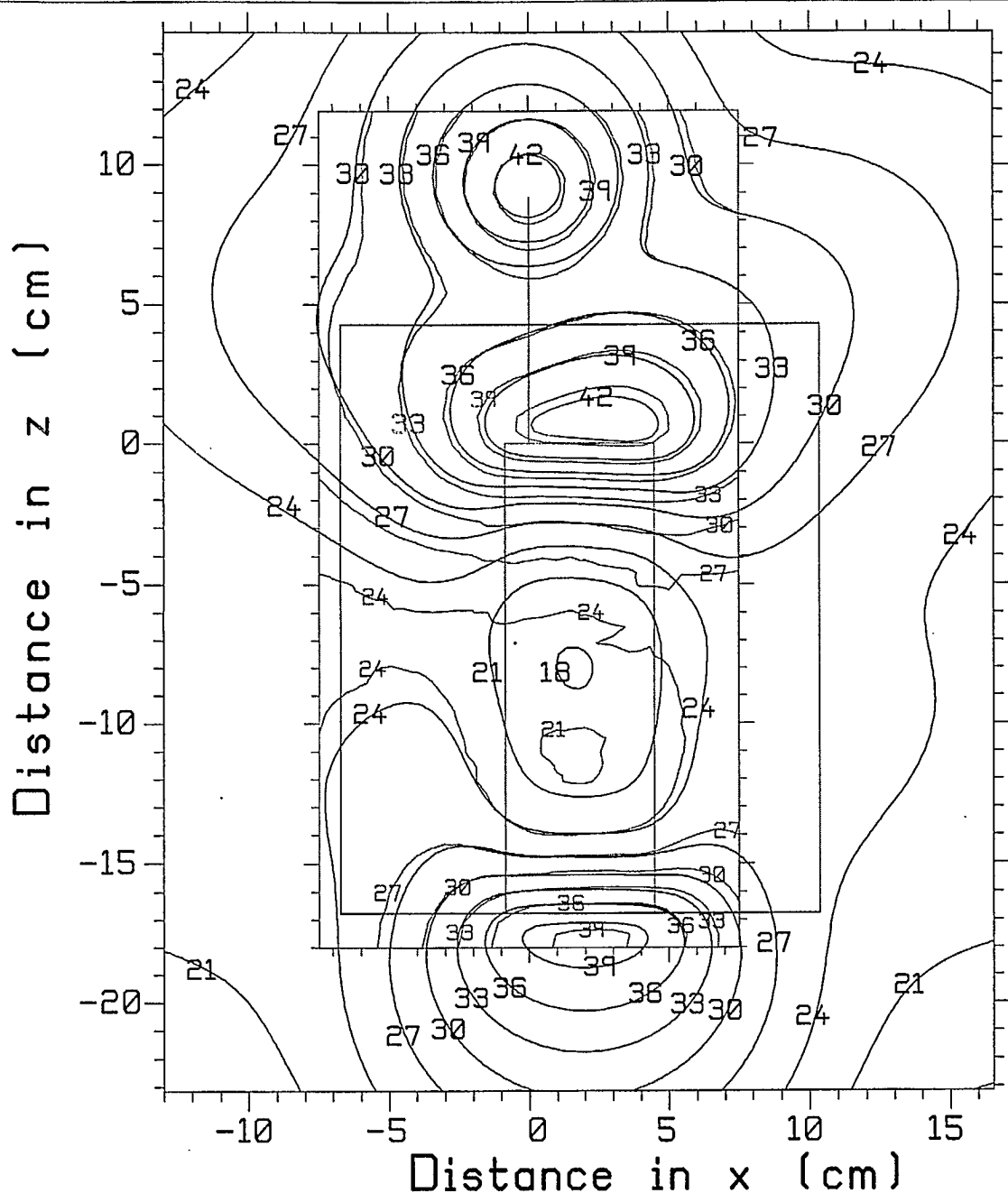


Fig. 4 Comparison of the computed(black) and measured(gray)  $E_z$  for the handset and box head, at 21.8 mm from the antenna.

tie line along the left edge of the measured contour map, at  $x = -7.494$  cm, from  $z = -18.01$  to  $z = 11.95$  cm. The measurement and computation agree very well near the tip of the antenna. At the top of the handset case, the computed 42 dB contour is somewhat smaller in the computation than in the measurement. Conversely at the base of the handset the computed 39 dB contour is larger than the measured 39 dB contour. Over the surfaces of the handset case, the measured field falls to values below 21 dB, considerably smaller than the smallest measured contour of 27 dB for the handset alone. We note that the computed field falls to below 18 dB, about 3 dB less than the measured

field. Also the location of the smallest fields in the measurement is more towards the bottom of the case than in the computation.

#### Handset and Sphere Head

The "sphere head" is 20.68 cm in diameter with a wall thickness of 3.65 mm. The box head and the sphere head have nearly the same volume. With the base of the antenna at the origin, the center of the sphere is at  $x=1.81$ ,  $y=12.15$  and  $z=-6.43$  cm. This puts the lowest point on the sphere at the same height as the bottom of the handset case. The sphere's curved surface was

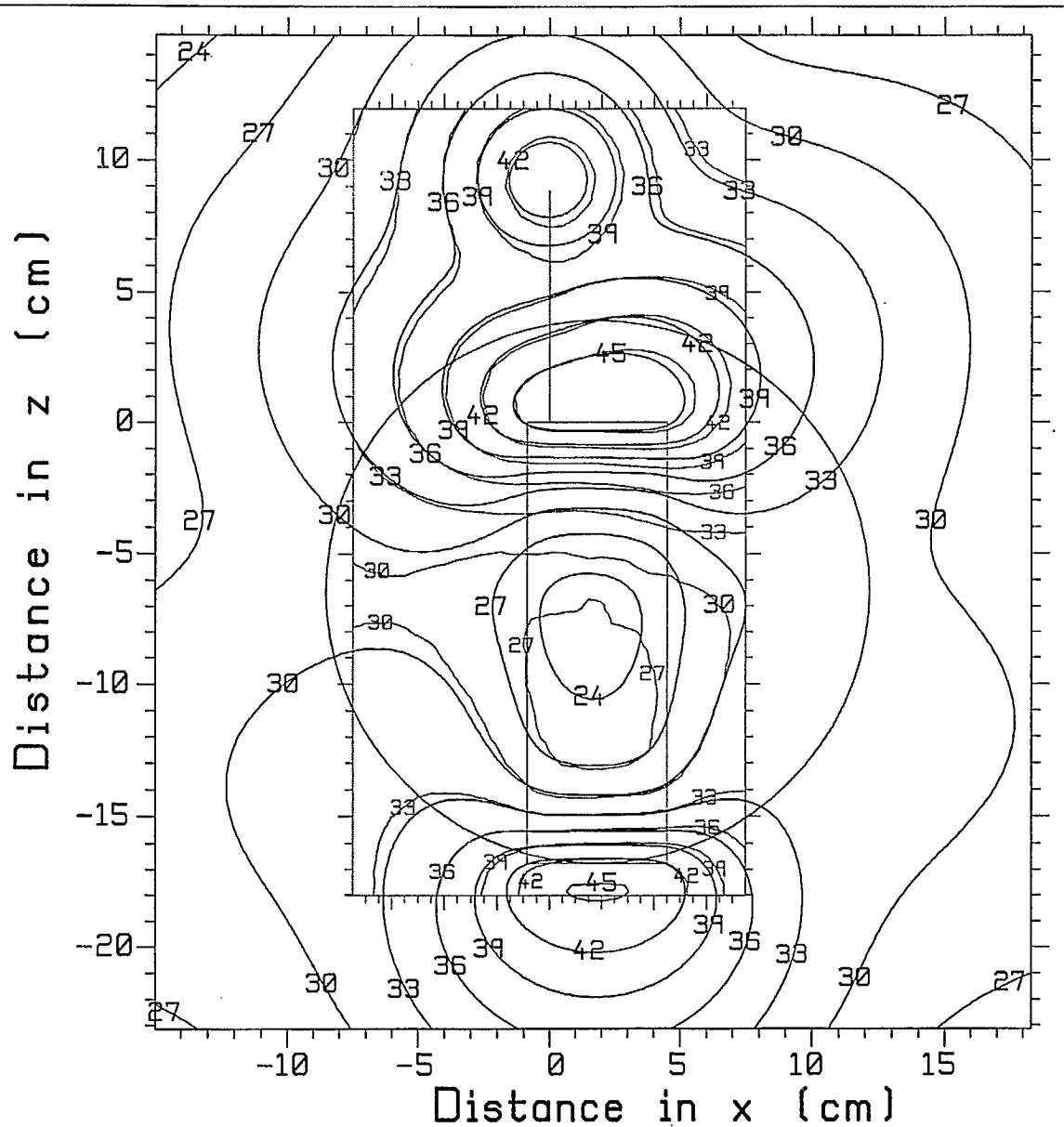


Fig. 5 Comparison of the computed(black) and measured(gray)  $E_z$  for the handset and sphere head, at 21.8 mm from the antenna.

approximated with a "staircase" of 2.205 mm cells. The 3.65 mm plexiglas wall thickness is about 1.65 cells thick; it was approximated as either one cell or two cells thick, being the difference

between the staircase modeling the outer sphere and the inner sphere defining the plexiglas wall. The sphere is 94 cells or 20.73 cm in diameter, a reasonable approximation of the true 20.68 cm diameter. The FDTD code uses coefficients for updating the electric field on each cell edge which average the permittivity and conductivity of the four adjacent cells. This tends to smooth the staircased surface of the sphere. The FDTD cell space was terminated with a PML as described above. The sphere head required a larger cell space than the box head, 166 by 178 by 188 cells, with the base of the antenna on cell edge 76, 41, 113.

Fig. 5 shows the vertical component of the near field of the sphere in an  $xz$  plane at  $y=-21.8$  mm. Comparing the near field of the handset and box head, Fig.4, and the handset and sphere head, Fig. 5, we see that the field around the tip of the antenna is about the same at 42 dB. At the top of the handset case the field of the handset and sphere head shows a large 45 dB contour, considerably stronger than that of the handset and box head. Again at the base of the handset case, the handset and sphere head field exceeds 45 dB, whereas the handset and box head field has a small 39 dB contour. Indeed, the fields of the handset and sphere head are much more like the fields of the handset alone in Fig. 3. The square shape of the box head keeps the box close to the handset case at the top and bottom of the handset case. The round surface of the sphere is close to the handset near the center of the case, but curves away from the handset at the top of the case and particularly at the bottom of the case.

Comparing the handset and sphere head fields of Fig. 5 with the handset fields of Fig. 3, the 45 dB contour around the top of the case is larger with the sphere head than for the handset alone. The handset and sphere head shows fields higher than 45 dB near the bottom of the case, whereas for the handset alone there is no 45 dB contour.

Fig. 5 compares the FDTD-computed field (black contours) with the measured field (gray contours). The measured data was scaled to the level of the computed data along the left edge of the contour map, as for the box head. The computation and measurement agree very well. The 42 and 39 dB contours at the tip of the antenna almost coincide. The 45 dB contour at the top of the handset case is almost the same. At the bottom of the case the 39 and 42 dB contours correspond well. However, the computation shows a small region with fields in excess of 45 dB, not seen in the measurement. Over the surface of the handset case the computed fields fall below 24 dB, but the measured fields never fall as low as this.

## Conclusion

This paper has presented a validation of FDTD computations of the vertical component of the near field of a portable radio handset in a plane close to the case of the handset. The field computed with FDTD was compared with a moment-method computation of the near field with excellent agreement. The near field of the handset was measured and shown to be in very good agreement with the computed near field. The field of the handset and box and sphere models of the head were measured, and very good agreement with the FDTD computation was shown. The fields are strong near the tip of the antenna, and near the top and bottom of the handset case. The computed fields in these regions agree very well with the measured fields particularly for the handset alone and for the handset and sphere head.

The agreement is slightly less good for the handset and box head. We note that the box head cell model uses 4 cells between the handset surface and the box surface, or 8.82 mm. However, the actual separation is 9.4 mm, almost half a cell further away. This modeling error could be reduced



by more sophisticated material averaging in the FDTD code, or by discarding the Yee FDTD algorithm in favor of scheme able to resolve the geometry more precisely.

This paper compared the fields of the handset, handset and box head, and handset and sphere head on the basis of equal *radiated* power. The box head near field in Fig. 4 is more different from the field of the handset in isolation, Fig. 3, than is the field of the handset and sphere head in Fig. 5. The box head reduces the field strength near the top and the bottom of the handset by 3 dB, but changes the field near the tip of the antenna very little. The sphere head curves away from the handset, and so the handset and sphere head fields are comparable to those of the handset alone near the top and bottom of the box.

A real head is neither a sphere nor a box. It is more like a sphere at the top of the head, and perhaps more box-like at the jaw and neck. Nor is the handset held vertically in normal operation. If held in a natural position, our rather large handset is close to the head at the top of the handset, above and behind the ear. There the fields are likely to be like those of the handset and box head. But the bottom of the handset juts out beyond the jaw, and so the fields are likely to be close to those of the handset and sphere. Measurements are planned for the handset and a realistic five-tissue phantom of the head, with the handset positioned realistically relative to the head.

## References

- [1] C.W. Trueman and S.J. Kubina, "A Research Study on Electromagnetic (EM) Fields Produced by Portable Transceivers", Final Report in Contract Number U68000-7-0726/001/ST, Technical Note No. TN-EMC-94-01, Dept. of Electrical and Computer Engineering, Concordia University, March 31, 1998.
- [2] "Advances in Computational Electrodynamics – The Finite-Difference Time-Domain Method", A. Taflove, editor, Artech House, 1998.
- [3] G.J. Burke, A.J. Poggio, J.C. Logan and J.W. Rockway, "NEC - Numerical Electromagnetics Code for Antennas and Scattering", 1979 IEEE International Symposium on Antennas and Propagation Digest, IEEE Publication No. 79CH1456-3AP, Seattle, Washington, June, 1979.
- [4] D. Cule and J. Bertrand, "Measurements of the Electromagnetic Near-Fields Produced by a Portable Radio Transmitter", CRC Technical Memorandum VPRB-02-98, August, 1998.
- [5] T. Schmid, O. Egger and N. Kuster, "Automated E-Field Scanning System for Dosimetric Assessments", IEEE Trans. On Microwave Theory and Techniques, Vol. MTT-44, No. 1, pp. 105-113, January, 1996.
- [6] G. Hartsgrrove, A. Kraszewski and A. Surowiec, "Simulated Biological Materials for Electromagnetic Radiation Absorption Studies", *Bioelectromagnetics*, Vol. 8, pp. 29-36, 1987.

## **Appendix 4**

### **“Radiation Patterns of a Portable Radio Handset and Simple Head Models”**

by

**C.W. Trueman, S.J. Kubina, W. Lauber and J. Roy**

Paper prepared for submission for the  
Canadian Journal of Electrical and Computer Engineering

# Radiation Patterns of a Portable Radio Handset With Simple Head Models

C. W. Trueman  
S.J. Kubina

Electromagnetic Compatibility Laboratory,  
Concordia University,  
7141 Sherbrooke Street West,  
Montreal, Quebec H4B 1R6

J.E. Roy  
W.R. Lauber

Communications Research Centre,  
P.O. Box 11490, Station H  
Ottawa, Ontario K2H 8S2

**Abstract-** This paper compares the computed and measured principal plane radiation patterns of a vertical handset operating near simple box and sphere models of the head, for both the principal component and the cross-polarized component of the electric field. The finite-difference time-domain method is used to model the handset and head and to predict the far fields. The radiation patterns are measured in a 6.1 m cubical anechoic chamber using a battery-operated oscillator within the handset. Very good agreement is shown for both polarizations of the electric field, for the handset alone and for the handset and the simple head models. The differences between the measured and computed patterns are about the same for the handset and sphere head as for the handset and box head. This suggests that modeling the curved surface of the sphere with a staircase of cubical cells does not significantly increase the modeling error.

## I. Introduction

A cellular telephone handset communicates with a base station typically located on top of a nearby building. Often the base station uses only the  $E_\theta$  component of the electric field[1]. The handset itself typically radiates both  $E_\theta$  and  $E_\phi$  over the whole radiation sphere. The user holds the handset against the ear tilted about 60 degrees to the vertical[2,3]. The tilt angle strongly affects the split of the radiated energy between the two electric field polarizations. And, the handset antenna's fields couple strongly to the head, which changes the radiation patterns and the split of energy between the two polarizations. Thus predicting the handset's field over the radiation sphere requires modeling the head, modeling handset in a typical orientation relative to the head, and possibly modeling the hand holding the handset as well.

The human head is made up of biological materials such as skin, muscle, bone and brain tissue that have high relative permittivity, typically 20 to 60, and conductivity from 0.3 to 1.1 S/m[3,4,5], high enough to be considered quite lossy. Some materials, such as the eye and cerebral spinal fluid, have even higher permittivity and loss. The finite-difference time-domain(FDTD) method[6,7] is commonly used to model the human head because it can solve lossy dielectric objects of arbitrary internal complexity. The head has been represented with simple models such as a sphere of muscle tissue[8], and with realistic models on anatomical cross-sections [2,3,4,5,9].



A project organized by the Communications Research Centre, Ottawa uses both measurement and numerical computation to study the near fields[10] and far fields[11] of a handset and a model of the head. In this paper the far fields of a vertical handset are examined for the handset in isolation and near simple box and sphere heads. The measured radiation patterns include both polarizations of the electric field in the three principal planes. We will compare the measured and computed  $E_\theta$  and  $E_\phi$  field components on the basis of equal radiated power. The objective of the present paper is to demonstrate the degree of agreement that is possible between measurements and FDTD computations for a typical handset and head configuration.

Further work in this project will model the handset held tilted relative to a realistic phantom representing the head. Both computations and measurements are underway for this new phase of the project[12].

### A. Comparisons with Measurements

Concern over the degree of agreement to be expected between fields computed with FDTD and measured fields has led to various published comparisons. Ref. [8] provides a validation of the FDTD-computed radiation patterns against measured patterns for a handset alone and for the handset and a sphere model of the head, at 914 and 1890 MHz. The agreement is not nearly as good as that presented below for the  $E_\theta$  or principal polarization, and is very poor for the cross-polarized field. Ref. [7] compares the computed azimuth pattern with a measured pattern at 835 MHz for a handset alone and for a handset and a realistic model of the head; only the principal polarization is shown, but the agreement is good. Ref. [13] compares gain measurements with FDTD computations at 900 MHz in the azimuth plane and in one elevation plane for a simple handset with no head model, with good agreement. The measurement setup includes a cable feeding the signal to the handset. Ref. [14] compares measurements and computations of the electric field in the azimuth plane for a handset tilted 70° to the vertical, at 1821 MHz. The agreement is much poorer than shown below. The setup includes a feed cable. The paper also compares computations and measurements for the handset near a head phantom, again with fair agreement. Ref. [15] examines the radiation patterns of a handset tilted at 30 degrees to a realistic model of the head. The vertical polarization in the azimuth plane only is compared between computations and measurements, with fair agreement. No cross-polarized field is shown. The computational model of the head is based on detailed anatomy; whereas the measurement model is a greatly simplified representation of the head's internal structure.

### B. Modeling of the Handset and Head with FDTD

In this paper the handset of Fig. 1 is oriented vertically with its surfaces parallel to the coordinate planes. The proportions of the handset's metallic case were chosen such that its size is accurately represented with 24 by 8 by 76 FDTD cells of size of 2.205 mm, to minimize the error associated with the FDTD model of the handset itself. The paper seeks to assess the accuracy of the computed radiation patterns by comparison with measured patterns.

FDTD models objects in terms of parallelepiped "cells" filled with dielectric material. The cell is usually chosen to be cubical. Such cell models represent flat surfaces parallel to the coordinate planes quite well; the true position of the surface is

approximated with the position of the nearest plane of cell surfaces. For a dielectric object, the relative permittivity and conductivity of the materials on either side of the surface enter into the update equations for the electric field components in the surface[6,7]. The value of the permittivity and conductivity used in the update equations can be averaged according to the fraction of the volume of the adjacent cells filled by each material[7,16]. This permits the position of a dielectric surface to be more closely approximated. Because the surfaces of the box model of the head are parallel to the coordinate planes, the box can be represented quite accurately with FDTD cells and so the fidelity of the computational model of the box head is expected to be good.

In FDTD, curved surfaces, must be approximated with a "staircase" of FDTD cells. Again, averaging the permittivity and conductivity used to update the electric field for cell edges in the surface of the staircase increases the fidelity of the representation of the true position of the surface. Such averaging tends to smooth the staircased surface. But a "modeling error" associated with "staircasing" the curved surface remains. We might expect the fidelity of the computational model of the sphere to be poorer than that of the box. In this paper, we will compare the differences between the computed principal plane patterns and the measured patterns for three configurations: the handset alone; the handset and box head; and the handset and sphere head. Examining the differences suggests that there is no greater error in the sphere model due to staircasing the sphere's surface.

## II. Radiation Patterns of the Handset Alone

Figure 1 shows a simple portable radio "handset" and gives the handset's orientation in the  $xyz$  coordinate system. Fig. 2 gives the handset dimensions. The handset comprises an aluminum box 5.35 by 1.74 by 16.77 cm, with an antenna 8.82 cm in length, located 0.86 cm from the edge of the case [17]. The antenna is a quarter-wave monopole operating at 850 MHz.

### A. FDTD Model of the Handset

The handset case is represented for computation with 24 by 8 by 76 FDTD cells of size of 2.205 mm, and thus measures 5.29 by 1.76 by 16.76 cm, close to the actual dimensions. The antenna is modeled with a row of 40 perfectly-conducting cell edges. A sinusoidal voltage generator is applied to the cell edge at the base of the antenna. The generator gradually turns on with a Gaussian envelope. Yee's FDTD algorithm[6] is used. The handset surfaces and the tip of the antenna are separated from the outer boundary of the cell space by ten cells. The four cells adjacent to the handset are free-space cells. The remaining 6 cells make up a "perfectly-matched layer" absorbing boundary[7,18] with a surface reflection coefficient of 0.001 and parabolic evolution of the conductivity. The FDTD algorithm is run for 4096 time steps for all the problems in this paper, though far fewer steps are sufficient to reach the sinusoidal steady state for the handset in isolation. The amplitude and phase of the electric field and magnetic field components are found on a closed integration surface that is located at the middle of the four-cell free-space layer. The far field are found efficiently after the FDTD computation is complete, using a frequency-domain near-to-far zone transformation[7].

## B. Computing the Radiated Power

Radiation patterns are compared in this paper on the basis of equal radiated power. The radiated field is computed over the whole radiation sphere by calculating the set of "conical cut" radiation patterns at  $\theta = 25^\circ, 37^\circ, 45^\circ, 53^\circ, 60^\circ, 66^\circ, 72^\circ, 78^\circ, 84^\circ, 90^\circ, 96^\circ, 102^\circ, 108^\circ, 114^\circ, 120^\circ, 127^\circ, 135^\circ, 143^\circ$ , and  $155^\circ$ . Each pattern is computed in one-degree steps for  $0^\circ \leq \phi \leq 360^\circ$ . Then the radiated power is evaluated using

$$P_{rad} = \frac{1}{2\eta} \int_{\theta=0}^{\pi} \int_{\phi=0}^{2\pi} (E_{\theta}^2 + E_{\phi}^2) \sin \theta d\phi d\theta \quad \dots(1)$$

The "isotropic level" is a reference field strength that, if radiated uniformly in one polarization over the whole radiation sphere, radiates the same amount of power. It is given by

$$E_{iso} = \sqrt{\frac{\eta P_{rad}}{2\pi}} \quad \dots(2)$$

The radiated fields will be graphed in dB with the isotropic level field strength as the 0 dB reference level.

## C. Radiation Patterns of the Handset Alone

Fig. 3 shows the principal plane patterns for the handset oriented vertically as in Fig. 1. In the "azimuth pattern",  $\theta = 90^\circ$  and  $0^\circ \leq \phi \leq 360^\circ$ , the handset has an approximately circular pattern in  $E_{\theta}$ , with a field strength of 1.3 dB in the "forward" or  $\phi = 0^\circ$  direction and -5.2 dB in the "backward" or  $\phi = 180^\circ$  direction. The cross-polarized field has a figure-eight pattern with maximum field strength -11.1 dB. To graph the "elevation pattern for  $\phi = 0^\circ$ " it is convenient to allow the  $\theta$  angle to vary from  $0^\circ$  to  $360^\circ$ , although strictly speaking the pattern should be graphed in two halves, with  $\phi = 0^\circ$  and  $\phi = 180^\circ$ , varying  $0^\circ \leq \theta \leq 180^\circ$  in each case. The elevation pattern in Fig. 3 shows that this handset oriented vertically directs much of its energy down towards the ground. There is a sharp minimum in the forward direction at about  $30^\circ$  elevation above the azimuth plane, and a minimum in the backward direction at about  $15^\circ$  elevation. The  $E_{\phi}$  field component should be zero in the handset-alone  $\phi = 0^\circ$  pattern due the symmetry of the handset model. In the FDTD computation the maximum field strength in  $E_{\phi}$  is about -65 dB, suggesting a "noise floor" for the computed pattern data when single-precision arithmetic is used. The "elevation pattern for  $\phi = 90^\circ$ " shows that much of the energy of the handset is directed at the ground. There are minima at about  $23^\circ$  elevation above the azimuth plane on either side. The cross-polarized field has a maximum value of about -10.7 dB.

## D. Errors due to Cell Size

To assess the dependence of the handset patterns on the cell size, the patterns presented in Fig. 3 using 2.205 mm cells were compared with patterns computed with



4.41 mm cells. In the  $\phi = 0^\circ$  elevation pattern, the large lobes in  $E_\theta$  at  $117^\circ$  and  $232^\circ$  are almost independent of the cell size, with differences of less than 0.03 dB. The smaller lobe at  $313^\circ$  changes by about 0.4 dB. The minimum at  $282^\circ$  changes by 1.6 dB. The deeper minimum at  $60^\circ$  changes by 3.4 dB. In the  $\phi = 90^\circ$  elevation pattern, the main lobe in  $E_\theta$  changes by only 0.01 dB with the change in cell size. The minor lobe changes by 0.4 dB. The minimum at  $69^\circ$  changes by 2.6 dB. Thus the dependence on the cell size is small in the main lobes but as much as 3.4 dB in the minima. We should not expect precise agreement with the measurements in the minima of the patterns.

### III. Measurement of the Radiation Patterns

#### A. Measurement Setup

The handset is an aluminum box with a removable cover, containing an 850 MHz oscillator and a battery to power it. The radiation patterns were measured[19] using the setup shown in Fig. 4. The handset and head model were mounted atop a styrofoam rotator column at the center of a 6.1x6.1x6.1 meter anechoic chamber. The handset was aligned with the column's axis of rotation as accurately as possible using a laser beam. An open-ended waveguide was mounted near the base of the rotator column to sample the field to provide a reference signal to phase-lock a network analyzer. The horizontal and vertical components of the field were measured by a dual-polarized ridged waveguide horn mounted about 330 cm from the handset. Considerable care was taken to optimize the quality of the measured data. Unwanted reflections in the anechoic chamber were identified and reduced with absorber. However, the absorber in the chamber is designed for best performance above 1.5 GHz. The relatively short range from the handset to the horns incurs errors approaching one degree in the angle from the antenna feed point to the horn, compared to the true "far field" angle. These errors will primarily affect the measured patterns in the minima.

#### B. Reference Level for the Measured Patterns

Ideally, the computations and measurements should be compared on the basis of equal radiated power. But the radiated power from the measurement model of the handset and head is not easily determined. The power output from the oscillator is not well known, nor the input impedance of the antenna, which is strongly affected by the presence of the head. Also, the lossy material of the head absorbs power. Only the principal plane patterns were measured. The radiated power was estimated from the total power radiated in the principal plane patterns,

$$P_{ref} = \frac{1}{2\eta} \left[ \int_{\phi=0}^{2\pi} (E_{1\theta}^2 + E_{1\phi}^2) d\phi + \int_{\theta=0}^{2\pi} (E_{2\theta}^2 + E_{2\phi}^2) d\theta + \int_{\theta=0}^{2\pi} (E_{3\theta}^2 + E_{3\phi}^2) d\theta \right] \quad \dots(3)$$

where  $E_{1\theta}$  and  $E_{1\phi}$  are the field strengths in the azimuth pattern,  $E_{2\theta}$  and  $E_{2\phi}$  are the fields of the  $\phi = 0^\circ$  elevation pattern and  $E_{3\theta}$  and  $E_{3\phi}$  are the fields of the  $\phi = 90^\circ$  elevation pattern. The power in the computed principal plane patterns,  $P_C$ , is calculated

with Eqn. (3), as is the power in the measured principal plane patterns,  $P_M$ . Then the measured field strengths are scaled by  $F = \sqrt{P_C/P_M}$  to compare the patterns on the basis of approximately equal radiated power. Note that this procedure uses all six measured patterns (two polarizations in three principal planes). The same factor is used to scale all six measured patterns, which preserves the relative field strength of the principal and cross-polarized field in all cases.

### C. Error Associated with the Finite Range of 330 cm.

The range of 330 cm from the handset to the measurement horn is approximately ten times the minimum required to be in the "far field" using the common  $2D^2/\lambda$  criterion. Hence we expect to measure the main lobes of the antenna patterns accurately. To assess the error that the 330 cm range introduces into the pattern minima, the handset was modeled with a wire grid, and solved with the "Numerical Electromagnetics Code"(NEC)[20]. NEC can compute both the true "far field" radiation patterns, and the radiation pattern that is seen by an observer 330 cm from the handset.

Comparing the  $\phi = 0^\circ$  far field pattern with the near field at 330 cm, both computed with the NEC code, shows that the error in the main lobe in  $E_\theta$  at  $116^\circ$  is only 0.08 dB. The minor lobe at  $315^\circ$  has an error of 0.28 dB. The minima are more strongly affected by the closeness of the observer. The minimum at  $60^\circ$  of -23.3 dB in the far field is -19.4 dB in the near field, a difference of 3.9 dB. The minimum at  $283^\circ$  of -14.2 dB in the far field falls at -15.5 dB in the near field, a difference of 1.3 dB. Thus the 330 cm range has a very small effect on the main lobes, introduces errors of 0.3 dB in minor lobes 8 dB below the main lobe, and in a minimum 23 dB down from the main lobe, the error is 3.9 dB.

## IV. Comparison of Computed and Measured Handset Patterns

Fig. 3 compares the computed and measured principal plane patterns for the handset. This section examines the degree of agreement between the measured and computed patterns in Fig. 3.

In assessing the agreement between measured and computed radiation patterns such as those of Fig. 3, it is natural to compare the computed maxima with the measured maxima, and the computed minima with the measured minima. To make this comparison quantitative, we will compare the angles at which the maxima or minima occur, and the field strength values. The  $\theta = 90^\circ$  pattern in  $E_\theta$  is very simple, with a computed maximum at  $0^\circ$ , 1.3 dB and a measured maximum at  $1.5^\circ$ , 0.8 dB. The patterns, both from FDTD and from measurement, are reported at one degree increments. The measured  $E_\theta$  is constant from  $0^\circ$  to  $3^\circ$  hence the position of the maximum will be taken as at  $1.5^\circ$ . Then the error between the measurement and the computation is  $1.5^\circ$  in the angular position of the maximum and 0.5 dB in the field strength.

Comparing the agreement for the  $E_\phi$  polarization is more complicated. The computed maxima fall at  $90^\circ$ , -11.14 dB and  $270^\circ$ , -11.14 dB; and the measured at  $86.5^\circ$ , -11.46 dB and  $270^\circ$ , -11.39 dB. The maxima have unsigned errors of  $3.5^\circ$ , 0.32 dB for

the first maximum and  $0^\circ$ , 0.25 dB for the second. We will characterize the error between the computation and the measurement with the *average error* in the position of the maxima,  $1.8^\circ$ , and the *average error* in the field strength at the maxima, 0.3 dB. These are reported in Table 1. The computed data has minima at  $0^\circ$ , -91.3 dB and  $180^\circ$ , -77.4 dB. The measured data has minima at  $8^\circ$ , -56.5 dB and  $178^\circ$ , -41.5 dB. The unsigned errors are  $8^\circ$ , 34.8 dB, and  $2^\circ$ , 35.9 dB. This illustrates that the agreement between the computation and the measurement in sharp, deep minima can be quite poor. As discussed above the accuracy of both the computation and the measurement is degraded in the minima. Averaging the unsigned errors over the two minima obtains an average positional error of  $5^\circ$  and an average field strength error of 35.4 dB, as reported in Table 1.

To further illustrate the concept of "average error" and how it is calculated, consider  $E_\theta$  in the  $\phi=0^\circ$  elevation pattern. The computed pattern has maxima at  $(31.5^\circ, -6.74 \text{ dB})$ ,  $(115.5^\circ, 4.3)$ ,  $(232.5^\circ, 3.53)$ , and  $(315^\circ, -4.15)$ , and the measured at  $(32.5^\circ, -6.51 \text{ dB})$ ,  $(115^\circ, 4.77)$ ,  $(232.5^\circ, 3.50)$ , and  $(316^\circ, -4.01)$ . The unsigned errors are  $(1^\circ, 0.23 \text{ dB})$ ,  $(0.5^\circ, 0.47)$ ,  $(0^\circ, 0.03)$  and  $(1^\circ, 0.14)$ . The "average error" in position is the average value over the four angular errors,  $0.6^\circ$ , and similarly the "average error" in the field strength is 0.2 dB. Thus the agreement in the maxima for  $E_\phi$  in the  $\phi=90^\circ$  pattern is described by the average error,  $(0.5^\circ, 0.2 \text{ dB})$ , reported in Table 1. The average error over all the minima in  $E_\theta$  in the  $\phi=0^\circ$  pattern is  $0.4^\circ$ , 2.1 dB. The error is higher in the field strength in the minima than in the maxima.

In Table 1 no errors are reported for the  $E_\phi$  component in the  $\phi=0^\circ$  elevation pattern. The  $E_\phi$  field strength should be zero due to the symmetry of the handset about an xz plane through the antenna. In the computation the maximum field strength in  $E_\phi$  is -65.8 dB. This is the residual obtained by computing the radiation pattern with single precision arithmetic in FDTD. In the wire-grid model, which uses double precision arithmetic, the  $E_\phi$  field is about -148 dB. In the measurement, the maximum  $E_\phi$  field is -21.2 dB, much larger.

In the  $\phi=90^\circ$  pattern, in  $E_\theta$  the maxima have an average error of  $1.2^\circ$ , 0.3 dB, and the minima,  $0.5^\circ$  and 13.1 dB. The fairly sharp minima agree well in position but not in depth. The almost-isotropic pattern in  $E_\phi$  has a large angular error in the position of the maxima and minima, but a small field strength error of 0.2 dB in the maxima, and 2.2 dB in the minima.

The cause of asymmetry in the measured patterns was sought extensively. The azimuth pattern for both  $E_\theta$  and  $E_\phi$  should be symmetric about  $\phi=0$  degrees. The  $E_\phi$  polarization in the  $\phi=0^\circ$  elevation pattern should be equal to zero. The  $\phi=90^\circ$  elevation pattern should be symmetric about  $\theta=0^\circ$ . Any asymmetry in the measurement setup can lead to unsymmetrical radiation patterns. Thus to measure the  $\phi=0^\circ$  pattern, the handset is lain upon its face on a styrofoam block; this puts a "half space" of styrofoam below the handset, and free space above, and so the setup is unsymmetrical. This may lead to unsymmetrical surface currents on two faces of the handset case, and hence raise the



level of the cross-polarized field in the  $\phi=0^\circ$  radiation pattern. For the measurement of the  $\phi=90^\circ$  pattern, the handset is laid on its edge on the styrofoam block and the setup is symmetrical about an  $xz$  plane through the center of the handset case. Also, for azimuth pattern the handset stands on its base and the measurement setup is quite symmetrical. But the handset itself has some lack of symmetry. Thus one side of the handset has two small holes in it for the switch that controls the oscillator, and for a red LED to show that the oscillator is switched on. Experiments with FDTD suggest that the holes could raise the cross-polarized field to about  $-40$  dB in the  $\phi=0^\circ$  elevation pattern. Also, it is difficult to maintain the wire antenna perfectly straight. Numerical experiments with the wire-grid model show that a 1 mm deviation in the 88.2 mm antenna from straightness could raise the cross-polarized field in this pattern to about  $-40$  dB. No single reason was found for the  $-21.2$  dB cross-polarized fields seen in the measurement in Fig. 3.

**Table 1**  
Comparison of the Average Error Between  
the Computed and Measured Patterns for the Handset Alone

Pattern	$E_\theta$		$E_\phi$	
	Maxima	Minima	Maxima	Minima
$\theta = 90^\circ$	1.5°, 0.5 dB	1.5°, 0.8 dB	1.8°, 0.3 dB	5°, 35.4 dB
$\phi = 0^\circ$	0.5°, 0.2 dB	0.4°, 2.1 dB	-	-
$\phi = 90^\circ$	1.2°, 0.3 dB	0.5°, 13.1 dB	21.2°, 0.2 dB	13.5°, 2.2 dB

### V. The Handset and Box Head

The “box head” is a thin-walled plexiglas box filled with liquid having the same electrical parameters as the brain. The box has outside dimensions 17.07 by 13.89 by 21.06 cm and wall thickness 0.5 cm. It is filled with a mixture of de-ionized water, sugar and salt[21] having a measured relative permittivity and conductivity at 850 MHz of 40.42 and 1.064 S/m, respectively[22]. The jig shown in Fig. 5 holds the handset in a well-known, reproducible position relative to the box head. The jig consists of a styrofoam top piece and bottom piece, fastened together with four long fiberglass bolts, with a plexiglas washer and a fiberglass bolt at each end. Fig. 6 shows the relative position of the handset, box head and fiberglass bolts. The bottom of the handset box is aligned with the bottom of the box head. The handset surface is 0.95 cm from the box, and is offset by 5.86 cm from the back of the box.

The fiberglass bolts are 316 mm in length, and 12.7 mm in diameter. The fiberglass nuts are hexagonal and are 22.3 mm across the flat surfaces of the hexagon. They are 16 mm thick. The plexiglas washers are 48.3 mm in diameter and 2.8 mm thick. Fig. 6 gives the position of the bolts, nuts and washers relative to the handset.

### A. FDTD Model of the Handset and Box Head

Because the fiberglass bolts affect the handset's radiation patterns, particularly in the minima, the bolts were included in the FDTD model. With a cell size of 2.205 mm the circular cross-section of the bolts can be reasonably represented with a staircase of cubical cells. The cell model was derived from the geometry of Fig. 6 by assigning to each cell the permittivity and conductivity of the material at the cell center. This leads to a box model having a plexiglas wall 2 cells or 4.41 mm thick, modeling a plexiglas layer 5 mm thick. The overall box dimensions in the cell model are 78 by 63 by 95 cells or 17.20 by 13.89 by 20.95 cm, compared to the true dimensions of 17.07 by 13.89 by 21.06 cm. The FDTD code derives a value of permittivity and conductivity to update each electric field component as the average of the values for the four cells adjacent to the edge. Thus to update an electric field component in a plane separating free-space cells from plexiglas cells, the average of the permittivity of free-space and plexiglas is used, as is the average conductivity. This leads to accurate alignment of the resonant frequencies of a dielectric cube resonator with the measured resonant frequencies[16]. The bolts, nuts and washers of the measurement jig of Fig. 4 were included in the cell model, but not the styrofoam blocks.

The electrical parameters of fiberglass were approximated with the values given in Ref. [23] for 3 GHz, of  $\epsilon_r = 3.99$  and loss tangent  $\tan \phi = 0.0241$ . The plexiglas washer was represented with relative permittivity  $\epsilon_r = 3.4$ , and no loss[24]. Of the materials in the model, the lossy, high-permittivity brain-equivalent liquid has the shortest wavelength and determines the cell model's limiting frequency of 2126 MHz for cells smaller than a tenth of a wavelength. This is well above our operating frequency of 850 MHz. The FDTD code was run with a ten-cell layer separating the model's surfaces from the outer boundary of the cell space. As above, the four layers adjacent to the model were free space and the remaining six layers make up a PML absorbing boundary. The FDTD code was run for 4096 steps. Although the cavity inside the box forms a dielectric resonator, the brain-equivalent liquid is so lossy that the sinusoidal steady state is reached long before 4096 time steps have been completed.

### B. Handset and Box Head Radiation Patterns

We will imagine that the user holds the handset in the right hand against the right ear. Thus in Fig. 1, the user faces in the  $+x$  direction and the head is located in the  $+y$  half space. Fig. 7 shows the principal plane patterns of the handset and box head. In the azimuth pattern, to the user's right, in the  $\phi = 270^\circ$  direction, the computed  $E_\theta$  field rises from  $-0.9$  dB with no box to  $1.6$  dB with the box head. Thus when the box lies behind the handset, the field strength is raised. This is expected to depend on the distance from the handset to the surface of the head[5]. To the user's left at  $\phi = 90^\circ$ , the handset lies between the head and the observer, and the field strength is reduced from  $-0.9$  dB with no head to  $-5.5$  dB with the box head. The head raises the level of the cross-polarized field and completely changes its radiation pattern. With the head, the  $E_\phi$  component has a maximum value of  $-4.4$  dB and a deep minimum near  $90$  degrees.

The  $\phi = 0^\circ$  or back-to-front pattern shows larger field strengths in  $E_\theta$  above the azimuth plane than for the handset alone. Thus the minor lobes in the handset-alone pattern at  $31^\circ$ ,  $-6.7$  dB and  $315^\circ$ ,  $-4.2$  dB rise in field strength and change angular

location to  $48^\circ$ ,  $-3.2$  dB and  $310^\circ$ ,  $-3.3$  dB. The sharp minima in the handset-alone pattern at  $60^\circ$  and  $316^\circ$  are filled in by the presence of the box head. Also, there is now a cross-polarized field of maximum field strength  $-1.6$  dB. The  $\phi = 90^\circ$  or side-to-side pattern in  $E_\theta$  is considerably changed to the user's left where the head lies between the handset and the observer. To the user's right with the head behind the handset, the maximum at  $322^\circ$ ,  $-6.6$  dB rises to  $327^\circ$ ,  $-2.5$  dB; the minimum at  $293^\circ$ ,  $-16.9$  dB rises to  $296^\circ$ ,  $-12.8$  dB; and the major lobe at  $240^\circ$ ,  $4.0$  dB for the handset alone rises to  $245^\circ$ ,  $5.4$  dB. The cross-polarized field pattern changes in shape but not greatly in maximum value, from  $-10.6$  dB for the handset alone to  $-10.9$  dB for the handset and box head.

### C. Comparison of the Measured and the Computed Patterns

Table 2 shows the average errors in the angular position and the field strength at the maxima and at the minima of the computed and measured patterns, for the handset and box head. The smooth  $E_\theta$  pattern in the  $\theta = 90^\circ$  plane has a  $7.5$  degree error in the angular position of the maximum, but the field strength in the maxima agrees to  $0.6$  dB. The minimum is  $10^\circ$  in error in position but only  $0.4$  dB in field strength. The  $E_\phi$  pattern agrees well in its two maxima, with an average positional error of  $1^\circ$  and average field strength error of  $0.2$  dB. The error in the sharp minimum near  $245$  degrees dominates the  $32$  dB average error in the minima. In the  $\phi = 0^\circ$  pattern, the average error in the position of the four maxima in  $E_\theta$  is  $1.1^\circ$  and in the field strength,  $0.3$  dB. The average error in the four minima is  $1.6^\circ$  and  $1.5$  dB. In  $E_\phi$ , the relatively smooth pattern shows a large  $15^\circ$  average error in the angular position of the minima, but only  $1.4$  dB average error in the field strength. In the  $\phi = 90^\circ$  pattern, in  $E_\theta$  the average error in the maxima is  $1.9^\circ$  and  $0.7$  dB, and in the minima,  $1.5^\circ$  and  $1.4$  dB. The  $E_\phi$  pattern has average errors of  $0.7$  dB in the maxima and  $1.7$  dB in the minima, which is surprising considering that we expect larger error in the sharp, deep minimum at about  $190$  degrees.

**Table 2**  
Comparison of the Computed and Measured Patterns  
for the Handset and Box Head

Pattern	$E_\theta$		$E_\phi$	
	Maxima	Minima	Maxima	Minima
$\theta = 90^\circ$	$7.5^\circ, 0.6$ dB	$10^\circ, 0.4$ dB	$1^\circ, 0.2$ dB	$2^\circ, 3.2$ dB
$\phi = 0^\circ$	$1.1^\circ, 0.3$ dB	$1.6^\circ, 1.5$ dB	$5^\circ, 1.0$ dB	$15^\circ, 1.4$ dB
$\phi = 90^\circ$	$1.9^\circ, 0.7$ dB	$1.5^\circ, 1.4$ dB	$1.5^\circ, 0.7$ dB	$2.5^\circ, 1.7$ dB

### D. Effect of the Bolts on the Radiation Patterns



To measure the radiation patterns of the handset and box head, they are held in the mounting jig shown in Fig. 5, with its four fiberglass bolts. The bolts are included in both the measurements and computations shown above. We wanted to assess whether the bolts have a minor or a major effect on the handset's radiation patterns and so whether the patterns of the handset and box head with the bolts are similar to those with no bolts.

The principal plane patterns of the handset and the four bolts, but with no head model, were computed with FDTD and are compared with the handset-alone patterns as follows. In the azimuth pattern the maximum field in  $E_\theta$  is changed by 0.09 dB. In the elevation pattern for  $\phi = 0^\circ$ , deep minimum at  $60^\circ$ , -26.9 dB, with no bolts is changed to -19.2 dB with the bolts, a change of 7.7 dB. The minimum at  $283^\circ$ , -13.6 dB with no bolts, deepens to -16.4 dB with the bolts. In the elevation pattern for  $\phi = 90^\circ$ , the minimum in  $E_\theta$  at  $67^\circ$ , -15.6 dB with no bolts falls to -19.9 dB with bolts. In conclusion, the fiberglass bolts cause little change in the maxima, but change the field strength in the deep minima by as much as 7.7 dB in the minima.

To assess the effect of the mounting jig by measurement, the patterns of the handset were measured with the handset in the jig with no head model, and compared with the measured patterns in Fig. 3, which used simple styrofoam blocks to hold the handset on the rotator column. In the azimuth plane pattern,  $E_\theta$  at  $0^\circ$  rises by 0.4 dB with the bolts. The minimum changes from -6.0 dB to -5.3 dB, a field strength difference of about 0.7 dB. In the  $\phi = 0^\circ$  elevation pattern, the main lobe in  $E_\theta$  at 4.8 dB with no bolts falls to 4.2 dB with the bolts. The minor lobes in the pattern change by about 0.6 dB. The sharp minimum at -22.0 dB with no bolts rises to -18.8 dB with bolts. The maximum cross-polarized field is -21.2 dB with no bolts, and is -23.1 dB with the bolts. In the  $\phi = 90^\circ$  pattern, the main lobe in  $E_\theta$  at 4.1 dB with no bolts rises to 4.5 dB with the bolts. The minimum with no bolts at -15.1 dB falls to -17.8 dB with the bolts. In summary the bolts introduce changes in the lobes of 0.4 to 1 dB, with 0.6 dB a typical change. The minima change more strongly, by as much as 3.2 dB.

## VI. The Handset and Sphere Head

The sphere is a much more realistic approximation of the shape of a human head than is the rectangular box. The "sphere head" is a thin-walled plexiglas sphere 20.68 cm in diameter with a wall thickness of 3.65 mm. It is filled with the same water, sugar and salt mixture used above. The volume occupied by the "brain liquid" is 4157 cc is almost the same as the box head's liquid volume of 4155 cc; both are almost the same as the sphere in Ref. [8], with a diameter of 20 cm and a volume of 4189 cc. However, in Ref. [8] the sphere was filled with liquid representing muscle tissue.

The handset and sphere are held in a jig similar to that of Fig. 5. The bottom of the sphere is aligned with the bottom of the handset as shown in Fig. 8, which gives the position of the center of the sphere relative to the handset. The bolt, nut and washer assemblies are the same as used for the box head jig. Fig. 8 shows the position of the bolts, nuts and washers relative to the handset.

### A. FDTD Model of the Sphere Head

The FDTD cell model must approximate the curved surface of the sphere with a staircase of cubical cells, and so the fidelity of the cell model is poorer than that of the box head. The sphere, modeled with 2.205 mm cells, is 94 cells in diameter, or 20.73 mm, slightly larger than its true size of 20.68 mm. The plexiglas wall is represented as 2 cells or 4.41 mm thick compared to its true thickness of 3.65 mm. The distance from the handset surface to the sphere is 4 cells or 8.82 mm, approximating the true distance of 9.3 mm. The FDTD model includes the four fiberglass bolts, and the washers and nuts. As before, the coefficients for updating the electric field component on each cell edge are derived from the permittivity and conductivity averaged over the four adjacent cells, which tends to smooth the staircased surface. The PML absorbing boundary is as described above.

### B. Handset and Sphere Head Patterns

Figure 9 shows the principal plane patterns of the handset operating near the sphere head. Comparing Figs. 7 and 9 shows that the azimuth pattern with the sphere head is quite similar to that with the box head, though the sphere and the box are quite different shapes. The field to the user's right, where the head is behind the handset, is larger with the box head than with the sphere. The maximum field for the box is 2.4 dB and for the sphere, 2.1 dB. The box blocks the field more effectively than the sphere, so that to the user's left at  $90^\circ$  the field with the box is -5.5 dB and with the sphere, -4.6 dB. The sphere introduces a shallow minimum at  $144^\circ$ , -12.1 dB that is not seen in the box patterns. The cross-polarized field for the box and for the sphere is remarkably similar. In the back-to-front or  $\phi = 0^\circ$  elevation pattern, comparing Fig. 3 with Fig. 7 and Fig. 9 shows that the sphere has less effect on the handset pattern for  $E_\theta$  than does the box. The cross-polarized field has a lower maximum value of -3.4 dB with the sphere than for the box at -1.6 dB. In the side-to-side or  $\phi = 90^\circ$  elevation pattern for  $E_\theta$  the deep minimum for the handset alone at  $-20.0$  dB,  $293^\circ$  is not as completely filled with the sphere head, at -18.3 dB, than with the box head, at -12.1 dB. Above the user's left hand, the handset alone has a minimum at  $67^\circ$  of -19.9 dB that is nearly completely filled in by the box head, but enhanced by the sphere head to -20.8 dB,  $77^\circ$ . Both the box and the sphere change the handset-alone deep null at  $180^\circ$ . With the box, the minimum falls at -13.2 dB,  $146^\circ$ ; and with the sphere -19.6 dB,  $155^\circ$ . The cross-polarized field for the handset alone has a maximum value of -10.6 dB; with the box head, -10.9 dB; and with the sphere head, -11.8 dB.

### C. Comparison of the Measured and Computed Patterns

Table 3 compares the computed and measured patterns for the handset and sphere head. As before, we will examine the average errors in the angular location and field strength at the maxima, and the average errors at the minima. The smooth  $E_\theta$  pattern in the  $\theta = 90^\circ$  plane has a large error in the angular location of the maximum and of the minimum, of  $6.5^\circ$  and  $3^\circ$  respectively. The maximum the field strength agrees to within 0.8 dB, and the minimum to 0.7 dB. The  $E_\phi$  pattern has angular errors of  $1.5^\circ$  in the location of the maxima and  $1.8^\circ$  in the minima. The average field strength error is 0.8

dB for the maxima, and 3 dB for the minima. In the  $\phi = 0^\circ$  pattern,  $E_\theta$  has average errors in the maxima of  $1.6^\circ$  and 0.2 dB, but the sharp, deep minimum near 180 degrees raises the average field strength error in the minima to 4 dB. The  $E_\phi$  pattern is smooth, with an average error in the maxima of 1.2 dB and in the minima of 3.2 dB. In the  $\phi = 90^\circ$  pattern, the average error in the maxima in  $E_\theta$  is  $2^\circ$  in angle and 0.6 dB in field strength. However, the deep minima incur an average error of 6.5 dB in the field strength. In the smooth  $E_\phi$  pattern, the average error in angular location of the maxima is  $12^\circ$  but the field strength error only 0.8 dB. The error in the position of the minima is  $6.3^\circ$  with a field strength error of 0.4 dB. We note that the measured field has a maximum at  $28^\circ$  of -13.7 dB and this maximum is entirely absent in the computed pattern.

**Table 3**  
Comparison of the Computed and Measured Radiation Patterns  
for the Handset and Sphere Head

Pattern	$E_\theta$		$E_\phi$	
	Maxima	Minima	Maxima	Minima
$\theta = 90^\circ$	$6.5^\circ, 0.8 \text{ dB}$	$3.0^\circ, 0.7 \text{ dB}$	$1.5^\circ, 0.8 \text{ dB}$	$1.8^\circ, 3.0 \text{ dB}$
$\phi = 0^\circ$	$1.6^\circ, 0.2 \text{ dB}$	$1.9^\circ, 4.0 \text{ dB}$	$4.5^\circ, 1.2 \text{ dB}$	$3.8^\circ, 3.2 \text{ dB}$
$\phi = 90^\circ$	$2.0^\circ, 0.6 \text{ dB}$	$2.1^\circ, 6.5 \text{ dB}$	$12^\circ, 0.8 \text{ dB}$	$6.3^\circ, 0.4 \text{ dB}$

## VII. Conclusion

This paper has presented the principal plane radiation patterns of a simple portable radio handset in isolation, and operating near a box model and near a sphere model of the head. Figs. 3, 7 and 9 show that the head has a considerable effect on the handset's fields, particularly on the cross-polarized field. The azimuth pattern is similar for the box head and sphere head despite their different shapes. The head reduces the handset's field when the head lies between the handset and the observer; and enhances the field when the head lies behind the handset. The sphere has less effect on the handset's elevation patterns than does the box.

This paper presents a validation of FDTD calculations for handset and head radiation patterns, using comparisons with measured patterns. The measured patterns have been scaled to approximately the same radiated power as the computed patterns. Both the principal polarization and the cross polarization have been compared. In general very good agreement has been shown between the computed and the measured patterns. The relative level of the principal polarization to the cross-polarization agrees very well for all three configurations.

In the computation it was found that the minima in the radiation patterns are more sensitive to the cell size than are the maxima. In the measurement, the 330 cm range from the handset to the measurement horns is not far enough for accurate field



strengths in the minima. Thus the agreement of our computations and measurements is better in the maxima than in the minima. The average errors in the minima in Tables 1, 2 and 3 reflects this reality. Since the radiation patterns were computed and measured at one degree increments, positional errors of less than one degree represent very good agreement.

The box head's surfaces are parallel to the coordinate planes. Hence the box head's geometry can be closely approximated by positioning the air-to-plexiglas and plexiglas-to-brain boundaries at the nearest cell surfaces. However the sphere's curved surface must be approximated with a staircase of cells. Hence we might expect the "modeling error" to be larger for the sphere head than for the box head, and that this would be reflected in the degree of agreement with the measurements.

Tables 1, 2 and 3 were prepared to test this conjecture. The tables compare the average error in the angular location of the maxima, and the average error in the field strength in the maxima, for both  $E_\theta$  and  $E_\phi$ . Because the accuracy of both the computation and the measurement is best in the maxima, we will compare the box and sphere head cases based on the maxima. Comparing the errors for the box head and for the sphere head in the azimuth pattern shows more positional error for  $E_\theta$  for the box than the sphere, but less error in the field strength. For  $E_\theta$  in the elevation patterns, the positional errors are slightly more for the sphere than the box, but the field strength errors are less for the sphere than for the box. In  $E_\phi$ , the positional errors are about the same except for the  $\phi=90^\circ$  pattern for the handset and sphere, where the angular position of the broad lobe near 250 degrees disagrees by  $23^\circ$  between the computed and the measured pattern. The field strength errors are slightly larger for the sphere than for the box.

These tables show that the agreement between the computation and the measurement is slightly better for the handset in isolation than for the handset with either of the heads. But the handset and box head patterns do not agree markedly better with the measurement than do the handset and sphere head patterns. In fact, the agreement is about the same for the handset and box head and for the handset and sphere head. We do not see a larger error due to staircasing the surface of the sphere. Evidently, a staircased model of the sphere's curved surface permits the prediction of the field strengths to an accuracy comparable to that of our measurements. Similar accuracy would be expected in using FDTD to predict the radiation patterns of a handset and a much more realistic model of the head.

This paper has not included a hand wrapped around the surfaces of the portable radio. Because the hand would be located in a region of high field strength at the base of the handset case, it would dissipate power and have a significant effect on the radiation patterns.

In this paper the handset has been oriented vertically, whereas in use handsets are tilted relative to the head. Tilting the handset couples a much larger portion of the handset's energy into the  $E_\phi$  field component. The radiation patterns of the tilted handset and head are found in FDTD by maintaining the handset vertical in the cell space coordinate system and tilting the dielectric structure representing the head, as described in Refs. [3] and [15]. This allows the handset's perfectly-conducting surfaces to be

represented without staircasing errors. Coordinate transformations are then used to obtain radiation patterns as if the head were vertical and the handset tilted. We would expect to solve the tilted handset and complex head problem by this scheme to the same accuracy as shown in this paper for the vertical handset and simple heads.

## References

- [1] S. Faruque, "Cellular Mobile Systems Engineering", Artech House, Boston, 1996.
- [2] Y. Rahmat-Samii and M.A. Jensen, "Personal Communications Antennas: Modern Design and Analysis Techniques Including Human Interaction", Short Course presented at the IEEE Antennas and Propagation Society International Symposium, Montreal, Quebec July 18, 1997.
- [3] G. Lazzi and O.P. Gandhi, "Realistically Tilted and Truncated Anatomically Based Models of the Human Head for Dosimetry of Mobile Telephones", IEEE Trans. on Electromagnetic Compatibility, Vol. 39, No. 1, pp. 55-61, February, 1997.
- [4] V. Hombach, K. Meier, M. Burkhardt, E. Kuhn and N. Kuster, "The Dependence of EM Energy Absorption Upon Human Head Modeling at 900 MHz", IEEE Trans. on Microwave Theory and Techniques, Vol. MTT-44, No. 10, pp. 1865-1873, October, 1996.
- [5] M. Okoniewski and M.A. Stuchly, "A Study of the Handset Antenna and Human Body Interaction", IEEE Trans. on Microwave Theory and Techniques, Vol. MTT-44, No. 10, pp. 1855-1864, October, 1996.
- [6] K.S. Yee, "Numerical Solution of Initial Value Problems Involving Maxwell's Equations in Isotropic Media", IEEE Trans. on Antennas and Propagation, Vol. AP-14, No. 3, pp. 302-307, May, 1966.
- [7] A. Taflove, "Advances in Computational Electrodynamics. The Finite-Difference Time-Domain Method", Artech House, Boston, 1998.
- [8] J. Toftgard, S.N. Hornsleth, and J. Bach Andersen, "Effects on Portable Antennas of the Presence of a Person", IEEE Trans. on Antennas and Propagation, Vol. 41, No. 6, pp. 739-746, June, 1993.
- [9] M.A. Jensen, Y. Rahmat-Samii, "E.M. Interaction of Handset Antennas and a Human in Personal Communication", *Proc. IEEE*, Vol. 83, No. 1, pp. 7-17, January, 1995.
- [10] C.W. Trueman, S.J. Kubina, D. Cule and W.R. Lauber, "Validation of the FDTD Near Fields of a Portable Radio Handset and a Simple Head", Conference Proceedings, 15th Annual Review of Progress of the Applied Computational Electromagnetics Society, pp. 660-667, Monterey, California, March 16-28, 1999.
- [11] C.W. Trueman, S.J. Kubina, J.E. Roy, W.R. Lauber, and M. Vall-llossera, "Validation of FDTD-Computed Handset Patterns by Measurement", Conference Proceedings, 14th Annual Review of Progress of the Applied Computational Electromagnetics Society, pp. 93-98, Monterey, California, March 16-20, 1998.
- [12] C.W. Trueman and S.J. Kubina, "Near Field Computations with Model Heads and Far Field Computations for the Model Cellular Radio", Final Report, Contract Number U6800-9-0390, Technical Note No. TN-EMC-99-01, Dept. of Electrical and Computer Engineering, Concordia University, March 31, 1999.

- [13] M. Burkhardt, N.Chavannes, K. Pokovic, T. Schmid and N. Kuster, "Study on the FDTD Performance for Transmitters in Complex Environments", ICECOM Symposium, Dubrovnik, October, 1997.
- [14] M. Siegbahn, S. Mazur and C. Tornevik, "Comparisons of Measurements and FDTD Calculations of Mobile Phone Electromagnetic Far-Fields and Near-Fields", 1997 IEEE AP-S International Symposium Digest, pp. 978-981, Montreal, July 13-18, 1997.
- [15] G. Lazzi, S.S. Pattnaik and O.P. Gandhi, "Experimental and FDTD-Computed Radiation Patterns of Cellular Telephones Held in Slanted Operational Conditions", IEEE Trans. On Electromagnetic Compatibility, Vol. 41, No. 2, pp. 141-144, May, 1999.
- [16] C.W. Trueman, S.R. Mishra, C.L. Larose and R.K. Mongia, "Resonant Frequencies and Q Factors of Dielectric Parallelepipeds by Measurement and by FDTD", IEEE Trans. on Instrumentation, Vol. 44, No. 2, pp. 322-325, April 1995.
- [17] J.M. Bertrand and W.R. Lauber, "CRC Model Transmitter", Communications Research Centre Technical Memorandum VPRB-05-97, May, 1997.
- [18] J.P. Berenger, "A Perfectly-Matched Layer for the Absorption of Electromagnetic Waves", Journal of Computational Physics, Vol. 114, pp. 185-200, 1994.
- [19] J.E. Roy, W.R. Lauber and J.M. Bertrand, "Measurements of the Electromagnetic Far-Fields Produced by a Portable Transmitter (Principal Planes)", Electromagnetics and Compatibility Group, Communications Research Centre report # CRC-RP-98-002, Ottawa, February, 1998.
- [20] G.J. Burke and A.J. Poggio, "Numerical Electromagnetics Code - Method of Moments, Part I: Program Description-Theory", Technical Document 116, Naval Electronic Systems Command(ELEX 3041), July, 1977.
- [21] G. Hartsgrrove, A. Kraszewski and A. Surowiec, "Simulated Biological Materials for Electromagnetic Radiation Absorption Studies", *Bioelectromagnetics*, Vol. 8, pp. 29-36, 1987.
- [22] CRC, private communication, Joe Seregelyi, September 11, 1997.
- [23] T. Moreno, "Microwave Transmission Design Data", Artech House, 1989, originally published by McGraw-Hill, 1948.
- [24] C.A. Balanis, "Advanced Engineering Electromagnetics", Wiley, New York, 1989.



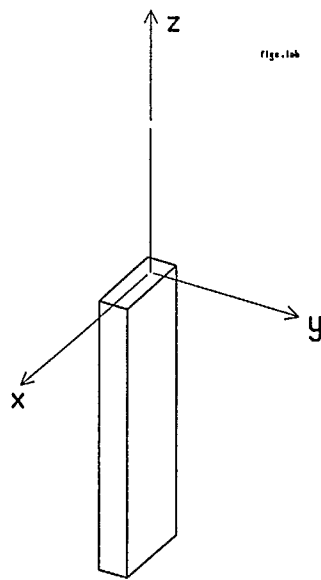


Fig. 1 The portable radio handset in the  $xyz$  coordinate system.

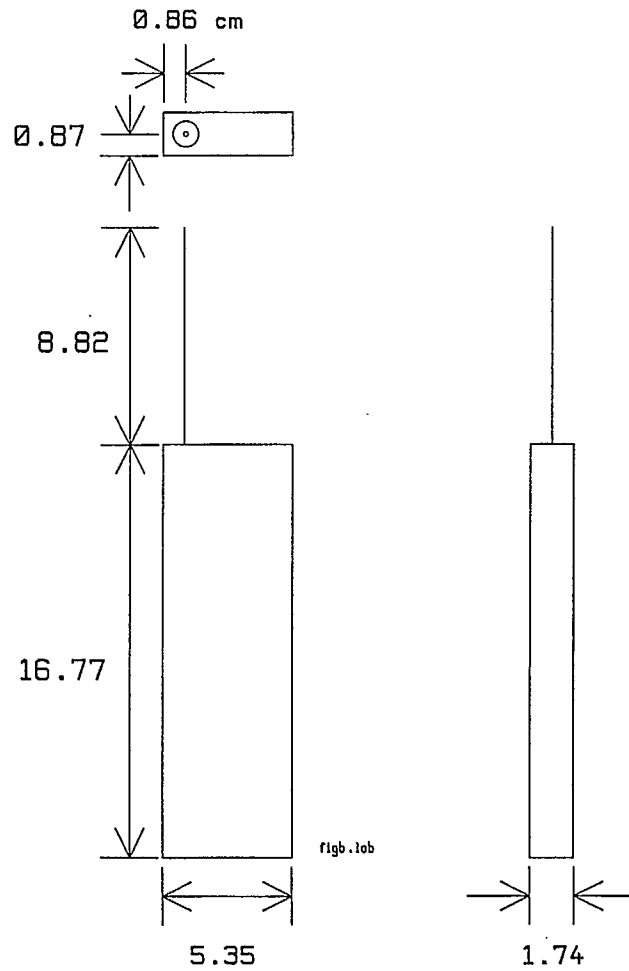
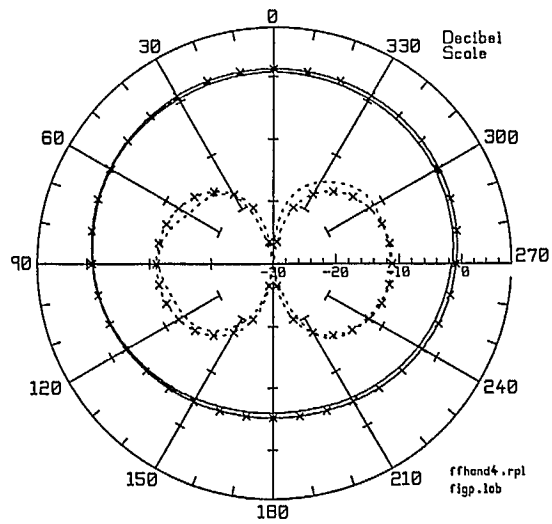
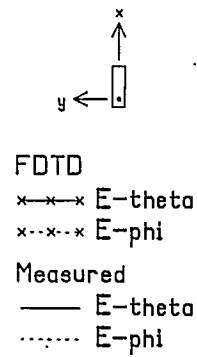
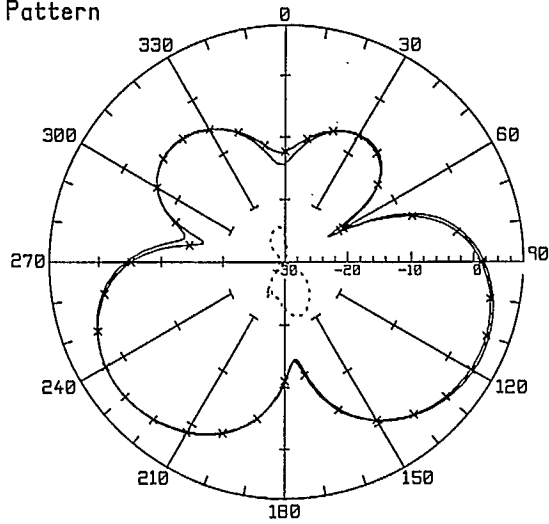
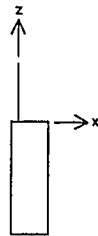


Fig. 2 The dimensions of the portable radio handset.

# Handset Alone Azimuth Pattern



## Phi=0 Elevation Pattern



## Phi=90 Elevation Pattern

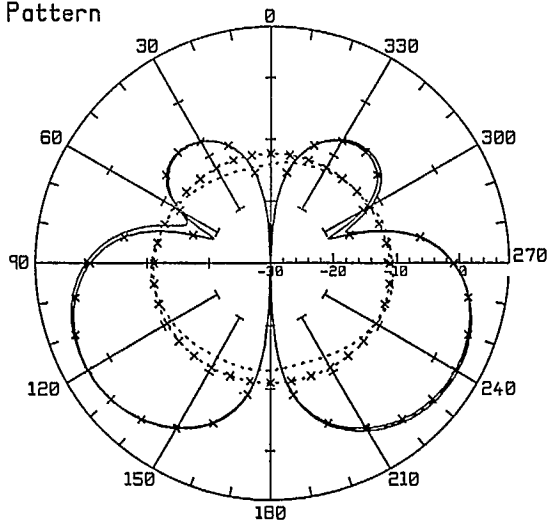
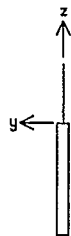


Fig. 3 The radiation patterns of the portable radio handset in isolation.

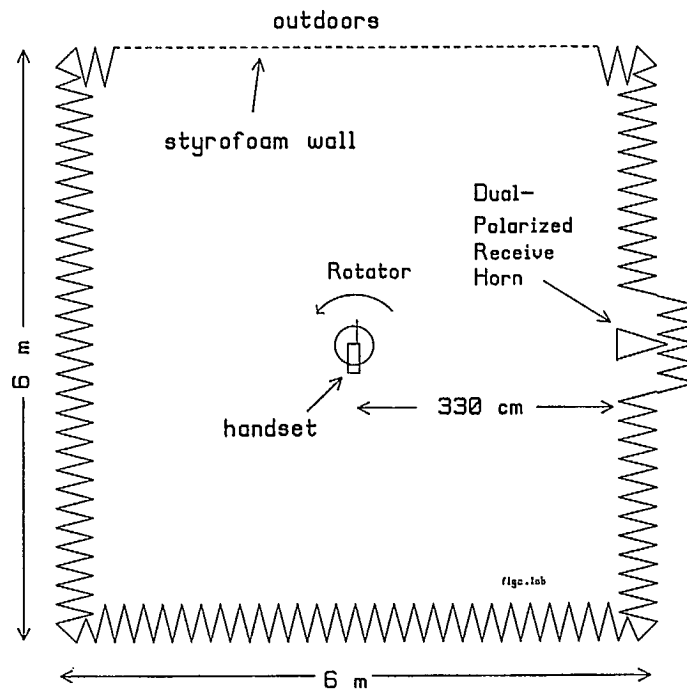


Fig. 4 The anechoic chamber setup used to measure the principal plane patterns.



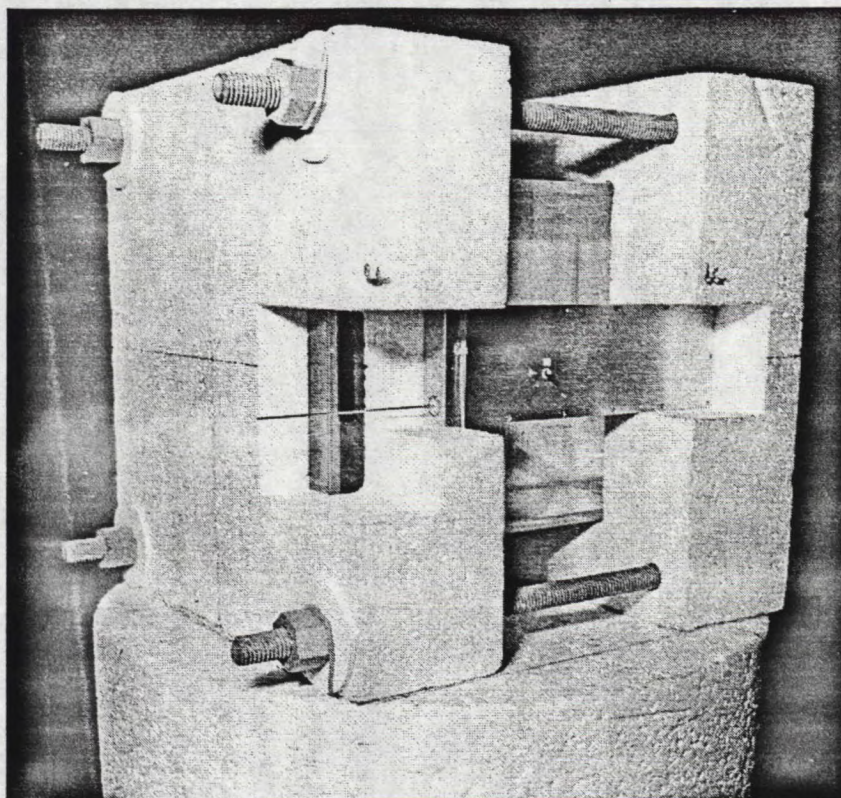


Fig. 5 The handset and box head mounted in the styrofoam jig, positioned on top of the rotator in the anechoic chamber.

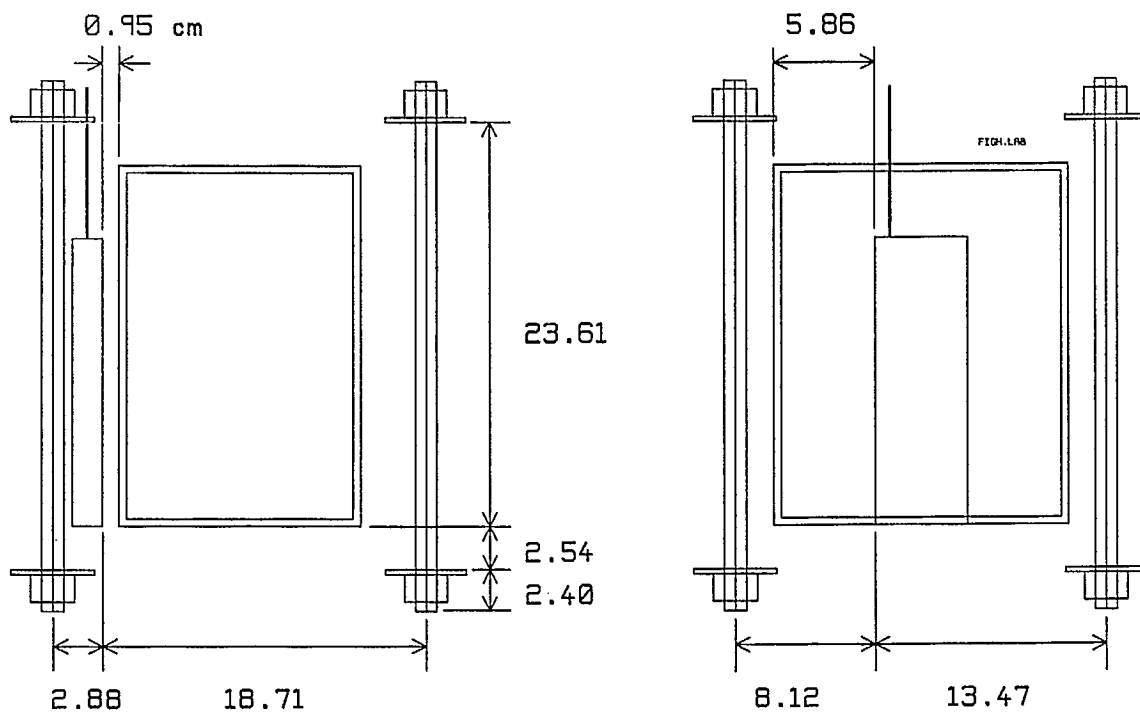
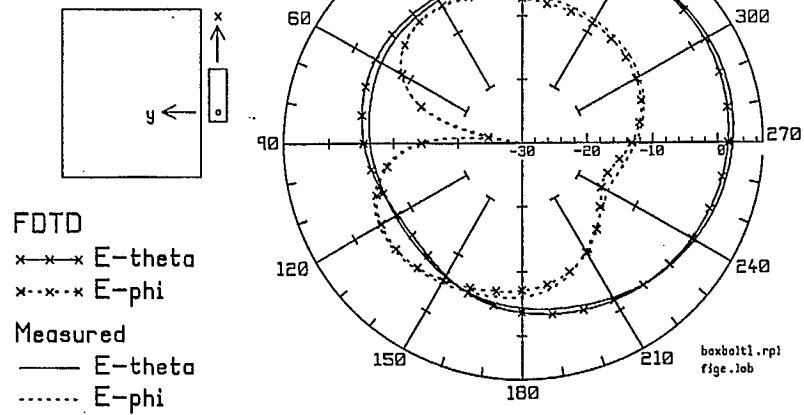
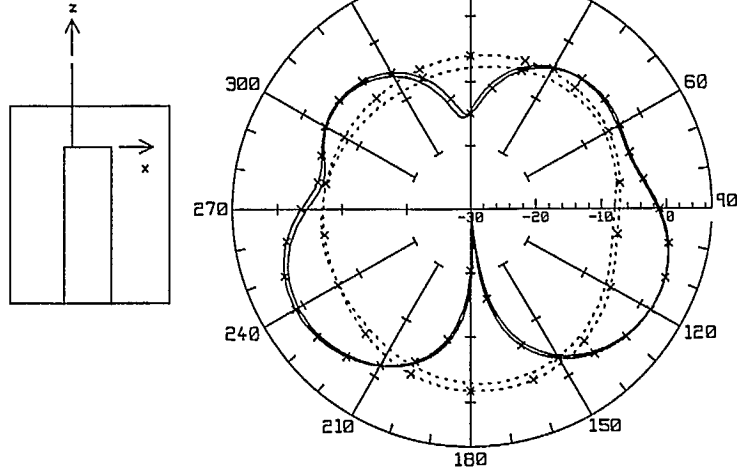


Fig. 6 The position of the box head and bolts relative to the handset.

# Handset and Box Head Azimuth Pattern



## Phi=0 Elevation Pattern



## Phi=90 Elevation Pattern

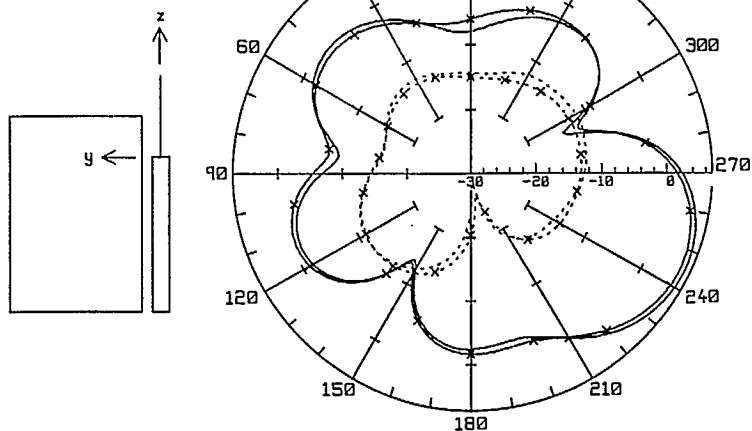


Fig. 7 The radiation patterns of the handset and box head.



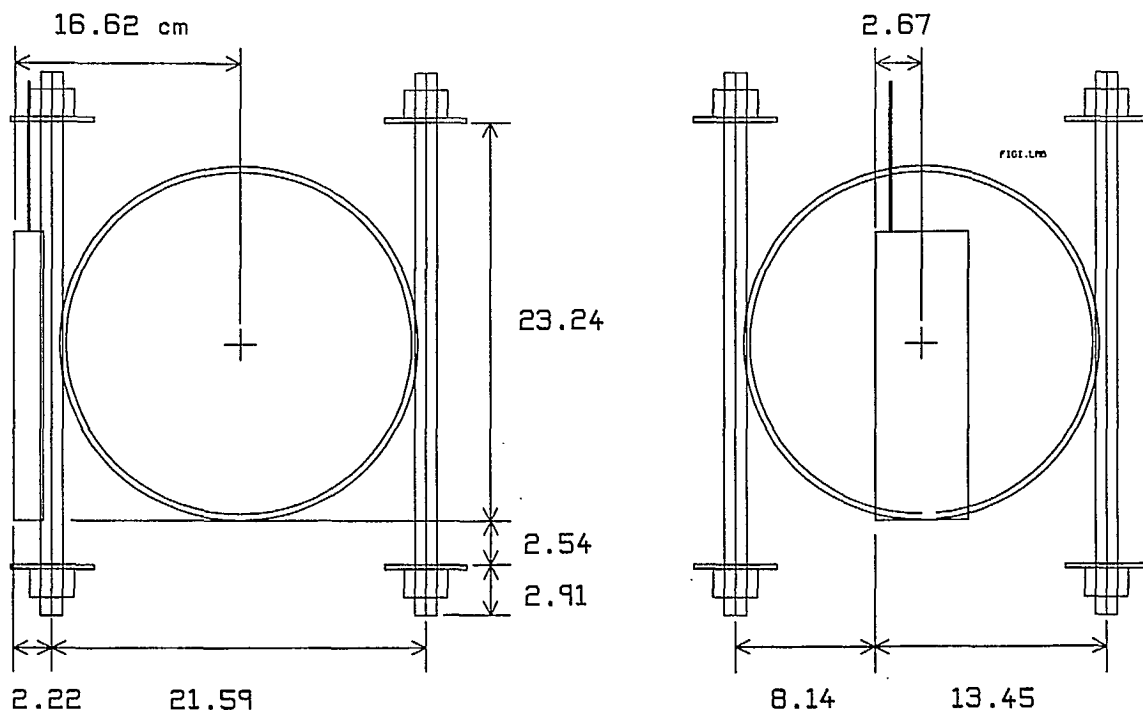
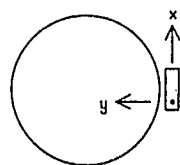


Fig. 8 The position of the sphere head and bolts relative to the handset.

# Handset and Sphere Head Azimuth Pattern



FDTD

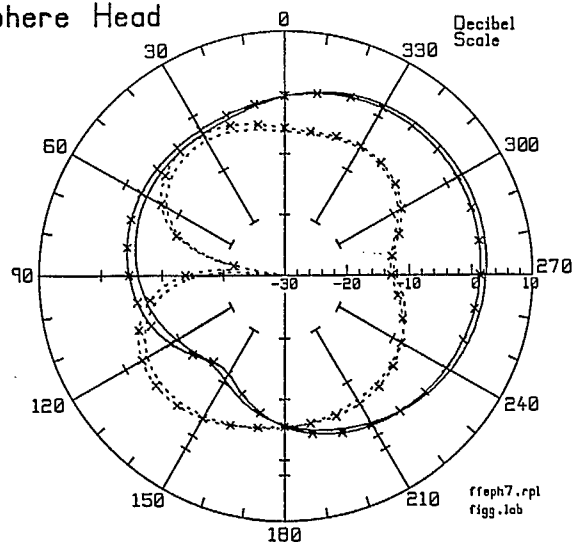
x-x-x E-theta

x--x--x E-phi

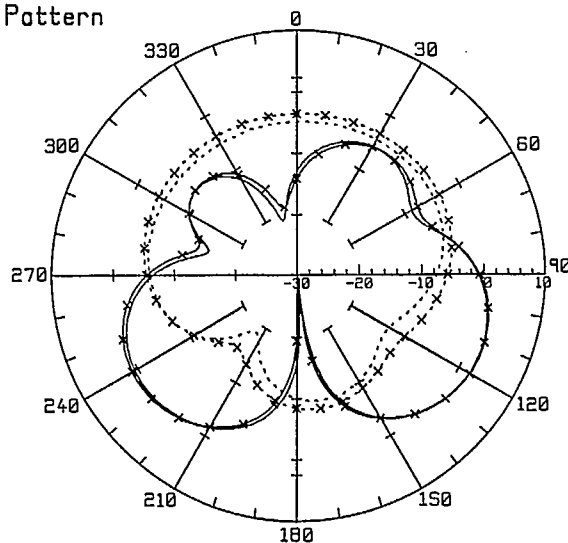
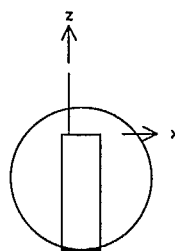
Measured

— E-theta

..... E-phi



## Phi=0 Elevation Pattern



## Phi=90 Elevation Pattern

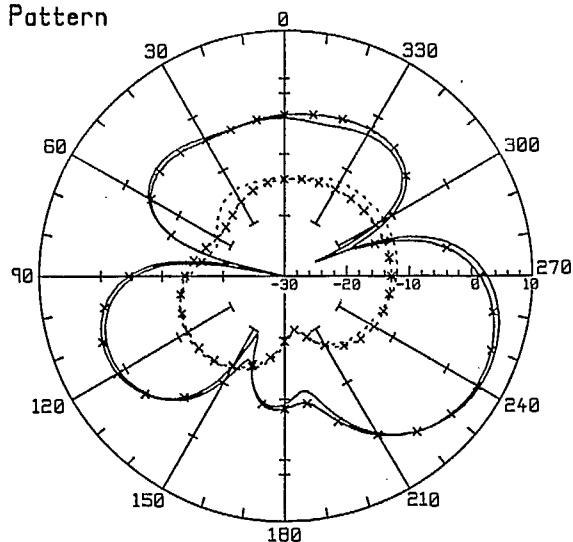
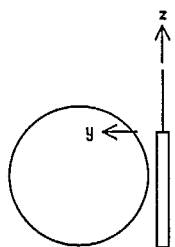


Fig. 9 The radiation patterns of the handset and sphere head.

## CRC Publication Approval and Record Form

This form is to be completed for the approval of all CRC publications and presentations. The level of approval varies with the category of the publication. For details of publication procedures, see the document: Publication Policy and Procedures. For items sponsored by DND, the DREO yellow and green sheets must also be prepared and submitted separately.

**Category A:** CRC Reports & CRC Technical Notes. **Category B:** Journal & conference papers. **Category C:** Contributions to outside documents such as TTCP, ITU, AGARD, standards, etc. **Category D:** Abstracts **Category E:** Documents with non-CRC employee as main author.

**Title:** Near Field Computations with Model Heads and Far Field Computations for the Model Cellular Radio

**Author(s):** Dr C.W. Trueman and Dr. S.J. Kubina

**Branch and Directorate** VPRS/REMC **Document category:** E

**Web Address (for CRC Reports & Technical Notes):** \_\_\_\_\_

**Details of Publication or Presentation:** (e.g. report type & number; name & sponsor of journal; technical body (ex. TTCP), or conference; date & place of publication or presentation; etc.)

Concordia University Contract report TN-EMC-99-01, March 31, 1999

CRC Contract No.U6800-9-0390

**Security Classification:** Unclassified

**Releasability:** Releasable ( ☒ ) Non releasable ( ☐ ) Conditionally releasable ( ☐ )

If limitations apply, describe the conditions: \_\_\_\_\_

**Intellectual Property:** May require IP protection. Copy sent to DMKT ( ☐ ) or Does not require IP protection ( ☐ ). Explain: \_\_\_\_\_

### Certifications

*All Categories:*

**Author and date:** \_\_\_\_\_

**Manager and date:** \_\_\_\_\_

*For Categories A and B:*

**Reviewer and date:** \_\_\_\_\_

**Editor and date:** \_\_\_\_\_

**VP and date:** \_\_\_\_\_

*For Category D:*

**VP and date:** \_\_\_\_\_



Bibliothèque CRC Library  
INDUSTRY CANADA / INDUSTRIE CANADA



208838